frontiers | Research Topics

Ultrasound micromanipulations and ocean acoustics: From human cells to marine structures

Edited by
Zhixiong Gong, Feiyan Cai, Wei Li and Thierry Baasch

Published in
Frontiers in Physics

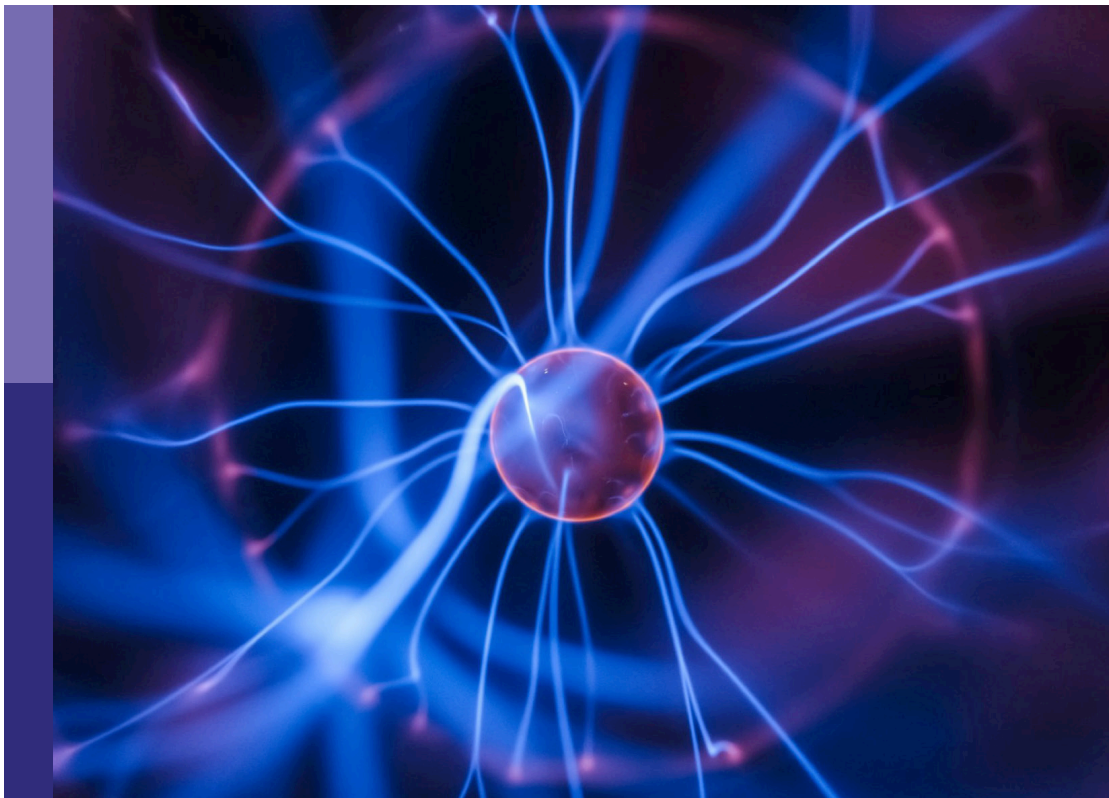

ISSN 1664-8714
ISBN 978-2-8325-2976-8
DOI 10.3389/978-2-8325-2976-8

About Frontiers

Frontiers is more than just an open access publisher of scholarly articles: it is a pioneering approach to the world of academia, radically improving the way scholarly research is managed. The grand vision of Frontiers is a world where all people have an equal opportunity to seek, share and generate knowledge. Frontiers provides immediate and permanent online open access to all its publications, but this alone is not enough to realize our grand goals.

Frontiers journal series

The Frontiers journal series is a multi-tier and interdisciplinary set of open-access, online journals, promising a paradigm shift from the current review, selection and dissemination processes in academic publishing. All Frontiers journals are driven by researchers for researchers; therefore, they constitute a service to the scholarly community. At the same time, the *Frontiers journal series* operates on a revolutionary invention, the tiered publishing system, initially addressing specific communities of scholars, and gradually climbing up to broader public understanding, thus serving the interests of the lay society, too.

Dedication to quality

Each Frontiers article is a landmark of the highest quality, thanks to genuinely collaborative interactions between authors and review editors, who include some of the world's best academicians. Research must be certified by peers before entering a stream of knowledge that may eventually reach the public - and shape society; therefore, Frontiers only applies the most rigorous and unbiased reviews. Frontiers revolutionizes research publishing by freely delivering the most outstanding research, evaluated with no bias from both the academic and social point of view. By applying the most advanced information technologies, Frontiers is catapulting scholarly publishing into a new generation.

What are Frontiers Research Topics?

Frontiers Research Topics are very popular trademarks of the *Frontiers journals series*: they are collections of at least ten articles, all centered on a particular subject. With their unique mix of varied contributions from Original Research to Review Articles, Frontiers Research Topics unify the most influential researchers, the latest key findings and historical advances in a hot research area.

Find out more on how to host your own Frontiers Research Topic or contribute to one as an author by contacting the Frontiers editorial office: frontiersin.org/about/contact

Ultrasound micromanipulations and ocean acoustics: From human cells to marine structures

Topic editors

Zhixiong Gong — Shanghai Jiao Tong University, China

Feiyan Cai — Shenzhen Institute of Advanced Technology, Chinese Academy of Sciences (CAS), China

Wei Li — Huazhong University of Science and Technology, China

Thierry Baasch — Lund University, Sweden

Citation

Gong, Z., Cai, F., Li, W., Baasch, T., eds. (2023). *Ultrasound micromanipulations and ocean acoustics: From human cells to marine structures*.

Lausanne: Frontiers Media SA. doi: 10.3389/978-2-8325-2976-8

Table of contents

frontiers | Frontiers in Physics

TYPE Editorial
PUBLISHED 27 June 2023
DOI 10.3389/fphy.2023.1237899

OPEN ACCESS

EDITED AND REVIEWED BY
Guoliang Huang,
University of Missouri, United States

*CORRESPONDENCE
Zhixiong Gong,
zhixiong.gong@sjtu.edu.cn
Feiyan Cai,
fy.cai@siat.ac.cn
Wei Li,
hustliw@hust.edu.cn
Thierry Baasch,
thierry.baasch@bme.lth.se

RECEIVED 10 June 2023
ACCEPTED 15 June 2023
PUBLISHED 27 June 2023

CITATION
Gong Z, Cai F, Li W and Baasch T (2023), Editorial: Ultrasound micromanipulations and ocean acoustics: from human cells to marine structures.
Front. Phys. 11:1237899.
doi: 10.3389/fphy.2023.1237899

Editorial: Ultrasound micromanipulations and ocean acoustics: from human cells to marine structures

Zhixiong Gong[1]*, Feiyan Cai[2]*, Wei Li[3]* and Thierry Baasch[4]*

[1]Key Laboratory of Marine Intelligent Equipment and System, State Key Laboratory of Ocean Engineering, School of Naval Architecture, Ocean and Civil Engineering, Shanghai Jiao Tong University, Shanghai, China, [2]Paul C. Lauterbur Research Center for Biomedical Imaging, Shenzhen Institutes of Advanced Technology, Chinese Academy of Sciences, Shenzhen, China, [3]School of Naval Architecture and Ocean Engineering, Huazhong University of Science and Technology, Wuhan, Hubei, China, [4]Department of Biomedical Engineering, Lund University, Lund, Sweden

KEYWORDS

acoustic scattering, acoustical tweezers, acoustic streaming, underwater acoustics, phononic crystals and artificial materials

Editorial on the Research Topic
Ultrasound micromanipulations and ocean acoustics: from human cells to marine structures

1 Introduction

This Research Topic focuses on acoustic phenomena spanning from the manipulation of micro-particles and fluids in micrometer-sized cavities (e.g., [1]; [2]) to ocean exploration at macro scales (e.g., [3]). From the point of view of physical acoustics, some general theories and numerical models are uniform. For instance, the form functions of acoustic scattering from a sphere in an ideal medium are the same for a typical radius $a = 1$ m at the incident frequency $f = 1$ KHz in the field of ocean acoustics and for $a = 100\ \mu$m at $f = 10$ MHz in the field of ultrasound manipulation since the dimensionless frequency ka of these two cases are the same (with the wavenumber $k = 2\pi f/c$ and sound speed c in the medium.) This also convinces readers that the underlying equations and the physical modeling remain the same over those length scales. The underlying research topic presents a collection of recent developments in acoustofluidics, wave modulation with artificial materials, and ocean acoustics. Additional goals of this Research Topic are to help researchers from different fields to understand the common principles of physical acoustics and conduct interdisciplinary research or collaborations. More details as well as the collected papers can be found at the link: https://www.frontiersin.org/research-topics/45393.

2 Recent developments in three groups

In this section, we will briefly introduce the main contents and scientific contributions of each work into three groups.

2.1 Acoustofluidics

The paper by Pavlic et al. introduces an efficient hybrid method combining the Fully Viscous modeling approach with the existing limiting velocity method for the acoustic streaming computation in sharp-edge acoustofluidics. This hybrid method was validated in 2D and extended for 3D configurations. This method may facilitate a full understanding of 3D streaming and new devices for this rapidly growing field.

2.2 Wave modulation with artificial materials

Xia et al. demonstrates that near-perfect absorption of low-frequency sound can be achieved in an open tunnel by using two deep sub-wavelength Mie resonators composed of a multiple-cavity structure and an outer frame on three sides. Increasing the number of Mie resonators in the tunnel enables broadband near-perfect sound absorption. The proposed Mie resonator has potential applications in architectural acoustics and mechanical engineering, as well as in sound communication, bio-sensing, and noise reduction. Qu et al. investigate interface phenomena in Willis media both analytically and by the finite-element method. The main findings are that wave transmission at an interface depends on the magnitude and direction of the coupling vector. Additionally, they found that edge waves exist at the interface between a Willis media and a hard boundary, an ordinary fluid, or another Willis media. The study of Ye et al. presents a general design scheme of Luneburg lenses for focusing higher-order Lamb waves based on physical properties of the phase velocity dependence on various plate thickness. This work may help guide the experimental implementation with the aid of phononic crystals (PCs) and metamaterials for applications of wave manipulation and energy harvesting in fields such as non-destructive testing techniques and spatial modulation of ocean acoustics.

2.3 Ocean acoustics: propagation, radiation, and scattering

Shi et al. use the spherical microphone arrays (SMAs) extrapolation method to enlarge the array aperture virtually to improve the performance of SMA signal processing algorithms for sound source localization and identification. Although the present simulation and experimental demonstration are conducted in air, it shows great potential for the source location and identification of marine structures in ocean acoustics. Tian et al. study the influence of physical properties on the compression wave speed of seafloor sediment with numerical models and experimental measurements from 42 samples collected from the South China Sea. The intergranular friction model is demonstrated effective to show the dependence of the compression wave speed on the physical properties of seafloor sediments, which could be used to predict the unknown compression wave speed assuming the physical parameters are provided. Li et al. proposes a coupled CFD-BEM approach to predict the acoustic radiation and scattering of moving bubbles for low velocities. Results indicate that as the frequency increases, the acoustic directionality of radiation and scattering exhibit main and side lobes, and the scattering energy gradually concentrates in the forward direction of the incident wave. The displacement and velocity of a moving bubble significantly impact the directionality of the scattered sound field, making it possible to study bubble localization based on directionality shift. Yang et al. extend the traditional semi-analytical and semi-numerical T-matrix method to compute the acoustic scattering of a pair of rigid spheroids with the addition theorems of the spherical basis functions. The physical mechanism of the interference and time delay between specular reflection and Franz waves is revealed. This work has potential applications in the detection of underwater objects in ocean engineering and particle assembly in the field of acoustofluidics. The study of Tang et al. focuses on the optimization of complex geometries of underwater vehicle models with conning tower to improve the acoustic stealth based on the physical acoustic method. The Kirchhoff-approximation-based planar element method is verified by on-site lake experiments. More importantly, this work provides an option to design new 3D shapes of underwater vehicles with the good ability of acoustic stealth. Qu et al. conducted a similarity analysis of the flow-induced noise of a benchmark submarine and tried to establish a similarity law based on the dimensional analysis method. An important rule of the sound power level spectrums is revealed for the scale effect if the inflow speeds are the same. This work makes it possible to predict the flow-induced noise of large-scale marine structures by using scaled models if the similarity law based on the dipole source is followed.

Author contributions

ZG prepared the first draft of this Editorial. FC, WL, and TB help work out the introduction of the papers they edited. All authors read throughout, revised, and approved the work for publication.

Funding

FC thanks for the support from Shenzhen Science and Technology Program (Grant No. RCJC2022100809280801) and National Natural Science Foundation of China (11974372). TB is supported by the Swedish Research Council (Grant Nos. 2019-00795 and 2022-04041).

Acknowledgments

We thank G. T. Silva for handling one paper as an editor on this Topic. Sincere thanks are gone to the reviewers for their valuable comments and time. The full support on the Research Topic and the Research Topic from the publication office is greatly appreciated. ZG is grateful for the startup funding from Shanghai Jiao Tong University and the Shanghai Overseas Talent program.

Conflict of interest

The authors declare that the research was conducted in the absence of any commercial or financial relationships that could be construed as a potential conflict of interest.

Publisher's note

References

1. Baudoin M, Thomas J-L. Acoustic tweezers for particle and fluid micromanipulation. *Annu Rev Fluid Mech* (2020) 52:205–34. doi:10.1146/annurev-fluid-010719-060154

2. Rufo J, Cai F, Friend J, Wiklund M, Huang TJ. Acoustofluidics for biomedical applications. *Nat Rev Methods Primers* (2022) 2:30. doi:10.1038/s43586-022-00109-7

3. Jensen FB, Kuperman WA, Porter H, Michael B, Schmidt H. *Computational Ocean acoustics*, New York: Springer (2011).

frontiers | Frontiers in Physics

TYPE Original Research
PUBLISHED 21 October 2022
DOI 10.3389/fphy.2022.1047892

OPEN ACCESS

EDITED BY
Feiyan Cai,
Shenzhen Institutes of Advanced Technology (CAS), China

REVIEWED BY
Nansha Gao,
Northwestern Polytechnical University, China
Yabin Jin,
Tongji University, China

*CORRESPONDENCE
Hong-Xiang Sun,
jsdxshx@ujs.edu.cn
Yun Lai,
laiyun@nju.edu.cn
Xiao-Jun Liu,
liuxiaojun@nju.edu.cn

†These authors have contributed equally to this work

SPECIALTY SECTION
This article was submitted to Physical Acoustics and Ultrasonics, a section of the journal Frontiers in Physics

RECEIVED 19 September 2022
ACCEPTED 10 October 2022
PUBLISHED 21 October 2022

CITATION
Xia J, Sun Y-Y, Guan Y-J, Wang Y, Lu Y-J, Hu H-G, Ge Y, Sun H-X, Yuan S-Q, Lai Y and Liu X-J (2022), Broadband low-frequency sound absorption in open tunnels with deep sub-wavelength Mie resonators. *Front. Phys.* 10:1047892. doi: 10.3389/fphy.2022.1047892

Broadband low-frequency sound absorption in open tunnels with deep sub-wavelength Mie resonators

Jianping Xia[1†], Ye-Yang Sun[1†], Yi-Jun Guan[1,2†], Yin Wang[1], Yu-Jing Lu[1], Hui-Gang Hu[1], Yong Ge[1,3], Hong-Xiang Sun[1,2*], Shou-Qi Yuan[1], Yun Lai[3*] and Xiao-Jun Liu[2,3*]

[1]Research Center of Fluid Machinery Engineering and Technology, School of Physics and Electronic Engineering, Jiangsu University, Zhenjiang, China, [2]State Key Laboratory of Acoustics, Institute of Acoustics, Chinese Academy of Sciences, Beijing, China, [3]Key Laboratory of Modern Acoustics, National Laboratory of Solid State Microstructures, Department of Physics and Collaborative Innovation Center of Advanced Microstructures, Nanjing University, Nanjing, China

We report both experimentally and numerically that near-perfect absorption of low-frequency sound is realized in an open tunnel embedded with two deep sub-wavelength (0.085 λ) Mie resonators. The resonators are composed of a multiple-cavity structure and an outer frame on three sides. In the eigenmode analysis, we obtain two types of monopolar Mie resonance modes (MMR I&II) in a single resonator around 250 Hz. The eigenfrequency of MMR I is mainly determined by the Helmholtz resonance of each cavity in the multiple-cavity structure, while that of MMR II is closely related to the coupling between the multiple-cavity structure and its outer frame, showing high performances of coupling and sound absorption. Based on the thermal viscous loss of sound energy in the channels created by the mutual coupling of MMR II of both Mie resonators with different diameters, the near-perfect sound absorption through the open tunnel is realized around 283 Hz. More interestingly, by increasing the number of Mie resonators in the tunnel, a broadband near-perfect sound absorption is observed, and the fractional bandwidth can reach about 0.25 and 0.46 for the tunnels with 6 and 13 resonators, The proposed deep sub-wavelength Mie resonator and its associated near-perfect sound absorptions have great potential applications in architectural acoustics and mechanical engineering.

KEYWORDS

acoustics, low-frequency sound absorption, Mie resonance, architectural acoustics, noise control

Introduction

Sound absorbers have attracted considerable interest from both the physics and engineering communities due to their important potential applications, such as noise control and architectural acoustics. Recent advancement of metamaterials [1–20] with the ability of manipulating wave propagation in unprecedented ways, has motivated a variety of sound absorber designs, which show superior absorptive features than conventional structures, such as porous and fibrous materials and micro-perforated plates. The demonstrated sound absorbers based on the acoustic metamaterials are usually composed of deep sub-wavelength resonant unit cells to absorb and dissipate sound energy inside, such as Helmholtz resonators [21–26], coiled Fabry-Perot resonators [27–29], sound membranes [30–33], acoustic metasurfaces [34–36], split-ring-resonators [37–39], Mie resonators [40, 41], *etc.* But in most of these types of absorbers, the structures are almost closed, which would inevitably affect the exchange of media between both sides, including heat, air, light and water.

To realize sound absorbers with an open structure, the coherent perfect sound absorbers [42–45] are proposed by using two sound beams with the same amplitudes and opposite phases which propagate into two ports simultaneously. Furthermore, by introducing lossy Bragg stacks or hybrid membrane resonators in two-port open systems [46, 47], the sound absorption can also be obtained. However, these systems usually impose high requirements in the structure design (such as loss factor and surface tensor). By attaching Helmholtz resonators with different sizes on both sides of an open tunnel, the sound absorption can be realized with a simpler structure [48]. However, these selected Helmholtz resonators inevitably require larger sizes for the absorption of low-frequency sound, which significantly affect their practical applications. Thus, the design of open structures for low-frequency sound absorption with deep sub-wavelength resonators still remain a technical challenge.

In this work, we demonstrate an open tunnel of near-perfect sound absorption with two deep sub-wavelength Mie resonators composed of a multiple-cavity structure and an outer frame on three sides. We find that two types of monopolar Mie resonance (MMR) modes exist in a single resonator around 250 Hz, and the eigenfrequency of MMR II decreases greatly by the coupling between the multiple-cavity structure and its outer frame. Based on the thermal viscous loss in the channels created by the mutual coupling of MMR II of both Mie resonators with different diameters, we can realize the near-perfect sound absorption through the open tunnel at 283 Hz. Additionally, by increasing the number of Mie resonators, we further increase the bandwidth of near-perfect sound absorption, and the fractional bandwidth can reach about 0.25 and 0.46 for the cases of 6 and 13 resonators, The measured results also demonstrate the characteristics of near-perfect sound absorption through the designed open tunnel, which agree with the simulated ones. The proposed deep sub-wavelength Mie resonator and its associated near-perfect sound absorption could potentially be applied in architectural acoustics, mechanical engineering, and noise reduction.

Design and performance of unit cell of Mie resonance

Figure 1A shows the photograph of the unit cell of Mie resonance, which consists of a circular multiple-cavity structure with the outer and inner radii R and r surrounded by hard sound boundaries with a thickness e on three sides. The bottom side of the unit cell is open with a length L. The unit cell is made of epoxy resin by the three-dimensional (3D) printing technology, and the background medium is air. The multiple-cavity structure is composed of a central circular cavity, surrounded by 8 interconnected cavities, which are divided by 4 channels. The thickness of all frames is t, the width of 4 channels is w, and the open width and radial length of all cavities are b and l, respectively. In our work, the sound absorption is caused by the visco-thermal loss inside the unit cell. When the acoustic wave propagates into the deep sub-wavelength resonators with narrow channels, the sound energy is attenuated owing to the thermal and viscous losses. Thus, we use the Thermoviscous Acoustic-Solid Interaction module of COMSOL Multiphysics software to numerically simulate sound characteristics. In the model, the structure parameters e = 10.0 mm, $t = b$ = 1.2 mm, w = 2.0 mm, and l = 17.6 mm, and the other parameters R, r and L are variables, in which their relations are $r = R$-2.0 cm and $L = 2R + 0.4$ cm. The material parameters of epoxy resin are the density ρ = 1,050 kg/m^3, the Young's modulus E = 5.08 GPa, and the Poisson ratio v = 0.35, and the material parameters of air are calculated as density $\rho = p_0 M/R_0 T$ and sound speed $c = \sqrt{\gamma R_0 T/M}$, respectively, where γ = 1.4, $M = 28.97 \times 10^{-3}$ kg/mol, R_0 = 8.31 J/(mol/K), p_0 = 101.325 kPa, and T = 293 K. Here, it is noted that the proposed sound absorber can also be applied in a 3D open tunnel *via* 3D Mie resonators [49]. In this work, we mainly design a two-dimensional open tunnel of sound absorption based on the proposed Mie resonator.

Figure 1B shows the simulated pressure amplitude and phase eigenfunctions of the unit cell with R = 5.0 cm. We can see that the pressure amplitude and phase distributions of both eigenmodes exhibit typical characteristics of monopolar Mie resonance (MMR), denoting as MMR I and II. Here, note that the sound amplitude outside the multiple-cavity structure for MMR II is much larger than that for MMR I, indicating that the coupling effect between the multiple-cavity structure and outer frame for MMR II is stronger. Furthermore, we simulate the real and imaginary eigenfrequencies of both MMR modes with different values of R, in which the parameters t, b, w and l are the same as those in Figure 1B. As shown in Figure 1C, with the increase of R, the real eigenfrequencies of both modes decrease gradually. However, the imaginary eigenfrequencies of MMR I are around zero (shown in Figure 1D), which is much lower than

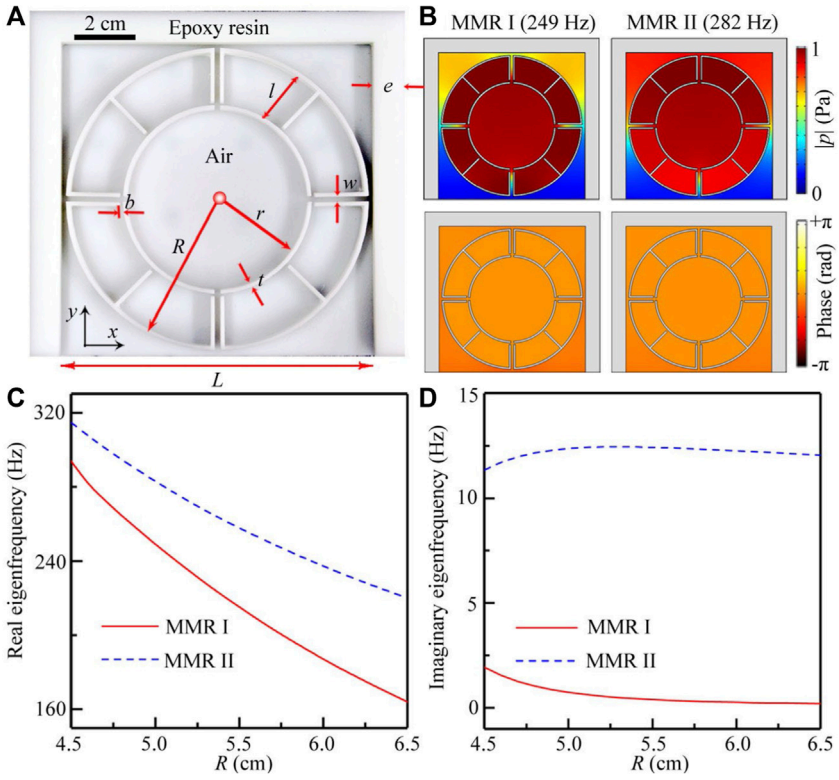

FIGURE 1
(A) Photograph of the unit cell of Mie resonance. **(B)** Simulated pressure and phase eigenfunctions of the unit cell with R = 5.0 cm. Eigenmodes of MMR I and II can be observed at 249 and 282 Hz, respectively. **(C)** Real and **(D)** imaginary parts of the eigenfrequencies for MMR I and II with different values of R.

those of MMR II, showing that performance of sound absorption for MMR II is much higher than that for MMR I.

Beyond that, we simulate both types of eigenmodes (MMR I'&II') for the unit cell without outer frames (see Supplementary Material). It is worth noting that the real eigenfrequencies of MMR II' are much larger than those of MMR II, but those of MMR I' and MMR I are almost the same. Therefore, MMR II is closely related to the coupling between the multiple-cavity structure and outer frame, but MMR I is mainly created by Helmholtz resonances of each cavity in the multiple-cavity structure (see Supplementary Material). Based on the aforementioned results, we also demonstrate that the coupling of MMR II is much stronger than that of MMR I.

Performance and mechanism of open tunnel

Figure 2A shows the schematic of an open tunnel of sound absorption for the left incidence of sound, which is composed of a straight waveguide with a height h and two types of unit cells with different values of R. The distance between both unit cells is d, and the other parameters of the tunnel are h = 40 cm, R_{I} = 4.9 cm, R_{II} = 5.0 cm and d = 18.5 cm. Here, it is worth mentioning that the height ratio between the open tunnel and the resonator is about 4.0, which is much larger than those of the previously demonstrated absorber [48]. Beyond that, compared with other sound absorption structures in the open tunnel, the proposed Mie resonators have a smaller size. Figure 2B shows the absorption spectrum through the open tunnel. The absorption coefficient of sound is calculated as $\alpha = 1-R-T$, in which R and T represent the acoustic reflectance and transmittance, respectively. We can see that, for the tunnel with both unit cells, three absorption peaks (denoted as A, B and C) can be observed, which corresponds to 249, 256, and 283 Hz, respectively. The absorption coefficient at the peak C can reach about 0.98, which is much larger than those at the peaks A and B. Therefore, the proposed open tunnel has a good practical applicability. Additionally, as shown in Figure 2C, the values of R and T through the tunnel with both unit cells are almost zero at the peak C, displaying a typical characteristic of near-perfect sound absorption in the open tunnel. To theoretically investigate the sound absorption performance at the peak C, we also calculate the relative

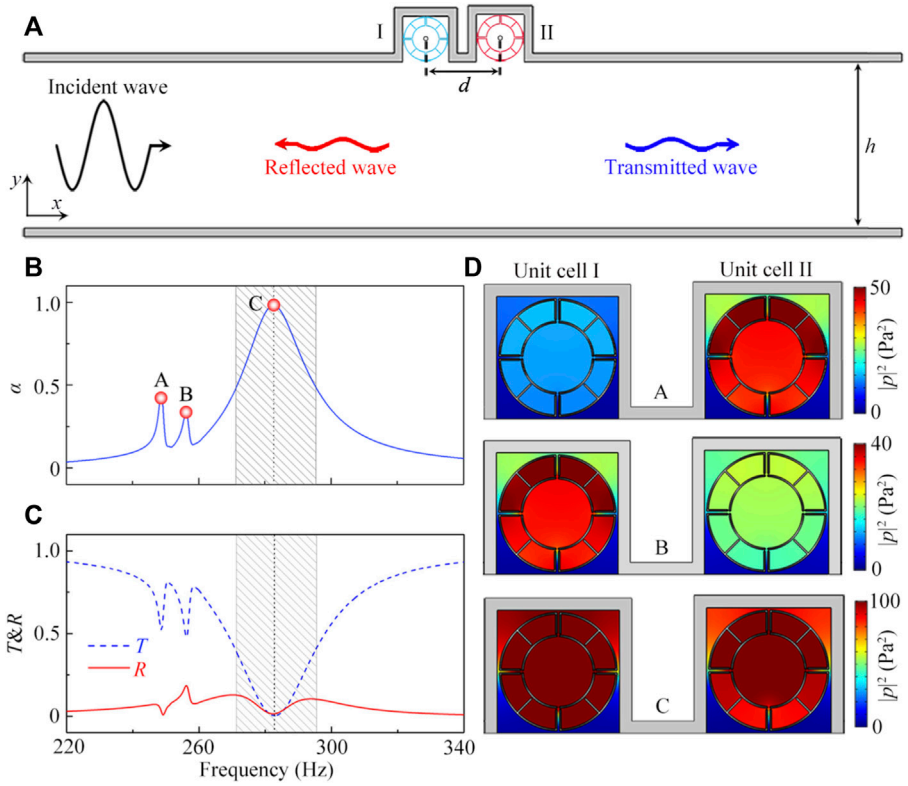

FIGURE 2
(A) Schematic of the open tunnel with the unit cells I and II, and the diameters of the unit cells I and II are R_I = 4.9 cm and R_{II} = 5.0 cm, respectively. **(B)** Simulated absorption spectra through the open tunnels. The frequencies of the peaks A, B and C in **(B)** are 249, 256 and 283 Hz, respectively. **(C)** Simulated transmittance and reflectance spectra through the tunnel with the unit cells I and II. **(D)** Simulated distributions of intensity field in both unit cells at 249, 256 and 283 Hz.

impedance of the open tunnel by using an acoustic equivalent circuit, which is shown in Supplementary Material. We can see that, at the peak C (283 Hz), the real part of the relative impedance Z/Z_0 is close to 1, and its imaginary part is close to 0, further demonstrating the near-perfect sound absorption of the open tunnel.

To investigate the mechanism of the three peaks, we simulate the distributions of intensity field in both unit cells created by the acoustic wave passing through the tunnel at three frequencies, which is shown in Figure 2D. We can see that, at the peaks A and B, the MMR of the unit cells II and I are excited, respectively, while those of both unit cells are obtained simultaneously at the peak C. Additionally, the frequencies of the peaks A and B are close to those of the MMR I for the unit cells II (249 Hz) and I (256 Hz), respectively, and the frequency of the peak C is between those of the MMR II of the unit cells II (282 Hz) and I (288 Hz). We therefore demonstrate that the absorption peaks A and B are created by the MMR I of the unit cells II and I, respectively, while the near-perfect sound absorption at the peak C is created by the coupling of the MMR II of both unit cells.

To verify this, we simulate the sound absorption spectra with different values of *d*, which is shown in Figure 3. We can see that,

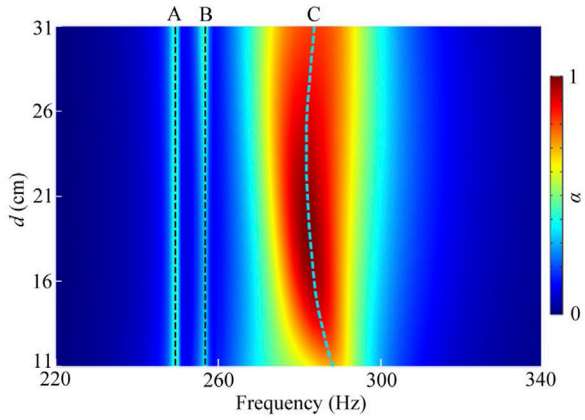

FIGURE 3
Simulated sound absorption spectra through the tunnel with different values of *d*. Dashed lines represent three absorption peaks A, B and C.

with the increase of *d*, the frequencies of both absorption peaks A and B remain unchanged, while the frequency of the peak C

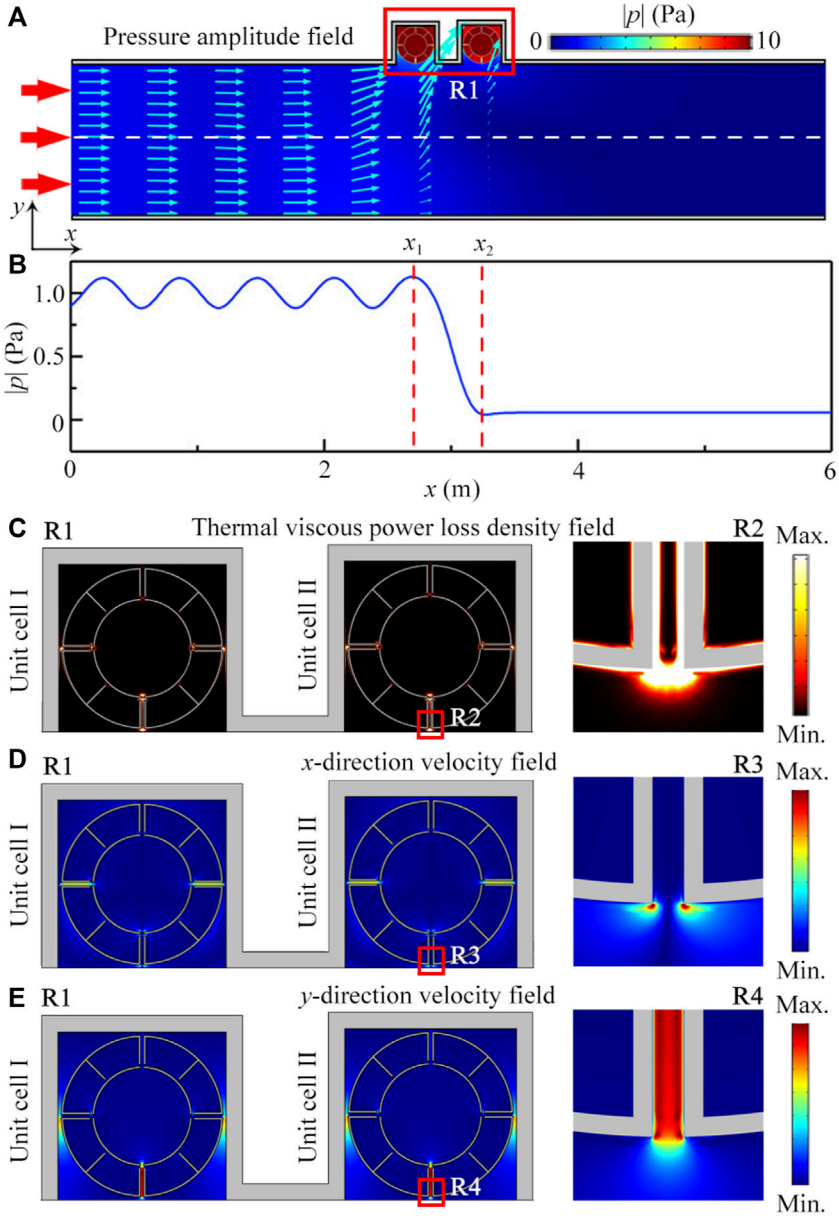

FIGURE 4
(A) Simulated pressure amplitude distribution created by the acoustic wave passing through the tunnel at 283 Hz. Red and sky blue arrows represent the directions of incident wave and propagating sound energy flux. **(B)** Simulated pressure amplitude distribution along the white dashed line in **(A)**. x_1 and x_2 are the center positions of the unit cells I and II. **(C)** Simulated distributions of thermal viscous power density, **(D)** x-direction and **(E)** y-direction vibration velocity in R1 in **(A)**. Zooms at the right side are the corresponding distributions in R2-R4.

changes gradually. Thus, we further demonstrate that the peak C is created by the coupling of both unit cells I and II.

To further show the characteristic of near-perfect sound absorption at the peak C, we simulate the pressure amplitude distribution created by the acoustic wave passing through the tunnel, which is shown in Figure 4A. We can see from the sky blue arrows that almost all sound energy is absorbed into both unit cells, and MMR II of both unit cells are excited simultaneously. Meanwhile, there is almost no sound energy reaching the right side of the unit cell II, which is obviously shown in Figure 4B.

Furthermore, we simulate the distributions of thermal viscous loss density in a red open rectangle R1 in Figure 4A, which is shown in Figure 4C. We can see that the viscous loss is mainly distributed on both sides and output port of the channels, especially the bottom three channels.

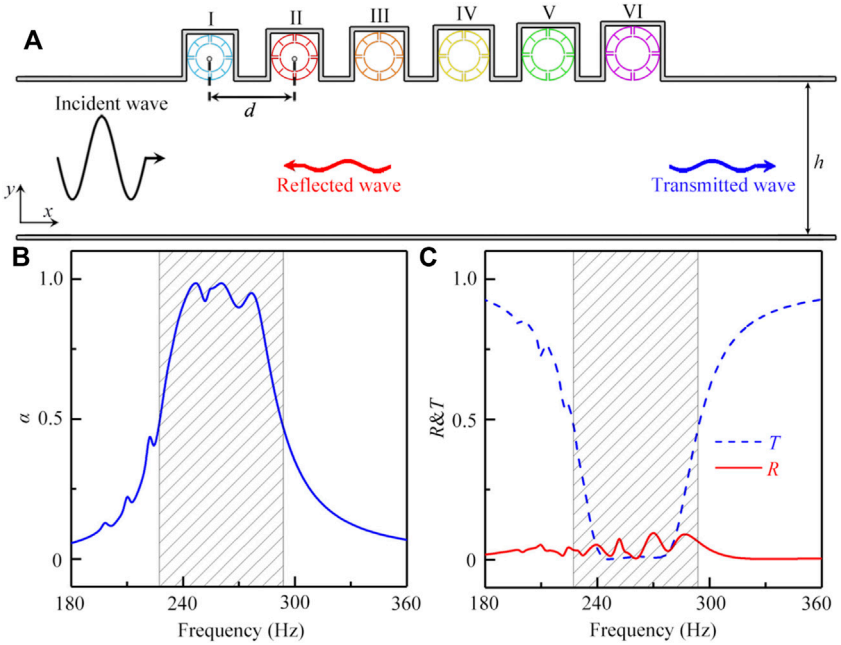

FIGURE 5
(A) Schematic of the open tunnel with 6 unit cells. The parameters *t* and *w* of the unit cells are fixed at 1.2 and 2.0 mm, and the diameters of the unit cells I-VI are R_{I} = 4.9 cm, R_{II} = 5.0 cm, R_{III} = 5.2 cm, R_{IV} = 5.4 cm, R_{V} = 5.6 cm and R_{VI} = 5.8 cm, respectively. **(B)** The absorption spectrum through the open tunnel with 6 unit cells. **(C)**Transmittance and reflectance spectra through the open tunnel with 6 unit cells.

This is because the viscous force is closely related to the vibration velocity gradient of sound, and so is the viscous loss. To demonstrate it, we present the corresponding vibration velocity of sound in *x* and *y* directions. We can see that, there exists a large velocity gradient in *x* direction at the output port (Figure 4D). For the case of the vibration velocity in *y* direction (Figure 4E), the value is large at the center, but is almost zero at the walls on both sides of the channel. Therefore, we deduce that the near-perfect sound absorption at the peak C is created by the thermal viscous loss of sound energy in the channels under the coupling of MMR II for both unit cells.

Beyond that, we also discuss the absorption performance through the open tunnel for the right incidence of sound, in which the parameters of the open tunnel remain constant. The simulated results show that the maximum absorption coefficient is only about 0.66, which is much smaller than that from the left incidence of sound (see Supplementary Material). Such a phenomenon arises from sound reflections created by the asymmetric design of both Mie resonators, and the proposed open tunnel of asymmetric sound absorption can be applied to exhaust pipes of cars with the need of unidirectional noise reduction. Additionally, we simulate the sound absorption through the open tunnel with a symmetric system of Mie resonators which is composed of a unit cell I and two unit cells II on both sides, and the maximum absorption coefficient is about 0.88, which is still lower than that in Figure 2B. The corresponding results are displayed in the Supplementary Material.

Bandwidth optimization of open tunnel

To optimize the bandwidth of sound absorption, we design another type of open tunnel by using 6 unit cells with different values of *R*, which is schematically shown in Figure 5A. The size of the open tunnel and the distance between adjacent unit cells are the same as those in Figure 2A, and the incident plane wave is still placed at the left port. Figure 5B shows the absorption spectra through the open tunnel around the peak C. It is found that, in the range 227–292 Hz (shaded region), the absorption coefficients of the open tunnel with 6 unit cells are larger than 0.5, and thus the fractional bandwidth can reach about 0.25. Beyond that, in the range 240–280 Hz, the absorption coefficient can exceed 0.9, and both coefficients *R* and *T* are close to zero (Figure 5C), showing the characteristic of broadband near-perfect sound absorption. Moreover, we can further broad the working bandwidth of the tunnel by increasing the number of the unit cells, and the fractional bandwidth can reach about 0.46 with 13 unit cells, which is shown in Supplementary Material.

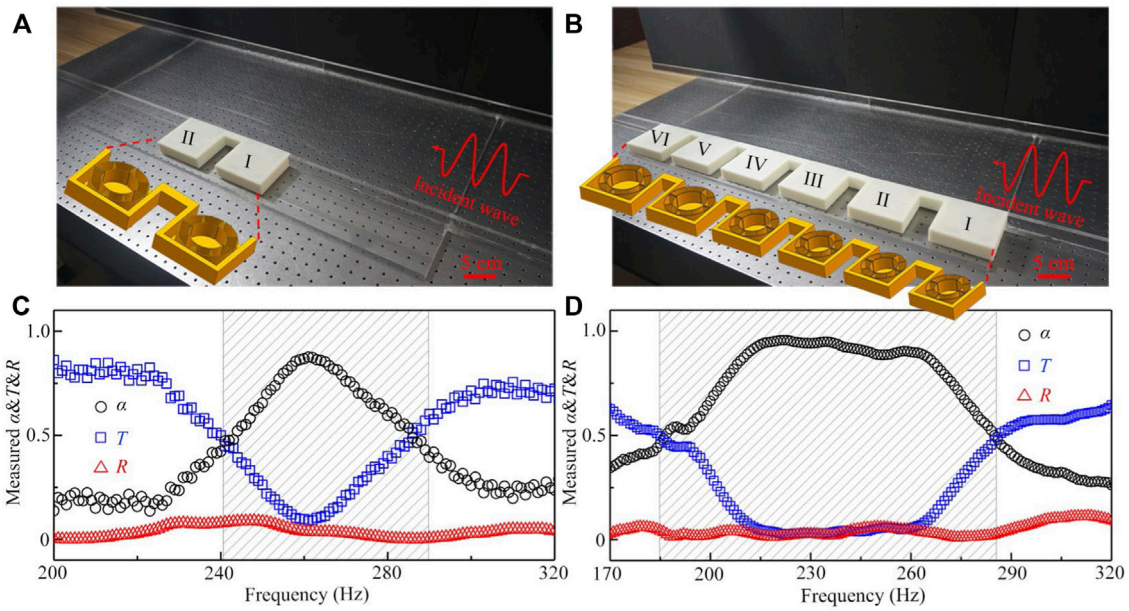

FIGURE 6
Photographs of the open tunnels with **(A)** 2 and **(B)** 6 unit cells in the experiment. Measured absorption, transmittance and reflectance spectra through the tunnels with **(C)** 2 and **(D)** 6 unit cells.

Experimental demonstration

Finally, we experimentally demonstrate the near-perfect sound absorption of the two types of open tunnels, in which the detailed description of the experimental setup is shown in Supplementary Material. As shown in Figures 6A,B, the samples are placed at the left side of a planar waveguide composed of two parallel plexiglass plates (dimension 3.0 m × 0.4 m×3 cm), The height of sample is selected as 3 cm to match the height of the waveguide, in which the thicknesses of each unit cell and the cover plate on both sides are 2.7 and 0.15 cm, respectively. The other parameters of the unit cells in Figures 6A,B are the same as those in Figures 2A, 5A.

Figures 6C,D show the measured absorption, transmittance and reflectance spectra through the two types of tunnels. Note that both results show the typical characteristics of the near-perfect sound absorption. The measured maximum sound absorption coefficients in Figures 6C,D can reach about 0.88 and 0.96, respectively, while the measured transmittance and reflectance are close to zero around the absorption peaks. However, the measured frequency ranges of the near-perfect sound absorption are not consistent with the simulated results in Figures 2, 5. This is because the sound absorption is very sensitive to the structure parameters of each unit cell, and the measured parameters of the unit cells in both samples are different from those in the simulations due to the fabrication accuracy of 3D printing and the deformation of the unit cells with circular structure. The error analysis of experimental measurement is shown in Supplementary Material.

Conclusion

In conclusions, we have experimentally demonstrated an open tunnel of near-perfect sound absorption by using a type of deep sub-wavelength Mie resonator composed of a multiple-cavity structure and an outer frame on three sides. The results show that there exist two types of MMR modes in a single resonator around 250 Hz. The eigenfrequencies of MMR I and II are mainly determined by the Helmholtz resonance of each cavity in the multiple-cavity structure and the coupling between the multiple-cavity structure and its outer frame, respectively. By combining the two Mie resonators with R_{I} = 4.9 cm and R_{II} = 5.0 cm, we can observe the near-perfect sound absorption through the open tunnel at 283 Hz, which arises from the thermal viscous loss of sound energy in the channels created by the mutual coupling of MMR II of both Mie resonators. Moreover, by increasing the number of Mie resonators in the tunnel, the broadband near-perfect sound absorption is realized, and the fractional bandwidths can reach about 0.25 and 0.46 for the cases of 6 and 13 resonators, respectively. Finally, we experimentally demonstrate the near-perfect sound absorption through the two types of tunnels with 2 and 6 Mie resonators, in which the measured results agree with the simulated ones. The

proposed Mie resonator has the advantages of deep sub-wavelength size ($L/\lambda \sim 0.085$) and high coupling performance, which has certain application prospect in the fields of architectural acoustics and mechanical engineering. It also advanced the deep sub-wavelength coupling resonance with versatile applications in sound communication, bio-sensing, and noise reduction.

Data availability statement

The original contributions presented in the study are included in the article/Supplementary Material, further inquiries can be directed to the corresponding authors.

Author contributions

J-PX, Y-YS, and Y-JG contributed equally to this work. All authors contributed to the article and approved the submitted version.

Funding

This work was supported by National Natural Science Foundation of China (Grant Nos. 12174159, 12274183, 11834008, 11974176, and 12174188), the National Key Research and Development Program of China (Grant No. 2020YFC1512403).

Conflict of interest

The authors declare that the research was conducted in the absence of any commercial or financial relationships that could be construed as a potential conflict of interest.

Publisher's note

All claims expressed in this article are solely those of the authors and do not necessarily represent those of their affiliated organizations, or those of the publisher, the editors and the reviewers. Any product that may be evaluated in this article, or claim that may be made by its manufacturer, is not guaranteed or endorsed by the publisher.

Supplementary material

The Supplementary Material for this article can be found online at: https://www.frontiersin.org/articles/10.3389/fphy.2022.1047892/full#supplementary-material

References

1. Liu Z, Zhang X, Mao Y, Zhu YY, Yang Z, Chan CT, et al. Locally resonant sonic materials. *Science* (2000) 289:1734–6. doi:10.1126/science.289.5485.1734

2. Lai Y, Wu Y, Sheng P, Zhang ZQ. Hybrid elastic solids. *Nat Mater* (2011) 10:620–4. doi:10.1038/nmat3043

3. Christensen J, Javier García de Abajo F. Anisotropic metamaterials for full control of acoustic waves. *Phys Rev Lett* (2012) 108:124301. doi:10.1103/PhysRevLett.108.124301

4. Liang Z, Li J. Extreme acoustic metamaterial by coiling up space. *Phys Rev Lett* (2012) 108:114301. doi:10.1103/PhysRevLett.108.114301

5. Cheng Y, Zhou C, Yuan BG, Wu DJ, Wei Q, Liu XJ. Ultra-sparse metasurface for high reflection of low-frequency sound based on artificial Mie resonances. *Nat Mater* (2015) 14:1013–9. doi:10.1038/NMAT4393

6. Cummer SA, Christensen J, Alù A. Controlling sound with acoustic metamaterials. *Nat Rev Mater* (2016) 1:16001. doi:10.1038/natrevmats.2016.1

7. Xie BY, Tang K, Cheng H, Liu ZY, Chen SQ, Tian JG. Metasurfaces: Coding acoustic metasurfaces. *Adv Mater* (2017) 29:1603507. doi:10.1002/adma.201603507

8. Bai L, Dong HY, Song GY, Cheng Q, Huang B, Jiang WX, et al. Impedance-matching wavefront-transformation lens based on acoustic metamaterials. *Adv Mater Technol* (2018) 3:1800064. doi:10.1002/admt.201800064

9. Tian ZH, Shen C, Li JF, Reit E, Gu YY, Fu H, et al. Programmable acoustic metasurfaces. *Adv Funct Mater* (2019) 29:2006376. doi:10.1002/adfm.202006376

10. Quan L, Sounas DL, Alu A. Nonreciprocal willis coupling in zero-index moving media. *Phys Rev Lett* (2019) 123:064301. doi:10.1103/PhysRevLett.123.064301

11. Nikkhah MR, Hiranandani M, Kishk A. Rotman lens design with wideband DRA array. *Prog Electromagn Res* (2020) 169:45–57. doi:10.2528/PIER20050801

12. Kumar S, Lee HP. Labyrinthine acoustic metastructures enabling broadband sound absorption and ventilation. *Appl Phys Lett* (2020) 116:134103. doi:10.1063/5.0004520

13. Allen KW, Dykes DJP, Reid DR, Lee RT. Multi-objective genetic algorithm optimization of frequency selective metasurfaces to engineer ku-passband filter responses. *Prog Electromagn Res* (2020) 167:19–30. doi:10.2528/PIER19112609

14. Zhu YF, Merkel A, Donda K, Fan SW, Cao LY, Assouar B. Nonlocal acoustic metasurface for ultrabroadband sound absorption. *Phys Rev B* (2021) 103:064102. doi:10.1103/PhysRevB.103.064102

15. Jia D, Wang Y, Ge Y, Yuan SQ, Sun HX. Tunable topological refractions in valley sonic crystals with triple valley hall phase transitions. *Prog Electromagn Res* (2021) 172:13–22. doi:10.2528/PIER21102002

16. Shen L, Zhu YF, Mao FL, Gao SY, Su ZH, Luo ZT, et al. Broadband low-frequency acoustic metamuffler. *Phys Rev Appl* (2021) 16:064057. doi:10.1103/PhysRevApplied.16.064057

17. Gao NS, Zhang ZC, Deng J, Guo XY, Cheng BZ, Hou H. Acoustic metamaterials for noise reduction: A review. *Adv Mater Technol* (2022) 7:2100698. doi:10.1002/admt.202100698

18. Yan QH, Chen HS, Yang YH. Non-hermitian skin effect and delocalized edge states in photonic crystals with anomalous parity-time symmetry. *Prog Electromagn Res* (2021) 172:33–40. doi:10.2528/PIER21111602

19. Zhou ZL, Huang SB, Li DT, Zhu J, Li Y. Broadband impedance modulation via non-local acoustic metamaterials. *Natl Sci Rev* (2022) 9:nwab171. doi:10.1093/nsr/nwab171

20. Liu L, Xie LX, Huang WC, Zhang XJ, Lu MH, Chen YF. Broadband acoustic absorbing metamaterial via deep learning approach. *Appl Phys Lett* (2022) 120:251701. doi:10.1063/5.0097696

21. Quan L, Zhong X, Liu XZ, Gong XF, Johnson PA. Effective impedance boundary optimization and its contribution to dipole radiation and radiation pattern control. *Nat Commun* (2014) 5:3188. doi:10.1038/ncomms4188

22. Li JF, Wang WQ, Xie YB, Popa BI, Cummer SA. A sound absorbing metasurface with coupled resonators. *Appl Phys Lett* (2016) 109:091908. doi:10.1063/1.4961671

23. Romero-Garcia V, Theocharis G, Richoux O, Merkel A, Tournat V, Pagneux V. Perfect and broadband acoustic absorption by critically coupled sub-wavelength resonators. *Sci Rep* (2016) 6:19519. doi:10.1038/srep19519

24. Jimenez N, Huang W, Romero-Garcia V, Pagneux V, Groby JP. Ultra-thin metamaterial for perfect and quasi-omnidirectional sound absorption. *Appl Phys Lett* (2016) 109:121902. doi:10.1063/1.4962328

25. Cheng Y, Jin YB, Zhou YK, Hao T, Li Y. Distinction of acoustically induced transparency and autler-townes splitting by Helmholtz resonators. *Phys Rev Appl* (2019) 12(4):044025. doi:10.1103/PhysRevApplied.12.044025

26. Gu TY, Cheng Y, Wen ZH, Boudouti EHE, Jin YB, Li Y, et al. Induced transparency based subwavelength acoustic demultiplexers. *J Phys D Appl Phys* (2021) 54(17):175301. doi:10.1088/1361-6463/abe07c

27. Zhang C, Hu X. Three-dimensional single-port labyrinthine acoustic metamaterial: Perfect absorption with large bandwidth and tunability. *Phys Rev Appl* (2016) 6:064025. doi:10.1103/PhysRevApplied.6.064025

28. Jimenez N, Romero-Garcia V, Pagneux V, Groby JP. Rainbow-trapping absorbers: Broadband, perfect and asymmetric sound absorption by subwavelength panels for transmission problems. *Sci Rep* (2017) 7:13595. doi:10.1038/s41598-017-13706-4

29. Yang M, Chen SY, Fuab CX, Sheng P. Optimal sound-absorbing structures. *Mater Horiz* (2017) 4:673–80. doi:10.1039/c7mh00129k

30. Mei J, Ma GC, Yang M, Yang ZY, Wen WJ, Sheng P. Dark acoustic metamaterials as super absorbers for low-frequency sound. *Nat Commun* (2012) 3:756. doi:10.1038/ncomms1758

31. Ma GC, Yang M, Xiao SW, Yang ZY, Sheng P. Acoustic metasurface with hybrid resonances. *Nat Mater* (2014) 13:873–8. doi:10.1038/NMAT3994

32. Yang M, Meng C, Fu CX, Li Y, Yang ZY, Sheng P. Subwavelength total acoustic absorption with degenerate resonators. *Appl Phys Lett* (2015) 107:104104. doi:10.1063/1.4930944

33. Yang M, Li Y, Meng C, Fu CX, Mei J, Yang ZY, et al. Sound absorption by subwavelength membrane structures: A geometric perspective. *Comptes Rendus Mecanique* (2015) 343:635–44. doi:10.1016/j.crme.2015.06.008

34. Cai XB, Guo QQ, Hu GK, Yang J. Ultrathin low-frequency sound absorbing panels based on coplanar spiral tubes or coplanar Helmholtz resonators. *Appl Phys Lett* (2014) 105:121901. doi:10.1063/1.4895617

35. Li Y., Assouar B. Acoustic metasurface-based perfect absorber with deep subwavelength thickness Appl. *Phys Lett.* (2016) 108: 063502. doi:10.1063/1.4941338

36. Donda K, Zhu YF, Fan SW, Cao LY, Li Y, Assouar B. Extreme low-frequency ultrathin acoustic absorbing metasurface. *Appl Phys Lett* (2019) 115:173506. doi:10.1063/1.5122704

37. Wu XX, Fu CX, Li X, Meng Y, Gao YB, Tian JX, et al. Low-frequency tunable acoustic absorber based on split tube resonators. *Appl Phys Lett* (2016) 109:043501. doi:10.1063/1.4959959

38. Long HY, Cheng Y, Tao JC, Liu XJ. Perfect absorption of low-frequency sound waves by critically coupled subwavelength resonant system. *Appl Phys Lett* (2017) 110:023502. doi:10.1063/1.4973925

39. Xu ZX, Meng HY, Chen A, Yang J, Liang B, Cheng JC. Tunable low-frequency and broadband acoustic metamaterial absorber. *J Appl Phys* (2021) 129:094502. doi:10.1063/5.0038940

40. Long HY, Gao SX, Cheng Y, Liu XJ. Multiband quasi-perfect low-frequency sound absorber based on double-channel Mie resonator. *Appl Phys Lett* (2018) 112: 033507. doi:10.1063/1.5013225

41. Sun YY, Xia JP, Sun HX, Yuan SQ, Ge Y, Liu XJ. Dual-band fano resonance of low-frequency sound based on artificial Mie resonances. *Adv Sci (Weinh)* (2019) 6: 1901307. doi:10.1002/advs.201901307

42. Wei PJ, Croenne C, Chu ST, Li JS. Symmetrical and anti-symmetrical coherent perfect absorption for acoustic waves. *Appl Phys Lett* (2014) 104: 121902. doi:10.1063/1.4869462

43. Meng C, Zhang XN, Tang ST, Yang M, Yang ZY. Acoustic coherent perfect absorbers as sensitive null detectors. *Sci Rep* (2017) 7:43574. doi:10.1038/srep43574

44. Ghaffarivardavagh R, Nikolajczyk J, Anderson S, Zhang X. Ultra-open acoustic metamaterial silencer based on fano-like interference. *Phys Rev B* (2019) 99:024302. doi:10.1103/PhysRevB.99.024302

45. Dong RZ, Mao DX, Wang X, Li Y. Ultrabroadband Acoustic ventilation barriers via hybrid-functional metasurfaces. *Phys Rev Appl* (2021) 15:024044. doi:10.1103/PhysRevApplied.15.024044

46. Long HY, Cheng Y, Zhang T, Liu XJ. Wide-angle asymmetric acoustic absorber based on one-dimensional lossy Bragg stacks. *J Acoust Soc Am* (2017) 142:EL69–EL74. doi:10.1121/1.4991677

47. Fu CX, Zhang XN, Yang M, Xiao SW, Yang Z. Hybrid membrane resonators for multiple frequency asymmetric absorption and reflection in large waveguide. *Appl Phys Lett* (2017) 110:021901. doi:10.1063/1.4973821

48. Long HY, Cheng Y, Liu XJ. Asymmetric absorber with multiband and broadband for low-frequency sound. *Appl Phys Lett* (2017) 111:143502. doi:10.1063/1.4998516

49. Zhang T, Bok E, Tomoda M, Matsuda O, Guo JZ, Liu XJ, et al. Compact acoustic metamaterial based on the 3D Mie resonance of a maze ball with an octahedral structure. *Appl Phys Lett* (2022) 120:161701. doi:10.1063/5.0084030

frontiers | Frontiers in Physics

TYPE Original Research
PUBLISHED 26 January 2023
DOI 10.3389/fphy.2023.1122617

OPEN ACCESS

EDITED BY
Wei Li,
Huazhong University of Science and Technology, China

REVIEWED BY
Yongyao Chen,
Harbin Engineering University, China
Igor Petrov,
Moscow Institute of Physics and Technology, Russia

*CORRESPONDENCE
Zhong Chen,
chzhsouth@scsio.ac.cn
Weixia Huang,
hwx@scsio.ac.cn

SPECIALTY SECTION
This article was submitted to Physical Acoustics and Ultrasonics, a section of the journal Frontiers in Physics

RECEIVED 13 December 2022
ACCEPTED 16 January 2023
PUBLISHED 26 January 2023

CITATION
Tian Y, Chen Z, Mo Y, Xie A, Huang W, Wang S and Yan W (2023), Effects of physical properties on the compression wave speed of seafloor sediment in the South China Sea: Comparisons between theoretical models and measured data. *Front. Phys.* 11:1122617. doi: 10.3389/fphy.2023.1122617

Effects of physical properties on the compression wave speed of seafloor sediment in the South China Sea: Comparisons between theoretical models and measured data

Yuhang Tian[1,2], Zhong Chen[1,2]*, Yaxiao Mo[3], Anyuan Xie[4], Weixia Huang[1]*, Shuhong Wang[1] and Wen Yan[1,5]

[1]Key Laboratory of Ocean and Marginal Sea Geology, South China Sea Institute of Oceanology, Chinese Academy of Sciences, Guangzhou, China, [2]Sanya Institute of Ocean Eco-Environmental Engineering, Sanya, China, [3]Key Laboratory of Underwater Acoustic Environment, Institute of Acoustics, Chinese Academy of Sciences, Beijing, China, [4]South China Sea Marine Survey Center, MNR, Guangzhou, China, [5]University of Chinese Academy of Sciences, Beijing, China

The compression wave speed and physical properties of seafloor sediments are significant in marine engineering and marine acoustics. Although most regression equations can be satisfactorily fitted to the data and provide a useful predictive method, there is little insight into the influence of physical properties on the compression wave speed of seafloor sediment in the South China Sea (SCS). To characterize the compression wave speed and physical properties of seafloor sediments, the compression wave speed, porosity, density, and mean grain size were measured and calculated for forty-two samples collected from the South China Sea. The results show that the RMS roughness of seafloor sediment in the South China Sea ranges from 0.2 to 15 μm, and the porosity and density are determined by the RMS roughness and mean grain size. The relationships between the compression wave speed and physical properties of seafloor sediments are consistent with the intergranular friction model. When we have the physical parameters but no compression wave speed, therefore, the intergranular friction model can be used to predict the compression wave speed of seafloor sediment. Compared with the Wood model curve, we also reveal that the intergranular friction of seafloor sediment is an important parameter in determining the compression wave speed.

KEYWORDS

compression wave speed, physical properties, theoretical model, seafloor sediment, South China Sea

1 Introduction

The compression wave and physical properties of seafloor sediments can provide basic information for use in submarine geomorphology and ocean acoustic field simulations [1–8]. Moreover, these parameters are vital for the theory of wave propagation in unconsolidated seafloor sediment [9–16]. In addition, these parameters can be used to evaluate the geological events of marine sedimentary environments and control seismoacoustic propagation in the ocean [17–23].

In recent decades, extensive studies have been conducted to reveal the relationships between compression waves and physical properties and textural parameters relative to various regions, such as the North Pacific [17], Yellow Sea of China [2,8,24–26], South China Sea (SCS) [7,14,15,23,27,28], South Sea of Korea [12,19,20,22,30], West coast of India [31], and West coast of Scotland [32]. These relationships show that the density, porosity, and mean grain size play a central role in determining the compression wave speed of seafloor sediment [33,34]. Furthermore, a number of empirical site-specific equations have been established for calculating the compression wave speed in seafloor sediment for different physical properties and textural parameters [14,30,35–38,40], that are consistent with the data measured at different sites. Regression equations can be fitted to the data well and offer a valuable forecasting tool, however, they offer little understanding of how physical properties influence the compression wave speed of unconsolidated seafloor sediment.

Although regression equations can be satisfactorily fitted to the data and provide a useful predictive method, they provide little insight into the influence of physical properties on the compression wave speed of unconsolidated seafloor sediment.

The random packing of rough spheres model and the intergranular friction model were developed by Buckingham to represent the compression wave propagation in an unconsolidated granular medium [41,42]. The random packing of rough spheres model demonstrates that the porosity and density are each correlated with the mean grain size, and the intergranular friction model relates the compression wave speed to the porosity, density, and mean grain size of seafloor sediment. These theoretical models show compelling agreement with published data [17,18]. However, less research has been conducted on whether these theoretical models match the data measured from the SCS and explains the effects of the physical properties on the compression wave speed.

In this paper, we measured and studied the compression wave speed and physical properties of seafloor sediment in the SCS. The purpose of this article is to investigate the influences of physical properties on the compression wave speed using the random packing of rough spheres model and the intergranular friction model.

2 Materials and methods

The data analyzed in this study area (11–22°N and 109–119°E) were collected from 42 stations in the SCS. We obtained 27 samples from the continental shelf, 3 samples from the continental slope, and 12 samples from the abysmal sea. Sediment samples were obtained using a box corer. After gathering the seafloor sediments, we used a box corer to extract small, cylindrical samples that varied in length from 0.2 to 0.5 m. Using a portable WSD-3 digital sonic instrument, the compression wave speed of the seafloor sediment was measured in a typical laboratory (23°C, atmospheric pressure). With the aid of Vaseline, the acoustic transducers were joined to the top and bottom of the sediment. The frequency of transducer is 100 kHz. The compression wave speed (v_p) was calculated as follows:

$$v_p = \frac{L}{t - t_0} \tag{1}$$

where L is the length of the sediment sample, t is the propagation time, and t_0 is the transducer-calibrated time.

The error analysis was performed using the accuracy calculation method.

$$\Delta A = S_x = \sqrt{\sum (x_i - x)^2 / n} \tag{2}$$

The uncertainty of the compression wave speed is approximately ±5 m/s. S_x is the variance value, x_i is the measured value, x is the average value, and n is the number of measurements.

The density and porosity of the seafloor sediment were measured. The density and porosity were measured and calculated by the core cutter method. The sediment textures were analyzed using Malvern Mastersizer 2000 at the South China Sea Institute of Oceanology of the Chinese Academy of Sciences. The associated standard deviations were <3%.

3 Results

The compression wave speed of seafloor sediment in the SCS is between 1,446 and 1773 m/s (Table 1). [14] obtained the compression wave speed of seafloor sediment in the SCS ranging from 1,420 to 1,880 m/s. The compression wave speed of seafloor sediment in the middle southern Yellow Sea measured by Sun were 1,456–1,653 m/s [8]. The measurement results of compression wave speed in this study are consistent with those measured by Lu and are higher than those in the middle southern Yellow Sea.

The average values of the density, porosity, and sediment textures are also given in Table 1. The porosity of seafloor sediment in the northern SCS ranges from 0.43 to 0.82 and that of the southern Yellow Sea ranges from 0.39 to 0.76 [8]. Our porosity (0.43-0.81) results are consistent with the northern SCS and higher than the middle southern Yellow Sea. The density of seafloor sediment in this study ranges from 1.21 to 2.08 g/cm^3, which is lower than that of the southern Yellow Sea sediment measured by Sun who obtained the density rang of 1.40–2.10 g/cm^3 [8]. There are five types of seafloor sediment: clayey silt, silt, sand-silt-clay, sandy silt, and silty sand (Figure 1). The clayey silt has smaller compression wave speed, lower density, lower mean grain size, higher porosity, and higher clay content, compared with other types of sediment, including silt, sand-silt-clay, sandy silt, and silty sand.

4 Discussion

4.1 Theoretical models

4.1.1 Wood model

Seafloor sediment is known as a two-phase medium consisting of loose mineral grains and seawater. In the absence of intergranular friction, the compression wave speed in such a medium would be given by the Wood model [43]. That is, the Wood model can be used to express the sound speed as a function of the known mechanical properties of mineral grains and seawater [44]. The Wood model for compression wave speed in seafloor sediment is defined as follows:

$$c_0 = \sqrt{\frac{\kappa}{\rho_0}} \tag{3}$$

$$\rho_0 = N\rho_w + (1 - N)\rho_g \tag{4}$$

TABLE 1 Average values of the physical properties of the seafloor sediments.

Sediment type	Compression wave speed (m/s)	Porosity (%)	Density (g/cm^3)	Sandy (%)	Silty (%)	Clayey (%)	Mean grain size (μm)
Clayey silt	1,489	70.10	1.50	7.967	61.923	31.038	9.214
Silt	1,475	59.50	1.70	4.400	77.489	18.112	17.170
Sand-silt-clay	1,540	59.30	1.70	33.615	43.014	23.044	21.246
Sandy silt	1,517	61.20	1.68	30.197	54.163	15.639	31.603
Silty sand	1,633	51.70	1.87	59.114	24.438	12.459	110.363

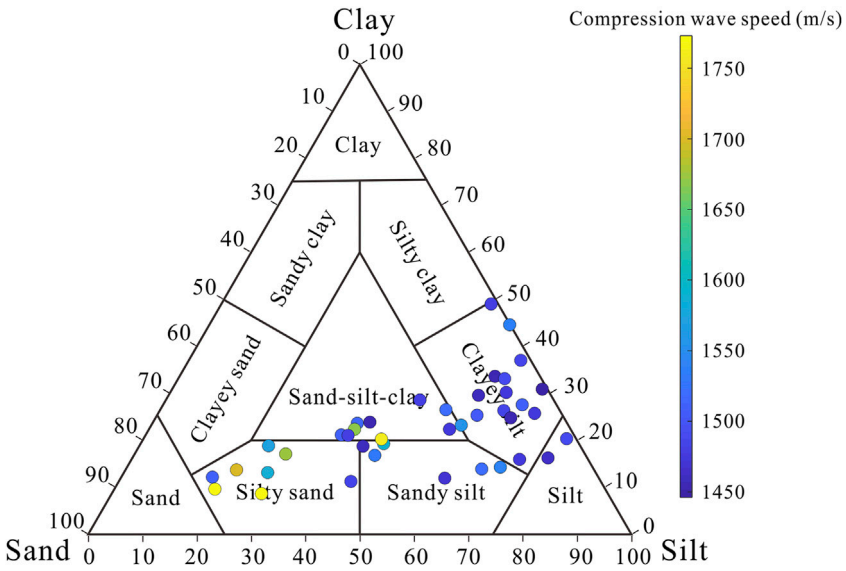

FIGURE 1
Sediment granularity triangle classification.

TABLE 2 Parameters in the Wood model, random packing of rough spheres model, and the intergranular friction model.

Material parameter	Symbol	Units	Value	References
Porosity	N	—	Variable	
Mean grain diameter	u_g	μm	Variable	
RMS grain size	Δ	μm	Variable	
Pore fluid density	ρ_w	g/cm^3	1.02	[44]
Grain density	ρ_g	g/cm^3	2.70	[44]
Bulk modulus of pore fluid	κ_w	Pa	2.25×10^9	[44]
Grains Bulk modulus	κ_g	Pa	1.47×10^{10}	[44]
Packing factor of a random arrangement of smooth spheres	P_s		0.63	[44]
Reference grain diameter	u_0	μm	1,000	[44]
Compressional frictional rigidity constant	μ_0	Pa	2×10^9	[44]

$$\frac{1}{\kappa} = N\frac{1}{\kappa_w} + (1-N)\frac{1}{\kappa_g} \tag{5}$$

Combining Eqs 3–5, the expression for c_0 is

$$c_0 = \sqrt{\frac{\kappa_w \kappa_g}{\left[N\rho_w + (1-N)\rho_g\right]\left[N\kappa_g + (1-N)\kappa_w\right]}} \tag{6}$$

where c_0 is the sound speed without intergranular interactions, κ is the bulk modulus, ρ_0 is the bulk density, N is the porosity of the medium, ρ_w is the density of seawater, ρ_g is the density of mineral grains, κ_w is the bulk modulus of the pore water, and κ_g is the bulk modulus of the mineral grain (Table 2).

4.1.2 The random packing of rough spheres model

Particle roughness is an important factor in determining the porosity and density of seafloor sediments [44]. To simulate porosity, the mineral particles constituting the sediment are assumed to be rough spheres of uniform size. For a sediment in which each grain is in close contact with the surrounding grains, the porosity is the volume fraction of sea water in the medium that can be expressed as

$$N = 1 - P \tag{7}$$

where P is the average volume of contiguous grains per unit volume.

For coarser-grained sediments, particle roughness effects represent a negligible departure, and thus, the packing is similar to the random packing of smooth spheres. However, in finer-grained sediments, the surface roughness may be comparable to or much greater than the mean grain size, in which case close contact between adjacent grains is prevented, thus allowing pore water to percolate between grains, and resulting in an increase in the porosity [45]. Based on the aforementioned analysis, Eq. 7 has been modified by Buckingham as follows [42]:

$$N = 1 - P_s\left\{\frac{u_g + 2\Delta}{u_g + 4\Delta}\right\}^3 \tag{8}$$

where P_s is the packing factor of a random arrangement of smooth spheres of uniform size, u_g is the mean grain size, and Δ is the root mean square (RMS) roughness height relative to the mean (Table 2).

4.1.3 Intergranular friction model

The intergranular friction model is derived from the Kroning-Kramers relationship without considering a specific loss mechanism [44] and the Hertz theory of deformation of spherical, elastic bodies in contact [46]. The advantage of using the intergranular friction model is that the compression wave speed can be computed using simple algebraic expressions that are functions of the physical properties of the sediments, including the porosity, density, and mean grain size. The intergranular friction model is proposed as follows:

$$c_p = c_0\sqrt{1 + x_f} \tag{9}$$

$$x_f = \left(\frac{u_g}{u_0}\right)^{1/3}\frac{\mu_0}{\rho_0 c_0^2} \tag{10}$$

Combining Eqs 9, 10, the expression for c_p is

$$c_p = \sqrt{c_0^2 + \left(\frac{u_g}{u_0}\right)^{1/3}\frac{\mu_0}{\rho_0}} \tag{11}$$

where c_p is the compression wave speed, x_f is the compression dissipation coefficient, u_0 is the reference grain size, and μ_0 is the compressional frictional rigidity constant (Table 2).

Equation 11 gives the compression wave speed in terms of grain size, which itself is related to the porosity and density through Eqs 4, 8. Thus, the compression wave speed of the seafloor sediment can be expressed in terms of the mean grain size, porosity, and density.

4.2 Relationship between physical porosities and mean grain size

4.2.1 Porosity versus mean grain size

The relationship between porosity and mean grain size from Eq. 8 is represented in Figure 2. The mean grain size varies from 4.12 to 224.07 μm, and the porosity varies from 0.43 to 0.81. As shown in Figure 2, the RMS roughness values of the random packing of rough spheres model are 0.2, 1, 3, 4.5, 9, and 15 from the top to down, respectively. These random packing of rough spheres model curves show that, the porosity value of seafloor sediment decreases slowly with increasing the mean grain size when the mean grain size is less than 10^0 μm. Because the seafloor sediment has a greater porosity and smaller mean grain size within this range. The porosity declines steeply with increasing the mean grain size when it is between 10^0 and 10^2 μm. When the mean grain size exceeds 10^2 μm, the porosity declines gently and gets closer to a constant as the mean grain size rises. Because the seafloor sediment has a smaller porosity and greater mean grain size within this range.

In Eq. 8, the porosity of seafloor sediment is controlled by the RMS roughness and the mean grain size. When the mean grain size is much larger than the RMS roughness, the porosity gets closer to its minimum value. At the limit of a large mean grain size ($u_g \to \infty$), the minimum porosity obtained from Eq. 8 is

$$N_{min} = 1 - P_s = 0.37 \tag{12}$$

Inversely, when the mean grain size is much smaller than the RMS roughness, the porosity approaches its maximum value. At the limit of a large mean grain size ($u_g \to 0$), the maximum porosity obtained from Eq. 8 is

$$N_{max} = 1 - \frac{P_s}{8} = 0.92 \tag{13}$$

The lowest measured porosity in clayey silt is 0.43, which is larger than N_{min} (0.37), and the highest measured porosity in silty sand is 0.81, which is smaller than N_{max} (0.92). These measured data lie between N_{min} and N_{max}, which is consistent with the result of [44], demonstrating the influences of the mean grain size and the RMS roughness on the porosity are notable. It is evident that the influence of the mean grain size on porosity is greater than that of the RMS roughness when the mean grain size is much greater than the RMS roughness, suggesting the porosity of the sandy silt is more sensitive to the mean grain size than the RMS roughness. When the mean grain size is much smaller than the RMS roughness, however, the influence of the RMS roughness on porosity is larger than that

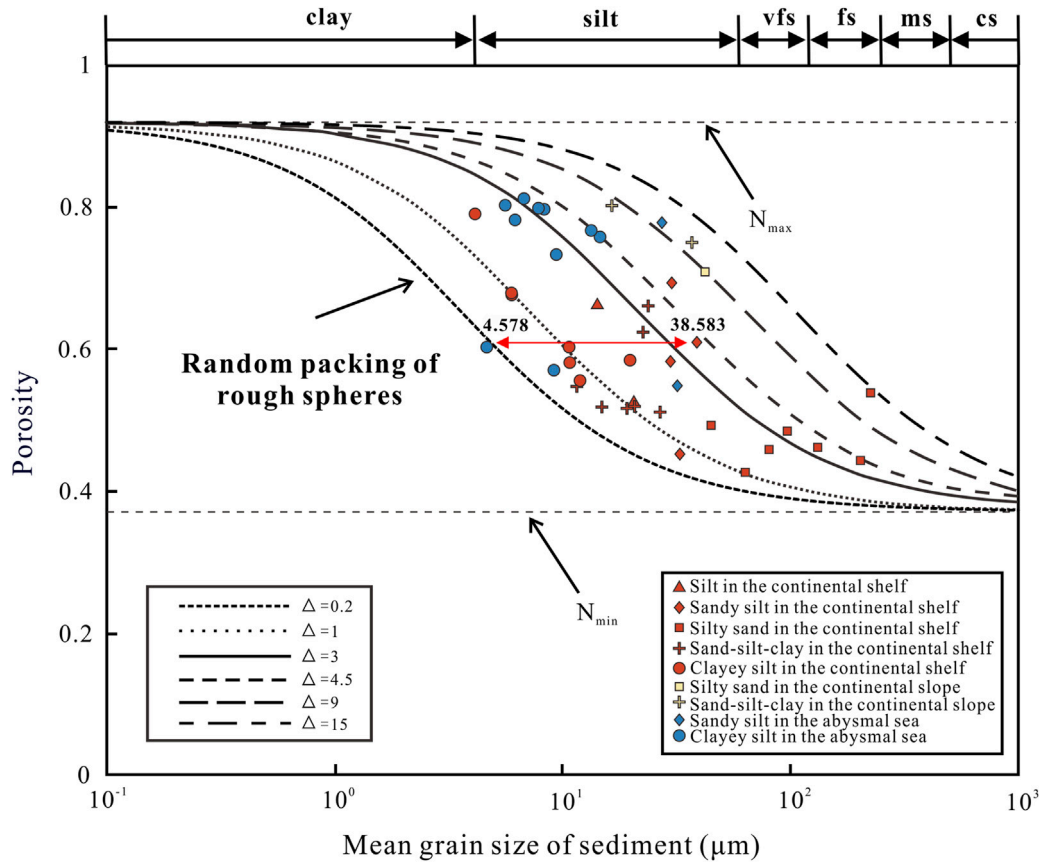

FIGURE 2
Relationship between the mean grain size and porosity of seafloor sediments. The line represents the mean grain size versus porosity and density curve of RMS (root mean square) roughness = 0.2, 1, 3, 4.5, 9, and 15 μm vfs is very fine sand; fs is fine sand; ms is medium sand; and cs is coarse sand.

of the mean grain size in clayey silt. Therefore, the silty sand tends to have lower porosity and the clayey silt tends to have higher porosity.

The lower boundary of the measured mean grain size and porosity data is the random packing of rough spheres model with the RMS roughness of 0.2, and the upper boundary of the measured data is the random packing of rough spheres model with the RMS roughness of 15. In addition, most measured data of the continental shelf and the continental slope lie on both sides of the random packing of rough spheres model with the RMS roughness of 3.

The results demonstrate that there is a complicated relationship between the porosity and mean grain size of seafloor sediment. The porosity of seafloor sediment is determined by the mean grain size and the RMS roughness, which means that the same value of porosity can have various compositions of the RMS roughness and the mean grain size. For example, the clayey silt with the porosity of 0.60 can have the mean grain size with 4.578 μm and the RMS roughness with 0.2, and the sandy silt with the porosity of 0.61 can have the mean grain size with 38.583 μm and the RMS roughness with 4.5. Without taking into account the RMS roughness, errors will be introduced when the porosity is only expressed using the mean grain size. Therefore, the RMS roughness of the seafloor sediment needs to be considered when analyzing the relationship between the compressional wave speed and porosity.

4.2.2 Density versus mean grain size

The measured density and porosity data of seafloor sediment in the SCS are shown in Figure 3. The porosity of seafloor sediment is between 0.43 and 0.81, and the density of seafloor sediment is between 1.21 and 1.78 g/cm^3. The measured porosity and density data are in accordance with the Eq. 4. Thus, the density of seafloor sediment can be directly evaluated from the porosity when the grain density and the fluid density are given. The results show that there is a good linear relationship between the measured porosity and density data in Figure 3. Therefore, the density can be expressed as porosity when studying the correlation between the porosity and the compression wave speed of seafloor sediment.

The correlation between the density and mean grain size from Eqs 4, 8 is represented in Figure 4. The mean grain size varies from 4.12 to 224.07 μm, and the density varies from 1.21 to 1.78 g/cm^3. And, the RMS roughness values of the random packing of rough spheres model are 0.2, 1, 3, 4.5, 9, and 15 from the top to down, respectively. When the mean grain size is less than 10^0 μm, the random packing of rough spheres model curve shows that the density increases slowly with increasing the mean grain size. Because the seafloor sediment has a lower density and smaller mean grain size within this range. The density increases steeply with increasing the mean grain size when it ranges from 10^0 to 10^2 μm. When the mean grain size exceeds 10^2 μm, the density increases gently again and gets closer to a constant as the mean

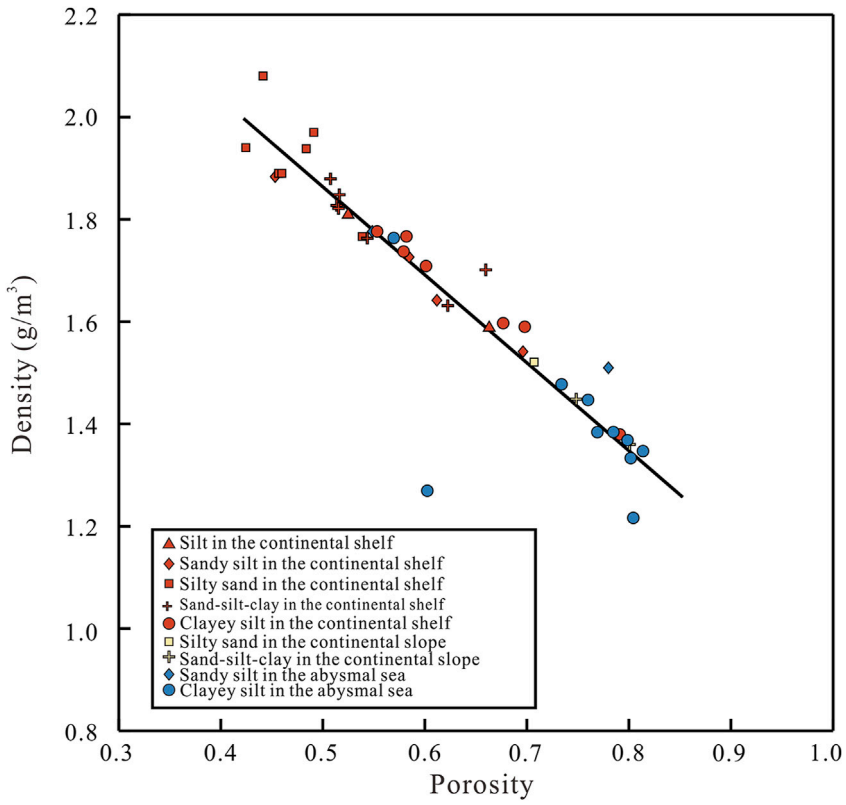

FIGURE 3
Relationship between the density and porosity of seafloor sediment.

grain size rises. Because the seafloor sediment has a higher density and greater mean grain size within this range.

Equations 4, 8 show the porosity versus density and the porosity versus mean grain size, respectively. Because the density can be expressed as porosity, Eq. 4 can be modified as follows:

$$\rho_0 = 1 + P_s\left(\rho_g - \rho_w\right)\left\{\frac{u_g + 2\Delta}{u_g + 4\Delta}\right\}^3 \tag{14}$$

In Eq. 14, when the mean grain size is much larger than the RMS roughness, the density approaches its maximum value. In the limit of a large mean grain size ($u_g \to \infty$), the maximum density obtained from Eq. 14 is

$$\rho_{max} = 1 + P_s \times 1.7 = 2.01 \tag{15}$$

when the mean grain size is much smaller than the RMS roughness, the porosity approaches its minimum value. In the limit of a large mean grain size ($u_g \to 0$), the minimum density obtained from Eq. 14 is

$$\rho_{min} = 1 + \frac{P_s \times 1.7}{8} = 1.13 \tag{16}$$

The lowest measured density is 1.21 g/cm^3, which is larger than ρ_{min} (1.13), and the highest measured porosity is 2.08 g/cm^3, which is close to ρ_{max} (2.01). These measured density data lie between N_{min} and N_{max}, which is also consistent with the result of [44], suggesting the influences of the mean grain size and the RMS roughness on the density are notable. And the influence of the mean grain size on density is greater than that of the RMS roughness when the mean grain size is much greater than the RMS roughness, suggesting the density of the silty sand is more sensitive to the mean grain size than the RMS roughness. When the mean grain size is much smaller than the RMS roughness, however, the influence of the RMS roughness on the density of the clayey silt is larger than the mean grain size. Therefore, the silty sand tends to have higher density and the clayey silt tends to have lower density.

The lower boundary of the measured mean grain size and density data is the random packing of rough spheres model with the RMS roughness of 0.2, and the upper boundary of the measured data is the random packing of rough spheres model with the RMS roughness of 15. On both sides of the random packing of rough spheres model with the RMS roughness of 3, the most measured mean grain size and density data of the continental shelf and the continental slope are located.

The results demonstrate that there is a complicated correlation between the density and the mean grain size of seafloor sediment. The density of seafloor sediment is determined by the RMS roughness and the mean grain size, suggesting that the same value of the density can have various constitutions of the mean grain size and the RMS roughness. As shown in Figure 4, the clayey silt with the density of 1.78 g/cm^3 can have the mean grain size with 11.975 μm and the RMS roughness with 1, and the sandy silt with the porosity of 1.77 g/cm^3 can have the mean grain size with 224.067 μm and the RMS roughness with 15. Without taking into account the RMS roughness, errors will

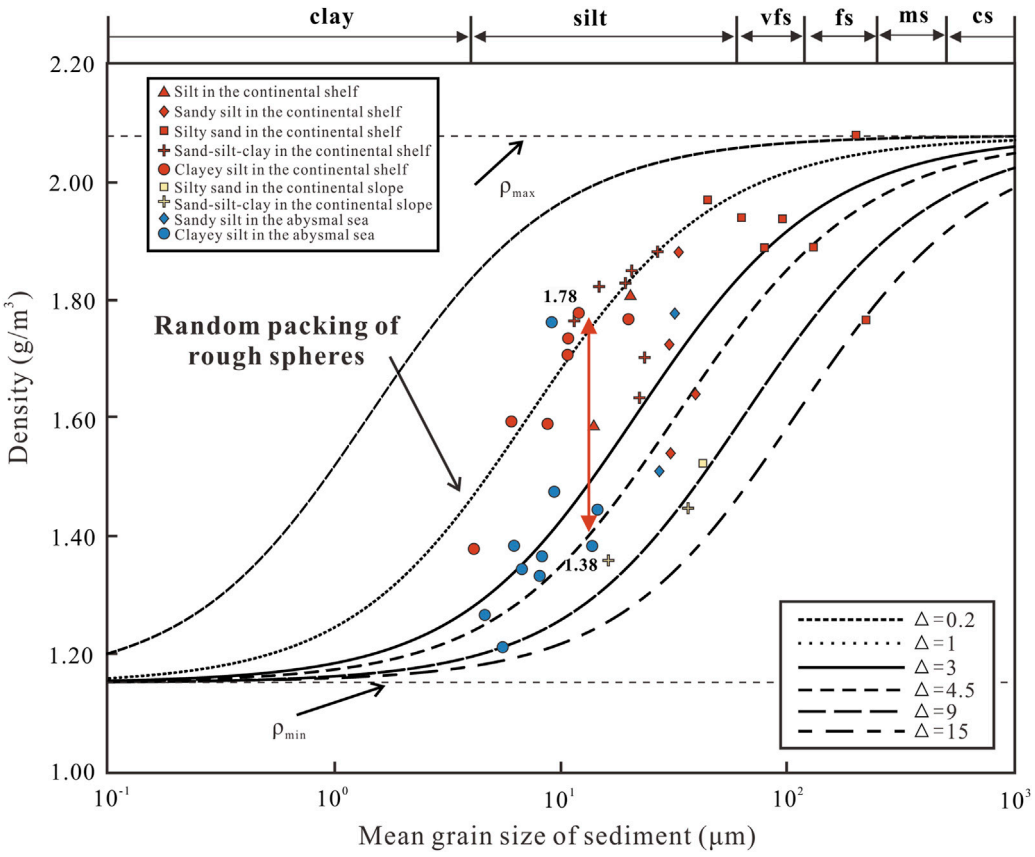

FIGURE 4
Relationship between the mean grain size and density of seafloor sediment from the SCS, respectively. The line represents the mean grain size versus porosity and density curve of RMS (root mean square) roughness = 0.2, 1, 3, 4.5, 9, and 15 μm vfs is very fine sand; fs is fine sand; ms is medium sand; and cs is coarse sand.

TABLE 3 Relationships of the compression wave speed with physical porosities.

	Cubic equation	R
Mean grain size	$c_p = 1457.47 + 3.64u_g - 0.02u_g^2 + 5.31 \times 10^{-5} \times u_g^3$	0.58
Porosity	$c_p = 6853.41 - 249.80N + 3.88N^2 - 0.02N^3$	0.64
Density	$c_p = -1597.27 + 6343.93\rho_0 - 4362.59\rho_0^2 + 1004.26\rho_0^3$	0.64

be introduced when the density is only expressed using the mean grain size. Thus, the RMS roughness of the seafloor sediment is also considered when studying the correlation between the density and the compressional wave speed.

4.3 Relationship between compression wave speed and mechanical properties

4.3.1 Compression wave speed versus mean grain size

The relationship between the mean grain size and compression wave speed can be developed in Eq. 9 by combining Eqs 7, 8. As a result, in the intergranular friction model, the mean grain size can be considered the only parameter of the compression wave speed, and the relationship between the compression wave speed and the mean grain size is a cubic equation.

The link between the measured compression wave speed and the mean grain size of seafloor sediment in the SCS is listed in Table 3. The compression wave speed ranges from 1,446 to 1773 m/s, and the mean grain size ranges from 4.12 to 224.07 μm. The measured data (Figure 5) are the compression wave speed and the mean grain size for different sediment types, and the distribution of these data are in agreement with the data obtained by [47], [48], and [17,49]. A trend common to these data is that the clayey silt, silt and sandy silt tend to exhibit lower compression wave speeds, while the sand-silt-clay and silty sand tend to exhibit higher compression wave speeds. In addition, most of these data from the abysmal sea are distributed around the intergranular friction model and this study curve. However, the measured data of the continental shelf are slightly higher than the prediction of the intergranular friction model.

The cubic curve of the mean grain size versus compression wave speed in this study and the curve of the intergranular friction model are plotted in Figure 5, where the change trend of the compression wave speed with the mean grain size is consistent in both curves. In the intergranular friction model, as the mean grain size grows, so does the compression wave speed of the seafloor sediments. The intergranular friction model curve has a very moderate slope when the mean grain

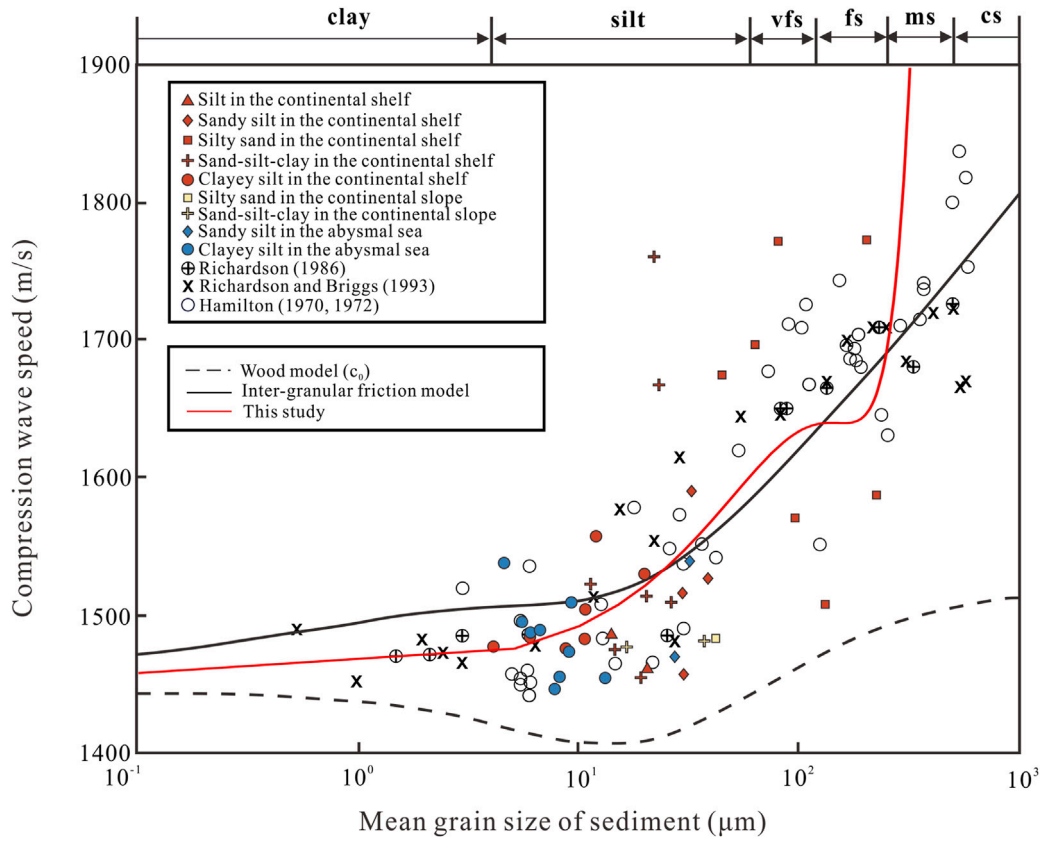

FIGURE 5
Relationship between the mean grain size and compression wave speed of seafloor sediments.

size is between 10^{-1}–10^{1} μm. The slope of the intergranular friction model curve steepens and the gradient of the compression wave speed increases when the mean grain size exceeds 10^{1} μm. This indicates that when the mean grain size is more than 10^{1} m, the compression wave speed is more sensitive to the mean grain size. But for the large mean grain size of seafloor sediment (10^{2}–10^{3} μm), it is also found that the deviation between measurement results and theoretical results is quite significant. In order to analyze the evident difference, the compression wave speed (c_0) is computed by the Wood model while taking no account of intergranular friction into account (Figure 5). As with the cubic curve and intergranular friction model curve, the slope of Wood model (c_0) curve reduces slowly when the mean grain size is low than 10^{1} and increases abruptly as the mean grain size increases (particularly between 10^{2} and 10^{3} μm). Thus, the intergranular friction of seafloor sediment is an important parameter contributing to the difference between the measured and theoretical values.

4.3.2 Compression wave speed versus porosity

Equation 8 expresses the link between the mean grain size and the porosity, and Eq. 11 is the link between the compression wave speed and mean grain size. Combining Eqs 8, 11, the link between the compression wave speed and the porosity is established. As a result, in the intergranular friction model, the porosity can be treated as the sole parameter of the compression wave speed.

The link between the measured compression wave speed and the porosity of seafloor sediment in the SCS is listed in Table 3. The compression wave speed ranges from 1,446 to 1773 m/s, and the porosity ranges from 0.43 to 0.81. The measured data (Figure 6) are the compression wave speed and the porosity for different sediment types, and the distribution of these data are in agreement with the data obtained by [47], [48], and [17,49]. As shown in Figure 6, the sand-silt-clay and silty sand have lower porosity and higher compression wave speed, and the clayey silt, silt and sandy silt have lower compression wave speed and higher porosity. It is evident that most of these data from the abysmal sea are located under the intergranular friction model curve. However, the measured data of the continental shelf are slightly higher than the prediction of the intergranular friction model curve.

The cubic curve of the porosity versus compression wave speed and the intergranular friction model curve are plotted in Figure 6, where the change trend of the compression wave speed with the porosity is consistent in both curves. The intergranular friction model curve has a relatively high slope when the sediment porosity is less than 0.6. And the intergranular friction model curve has a softer slope when the sediment porosity is greater than 0.6. The findings indicate that as porosity rises, the compression wave speed seafloor of sediment decreases. Additionally, the findings on compression wave speed and porosity match with the intergranular friction model curve. The intergranular friction model curve has a steep slope when the porosity is less than 0.6.

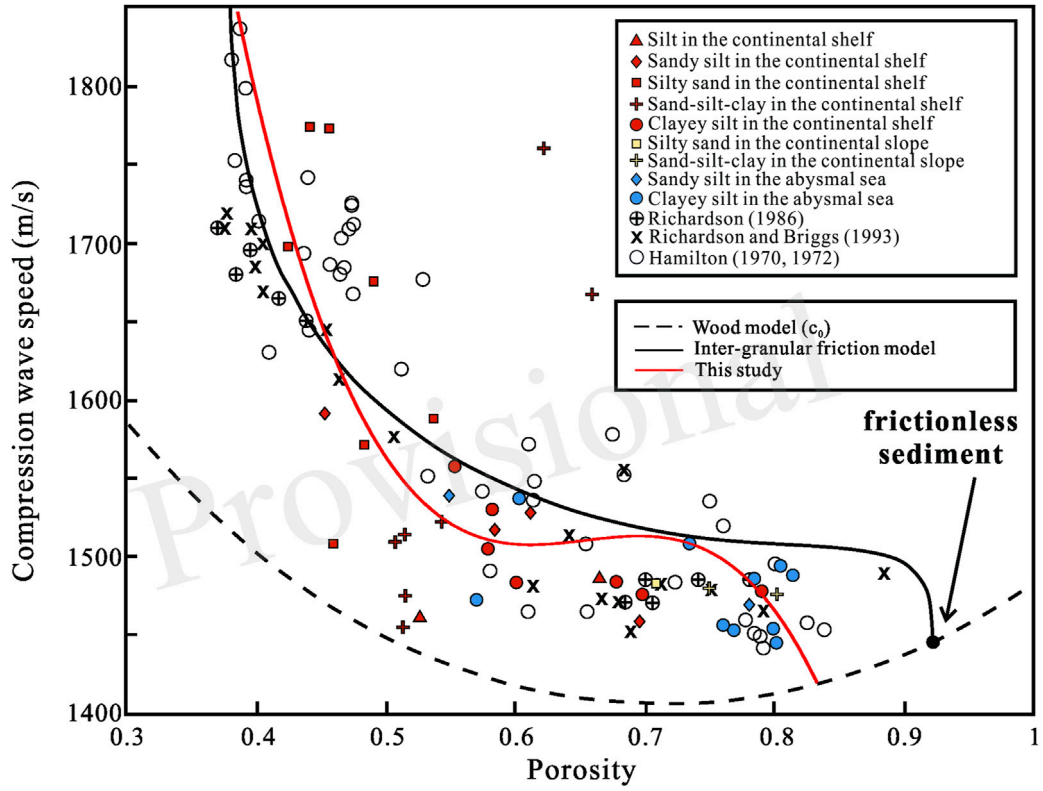

FIGURE 6
Relationship between the porosity and compression wave speed of seafloor sediments.

Thus, the compression wave speed of seafloor sediment is more sensitive to the porosity when the porosity is less than 0.6. Comparison with the Wood model curve, the measured data lie above the Wood model curve, suggesting the intergranular friction is also an important parameter in determining the compression wave speed.

4.3.3 Compression wave speed versus density

Combining Eqs 4, 8, the density can be expressed by the mean grain size, and the link between the compression wave speed and the density can be developed by Eqs 9, 10. As a result, in the intergranular friction model, the density can be viewed as the sole parameter of the compression wave speed.

Table 3 shows the correlation between the measured compression wave speed and the density of seafloor sediment in the SCS. The density ranges from 1.21 to 1.78 g/cm^3, and the compression wave speed ranges from 1,446 to 1773 m/s. Figure 6 shows that the measured data are consistent with the data obtained by [47], [48], and [17,49]. Moreover, the sand-silt-clay and silty sand have higher porosity and compression wave speed, but the clayey silt, silt and sandy silt have lower compression wave speed and porosity. Most of these data from the continental shelf are slightly higher than those predicted by the intergranular friction model curve. However, the data in abysmal sea are situated near the intergranular friction model curve.

The intergranular friction model curve and the cubic curve of the density versus compression wave speed are also plotted in Figure 6. In both curves, the compression wave speed changes consistently with density. The intergranular friction model curve has a relatively moderate slope when the sediment density is lower than 1.6 g/cm^3. As the density exceeds 1.6 g/cm^3, there is a slope in the intergranular friction model curve. These results demonstrate that the drastically elevated compression wave speed of seafloor sediment increases with increasing the density. It is evident that these measured data are agreement with the intergranular friction model curve. Because when the density is more than 1.6 g/cm^3, the intergranular friction model curve drastically elevate. Thus, the compression wave speed of seafloor sediment is more sensitive to the density when the density is more than 1.6 g/cm^3.

According to Figures 5–7, the measured compression wave speed and physical properties data in the SCS are agreement with the intergranular friction model curve. When we have the physical parameters but no compression wave speed, the intergranular friction model can be used to calculate the compression wave speed of seafloor sediment. Besides, the compression wave speed of seafloor sediment is influenced by many factors. In the intergranular friction model, the intergranular friction of seafloor sediment is considered to be an important factor in controlling the compression wave speed. This is because the particle packing and macroscopic shear strength of seafloor sediment with different intergranular friction are different. The stronger the intergranular friction, the denser the particle packing, and the greater the compression wave speed of seafloor sediment. Moreover, the compression wave speed and physical properties of seafloor sediment are also affected by the seafloor sediment types and geomorphic units, which are affected by the

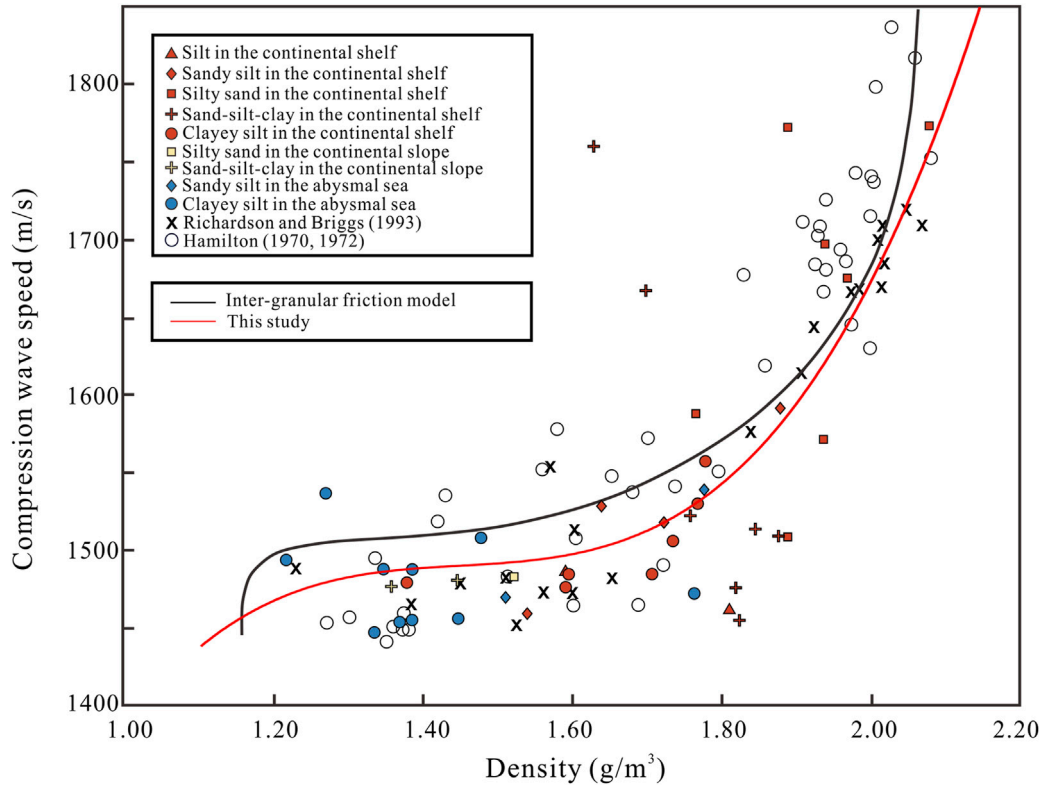

FIGURE 7
Relationship between the density and compression wave speed of seafloor sediments.

mineral composition and depositional environment of seafloor sediment.

5 Conclusion

The new relationships of seafloor sediment between the compression wave speed and physical properties are studied. Detailed comparisons were made between measured data taken from the SCS and the intergranular friction model of wave propagation in unconsolidated seafloor sediments. The conclusions are outlined as follows:

(1) The RMS roughness of seafloor sediment in the SCS is between 0.2 and 15 μm, and the RMS roughness of seafloor sediment needs to be considered when studying the relationship between the compressional wave speed and physical properties.
(2) There are significant effects of the mean grain size and the RMS roughness on the porosity of seafloor sediment. When the porosity of seafloor sediment is the same, the seafloor sediment could be consisted of complicated the mean grain sizes and the RMS roughness. The measured porosity of seafloor sediment in the SCS lie between the theoretical minimum porosity (0.37) and maximum porosity (0.92).
(3) The relationship between the measured porosity and density of seafloor sediment is linear. Thus, the density can be calculated directly by the porosity when the fluid density and the grain density of seafloor sediment are given. Additionally, the mean grain size and the RMS roughness affect the density. Even though the density is constant, the mean grain sizes and RMS roughness of seafloor sediment may vary. The measured density of seafloor sediment is between 1.21 and 1.78 g/cm^3, which is between the theoretical minimum density (1.13 g/cm^3) and theoretical maximum density (2.01 g/cm^3).
(4) The intergranular friction model and the measured data (compressional wave speed, porosity, density and mean grain size) are agreement. When the mean grain size is greater than 10^1 μm, the compression wave speed of seafloor sediment is more sensitive to the mean grain size; The compression wave speed is more sensitive to the porosity when the porosity is less than 0.6; And, the compression wave speed is more sensitive to the density when the density is more than 1.6 g/cm^3. Moreover, the intergranular friction is an important parameter in determining the compression wave speed.

Data availability statement

The datasets presented in this study can be found in online repositories. The names of the repository/repositories and accession number(s) can be found here: https://pan.baidu.com/s/1yeXNCQV6XUUkKZeRAb5mag accession number 0615.

Author contributions

YT contributed to the conception of the study; YT and AX performed the experiment; ZC and WH contributed significantly to analysis and manuscript preparation; YT performed the data analyses and wrote the manuscript; WY, SW, and YM helped perform the analysis with constructive discussions.

Funding

This work was financially supported by the following projects: 2020 Research Program of Sanya Yazhou Bay Science and Technology City (SKJC-2020-01-012), National Key R&D Program of China (2021YFC3100600), Chinese National Science Foundation (41976065).

Conflict of interest

The authors declare that the research was conducted in the absence of any commercial or financial relationships that could be construed as a potential conflict of interest.

Publisher's note

References

1. Brandes HG, Silva AJ, Sadd MH. Physical and acoustic measurements on cohesionless sediments from the northwest Florida Sand Sheet. *Geophys Res Lett* (2001) 28(5):823–6. doi:10.1029/2000GL011937

2. Liu B, Han T, Kan G, Li G. Correlations between the *in situ* acoustic properties and geotechnical parameters of sediments in the Yellow Sea, China. *J Asian Earth Sci* (2013) 77: 83–90. doi:10.1016/j.jseaes.2013.07.040

3. Zou DP, Yan P, Zhou JP. Research on acoustic properties of seafloor sediment with temperature and pressure controlled. *Mar Georesources Geotechnology* (2014) 32(2): 93–105. doi:10.1080/1064119X.2012.661032

4. Wang J, Liu B, Kan G, Li G, Zheng J, Meng X. Frequency dependence of sound speed and attenuation in fine-grained sediments from 25 to 250 kHz based on a probe method. *Ocean Eng* (2018) 160:45–53. doi:10.1016/j.oceaneng.2018.04.078

5. Zou D, Kan G, Long J, Xiao T. Influence of hydrostatic pressure on the sound speed of surficial seafloor sediments. *Mar Georesources Geotechnology* (2019) 37(3):277–81. doi:10.1080/1064119X.2017.1409300

6. Li G, Wang J, Liu B, Meng X, Kan G, Pei Y. Measurement and modeling of high-frequency acoustic properties in fine sandy sediments. *Earth Space Sci* (2019) 6(11): 2057–70. doi:10.1029/2019EA000656

7. Li G, Hou Z, Wang J, Kan G, Liu B. Empirical equations of P-wave velocity in the shallow and semi-deep sea sediments from the South China sea. *J Ocean Univ China* (2021) 20(3):532–8. doi:10.1007/s11802-021-4476-y

8. Sun Z, Kan G, Wang J, Jia Y, Meng X, Li G, et al. Characteristics of shear waves in shallow seafloor sediment in the Middle Southern Yellow Sea. *Mar Georesources Geotechnology* (2021) 40:383–91. doi:10.1080/1064119X.2021.1900473

9. Biot MA. Theory of propagation of elastic waves in a fluid-saturated porous solid. II. Higher frequency range. *The J Acoust Soc America* (1956) 28(2):179–91. doi:10.1121/1.1908241

10. Gassmann F. Elastic waves through a packing of spheres. *Geophysics* (1951) 16(4): 673–85. doi:10.1190/1.1437718

11. Dvorkin J, Nur A. Dynamic poroelasticity: A unified model with the squirt and the biot mechanisms. *Geophysics* (1993) 58(4):524–33. doi:10.1190/1.1443435

12. Kim DC, Sung JY, Park SC, Lee GH, Choi JH, Kim GY, et al. Physical and acoustic properties of shelf sediments, the South Sea of Korea. *Mar Geology* (2001) 179(1-2):39–50. doi:10.1016/S0025-3227(01)00200-6

13. Chotiros NP, Isakson MJ. A broadband model of sandy ocean sediments: Biot–Stoll with contact squirt flow and shear drag. *The J Acoust Soc America* (2004) 116(4):2011–22. doi:10.1121/1.1791715

14. Lu B, Li G, Huang S, Li C. Physical properties of sediments on the northern continental shelf of the South China sea. *Mar Georesources Geotechnology* (2006) 24(1): 47–60. doi:10.1080/10641190600559523

15. Zou DP, Wu BH, Lu B. Seafloor deposition state based geoacoustic model of the South China Sea. *Mar Georesources Geotechnology* (2011) 29(1):61–75. doi:10.1080/1064119X.2010.514256

16. Martin K, Wood W. A new model of marine sediment compression. *Earth Planet Sci Lett* (2017) 477:21–6. doi:10.1016/j.epsl.2017.08.008

17. Hamilton EL. Sound velocity and related properties of marine sediments, North Pacific. *J Geophys Res* (1970) 75(23):4423–46. doi:10.1029/JB075i023p04423

18. Richardson MD, Briggs KB, Bentley SJ, Walter DJ, Orsi TH. The effects of biological and hydrodynamic processes on physical and acoustic properties of sediments off the Eel River, California. *Mar Geology* (2002) 182(1-2):121–39. doi:10.1016/S0025-3227(01)00231-6

19. Kim GY, Kim DC, Yoo DG, Shin BK. Physical and geoacoustic properties of surface sediments off eastern geoje island, South Sea of Korea. *Quat Int* (2011) 230(1-2):21–33. doi:10.1016/j.quaint.2009.07.028

20. Bae SH, Kim DC, Lee GS, Kim GY, Kim SP, Seo YK, et al. Physical and acoustic properties of inner shelf sediments in the South Sea, Korea. *Quat Int* (2014) 344:125–42. doi:10.1016/j.quaint.2014.03.058

21. Kim SR, Lee GS, Kim DC, Bae SH, Kim SP. Physical properties and geoacoustic provinces of surficial sediments in the southwestern part of the Ulleung Basin in the East Sea. *Quat Int* (2017) 459:35–44. doi:10.1016/j.quaint.2017.08.027

22. Kim S, Lee GS, Kim D, Hahn J, Ryang WH. Variation of temperature-dependent sound velocity in unconsolidated marine sediments: Laboratory measurements. *Mar Georesources Geotechnology* (2018) 36(3):280–7. doi:10.1080/1064119X.2016.1277442

23. Tian Y, Chen Z, Hou Z, Luo Y, Xu A, Yan W. Geoacoustic provinces of the northern South China Sea based on sound speed as predicted from sediment grain sizes. *Mar Geophys Res* (2019) 40(4):571–9. doi:10.1007/s11001-019-09387-5

24. Meng X, Kan G, Li G, Sun L. Spatial characteristics and geotechnical properties of seafloor sediment in west-central area of Southern Yellow Sea. *J Eng Geology* (2015) 23(6): 1202–10. doi:10.13544/j.cnki.jeg.2015.06.023

25. Zheng J, Liu B, Kan G, Li G, Pei Y, Liu X. The sound velocity and bulk properties of sediments in the Bohai Sea and the Yellow Sea of China. *Acta Oceanologica Sinica* (2016) 35(7):76–86. doi:10.1007/s13131-016-0906-x

26. Kan G, Liu B, Wang J, Meng X, Li G, Hua Q, et al. Sound speed dispersion characteristics of three types of shallow sediments in the southern yellow sea. *Mar Georesources Geotechnology* (2018) 36(7):853–60. doi:10.1080/1064119X.2017.1392659

27. Wang J, Guo C, Liu B, Hou Z, Han G. Distribution of geoacoustic properties and related influencing factors of surface sediments in the southern South China Sea. *Mar Geophys Res* (2016) 37(4):337–48. doi:10.1007/s11001-016-9294-z

28. Meng Q, Liu S, Jia Y, Xiao Z, Wang X. Analysis on acoustic velocity characteristics of sediments in the northern slope of the South China Sea. *Bull Eng Geology Environ* (2018) 77(3):923–30. doi:10.1007/s10064-017-1070-z

29. Li G, Wang J, Meng X, Liu B, Kan G, Han G, et al. Relationships between the sound speed ratio and physical properties of surface sediments in the South Yellow Sea. *Acta Oceanologica Sinica* (2021) 40(4):65–73. doi:10.1007/s13131-021-1764-8

30. Kim GY, Park KJ, Lee GS, Yoo DG, Kong GS. Physical property characterization of quaternary sediments in the vicinity of the paleo-Seomjin River of the continental shelf of the South Sea, Korea. *Quat Int* (2019) 503:153–62. doi:10.1016/j.quaint.2018.09.002

31. Anu AP, Nair PV, Uthaman CP, Kumar TP. Estimation of compressional wave speed in marine sediments using biot-stoll model and buckingham's grain-shearing model. *Defence Sci J* (2020) 70(3):336–41. doi:10.14429/dsj.70.14365

32. Hunt C, Demšar U, Dove D, Smeaton C, Cooper R, Austin WE. Quantifying marine sedimentary carbon: A new spatial analysis approach using seafloor acoustics, imagery, and ground-truthing data in Scotland. *Front Mar Sci* (2020) 7:588. doi:10.3389/fmars.2020.00588

33. Best AI, Tuffin MD, Dix JK, Bull JM. Tidal height and frequency dependence of acoustic velocity and attenuation in shallow gassy marine sediments. *J Geophys Res Solid Earth* (2004) 109(B8). doi:10.1029/2003JB002748

34. Jackson D, Richardson M. *High-frequency seafloor acoustics*. Berlin, Germany: Springer Science and Business Media (2007).

35. Williams KL, Jackson DR, Thorsos EI, Tang D, Schock SG. Comparison of sound speed and attenuation measured in a sandy sediment to predictions based on the Biot theory of porous media. *IEEE J oceanic Eng* (2002) 27(3):413–28. doi:10.1109/JOE.2002.1040928

36. Goto S, Matsubayashi O. Relations between the thermal properties and porosity of sediments in the eastern flank of the Juan de Fuca Ridge. *Earth, Planets and Space* (2009) 61(7):863–70. doi:10.1186/BF03353197

37. Zimmer MA, Bibee LD, Richardson MD. Measurement of the frequency dependence of the sound speed and attenuation of seafloor sands from 1 to 400 kHz. *IEEE J Oceanic Eng* (2010) 35(3):538–57. doi:10.1109/JOE.2010.2056230

38. Chen X, Schmitt DR, Kessler JA, Evans J, Kofman R. Empirical relations between ultrasonic P-wave velocity porosity and uniaxial compressive strength. *CSEG Rec* (2015) 40(5):24–9.

39. Kim BN, Kim E, Ji HY, Sim MS, Choi BK, Kim SH. Quick method to measure acoustic properties of the piston core sediment under laboratory conditions. *Jpn J Appl Phys* (2019) 58(SG):SGGF04. doi:10.7567/1347-4065/ab19b4

40. De Sousa MC, de Figueiredo JJ, da Silva CB, Nascimento MJDS. Prediction of S-wave velocity by a hybrid model based on the Greenberg-Castagna equation. *J Pet Sci Eng* (2019) 172:303–13. doi:10.1016/j.petrol.2018.09.014

41. Buckingham MJ. Wave propagation, stress relaxation, and grain-to-grain shearing in saturated, unconsolidated marine sediments. *J Acoust Soc America* (2000) 108(6):2796–815. doi:10.1121/1.1322018

42. Buckingham MJ. Compressional and shear wave properties of marine sediments: Comparisons between theory and data. *J Acoust Soc America* (2005) 117(1):137–52. doi:10.1121/1.1810231

43. Wood AB, Lindsay RB. A textbook of sound. *Phys Today* (1956) 9(11):37. doi:10.1063/1.3059819

44. Buckingham MJ. Theory of acoustic attenuation, dispersion, and pulse propagation in unconsolidated granular materials including marine sediments. *J Acoust Soc America* (1997) 102(5):2579–96. doi:10.1121/1.420313

45. Wyllie MRJ, Gregory AR, Gardner LW. Elastic wave velocities in heterogeneous and porous media. *Geophysics* (1956) 21(1):41–70. doi:10.1190/1.1438217

46. Kaye GWC, Laby TH. *Tables of physical and chemical constants and some mathematical functions* (1966).

47. Richardson MD. *Ocean seismo-acoustics*. Boston, MA: Springer (1986). p. 527–36. doi:10.1007/978-1-4613-2201-6-51Spatial variability of surficial shallow water sediment geoacoustic properties

48. Richardson MD, Briggs KB. *On the use of acoustic impedance values to determine sediment properties*. John C. Stennis Space Center, MS, USA: Naval Research Lab Stennis Space Center MS (1993).

49. Hamilton EL. Compressional-wave attenuation in marine sediments. *Geophysics* (1972) 37(4):620–46. doi:10.1190/1.1440287

50. Del Grosso VA. New equation for the speed of sound in natural waters (with comparisons to other equations). *J Acoust Soc America* (1974) 56(4):1084–91. doi:10.1121/1.1903388

51. Hamilton EL. Prediction of *in-situ* acoustic and elastic properties of marine sediments. *Geophysics* (1971) 36(2):266–84. doi:10.1190/1.1440168

frontiers | Frontiers in Physics

TYPE Original Research
PUBLISHED 07 February 2023
DOI 10.3389/fphy.2023.1105787

OPEN ACCESS

EDITED BY
Zhixiong Gong,
Shanghai Jiao Tong University, China

REVIEWED BY
Yongou Zhang,
Wuhan University of Technology, China
Chengzhi Shi,
Georgia Institute of Technology,
United States

*CORRESPONDENCE
Xueren Wang,
wangxueren@aliyun.com

SPECIALTY SECTION
This article was submitted to Physical Acoustics and Ultrasonics, a section of the journal Frontiers in Physics

RECEIVED 23 November 2022
ACCEPTED 16 January 2023
PUBLISHED 07 February 2023

CITATION
Tang Y, Wang X, Miao X, Gao S, Li B and Peng Z (2023), Optimum design of acoustic stealth shape of underwater vehicle model with conning tower. *Front. Phys.* 11:1105787. doi: 10.3389/fphy.2023.1105787

Optimum design of acoustic stealth shape of underwater vehicle model with conning tower

Yuhang Tang[1], Xueren Wang[1]*, Xuhong Miao[1], Shengyao Gao[1], Bing Li[2] and Zilong Peng[1,2]

[1]Unit 92578 of the People's Liberation Army, Beijing, China, [2]School of Energy and Power Engineering, Jiangsu University of Science and Technology, Zhenjiang, China

We present an optimization algorithm for achieving optimal acoustic stealth performance during designing an underwater vehicle shape in the free field using COMSOL-MATLAB integrated software. A component superposition method based on phase interference is adopted to simplify and decompose a nonaxisymmetric complex underwater vehicle model into two main parts: the hull and the conning tower. The shape of underwater vehicle hull is described mathematically with a sequence of undetermined coefficients for optimization. The basic mathematical principle of the proposed method is Kirchhoff approximation, also called planar element method (PEM). Additionally, some examples and experimental results show that this method can realize the automatic optimization design of acoustic stealth shapes for underwater vehicle model in a given frequency band and acoustic incident angle range. The underwater vehicle design has a smooth appearance with low target strength (TS) or angle detection rate for most detection angles and frequency bands after optimized.

KEYWORDS

target strength, acoustic stealth, phase interference, optimization design, underwater vehicle model, conning tower

1 Introduction

With the development of underwater acoustic countermeasure technology, developing a means of designing the shapes of underwater vehicles more scientifically to reduce their TSs and improve their acoustic stealth ability is a topic of great interest in underwater acoustic physics. Underwater vehicles constitute the most important type of equipment among the underwater weapons of all countries, and their shape design is a major and complicated task. The shape design of early underwater vehicles was generally performed empirically, and the drag coefficient was obtained through experimentation or simulation (computational fluid dynamics, CFD). Finally, the performance was compared to determine an optimum shape. Mackay [1] experimentally measured the drag coefficient of the standard underwater vehicle model under different Reynolds numbers and compared the results with the DSSP20 simulation data. Suman et al. [2] calculated and evaluated the hydrodynamic performance of different ellipsoidal shapes of underwater vehicle heads based on CFD and obtained an optimum underwater vehicle head shape, which was verified experimentally. Praveen [3] used CFD simulation and experiments to study the influence of the length of an underwater vehicle on the hydrodynamic performance caused by the attack angle of an axisymmetric underwater vehicle and studied the linear variation of the drag coefficient with the length-to-diameter ratio (L/D). Moh et al. [4] performed CFD analysis on all available equations of the stern shapes of all underwater vehicles from the perspective of minimum resistance and discussed the optimum

hydrodynamic shape of the stern of the underwater vehicle. The next work [5] involved examining an underwater vehicle or torpedo-segmented bare hull (bow, middle, and stern) using different linear CFD calculations and comparing the results to obtain an underwater vehicle hull shape with less resistance. Using the CFD method and FLOW VISION software, the optimal L/D of the hydrodynamic shape of a cylindrical hull was proposed [6].

With the introduction of optimization algorithms, the design of underwater vehicle shapes has entered a new stage. Vasudev et al. [7] established a multi-objective optimization framework for underwater vehicle shape design and optimized the internal volume and hydrodynamic resistance of the underwater vehicle by integrating the non-dominant sequencing genetic algorithm and Reynolds-average Navier–Stokes solver into one code. In a follow-up study [8], a genetic algorithm (GA) was used to solve the design optimization problem of an autonomous underwater vehicle (AUV) under the five-parameter axisymmetric description. Through this approach, the hull shape at a constant speed was optimized, and the flow resistance coefficient was significantly reduced. Paz et al. [9] established a comprehensive model of underwater vehicle conceptual design (hull geometry parameterization, mobility model based on slender body theory, and resistance formula) applicable to a multi-objective optimization technique (GA) to find a design solution that minimized the turning diameter and created resistance requirements. Ting et al. [10] proposed an underwater vehicle shape optimization platform composed of multiple commercial software packages to reduce the navigation resistance of underwater vehicles and to improve their energy utilization and endurance. These scholars obtained excellent results in the automatic optimization design of ship shapes, but their work did not consider the TS changes caused by the development of active detection in the shape design of underwater vehicles.

A considerable breakthrough has been made in the method of calculating the acoustic scattering of underwater targets, but for the complex structures of underwater vehicles, only numerical calculations or approximate calculations using acoustic scattering can be employed. More complete numerical calculation methods and approximation methods include the finite element method (FEM) and boundary element method (BEM) [11, 12], T-matrix method [13–15], time domain finite difference method (TDFDM) [16, 17], deformation column method (DCM) [18–20], and wave superposition method (WSM) [21]. There are many other approximate methods. The highlight model (HM) proposed by Tang [22] decomposes a target into simple sub-targets, calculates the highlight parameters of the sub-targets separately, and finally obtains the TS of the whole target according to the principle of linear superposition. Abawi [23] used the Kirchhoff Approximation (KA) to establish a method of obtaining the frequency- and time-domain solutions of an acoustic scattering field of arbitrary shape. To improve the calculation rate of the PEM, Lavia [24] proposed using curved elements instead of planar elements. The numerical solution of the TS agrees well with the precise solution. Kookhyun [25] proposed a method of quickly estimating the sonar cross-sections of large and complex underwater targets such as Underwater vehicles and torpedoes. This method is based on the deterministic scattering center model, uses a combination of physical and geometric optics to construct a scattering center database, and then utilizes the database to perform polynomial interpolation on the incident angle to reconstruct the sonar cross-section. Fan et al. [26] established

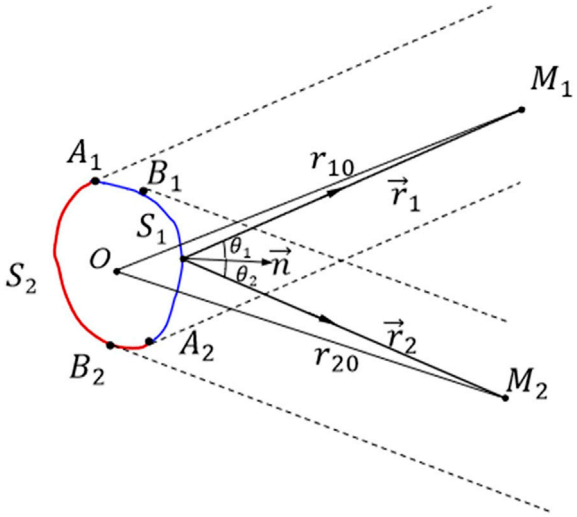

FIGURE 1
Schematic diagram of the derivation of the physical acoustic method with the source and receiver separated.

visual graphical acoustics computing based on the Kirchhoff approximate equation. Based on OpenGL technology, this method involves converting the geometric model into the visual pixel graphics of the target on the screen, obtaining the target surface normal vector and space distance information contained in the pixel, and finally converting the surface integral in the prediction of echo characteristics into the pixel summing calculation of the visual graphics on the screen. Using the Kirchhoff approximation method, Peng et al. [27] performed a scattering time-domain echo simulation of a surface ship radiated through the sonar area, and verified the effectiveness of this method experimentally. However, the research work of these scholars only predicts the acoustic target intensities of existing underwater vehicles and does not include a low-TS underwater vehicle shape design method. Li et al. proposed an optimal design method for the acoustic stealth shape of the underwater vehicle head [28] and bottom object [29] with relatively lower TS, based on the Nelder–Mead optimization algorithm and finite element method.

To address this shortcoming, a non-axisymmetric complex underwater vehicle target was simplified and decomposed in this study using the component phase interference superposition method into two main parts: the hull and the conning tower (both considered as rigid targets). Then, the underwater vehicle hull and conning tower were utilized as the optimization objects to explore the optimization design of an acoustically concealed shape in a given incident angle range and frequency band. This approach overcomes the limitations of the previous underwater vehicle shape optimization design method that only considers hydrodynamic performance and opens a new channel for underwater vehicle shape design.

In this paper, the benchmark underwater vehicle models are selected as our research object. The optimization method of the head shape of benchmark hull and conning tower with lower TS under the incidence of plane wave with multi-frequencies and multi-angles is studied. This paper is organized as follows. In Section 2, the physical acoustical method is introduced, which is the basis of calculating TS of the arbitrary target. In Section 3, we introduce

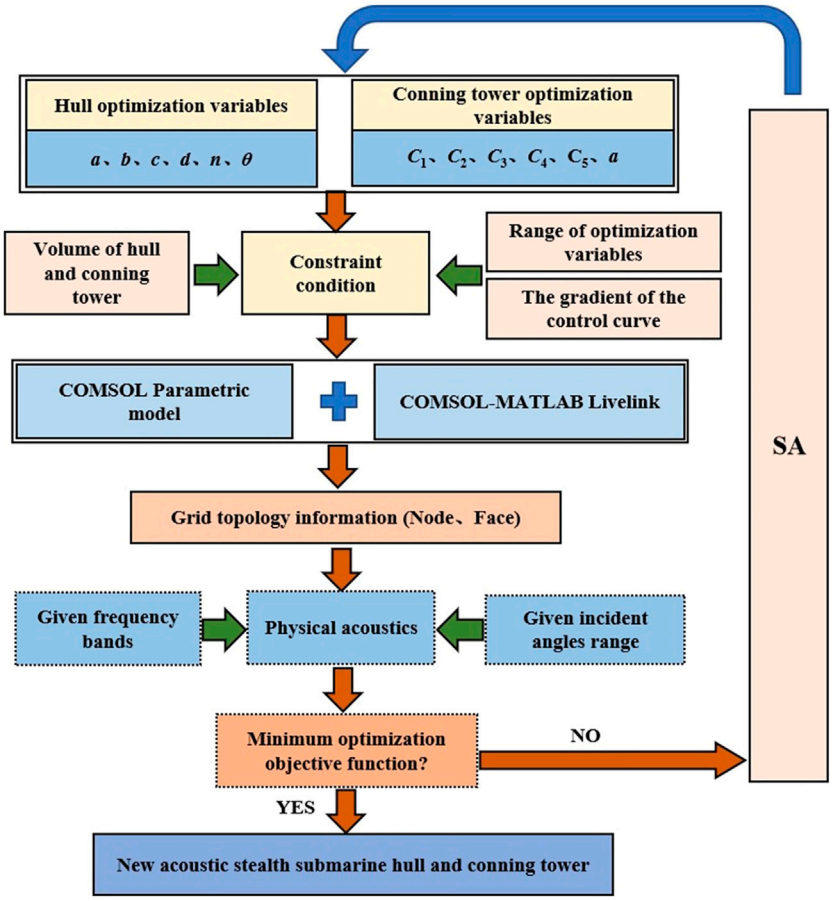

FIGURE 2
Schematic diagram of hull and conning tower optimization method.

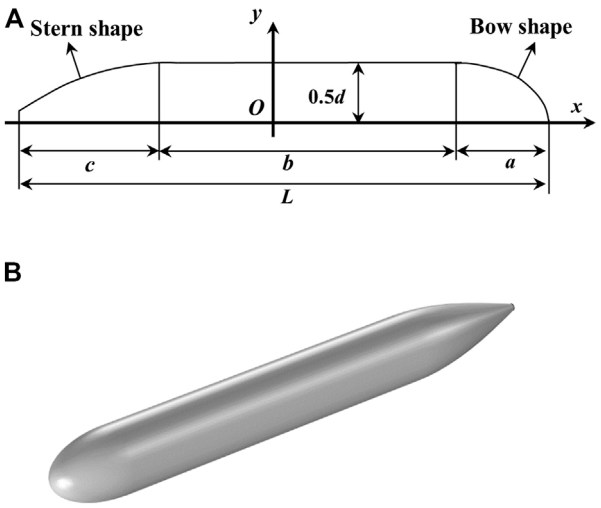

FIGURE 3
(A) Geometric description of axisymmetric hull. **(B)** Original hull.

the optimum design of acoustic stealth shapes of underwater vehicle hull and conning Tower, respectively. In Section 4, we present the optimization results of hull and conning tower for a give frequency band and detection angle. In Section 5, the PEM method is verified by experimental results. Finally, a summary and a discussion of the results are presented in Section 6.

2 Physical acoustical method

The difficulty of solving the problem of acoustic scattering from complex targets such as underwater vehicles has led to many approximate solution theories, such as physical acoustics. Figure 1 shows a schematic diagram of the derivation of the physical acoustic method.

Omitting the time factor $e^{-j\omega t}$, the basic formula for the scattering problem based on physical acoustics is given by

$$p_s(\vec{r}_2) = \frac{1}{4\pi}\int_{S_1+S_2}\left[p_s\frac{\partial}{\partial n}G(\vec{r}_2) - \frac{\partial p_s}{\partial n}G(\vec{r}_2)\right]ds, \quad (1)$$

where S_1 is the area directly illuminated by the incident sound wave, called the bright area, and S_2 is the area not illuminated by the incident sound wave, called the shadow area. $G(\vec{r}_2) = e^{ikr_2}/r_2$ is Green's function. Considering a rigid target, the KA formulation satisfies the bright and shadow areas, which can be expressed as

TABLE 1 Optimization variable range settings for hull.

Parameter	Initial value	Least value	Maximum value
a	7.5 m	$0.5d$	$3.5d$
b	37.5 m	0	$6.5d$
c	15 m	D	$4.5d$
d	7.5 m	7.25 m	7.75 m
n	2	1	4
θ	22°	10°	30°

$$\begin{cases} p_s = p_i, \dfrac{\partial(p_s + p_i)}{\partial n} = 0 \\ p_s = -p_i, \dfrac{\partial(p_s + p_i)}{\partial n} = 0 \end{cases}. \tag{2}$$

where P_i, P_s is the incident sound pressure and the scattering sound pressure. And the incident pressure is expressed as $p_i = e^{ikr_1}/r_1$.

Considering the far-field conditions $kr_1 \gg 1$, $kr_2 \gg 1$, $\cos\theta_1 = -\partial r_1/\partial n$, and $\cos\theta_2 = -\partial r_2/\partial n$, the terms in Eq. 1 can be expressed as

$$\frac{\partial p_s}{\partial n} = -\frac{\partial p_i}{\partial n} = \frac{ikr_1 - 1}{{r_1}^2} e^{ikr_1} \frac{\partial r_1}{\partial n} \approx \frac{ik}{r_1} e^{ikr_1} \cos\theta_1 \tag{3}$$

$$\frac{\partial G(\vec{r}_2)}{\partial n} = \frac{\partial}{\partial n}\left(\frac{e^{ikr_2}}{r_2}\right) \approx -\frac{ik}{r_2} e^{ikr_2} \cos\theta_2. \tag{4}$$

Substituting Eqs 2–4 into Eq. 1 yields

$$p_s(\vec{r}_2) = -\frac{ik}{4\pi}\left[\int_{S_1} \frac{e^{ik(r_1+r_2)}}{r_1 r_2}(\cos\theta_1 + \cos\theta_2)ds + \int_{S_2} \frac{e^{ik(r_1+r_2)}}{r_1 r_2}(-\cos\theta_1 + \cos\theta_2)ds\right] \tag{5}$$

In monostatic situation, $r_1 = r_2$, $\theta_1 = \theta_2$, and Eq. 5 can be simplified as

$$p_s(\vec{r}_2) = -\frac{ik}{2\pi}\int_{S_1} \frac{e^{i2kr_1}}{{r_1}^2} \cos\theta_1 ds \tag{6}$$

The details of calculation of Eq. 6 can be found in Ref. [28], which is omitted here.

3 Optimum design of acoustic stealth shapes of underwater vehicle hull and conning tower

Based on the PEM, this section considers the underwater vehicle hull and conning tower (considered as a rigid target at this stage) as the optimization objects and establishes the method of obtaining an optimized shape for acoustic concealment with a plane wave of a given frequency band and incident angle range. The optimized hull is a simplified benchmark hull model. During the optimization process, the generatrix line type of underwater vehicle hull is parameterized and controlled by a specific segment function that uses six hull optimization variables to describe it quantitatively. Before optimization, the conning tower is a simplified model of the benchmark conning tower. During the optimization process, the shape of the conning tower is regulated by the bottom and top contour lines and four optimized lofting control curves. The bottom contour line type remains the same as that of the original benchmark conning tower, and the top contour line type is obtained by scaling the bottom contour line type (by a scaling factor a). The deviation of each optimized lofting control curve from its corresponding initial lofting control curve is characterized by a Bernstein polynomial and scaling factor a.

The optimization method takes the displacement change rate of the hull and conning tower and the gradient of the lofting control curve as the constraints. The simulated annealing (SA) optimization algorithm is used to iterate the hull generatrix segmentation function. The six variables in the segmented function of the generatrix of the boat body to be determined, parameterized model of the conning tower of the command board, segmented function of the boat body generatrix, and contour control of the conning tower of the command board are iterated when the minimum optimal objective function is obtained through optimization calculation. Then, the optimal hull and conning tower shapes for acoustic concealment are determined. The optimized objective function is obtained by combining the COMSOL-MATLAB integrated modeling technology and the PEM to calculate the TSs of the hull and conning tower in a given frequency band and angle range and is weighted in a specific way. Figure 2 provides the details of the optimization algorithm flow.

3.1 Underwater vehicle hull geometry description and optimized variable control

Most underwater vehicle hulls are axisymmetric targets and can be divided into three parts: bow, middle, and stern. Figure 3A provides a schematic diagram of the linear piecewise function of the hull.

The overall length of the hull is $L = a + b + c = 8d$, where a, b, c, and d can be changed within certain ranges, and d is the diameter of the hull. Half of the total length is selected as the geometric origin position, and the line type of the bow and stern is described by a certain function.

$$y = 0.5d\left(1 - \left(\frac{x + a - 0.5L}{a}\right)^2\right)^{\frac{1}{n}} \tag{7}$$

$$y = 0.5d - \left(\frac{1.45d}{c^2} - \frac{\tan\theta}{c}\right)(x - c + 0.5L)^2 - \left(\frac{d}{c^3} - \frac{\tan\theta}{c^2}\right)(x - c + 0.5L)^3 \tag{8}$$

Equation 7 is the bow linear function. Linear bow control can be achieved by introducing variable n and combining variable a. Equation 8 is the stern linear function. Through variables c and θ linear stern control can be realized.

The overall shape of the hull can be controlled by variables a, b, c, d, n, and θ. To make the optimized hull shape more reasonable, the range of optimization variables and optimization constraints should be set. Table 1 shows the ranges of the optimization variables.

It can be seen from Table 1 that the total length L changes with the diameter of the hull in the optimization process. To obtain a reasonable shape, additional hull volume constraints need to be imposed. Figure 3B depicts the initial hull shape. The initial hull

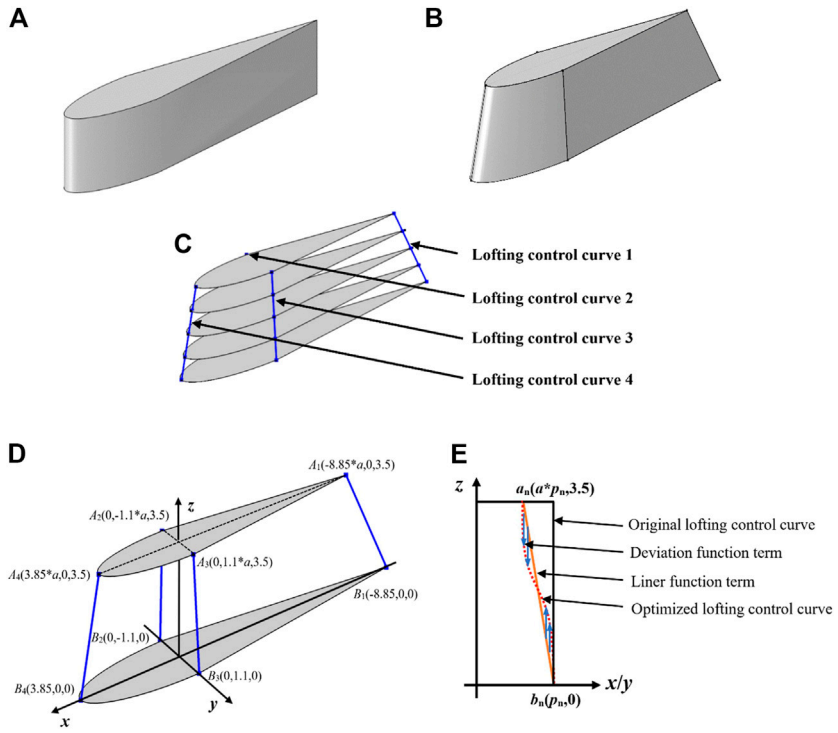

FIGURE 4
Basic idea of conning tower parametric modeling in the optimization process. **(A)** Original benchmark conning tower. **(B)** Optimized conning tower. **(C)** Lofting control curve of the conning tower. **(D)** Key points of 3D lofting control curve optimization. **(E)**Two-dimensional deviation function.

volume is $V_0 = 2{,}220.4\ \mathrm{m}^3$. During the optimization process, V satisfies $85\%\ V_0 \le V \le 115\%\ V_0$.

The stern linear function is more complicated and changeable. To make the optimized stern result more reasonable and to avoid a concave stern, the boundary constraints are shown as

$$\begin{cases} dy/dx \ge 0 \\ \dfrac{d^2y}{dx^2} \le 0 \end{cases}. \tag{9}$$

3.2 Geometric description of conning tower and optimal variable control

The conning tower, also known as the underwater vehicle bridge, is one of the most important parts of a underwater vehicle. As a complex structure, there is no general function expression for the shape of a conning tower. Hence, parametric modeling of the conning tower was performed using the lofting tool in the geometric modeling software. Basic geometric modeling software has such a modeling tool.

It can be seen from Figure 4 that parametric modeling of the conning tower can be realized in the optimization process through four lofting control curves. The steps of the parametric modeling process for the conning tower are as follows. Firstly, the contour shape of the bottom surface of the conning tower remains unchanged. Then, the uppermost contour of the conning tower becomes the bottom contour after plane scaling (by a zoom factor a). Next, moving up 3.5 m along the z-axis, the zoom center is located at the origin of the x-y coordinate system. Finally, using the lofting operation, based on the bottom and top contours, lofting is performed along the four lofting curves to obtain the new conning tower.

The optimized lofting control curve function can be obtained by adding the designed deviation function based on the lofting curve (linear function), as shown in Figure 4.

As shown in Figure 4D, there are two important position points for the four fitting control curves. Each lofting control curve is converted into a two-dimensional plane. As shown in Figure 4E, the corresponding points are converted, where A_n and B_n are converted into a_n and b_n, respectively. The coordinates of a_n and b_n are $(a \times p_n, 4)$ and $(p_n, 0)$, respectively, and p_1, p_2, p_3, and p_4 are −8.85, −1.1, 1.1, and 3.85, respectively. When the first and second control curves are distributed on the negative semi-axes in the x and y directions, Figure 4E is not applicable. At this time, only the corresponding points and curves are mirrored on the z-axis.

The optimized lofting control curve function is composed of two items: a linear function item and a deviation function, as shown in Figure 4E. The deviation function is shown in Eq. 10. The basic expression of the fifth-order Bernstein polynomial, which serves as the basis function to express the deviation function (without the i = 0 term) is

TABLE 2 Optimization variable ranges for conning tower.

Parameter	Initial value	Least value	Maximum value
a	1	0.7	1.3
C_1	0	−20	20
C_2	0	−20	20
C_3	0	−20	20
C_4	0	−20	20
C_5	0	−20	20

$$\Delta z = \sum_{i=1}^{5} C_i x^i (1-x)^{5-i}. \tag{10}$$

Taking the third optimized lofting control curve function as an example, its two-dimensional plane is the y-z plane and the formula is expressed as

$$z = \frac{3.5}{1-a}\left(1 - \frac{y}{p_3}\right) + \Delta z \tag{11}$$

$$z = \frac{3.5}{1-a}\left(1 - \frac{y}{p_3}\right) + \sum_{i=1}^{5} C_i \left(\frac{y-p_3}{(a-1)p_3}\right)^i \left(1 - \frac{y-p_3}{(a-1)p_3}\right)^{5-i}. \tag{12}$$

Gradient constraints of the optimized lofting control curve are set to avoid the discontinuity of echoes of the optimized conning tower, which can be expressed as

$$\begin{cases} dz/dy \geq 0 \\ dz/dy \leq 0 \\ dz/dx \leq 0 \end{cases}. \tag{13}$$

The boundary gradient constraints of the second, third, and fourth optimized lofting control curves correspond to the first, second, and third terms of Eq. 13, respectively. In the first one, the lofting control curve is optimized, and $\Delta z = 0$ is set without the boundary gradient constraint.

The volume constraint is also set. The volume of the original benchmark conning tower is $V_0 = 28.6\ \mathrm{m}^3$, and the volume constraint is 85% $V_0 \leq V \leq$ 115% V_0.

The overall shape of the conning tower can be controlled by variables a, C_1, C_2, C_3, C_4, and C_5, and the ranges of the optimized variables are set, as shown in Table 2.

3.3 Objective function

In the optimization process, the objective function of the optimization design must be clarified. Considering the deficiencies of the optimization objective function, a new type of acoustic stealth shape optimization objective function suitable for the hull and conning tower is proposed. The optimized objective function is determined by taking the product of the energy superposition of the TS at different incident angles and different frequency points and the linear average of all TS in the optimization process, to obtain the underwater vehicle hull and conning tower shapes for acoustic concealment. Equation 14 gives the optimization target used by this algorithm.

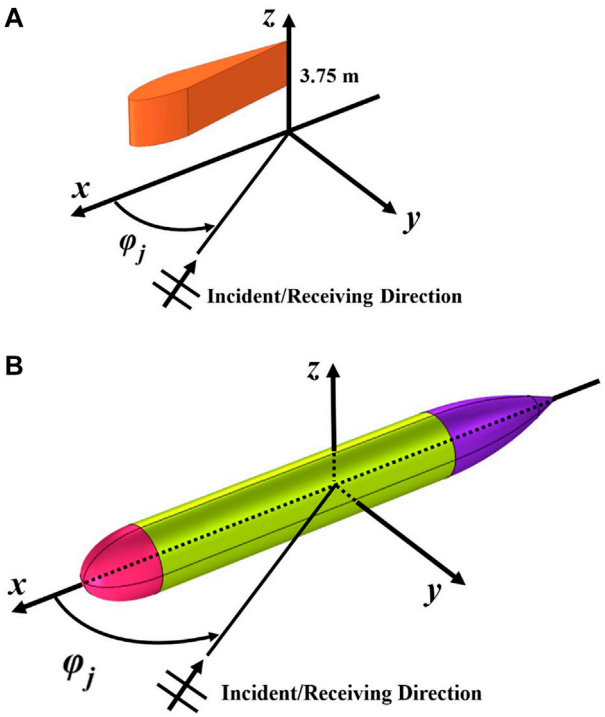

FIGURE 5
Schematic diagram for calculating the TSs of the hull and conning tower. **(A)** Conning tower. **(B)** Hull target.

$$TS_T = 10\lg\left(\sum_{\varphi_j=m}^{M}\sum_{f_i=n}^{N} 10^{\left(\alpha(f_i)\beta(\varphi_j)TS(f_i,\varphi_j)/10\right)}\right) \times \left(\sum_{\varphi_j=m}^{M}\sum_{f_i=n}^{N} TS\left(f_i,\varphi_j\right)\right) \Big/ (M_1 N_1), \tag{14}$$

where n and N is the start frequency and end frequency of optimization, respectively. N_1 is the number of frequency points, m is the start angle of incidence, M is the end angle of incidence, M_1 is the optimized number of angles, $TS(f_i, \varphi_j)$ is the single-station TS of the hull or conning tower at the incident angle φ_j of the plane wave with frequency f_i, TS_T is the product of the total TS of the hull or conning tower with different frequencies of incident plane waves at different incidence angles.

Figure 5 presents the TS calculation diagrams of the underwater vehicle hull and conning tower used in the optimization process. When calculating the TS of the conning tower, the z-axis coordinate of the lowest profile surface of the conning tower is 3.75 m, and the acoustic geometric center of the hull is set at the center of the hull when calculating the TS. That is, for both the hull and conning tower, the acoustic geometric center of the TS calculation is at the coordinate origin (0, 0, 0) to ensure that the relative positions of the hull and conning tower space remain unchanged and the correctness of the echoes from the hull and conning tower assembly are obtained by overlapping the complex sound pressures of the sub-components.

It should be noted that the parametric modeling method given in Section 3.1 is only for the conning tower. When calculating the TS of the conning tower, the z-axis coordinate of the lowest surface of the

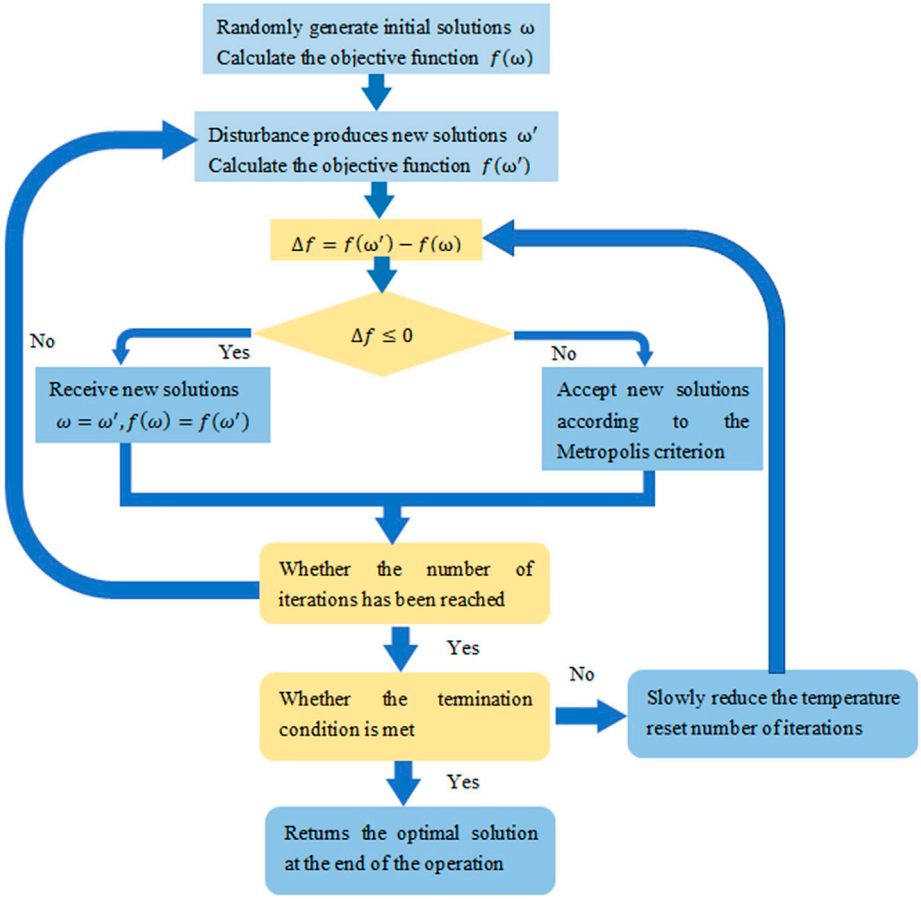

FIGURE 6
Basic concept of SA.

conning tower is 3.75 m to ensure that the relative position of the conning tower space remains unchanged.

3.4 Introduction to SA optimization algorithm

The SA algorithm was firstly proposed by Metropolis et al. [30] in 1953. This approach is a stochastic optimization algorithm based on the Monte Carlo iterative solution strategy. Its starting point is based on the similarity between the annealing process of solid matter in physics and general combinatorial optimization problems. The SA algorithm starts from a certain high initial temperature, and with the continuous decrease of the temperature parameters, combined with probabilistic sudden jump characteristics, it randomly finds the global optimal solution of the objective function in the solution space. That is, the local optimal solution can jump out probabilistically and eventually tend to the global optimum.

The SA algorithm is an optimization algorithm that can effectively avoid falling into local minima and finally approaches the global optimal serial structure by giving the search process a time-varying probability jump ability that eventually approaches zero. Figure 6 presents a flow chart of the basic concept.

4 Optimization results

4.1 Multi-frequency and multi-angle optimization of hull

When the plane wave is irradiated onto the underwater vehicle hull with a frequency modulation signal, the unknown detection angle greatly increases the possibility of exposure. To reduce the probability of being discovered, this section presents the optimal hull design for acoustic concealment considering multiple frequencies and angle. The optimized objective function under the working conditions in Eq. 14 should be simplified, as shown in Eq. 15:

$$TS_T = 10\lg\left(\sum_{\varphi_j=m}^{M}\sum_{f_i=n}^{N}10^{\left(TS\left(f_i,\varphi_j\right)/10\right)}\right)\left(\sum_{\varphi_j=m}^{M}\sum_{f_i=n}^{N}TS\left(f_i,\varphi_j\right)\right)\Big/\left(M_1N_1\right), \tag{15}$$

where n is the optimized start frequency, N is the optimized stop frequency, N_1 is the number of optimized frequency points, m is the optimized initial angle of incidence, M is the optimized final angle of incidence, M_1 is the optimized number of angles, $TS(f_i, \varphi_j)$ is the single-station TS of the hull or conning tower at the incident angle φ_j of the plane wave with frequency f_i, and TS_T is the product of the

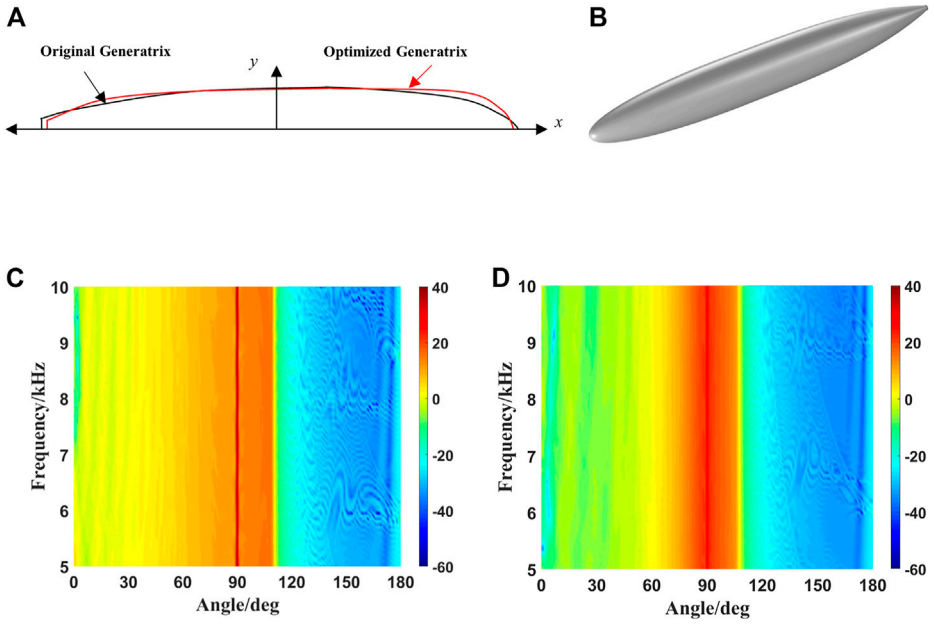

FIGURE 7
Comparison of the hull generatrices before and after optimization and three-dimensional diagram after optimization. **(A)** Front and rear hull generatrices. **(B)** Optimized 3D model of the hull. **(C)** Angle–frequency spectra of hull *TS* before optimization. **(D)** Angle–frequency spectra of hull TS after optimization.

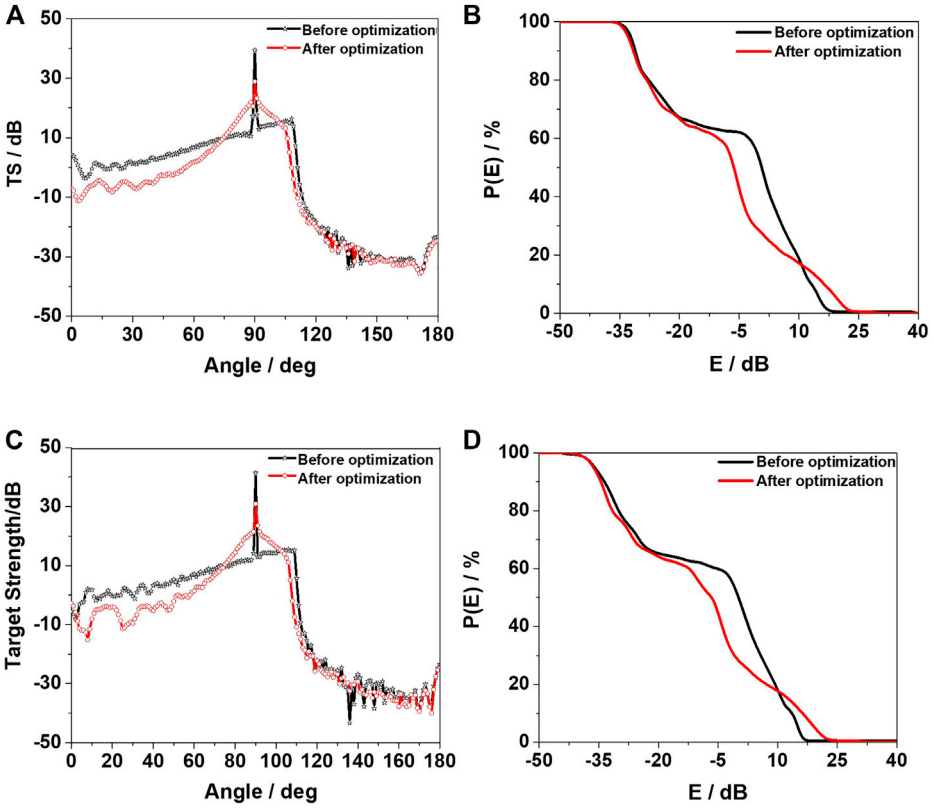

FIGURE 8
Azimuth characteristics and detection rate with respect to angle of the TS of the hull before and after optimization. **(A,B)** are *f* = 5.0 kHz. **(C,D)** are *f* = 10.0 kHz.

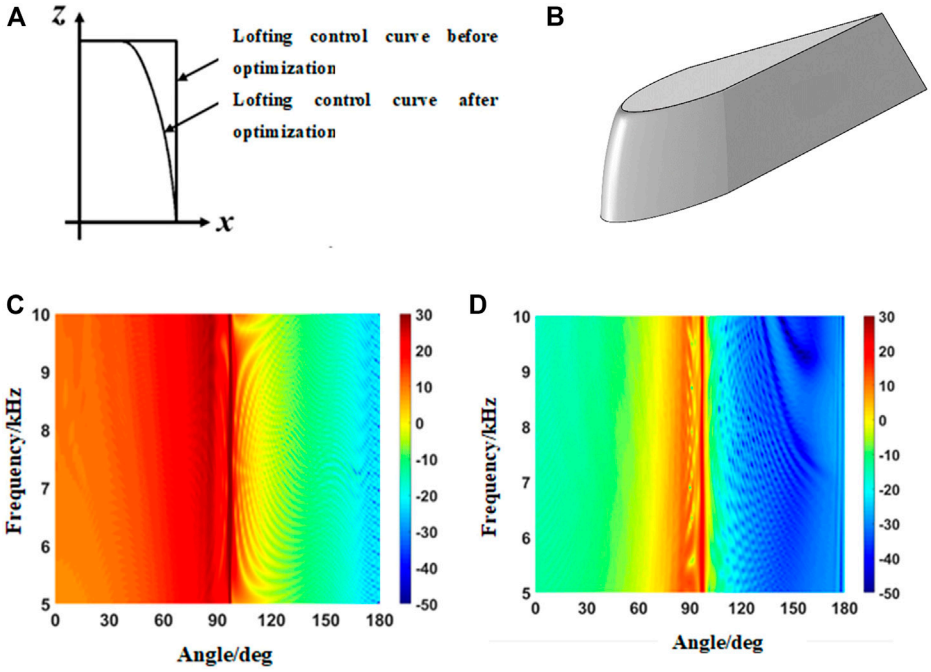

FIGURE 9
Optimized conning tower models. **(A)** Lofting control curve comparison. **(B)** Optimized conning tower model. **(C)** Angle–frequency spectra of the conning tower TS before optimization. **(D)** Angle–frequency spectra of the conning tower TS after optimization.

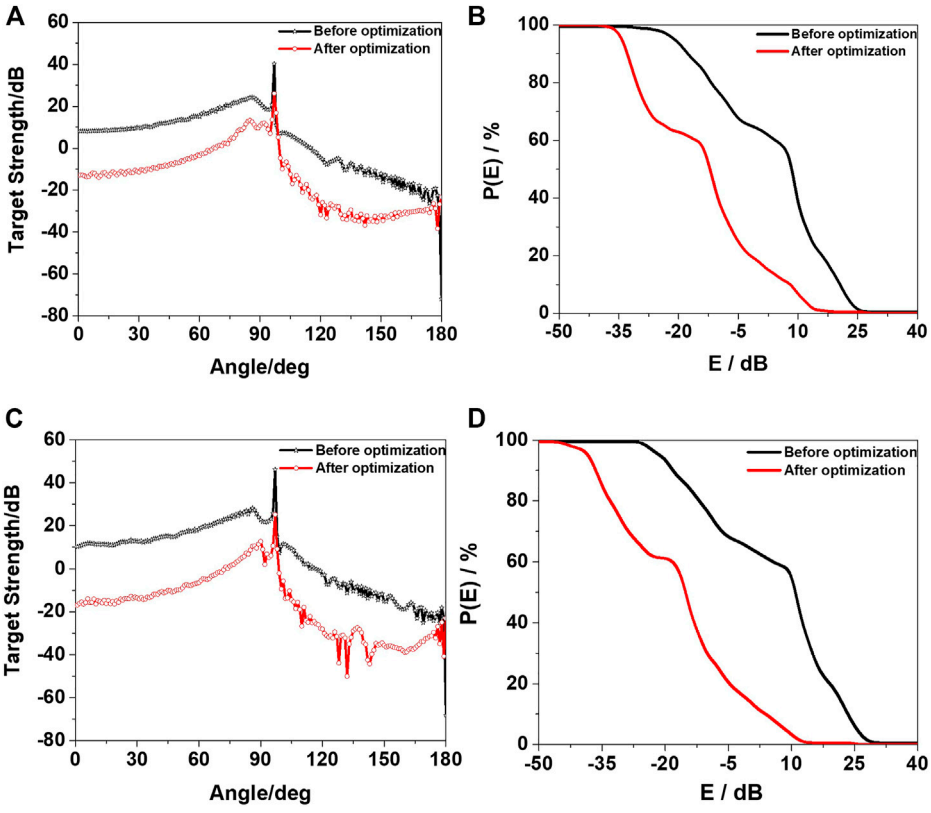

FIGURE 10
Azimuth characteristics and angle detection rate of the conning tower TS before and after optimization. **(A,B)** are *f* = 5.0 kHz. **(C,D)** are *f* = 10.0 kHz.

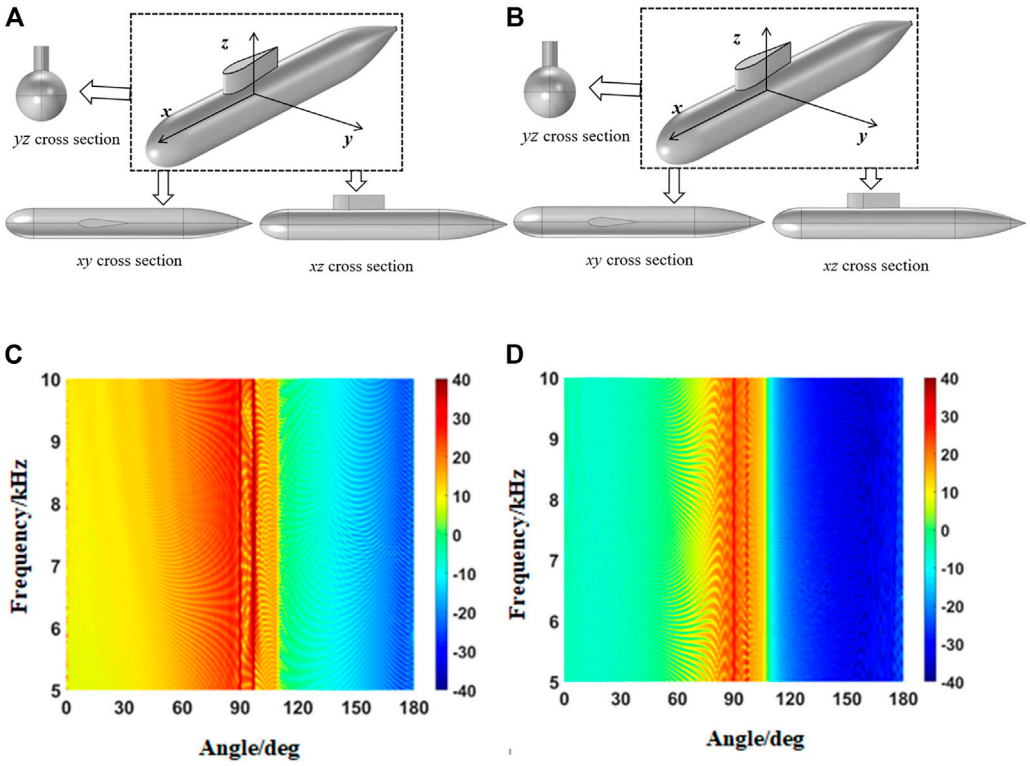

FIGURE 11
(A) Original model. **(B)** Optimized model. **(C)** Angle–frequency spectra of the TS of the assembly of the hull with conning tower before optimization. **(D)** Angle–frequency spectra of the TS of the assembly of the hull with conning tower after optimization.

energy weighted value of the hull TS and the linear mean value considering different plane wave incident angles and different frequencies. The optimized incident angle range was set as 0°–180° with a step length of 1°, and the incident sound wave frequency band was 5.0–10.0 kHz with the step length of 0.25 kHz. The computer used for the calculations had a main frequency of 4.20 GHz, running memory of 32 GB, and the calculation time of 158 h. Based on iteration of the optimization algorithm, Figure 7 compares the generatrix types before and after hull optimization and presents the optimized three-dimensional diagram.

The six optimized variables of the bus-line type control in the optimized new hull are a = 23.6259 m, b = 5.6487 m, c = 31.2789 m, d = 7.5690 m, n = 2.1950, and θ = 18.3310°. When the hull before and after optimization is irradiated by plane acoustic wave at a frequency of 5.0–10.0 kHz and an incident angle of 0°–180°, the TS angle–frequency spectrum can be calculated, as shown in Figures 7C, D.

The TS angle–frequency spectra of hull before and after hull optimization have their limitations. Therefore, Figure 8 compares the horizontal azimuth characteristics and angle detection rate of the hull at different frequency points. Because the azimuth characteristics and angular detection rate of the hull are the same at each frequency point, the results are only under two frequency points.

Figures 8A–D compare the azimuth characteristics and angle detection rate of the TS before and after optimization of the hull at f = 5.0 kHz and f = 10.0 kHz. The TS of the optimized hull is lower than that of the original hull at most angles and frequencies. Although the optimization has a certain effect, the optimized objective function has certain limitations and does not specifically consider the changes in the TS at all angles and frequencies. Within the range of 120°–180°, the TS of the hull before and after optimization does not differ much. After optimization, it is reduced by approximately 3 dB compared to that before optimization. The reason is that the echo energy at the stern part of the hull is relatively weak in this angle range, and the reduction range is limited, making little contribution to the optimization objective function. The algorithm ignores this part in the process of optimization through iteration. The same conclusion can be obtained from the angle detection rate graph, where the angle is 0°–180° with a step length of 1° and the frequency range is 5.0–10.0 kHz with a step length of 0.05 kHz. After calculation, the total average TS after optimization is reduced by 5.89 dB compared to that before optimization. For the abeam direction (90°), the total average TS after optimization is reduced by 10.37 dB compared to that before optimization. After optimization, the hull displacement is 85.2% of V_0.

4.2 Multi-frequency and multi-angle optimization of the conning tower

The optimization objective function used for conning tower shape optimization is given by Eq. 14. The optimized frequency band was selected to be 5.0–10.0 kHz, and the step length was 0.25 kHz for optimization. The optimization angle range was 0°–180° with a step length of 1°. Figure 9 compares the fourth lofting control curve of the optimized conning tower and shows the optimized three-dimensional

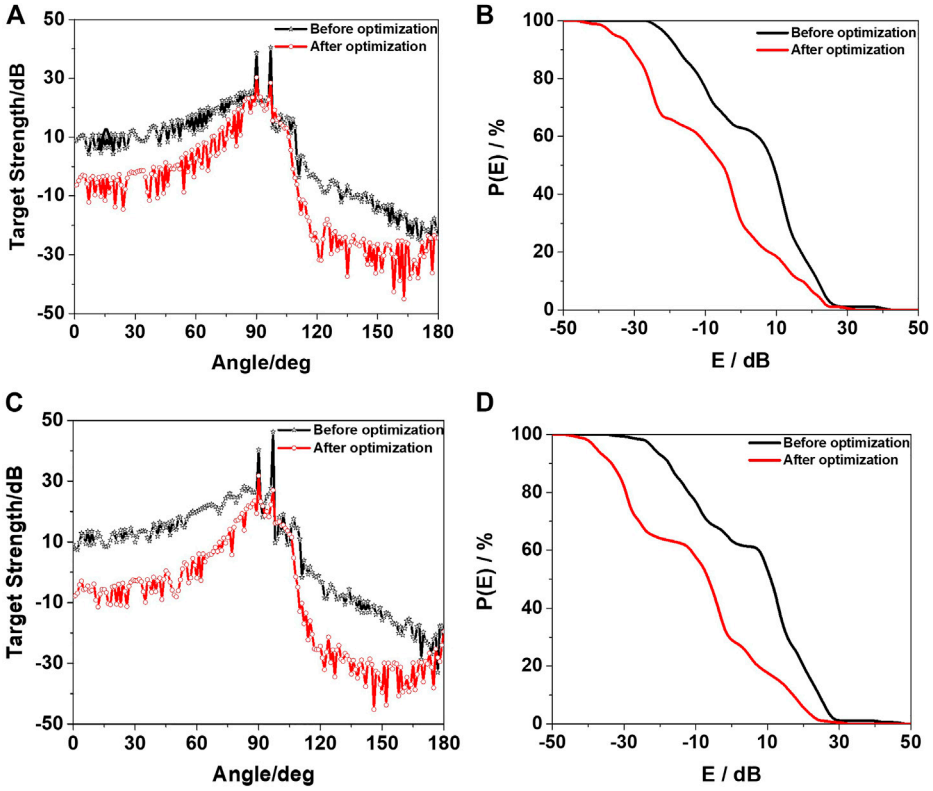

FIGURE 12
Comparison of azimuth characteristics and angle detection rate of TS of the assembly of the hull and conning tower before and after optimization. **(A,B)** are f = 5.0 kHz. **(C,D)** are f = 10.0 kHz.

diagram. The calculation time was 113 h, and the computer parameters were as mentioned earlier.

The six optimized variables of the tower model obtained through optimization are a = 0.7730, C_1 = 3.3020, C_2 = 16.0461, C_3 = 18.1762, C_4 = 16.0281, and C_5 = 8.1101. Figures 9C, D shows the angle–frequency spectra of the TS of the conning tower before and after optimization.

The horizontal azimuth characteristics of the TS and angle detection rate of the conning tower under different frequency were compared as well, as shown in Figure 10. It can be seen from Figure 10 that in the optimized frequency band and angle range, the optimized conning tower has a lower TS than the original conning tower. This conclusion can also be seen from the comparison of the conning tower detection rate before and after optimization, where the incident angle range is 0°~180° with a step size of 1° and the frequency range is 5.0–10.0 kHz with a step size of 0.05 kHz. After calculation, the total average TS after optimization is reduced by 18.21 dB compared to that before optimization, and the optimized volume is 85.1% V_0.

4.3 Evaluation of optimization effect of hull and conning tower combination

Sections 4.1, Sections 4.2 described the optimization of the acoustic stealth shapes of the hull and conning tower. The original benchmark hull and conning tower combination and optimized hull and conning tower combination were used to calculate the TS (ignoring the errors caused by assembly). The specific dimensions were described in the text. TS calculation diagram is shown in Figure 11.

Using the PEM to calculate the original and optimized benchmark hull and conning tower combinations, the angle–frequency spectrum of the TS was obtained in Figure 11. Figure 12 presents the azimuth angle characteristics and detection rate according to the angle for the optimized front and rear hull and conning tower combination at different frequency points.

It can be seen from Figures 11, 12 that the TS of the hull and conning tower combination before and after optimization are quite different. In most angle ranges, the sound concealment of the optimized hull and conning tower combination is obviously better than that before optimization, where the incident angle range is 0°–180° with a step size of 1° and the frequency range is 5.0–10.0 kHz with a step size of 0.01 kHz. After calculation, the total average TS after optimization is reduced by 10.58 dB compared to that before optimization. The total average TS after optimization is reduced by 10.36 dB at the abeam direction compared with that before optimization.

5 Experimental verification

The specific Benchmark submarine model and the test equipment are shown in Figure 13. It is a scale single shell benchmark model with a scaling value of 1:15.

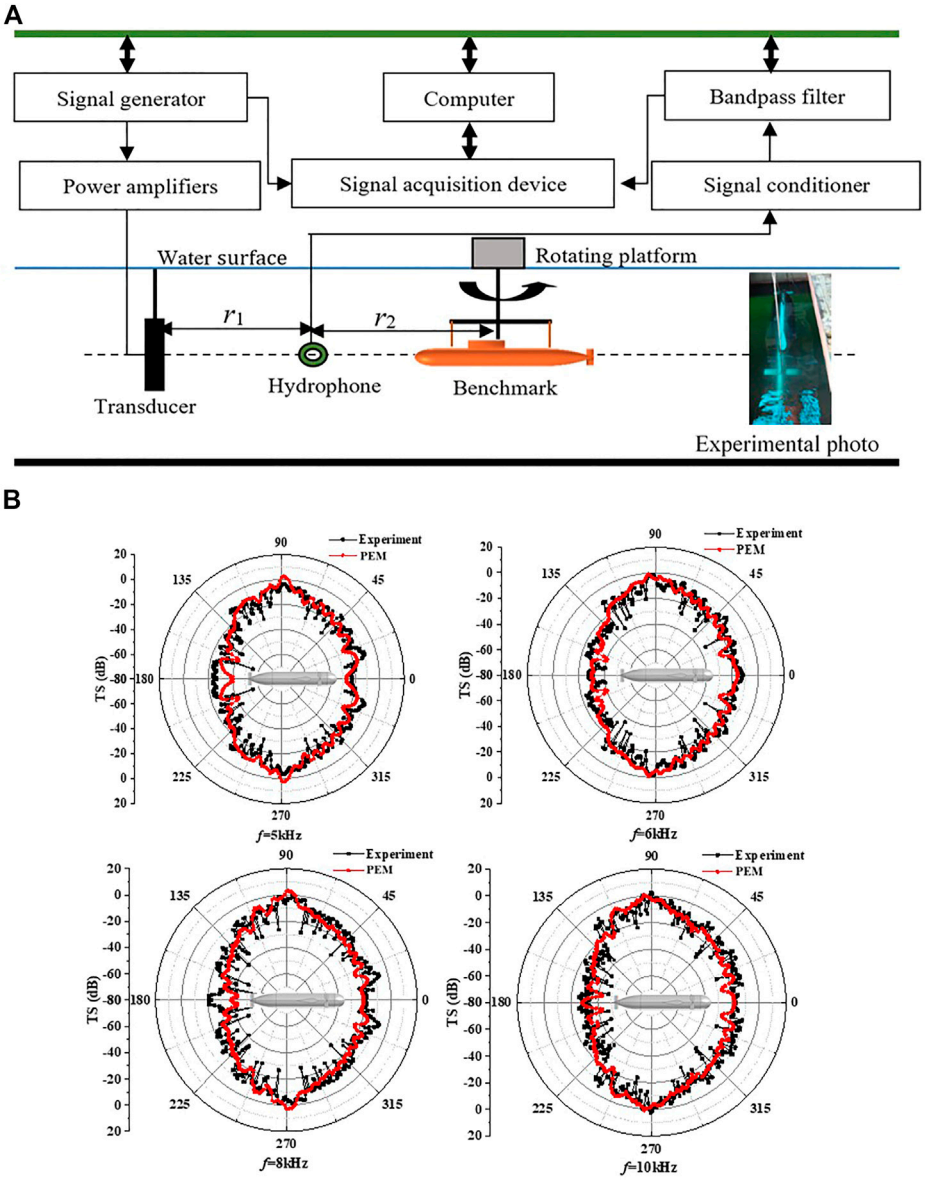

FIGURE 13
(A) Test equipment layout. **(B)** TS results comparisons between the experimental and PEM results at different frequencies.

The TS calculation formula is as follows

$$TS = 20\lg\left|\frac{p_{s@1m}}{p_i}\right| = 20\lg\left|\frac{p_s r_2 (r_1 + r_2)}{p_1 r_1}\right| = 20\lg\left|\frac{V_s r_2 (r_1 + r_2)}{V_1 r_1}\right|, \quad (16)$$

where p_s and $p_{s@1m}$ are the echo pressure from Benchmark submarine received by the hydrophone and at 1 m, respectively. p_1 is sound pressure of sound source received by hydrophone. r_1 and r_2 are the distances between hydrophone and transducer or target center, respectively. V_s and V_1 are voltage amplitudes of target echo and sound source received by hydrophone, respectively.

The shell is considered as a rigid target in the simulation calculation. TS comparisons of a Benchmark submarine between the experimental results and PEM in monostatic configuration are shown in Figure 13.

As illustrated in Figure 13, at the frequency of 5, 6, 8, and 10 kHz, the TS directivity of Benchmark presents a butterfly shape for both simulation results and experimental results, that is, the TS is low when the acoustic wave is incident from bow and stern, and highest during the abeam incident.

By conducting the acoustic scattering experiment of Benchmark submarine scale model in lake, the experimental results at different frequencies are obtained. From Figure 13B, the TS average errors between PEM and experimental results are within ±3 dB with a good agreement.

6 Conclusion

In this study, the hull and conning tower of an underwater vehicle (considered as rigid targets) were used as the optimization objects, and the method of optimizing the underwater vehicle shape for acoustic concealment considering incident plane waves of multiple angles and frequencies was established based on the PEM. Experiment results is

used to prove that PEM and experimental results are in good agreement. The volume change rates of the hull and the conning tower, and the gradient of the generatrix or lofting control curve is chosen as constraints. the. The six variables in the precise section function of the hull generatrix and the six variables in the parametric model of the conning tower were determined respectively by applying SA optimization algorithm. The weight of the TS in the given frequency band and angle range of the hull and conning tower shell was chosen as the optimized objective function by applying COMSOL-MATLAB integrated modeling technology combined with the PEM. After optimization, the six variables in the segmental function of the hull generatrix and the shape control function of the conning tower were obtained to determine the optimal hull and conning tower shapes for acoustic concealment, when the optimized objective function was the smallest.

(1) The optimization method proposed in this paper overcomes the original limitation of relying only on experience or hydrodynamic performance optimization to modify the line shapes of the underwater vehicle hull and conning tower. Further, it can be utilized to perform automatic optimization of the shapes of the hull and conning tower for acoustic concealment within a given frequency band and angle range.
(2) When the plane wave was f = 5.0–10.0 kHz and an incident angle range of 0°–180°, the optimized hull has a total average TS 5.89 dB lower than that before optimization when this method is applied. In particular, the abeam angle is reduced by about 10.37 dB, and the optimized volume is 85.2% V_0. The total averaged TS of the optimized conning tower is 18.21 dB lower than that before optimization in the optimized frequency band, and the optimized volume is 85.1% V_0.
(3) When the plane wave was f = 5.0–10.0 kHz and the incident angle range is 0°–180°, the total average TS of the hull and conning tower combination is reduced by 10.58 dB compared with combination of hull and conning tower before optimization. When the abeam angle is 90°, the total average TS after optimization is reduced by 10.36 dB compared to that before optimization.

The optimization method proposed in this paper has still some deficiencies. For example, one of the constraint conditions is the volume or displacement of optimization model should be within 15%, which makes the reduction of TS depends on two factors, i.e., both the shape modification and the volume variation. However, if the volume variation can be constrained within 1%, the optimization work will be more rigorous and convincing. But meanwhile, the convergence performance of this optimization will be worse and unsatisfied, and the optimization process will be more time-consuming. Thus the optimization algorithm need further research and improvement in the future. In conclusion, the optimization method can greatly reduce the TS of the hull and conning tower in a given frequency band and incident angle range, enabling the automatic optimization of underwater vehicle hull and conning tower shapes for acoustic stealth. This optimization method can serve as a reference for the design of underwater acoustic stealth vehicle shapes.

Data availability statement

The original contributions presented in the study are included in the article/supplementary material, further inquiries can be directed to the corresponding author.

Author contributions

We thank YT and BL for in modeling and simulation. We thank XW and ZP for instruction. We also thank XM and SG for their helpful discussions.

Funding

This work was supported by the Foundation Strengthening Program Area Fund of Science and Technology Commission of the Central Military Commission (No. 2020-JCJQ-JJ-228), Natural Science Foundation of Jiangsu Province (No. BK20200995) and National Youth Science Foundation of China (No.52201397).

Acknowledgments

We are grateful for the proofreading of the article by Jiaman Du. Finally, we would like to thank the reviewers for the insightful comments and helpful suggestions made.

Conflict of interest

The authors declare that the research was conducted in the absence of any commercial or financial relationships that could be construed as a potential conflict of interest.

Publisher's note

References

1. Mackay M, Defence R. *The standard submarine model: A survey of static hydrodynamic experiments and semiempirical predictions*. Halifax, Canada: Defence R&D (2003).

2. Suman KNS, Rao DN, Das HN, Bhanu Kiran G. Hydrodynamic performance evaluation of an ellipsoidal nose for a high speed under water vehicle. *Jordan J Mech Ind Eng* (2010) 4(5):641–52.

3. Praveen PC, Krishnankutty P. Study on the effect of body length on the hydrodynamic performance of an axi-symmetric underwater vehicle. *Indian J Geo-Marine Sci* (2013) 42(8): 1013–22.

4. Moonesun M, Korol YM, Brazhko A. CFD analysis on the equations of submarine stern shape. *J Taiwan Soc Naval Architects Mar Eng* (2015) 34(1):21–32.

5. Moonesun M, Korol Y, Dalayeli H. CFD analysis on the bare hull form of submarines for minimizing the resistance. *Int J Maritime Tech* (2015) 3:1–16.

6. Moonesun M, Korol YM, Dalayeli H, Tahvildarzade D, Javadi M, Jelokhaniyan M, et al. Optimization on submarine stern design. *Proc Inst Mech Eng M: J Eng Maritime Environ* (2017) 231(1):109–19. doi:10.1177/1475090215625673

7. Vasudev KL, Sharma R, Bhattacharyya SK. Multi-objective shape optimization of submarine hull using genetic algorithm integrated with computational fluid dynamics. *Proc Inst Mech Eng Part M: J Eng Maritime Environ* (2019) 233(1):55–66. doi:10.1177/1475090217714649

8. Vasudev KL, Sharma R, Bhattacharyya SK. Shape optimisation of an AUV with ducted propeller using GA integrated with CFD. *Ships and Offshore Structures* (2018) 13(2): 194–207. doi:10.1080/17445302.2017.1351292

9. Paz JDM, Muñoz ODT. Multiobjective optimization of a submarine hull design. *Ciencia y tecnología de buques* (2014) 7(14):27–42. doi:10.25043/19098642.92

10. Gao T, Wang Y, Pang Y, Cao J. Hull shape optimization for autonomous underwater vehicles using CFD. *Eng Appl Comput Fluid Mech* (2016) 10(1):599–607. doi:10.1080/19942060.2016.1224735

11. Wu TW, Li WL, Seybert AF. An efficient boundary element algorithm for multi-frequency acoustical analysis. *The J Acoust Soc America* (1993) 94(1):447–52. doi:10.1121/1.407056

12. Everstine GC, Henderson FM. Coupled finite element/boundary element approach for fluid–structure interaction. *J Acoust Soc America* (1990) 87(5):1938–47. doi:10.1121/1.399320

13. Waterman PC. New formulation of acoustic scattering. *J Acoust Soc America* (1969) 45(6):1417–29. doi:10.1121/1.1911619

14. Waterman PC. Matrix theory of elastic wave scattering. *J Acoust Soc America* (1976) 60(3):567–80. doi:10.1121/1.381130

15. Boström A. Scattering of stationary acoustic waves by an elastic obstacle immersed in a fluid. *J Acoust Soc America* (1980) 67(2):390–8. doi:10.1121/1.383925

16. Jie S, Weisong Z, Xiangjun J, Xin Z, Malekian R. Underwater broadband acoustic scattering modelling based on FDTD. *Elektronika ir Elektrotechnika* (2015) 21(2):58–64. doi:10.5755/j01.eee.21.2.11513

17. Ma L, Wang R, Xiang H. Computation of bi-static target strength and separation of forward-scattering sound from objects. *Acta Acustica* (2009) 6.

18. Stanton TK. Sound scattering by cylinders of finite length. III. Deformed cylinders. *J Acoust Soc America* (1989) 86:691–705. doi:10.1121/1.398193

19. Stanton TK. Sound scattering by spherical and elongated shelled bodies. *J Acoust Soc America* (1990) 88(3):1619–33. doi:10.1121/1.400321

20. Partridge C, Smith ER. Acoustic scattering from bodies: Range of validity of the deformed cylinder method. *J Acoust Soc America* (1995) 97(2):784–95. doi:10.1121/1.412943

21. Sarkissian A. Method of superposition applied to scattering from a target in shallow water. *J Acoust Soc America* (1994) 95(5):2340–5. doi:10.1121/1.409870

22. Tang W. Highlight model of echoes from sonar targets. *Acta Acustica* (1994) 2: 92–100.

23. Abawi AT. Kirchhoff scattering from non-penetrable targets modeled as an assembly of triangular facets. *J Acoust Soc America* (2016) 140(3):1878–86. doi:10.1121/1.4962735

24. Lavia EF, Gonzalez JD, Blanc S. Modeling high-frequency backscattering from a mesh of curved surfaces using Kirchhoff Approximation. *J Theor Comput Acoust* (2019) 27(04):1850057. doi:10.1142/s2591728518500573

25. Kim K, Cho JH, Kim JH, Cho DS. A fast estimation of sonar cross section of acoustically large and complex underwater targets using a deterministic scattering center model. *Appl Acoust* (2009) 70(5):653–60. doi:10.1016/j.apacoust.2008.07.009

26. Fan J, Tang WL, Zhuo LK. Planar elements method for forecasting the echo characteristics from sonar targets. *J Ship Mech* (2012) 16(1-2):171–80.

27. Peng Z, Wang B, Fan J. Simulation and experimental studies on acoustic scattering characteristics of surface targets. *Appl Acoust* (2018) 137:140–7. doi:10.1016/j.apacoust.2018.02.014

28. Li B, Peng Z, Wen H, Fan J, Song H. Research on the optimization design of acoustic stealth shape of the underwater vehicle Head. *Acoust Aust* (2020) 48:39–47. doi:10.1007/s40857-019-00170-5

29. Li B, Zhou F, Fan J, Wang B, Peng Z. Research on the optimization design of the acoustic stealth shape of a bottom object. *J Theor Comput Acoust* (2022) 30(02):2150009. doi:10.1142/s2591728521500092

30. Metropolis N, Rosenbluth AW, Rosenbluth MN, Teller AH, Teller E. Equation of state calculations by fast computing machines. *J Chem Phys* (1953) 21(6):1087–92. doi:10.1063/1.1699114

frontiers | Frontiers in Physics

TYPE Original Research
PUBLISHED 16 March 2023
DOI 10.3389/fphy.2023.1141129

OPEN ACCESS

EDITED BY
Thierry Baasch,
Lund University, Sweden

REVIEWED BY
Hui Chen,
Ningbo University, China
Zongliang Du,
Dalian University of Technology, China

*CORRESPONDENCE
Xiaoning Liu,
liuxn@bit.edu.cn

SPECIALTY SECTION
This article was submitted to Physical Acoustics and Ultrasonics, a section of the journal Frontiers in Physics

RECEIVED 10 January 2023
ACCEPTED 27 February 2023
PUBLISHED 16 March 2023

CITATION
Qu H, Liu X and Zhang A (2023), Interface transmittance and interface waves in acoustic Willis media.
Front. Phys. 11:1141129.
doi: 10.3389/fphy.2023.1141129

Interface transmittance and interface waves in acoustic Willis media

Hongfei Qu[1,2], Xiaoning Liu[3]* and Anfu Zhang[4]

[1]State Key Laboratory of Mechanical Behavior and System Safety of Traffic Engineering Structures, Shijiazhuang Tiedao University, Shijiazhuang, China, [2]Key Laboratory of Mechanical Behavior Evolution and Control of Traffic Engineering Structures in Hebei, Shijiazhuang Tiedao University, Shijiazhuang, China, [3]School of Aerospace Engineering, Beijing Institute of Technology, Beijing, China, [4]Wuhan Second Ship Design and Research Institute, Wuhan, China

Acoustics Willis media, known as bianisotropic acoustic media, incorporate additional coupling between pressure and velocity and between momentum and volumetric strain in their constitutive equation. The extra coupling terms have a significant influence on acoustic wave behavior. In this paper, the unusual wave phenomena relevant to interfaces between homogeneous acoustic Willis media are theoretically studied. We show that Willis media offer more flexible control in wave front and energy flow when waves are transmitted through an interface. Different from traditional acoustic fluid, Willis acoustic media support edge and interface waves, for which the existence conditions and corresponding wave features are systematically investigated. The study unveils more possibilities for manipulating acoustic waves and may inspire new functional designs with acoustic Willis metamaterials.

KEYWORDS

metamaterial, Willis medium, wave manipulation, interface transmittance, interface wave

1 Introduction

In the past 20 years, with the emergence and development of metamaterials, the design space of wave devices and other functionality structures has been enlarged unprecedentedly. Metamaterials often exhibit abnormal material properties that natural materials usually do not have, which can lead to many novel wave phenomena, such as negative refraction [1, 2], super lens [3, 4], and wave cloaking [5–7], providing broad application prospects and meanwhile appealing more sophisticated homogenization for the characterization of the dynamic effective properties. In this background, the theory of Willis materials, initially proposed by Willis [8] in the 1980s for the dynamic behavior of solid composite materials, has regained much attention [9–12].

Acoustic Willis media (known as acoustic bianisotropic media) incorporate coupling between pressure and velocity and between momentum and volumetric strain. It has been found that the local Willis coupling is directly related to the local asymmetry of unit cells [12]. Accordingly, different designs of acoustic Willis meta-atoms have been proposed, such as the membrane unit [13, 14], folded channel [15], and Helmholtz resonators [16, 17]. The extra degree of design freedom offered by the Willis coupling is utilized to realize various novel wave functionalities. Several studies have observed asymmetric reflection [11, 18–20] when waves are incident from different directions, based on which the unidirectional absorber may be realized [21–23]. When Willis meta-atoms are used in metasurfaces [13, 24–26] or metagratings [15, 27, 28] for anomalous refraction or reflections, independent and

more efficient control of transmission and reflection can be realized. In addition, active mechanisms can be introduced to enhance the significance and flexibility of the coupling effect [29, 30], with which many non-reciprocal phenomena are demonstrated [30, 31]. Although remarkable progress has been made in recent years, most of the research on acoustic Willis coupling concentrates on the physical origin and design of Willis meta-atoms. Extended wave functionalities are usually demonstrated in reduced dimensionality, such as metasurfaces. Relatively, systematic theoretical study of wave behaviors in continuous Willis media has not received much attention. In recent works, some phenomena, such as sound scattering [32], sound focusing [33], and the topological phase transition [34] in Willis acoustic media, have been investigated.

In this paper, the unusual wave phenomena relevant to interfaces between homogeneous acoustic Willis media are theoretically studied. Section 2 discusses the general properties of bulk waves in Willis media, such as slowness curves, wave modes, and impedance. Section 3 explains the interface transmittance when a wave is incident into a Willis medium, which exhibits more flexible control in wave front and energy flow through material parameters. Section 4 considers the edge and interface waves in Willis media, partly demonstrated in [35]. Here, we present a more systematical examination considering other possibilities along with the corresponding parameter conditions and wave modes. Finally, conclusions are drawn in Section 5.

2 General bulk wave properties

Assuming harmonic motion with circular frequency ω and time convention $e^{-i\omega t}$, the momentum and continuity equations of Willis media are, respectively, as follows:

$$i\omega\boldsymbol{\mu} = \nabla p \quad \text{and} \quad -i\omega\varepsilon = \nabla\cdot\mathbf{v}, \tag{1}$$

where p is the acoustic pressure, ε the volumetric strain, $\mathbf{v}$ the particle velocity, and $\boldsymbol{\mu}$ the momentum density. Distinct from traditional acoustic fluid, the constitutive relations of Willis media are characterized by

$$\begin{cases} -p = \kappa\varepsilon + \mathbf{S}\cdot\mathbf{v}, \\ \boldsymbol{\mu} = \boldsymbol{\rho}\cdot\mathbf{v} + \mathbf{S}\varepsilon, \end{cases} \tag{2}$$

where κ and $\boldsymbol{\rho}$ are the bulk modulus and mass density, respectively. The density is in tensorial form and can be anisotropic. The vector $\mathbf{S}$ represents the acoustic Willis coupling term, whose fundamental physics originates from the locally monopolar–dipolar coupling and non-local phase effects of acoustic scatterers [12]. Here, we assume that the non-local effects could be ignored; hence, $\mathbf{S}$ is purely imaginary.

Combining Eqs 1, 2 gives the wave equation of Willis acoustic media:

$$\left(\kappa - \mathbf{S}^{\mathrm{T}}\boldsymbol{\rho}^{-1}\mathbf{S}\right)^{-1}\ddot{p} = \nabla\cdot\left(\left(\boldsymbol{\rho}^{-1} + \left(\kappa - \mathbf{S}^{\mathrm{T}}\boldsymbol{\rho}^{-1}\mathbf{S}\right)^{-1}\left(\boldsymbol{\rho}^{-1}\mathbf{S}\right)\otimes\left(\boldsymbol{\rho}^{-1}\mathbf{S}\right)\right)\cdot\nabla p\right). \tag{3}$$

The wave equation is quite complex, and to simplify the analysis and highlight the Willis coupling effect, we consider in this section the isotropic density $\boldsymbol{\rho}$, i.e., $\boldsymbol{\rho} = \rho\mathbf{I}$. According to [32], a dimensionless real vector $\mathbf{W} = i\mathbf{S}/\sqrt{\kappa\rho}$ is introduced for the Willis coupling for the sake of convenience. For a plane wave $p = \hat{p}\exp(i\mathbf{k}\cdot\mathbf{r})$ with $\hat{p}$ and $\mathbf{k}$ being the complex amplitude and the wave vector, respectively, the dispersion equation is

$$(1 + W^2)k^2 - (\mathbf{W}\cdot\mathbf{k})^2 = \frac{\rho}{\kappa}\omega^2, \tag{4}$$

where $W = |\mathbf{W}|$ and $k = |\mathbf{k}|$. Eq. 4 has been formulated by [32]. In a two-dimensional (2D) case, the scenario of involved directions regarding the bulk wave propagation is depicted in Figure 1A, where ϕ is the azimuthal angle of $\mathbf{W}$ and ϕ' is the angle between $\mathbf{W}$ and $\mathbf{k}$.

Eq. 4 clearly shows that the slowness curve is an ellipse because of $\mathbf{W}$. This is a natural consequence because the coupling vector brings directionality. Without loss of generality, align the x-axis with $\mathbf{W}$, then Eq. 4 is simplified as

$$k_x^{\,2} + (1 + W^2)k_y^{\,2} = \frac{\rho}{\kappa}\omega^2. \tag{5}$$

Figure 1C shows the slowness curves of Willis media with different values of W. The major axis of the ellipse is collinear with the direction of $\mathbf{W}$, and the ellipse tends to be flatter as W becomes larger. Compared with ordinary medium ($W = 0$), the phase velocity parallel to $\mathbf{W}$ remains unchanged, whereas the phase velocity perpendicular to $\mathbf{W}$ increases.

To further characterize the particle movements in Willis media, we investigate the velocity field of plane waves. Expressing the velocity field in the medium as $\mathbf{v} = \hat{\mathbf{v}}\exp(i\mathbf{k}\cdot\mathbf{r})$, the complex amplitude $\hat{\mathbf{v}}$ can be derived as

$$\begin{aligned}\hat{\mathbf{v}} &= \begin{pmatrix} v_{\parallel} \\ v_{\perp} \end{pmatrix} \\ &= \frac{1}{\omega\rho}\left[k\begin{pmatrix} 1 \\ 0 \end{pmatrix} - \frac{W^2}{1+W^2}k\cos\phi'\begin{pmatrix} \cos\phi' \\ \sin\phi' \end{pmatrix} - i\sqrt{\frac{\rho}{\kappa}}\omega\frac{W}{1+W^2}\begin{pmatrix} \cos\phi' \\ \sin\phi' \end{pmatrix}\right]\hat{p},\end{aligned} \tag{6}$$

where the velocity components are decomposed in directions parallel to and perpendicular to the wave vector, represented by subscripts "$\parallel$" and "$\perp$," respectively. Eq. 6 reveals that waves in the Willis acoustic medium are generally elliptically polarized, and because $|v_{\perp}| \geq |v_{\parallel}|$, the long axis of the ellipse is collinear with the wave vector direction. This is a typical feature different from the traditional acoustic media that only supports the longitudinal wave. A pure longitudinal wave ($v_{\perp} = 0$) only happens when the coupling vector is collinear with the wave vector ($\phi' = 0$ or π). A typical wave picture is shown in Figure 1B, where the grid points of solid lines represent the real-time positions of particles, different colors represent their phases, and the dotted grid points represent their initial positions. For a wave propagating to the right, particles rotate clockwise around their equilibrium position in an elliptical orbit.

In the aforementioned discussion, ρ and κ are assumed to have positive values. As the Willis medium is often used to characterize metamaterials, it is reasonable to allow the negative values as well. If one of ρ and κ is negative, the definition of $\mathbf{W}$ should be modified as $\mathbf{W} = i\mathbf{S}/\sqrt{-\kappa\rho}$. As a result, Eq. 5 changes to

$$k_x^2 + (1 - W^2)k_y^2 = \frac{\rho}{\kappa}\omega^2. \tag{7}$$

In Eq. 7, if $W \leq 1$, the medium does not support any traveling waves as no real solution of $\mathbf{k}$ exists. However, if $W > 1$, it is possible

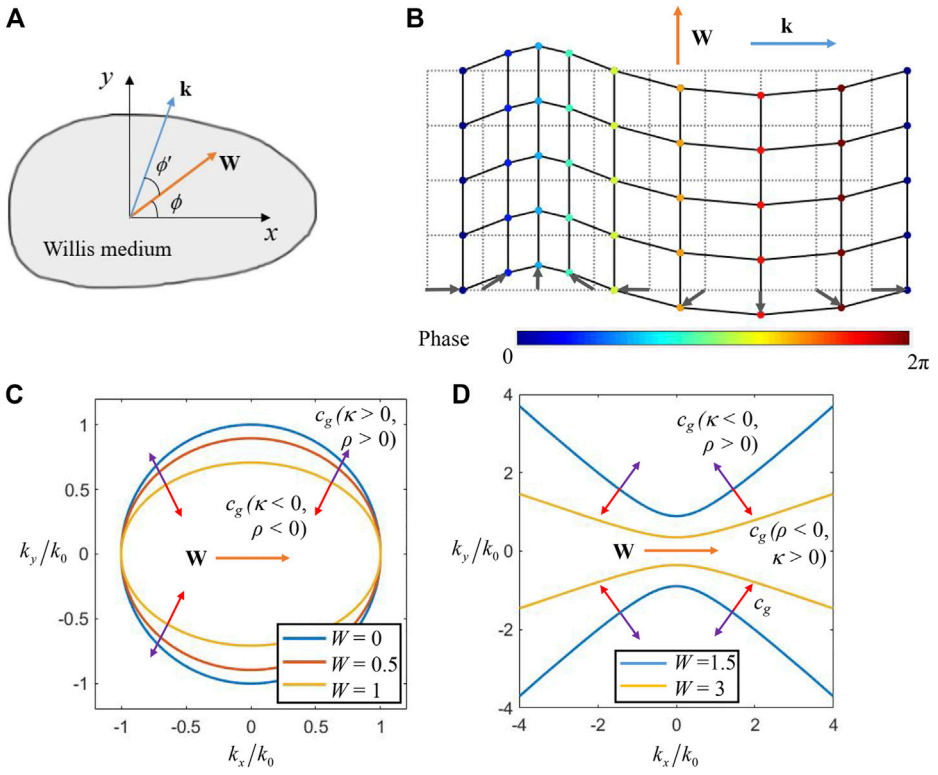

FIGURE 1
(A) Schematic representation of directions of the coupling vector and wave vector in the Willis acoustic medium. **(B)** Particle motion of a plane wave in the Willis acoustic medium. **(C)** Slowness curve of the positive or double negative Willis medium, $k_0 = \omega\sqrt{\rho/\kappa}$. The purple arrows denote the group velocity of the medium with $\rho > 0$ and $\kappa > 0$, and the red arrows denote the group velocity of the medium with $\rho < 0$ and $\kappa < 0$. **(D)** Slowness curve of a single negative Willis medium, $k_0 = \omega\sqrt{-\rho/\kappa}$. The red arrows denote the group velocity of the medium with $\rho < 0$ and $\kappa > 0$, and the purple arrows denote the group velocity of the medium with $\rho > 0$ and $\kappa < 0$.

to find a real solution of **k**. In that case, the media have hyperbolic slowness curves, as shown in Figure 1D. The real axis of the hyperbola is perpendicular to **W**, and its eccentricity increases with W.

The group velocity can be determined by calculating the time-averaged intensity of power flow $\mathbf{I} = \mathrm{Re}(p^{\dagger}\mathbf{v})/2$. For different sign combinations of ρ and κ, from Eqs 5, 7, respectively, they are expressed as

$$\begin{pmatrix} I_x \\ I_y \end{pmatrix} = \frac{|\hat{p}|^2}{2\omega\rho}\begin{pmatrix} \frac{k_x}{1+W^2} \\ k_y \end{pmatrix}, \quad \text{for}\,(\rho>0,\kappa>0)\,\text{or}\,(\rho<0,\kappa<0),$$
$$\begin{pmatrix} I_x \\ I_y \end{pmatrix} = \frac{|\hat{p}|^2}{2\omega\rho}\begin{pmatrix} \frac{k_x}{1-W^2} \\ k_y \end{pmatrix}, \quad \text{for}\,(\rho>0,\kappa<0)\,\text{or}\,(\rho<0,\kappa>0). \tag{8}$$

The corresponding directions of group velocity are also plotted in Figures 1C,D for elliptic and hyperbolic slowness curves. For a medium with $\rho < 0$ and $\kappa > 0$, the group velocity points to the outer normal of the hyperbola, whereas for a medium with $\rho > 0$ and $\kappa < 0$, the group velocity points to the inner normal, as depicted in Figure 1D. If both ρ and κ are negative, Eq. 5 remains unchanged, so the slowness curve is elliptic. However, **v** changes in the opposite direction, as well as **I**. Hence, the group velocity points to the inner normal of the ellipse, as depicted in Figure 1C. The directions of group velocity can also be derived from the gradient of Eq. 5 or Eq. 7, but the causality constraint must be considered as in [36]. Further analysis shows that allowing the density to be anisotropic only changes the eccentricity of the ellipse or hyperbola (see Supplementary Material S1).

3 Interface transmittance and abnormal refraction

Having been acquainted with the wave properties, we consider in this section the transmittance of acoustic waves through the interface between an ordinary acoustic medium (Medium I) and a Willis medium (Medium II), as presented in Figure 2A. A plane wave is incident from the left side, and the incident, reflection, and refraction angles are θ_i, θ_r, and θ_t, respectively. The parameters on both sides are marked in the figure.

The reflected wave is on the side of the ordinary medium, and the reflection angle follows $\theta_r = \theta_i$. On the other hand, the refraction angle in the Willis medium can be determined by the continuity of the tangential wave vector on the interface ($k^{\mathrm{II}} \sin\theta_t = k^{\mathrm{I}} \sin\theta_i$) as well as Eq. 4, where k^{I} and k^{II} are wave numbers on both sides, respectively. The refraction angle θ_t is ruled by

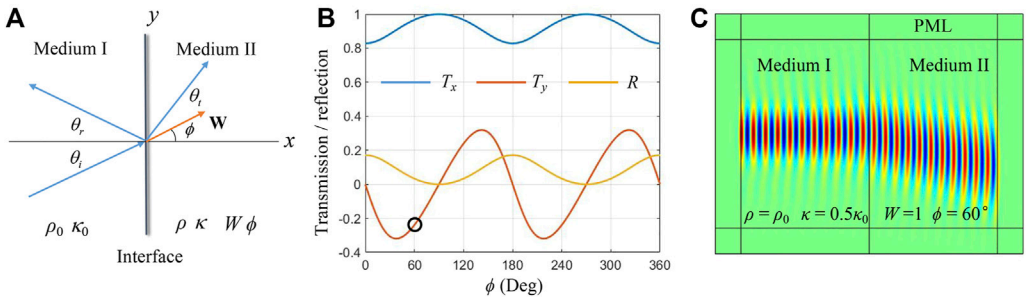

FIGURE 2
(A) Problem setup of the wave transmission across an interface between ordinary acoustic and Willis media. **(B)** Transmission and reflection power vary with ϕ for normal incidence. **(C)** FEM simulation of a normal incident Gaussian beam, corresponding to the dot in **(B)**.

$$\sqrt{\left(1+W^2-W^2\left(\cos\left(\theta_t-\phi\right)\right)^2\right)}\sin\theta_i=\sqrt{\frac{\kappa_0\rho}{\kappa\rho_0}}\sin\theta_t. \tag{9}$$

As it is a transcendental equation, in general, θ_t can only be calculated numerically. However, for normal incidence ($\theta_i = 0$), it is obvious that $\theta_t = 0$, regardless of the magnitude and direction of the Willis coupling vector. In this case, the impedance of the Willis medium in the normal direction of the interface is $Z_n = p/v_\parallel$. Substituting Eq. 6 and noting that $\phi' = \phi$, we get

$$Z_n=\pm\sqrt{\kappa\rho}\left(\sqrt{1+W^2\sin^2\phi}\pm iW\cos\phi\right). \tag{10}$$

Therein, "±" represents the different signs when propagating to the positive or negative direction of the x-axis. In comparison to traditional acoustic fluid, an extra factor ($\sqrt{1+W^2\sin^2\phi}\pm iW\cos\phi$) is added to the impedance. As the absolute value of this factor is greater than 1, the presence of Willis coupling will always increase the impedance, regardless of its azimuthal angle. The impedance matching condition at the interface is

$$\sqrt{\kappa_0\rho_0}=\sqrt{\kappa\rho\left(1+W^2\right)}\ \text{ and }\ \cos\phi=0\,, \tag{11}$$

which indicates that the direction of the coupling vector must be perpendicular to the wave vector if the full transmission is required.

We learn in Section 2 that the direction of energy transmission may differ from the wave vector in the Willis medium. Even for the normal incidence, the energy flow direction may still deviate. Using Eq. 4, the reflection power ($R = |\mathbf{I}_r|/|\mathbf{I}_i|$) and the two components of the transmitted power flux ($T_x = I_{tx}/|\mathbf{I}_i|$; $T_y = I_{ty}/|\mathbf{I}_i|$) are calculated. Figure 2B presents the variation of transmission and reflection power *versus* the azimuthal angle ϕ under normal incidence. Other parameters are set as $\rho = \rho_0$, $\kappa = 0.5\kappa_0$ ($\rho_0 = 1.2$ kg/m^3, $\kappa_0 = 1.4 \times 10^5$Pa, here and after), and $W = 1$ so that when $\phi = 90^\circ$ or $\phi = 270^\circ$, the impedance matching conditions are satisfied. The calculated frequency is 7,000 Hz. Figure 2B shows that at these two points, the full transmission happens. When **W** points to other directions, there will be energy flow in the y direction and reflection. In Figure 2C, the deflected energy propagation for the case of Willis coupling with $\phi = 60^\circ$ (as indicated by the dot in Figure 2B) is verified by finite element method (FEM) simulation considering the normal Gaussian beam incidence. All FEM simulations in this paper study are carried out *via* COMSOL software. The energy flux component in the y-direction corresponding to $\phi = 60^\circ$ is negative. Correspondingly, it is observed that the wave beam deflects downward after passing through the interface.

For oblique incidence and considering negative parameters, more interesting phenomena can be obtained, as exemplified in Figure 3, wherein panels in the first row are the refractive patterns drawn from the slowness curve analysis, whereas the second row presents the results of FEM simulations of wave beams with 7,000 Hz. As shown in Figures 3A,D, we use a Willis medium with $\rho > 0$ and $\kappa < 0$, whereas in Figures 3B,E, we use a Willis medium with $\rho < 0$ and $\kappa > 0$. The used material parameters are given in Figures 3D,E. Because of the hyperbolic slowness curve, the wave number k_y of the incident wave cannot be less than a certain critical value to get a real wave number for the refraction wave, which is opposite to the case of positive parameters. Taking the 60° incident angle as an example, as indicated by the $\mathbf{k}_i$ arrow, the refractive $\mathbf{k}_r$ is determined from Figures 3A,B. The group velocity must have a positive x component to ensure energy always goes forward. For $\kappa < 0$ cases, as the group velocity points to the inner normal of the hyperbolic, negative refraction of phase velocity and positive refraction of group velocity are predicted, as shown in Figure 3A. Conversely, for the $\rho < 0$ case, as shown in Figure 3B, group velocity points to the outer normal of the hyperbolic. Thus, positive refraction of phase velocity and negative refraction of energy flow are predicted. From the FEM simulations in Figures 3D,E, the aforementioned analysis is confirmed by observing the refracted wave beam and wave front. As shown in Figures 3C,F, we use a Willis medium with $\rho < 0$ and $\kappa < 0$. The typical negative refraction is realized like the double ordinary doubly negative medium.

4 Edge and interface waves

When boundary condition is considered in solving the wave equation, it is possible to find surface modes, for example, the

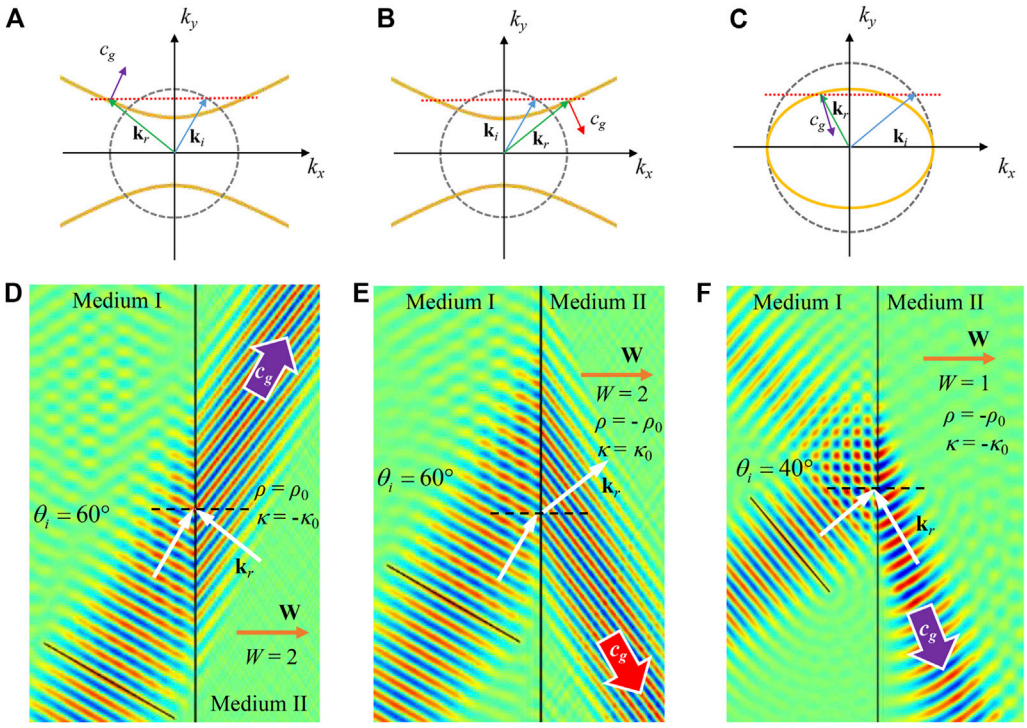

FIGURE 3
Interface refraction of Willis media with negative parameters. **(A), (B),** and **(C)** Slowness curves of the medium on the incident side (the gray dashed) and the refractive side (yellow solid). Blue and green arrows are the incident and refractive wave vectors, with equal tangential components indicated by the red dotted line. The red or purple arrows indicate the direction of group velocities. **(D), (E),** and **(F)** Corresponding FEM simulations of the cases of **(A), (B),** and **(C)**, respectively, (pressure field).

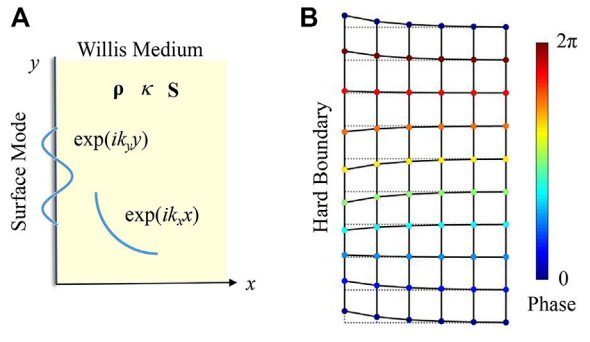

FIGURE 4
(A) Schematic representation of the surface mode of a semi-infinite Willis medium. **(B)** Typical wave pattern of edge mode for Willis acoustic media with isotropic density.

well-known Rayleigh surface wave for solids. For an ordinary acoustic fluid, surface modes are not supported. However, in the realm of acoustic metamaterials, surface modes can be found in acoustic media with negative parameters [3, 37] or with gyrotropic mass [38]. In [35], we have partly demonstrated the existence of interface waves at the interface of two Willis media. Here, we present a more systematic examination of the edge and interface waves of Willis media.

4.1 Edge waves with sound hard boundary

As sketched in Figure 4A, we consider a semi-infinite of Willis acoustic medium, and the Cartesian coordinate system is established to make the open edge along the y-axis. Considering acoustic field explicitly expressed by $p = \hat{p}\exp(ik_x x + ik_y y)$, for a possible edge mode, the field is traveling along the y-direction and attenuated away from the surface. Thus, k_y must be real, and k_x must have a positive (negative) imaginary part when the surface is on the left (right).

For sound soft (free) boundary, the requisite boundary condition is $p\ (x = 0) = 0$, which holds only for $\hat{p} = 0$. Then, the velocity $\hat{\mathbf{v}}$ vanishes at the same time, and it is concluded that no edge mode is supported on the sound soft boundary. For sound hard boundary, it is required that the normal velocity on the boundary vanishes, that is, $v_x\ (x = 0) = 0$. Combining the boundary condition and the requirements of the wave vectors, we can conclude that surface waves may exist on the hard boundaries, and the parameter conditions for their existence are (Supplementary Material S2)

$$\begin{aligned} &\frac{\rho_{yy}}{\kappa} > 0 \text{ and } i\left(S_x\rho_{yy} - S_y\rho_{xy}\right) > 0, \quad \text{when the surface is on the left,} \\ &\frac{\rho_{yy}}{\kappa} > 0 \text{ and } i\left(S_x\rho_{yy} - S_y\rho_{xy}\right) < 0, \quad \text{when the surface is on the right.} \end{aligned} \tag{12}$$

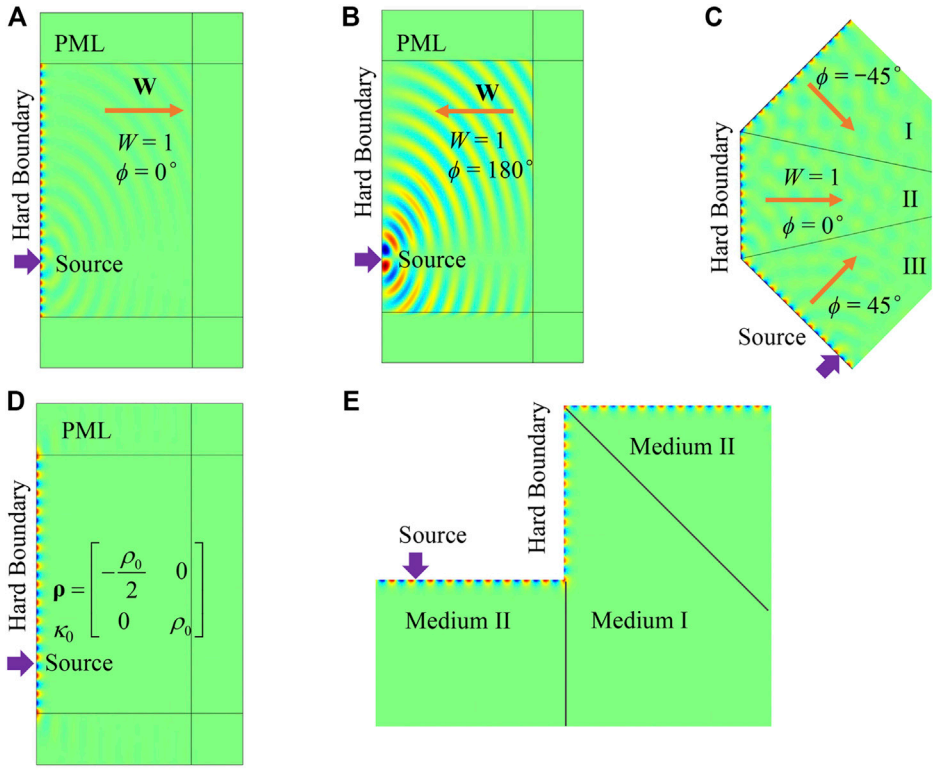

FIGURE 5
FEM simulations of surface waves on hard boundaries of Willis media (pressure field). **(A)** W points away from the surface. **(B)** W points to the surface. **(C)** Waveguide for the edge wave with possible leaking into bulk. **(D)** Edge wave without bulk leaking using an anisotropic density. **(E)** Robust edge waveguide with sharper corners using an anisotropic density.

The wave number along the surface is $k_y = \pm\,\omega\sqrt{\rho_{yy}/\kappa}$. For the case of isotropic density and $\rho > 0$, $\kappa > 0$, the aforementioned condition reduces to be simply

$$\begin{aligned} W_x &> 0, \quad \text{when the surface is on the left,} \\ W_x &< 0, \quad \text{when the surface is on the right.} \end{aligned} \tag{13}$$

Eq. 13 has an obvious geometric meaning that the vector **W** has to point away from the edge to find the edge wave. In this case, the wave mode can be analytically expressed as

$$\begin{aligned} p &= \hat{p}\exp\left(ik_x x + ik_y y\right), \\ v_y &= \left[\pm\frac{1}{\sqrt{\kappa\rho}\left(1+W_y^2\right)} - \frac{iW_y}{\sqrt{\kappa\rho}\left(1+W_y^2\right)}\right]\hat{p}\exp\left(ik_x x + ik_y y\right), \\ k_x &= \pm\frac{W_x W_y}{\left(1+W_y^2\right)}\omega\sqrt{\rho/\kappa} + \frac{iW_x}{\left(1+W_y^2\right)}\omega\sqrt{\rho/\kappa}, \quad k_y = \pm\,\omega\sqrt{\rho/\kappa}. \end{aligned} \tag{14}$$

In Eq. 14, k_x is purely imaginary only when **W** is perpendicular to the boundary ($W_y = 0$), and the wave is exponentially attenuated away from the boundary. In other cases, k_x has both real and imaginary parts, which means that the edge wave is oscillatory attenuated away from the boundary (see Supplementary Material S3). In addition, non-zero W_y will make the imaginary part of k_x smaller. Hence, the attenuation will slow down further. It is also noticed that, unlike the bulk wave, the edge wave is linearly polarized, and particle velocity possesses only components along the interface. The wave pattern of the edge mode is shown in Figure 4B. The grid points on the solid lines represent the real-time position of particles, and the colors represent their phases. The dotted lines represent their initial positions.

FEM simulations are performed to verify the surface wave on the hard boundaries, as shown in Figure 5. Material parameters of the Willis medium are $\rho = \rho_0$, $\kappa = \kappa_0$, and $W = 1$. Two directions of the coupling vector, $\phi = 0^\circ$ (Figure 5A) and $\phi = 180^\circ$ (Figure 5B), are used here. The calculated frequency is 5,000 Hz. A pair of point sources with a half wavelength distance and opposite phases is set on the hard boundary to form a dipole, which can stimulate the surface mode more efficiently. In Figure 5A, the condition that **W** points away from the surface is satisfied. Correspondingly, the edge wave is observed along the y-axis. When **W** points to the surface, as in Figure 5B, no surface mode exists, and only the bulk mode is excited. Figure 5A shows that, for large **W** perpendicular to the edge, the wave vectors of edge mode and bulk mode differ much, so they are not easily coupled with each other. For edge waveguides having corners not so sharp, the edge wave can pass through without obvious scattering into the bulk, showing some robustness, as depicted in Figure 5C.

To design a waveguide with more robustness, we can utilize a medium supporting edge wave that does not allow bulk waves. A simple choice is to use a single negative medium with isotropic

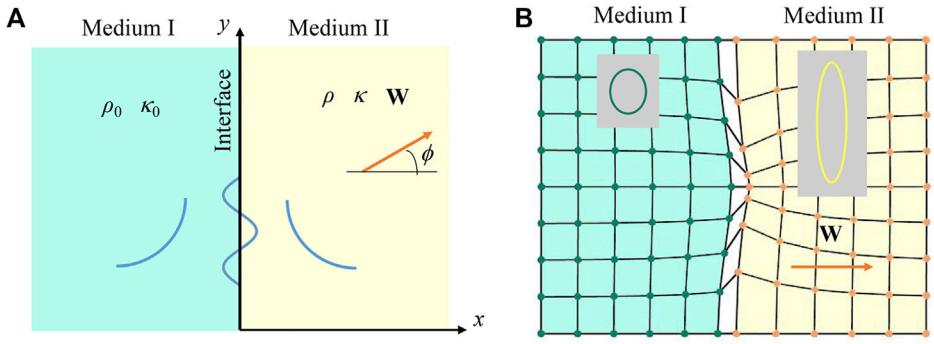

FIGURE 6
(A) Schematic representation of the interface mode between an ordinary medium (Medium I) and a Willis medium (Medium II). The interface mode is a traveling mode along the surface and evanescent away from the interface. **(B)** Wave mode of the interface wave, where the interface expands at a finite width to clearly display the particle motion on both sides. The insets show typical particle orbits on each side.

density. However, such a medium does not possess edge mode because Eq. 12 cannot be satisfied, so we seek the possibility in the Willis medium with anisotropic density. The derived condition for the Willis medium that does not support bulk waves is (see Supplementary Material S4)

$$\frac{\kappa}{S_y^2\rho_{xx} - 2S_xS_y\rho_{xy} + S_x^2\rho_{yy} + \kappa\left(\rho_{xy}^2 - \rho_{xx}\rho_{yy}\right)} < 0 \quad \text{and}$$
$$\left(\rho_{xx}\rho_{yy} - \rho_{xy}^2\right)\left(S_y^2 + S_x^2 - \kappa\rho_{xx} - \kappa\rho_{yy}\right) > 0. \tag{15}$$

If a set of material parameters can satisfy Eq. 12 and 15 at the same time, the edge wave transmission would be very stable. In the example in Figure 5D, we choose a set of parameters as $\rho_{xx} = -\rho_0/2$, $\rho_{yy} = \rho_0$, $\rho_{xy} = 0$, $\kappa = \kappa_0$, $S_x = -i\sqrt{\kappa_0\rho_0}$, and $S_y = 0$ so that Eqs 12, 15 are simultaneously met for the edge on the left. All energy is concentrated at the boundary without any bulk waves. Moreover, in this exclusively edge-mode medium, a single monopole source is enough to excite the edge wave without matching its mode. In Figure 5E, a waveguide containing corners with the right angle is established using two different Willis media to meet the corresponding parameter requirements on the boundary of different orientations. Therein, Medium I is the same as that in Figure 5D, and Medium II is simply obtained by rotation from Medium I. The edge wave transmits through the designed route without energy leaking into the bulk.

4.2 Interface waves between two media

In practice, if the impedance of the Willis and adjacent media significantly differs, their interface can be treated as an ideal soft or hard boundary. For other cases, further analysis is required to estimate whether interface modes exist.

Consider the problem shown in Figure 6A. The ordinary acoustic medium (Medium I) on the left side and the Willis medium (Medium II) on the right side form an interface along the *y*-axis. In order to simplify the problem, the discussion is limited to Willis media with isotropic density and $\rho > 0$, $\kappa > 0$. The density and bulk modulus of the ordinary medium are ρ_0 and κ_0, respectively. The parameters of the Willis medium are ρ, κ, and **W**. For an interface wave, the pressure fields on the two sides can be written as $p^{\mathrm{I}} = \hat{p}\exp\left(ik_x^{\mathrm{I}}x + ik_s y\right)$ and $p^{\mathrm{II}} = \hat{p}\exp\left(ik_x^{\mathrm{II}}x + ik_s y\right)$, respectively, where k_s is the tangential wave vector along the interface. It must be continuous and real on both sides. k_x^{I} and k_x^{II} are normal wave vectors, which should satisfy $\mathrm{Im}\left(k_x^{\mathrm{I}}\right) < 0$ and $\mathrm{Im}\left(k_x^{\mathrm{II}}\right) > 0$ to ensure attenuation in the direction away from the interface. The conditions for the existence of interfacial waves are as follows (see Supplementary Material S5):

$$W_x > 0, \quad \frac{\bar{\rho}}{\bar{\kappa}} > 1, \quad \frac{W_x^2}{\bar{\kappa}^2} + \frac{\bar{\rho}}{\bar{\kappa}}\left(1 + W^2\right) > \left(\frac{\bar{\rho}}{\bar{\kappa}}\right)^2\left(1 + W^2\right)\left(1 + W_y^2\right), \tag{16}$$

where $\bar{\rho} = \rho/\rho_0$ and $\bar{\kappa} = \kappa/\kappa_0$. The interface mode is difficult to be expressed analytically, so we demonstrate it with a specific numerical example in Figure 6B. The parameters are set as $\bar{\rho} = 0.2$, $\bar{\kappa} = 0.1$, $W = 1$, and $\phi = 0^\circ$. The grid points in Figure 6B represent the real-time positions of the particle. Due to the non-zero normal velocity, particles near the interface rotate in an elliptical trajectory around their equilibrium positions, which is very different from the edge mode. At the interface, only the normal velocity maintains continuity. The two media have a relative slip in the tangential direction. The FEM simulation of the interface wave is shown in Figure 7A with the same parameters. The influence of the material parameters on the robustness of interface waves is analyzed in Supplementary Materials S6.

In the problem setup shown in Figure 6A, if the two domains are both Willis media, the analysis of the interface wave is more complex, so the general situation is not studied. However, if the two media meet some specific conditions, the problem will become intuitive. In Section 4.1, we use the boundary condition that the normal velocity is zero to derive the existence condition Eq. 12 for edge waves and the corresponding edge wave number $k_y = \pm\omega\sqrt{\rho_{yy}/\kappa}$. The derivation is reversible; that is, if $k_y = \pm\omega\sqrt{\rho_{yy}/\kappa}$ and Eq. 12 holds, the normal velocity on the boundary must be zero. Thus, we conclude that, in the current problem of two Willis domains, if the tangential wave numbers on both sides of the interface are the same and Eq. 12 holds for each side, the continuity condition of the interface will always be met. In this situation, the media on both sides are mutually sound hard

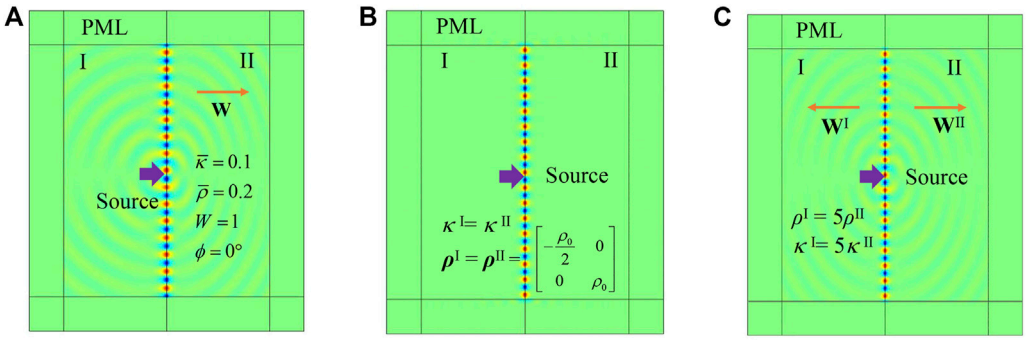

FIGURE 7
FEM simulations of interface waves (pressure field). **(A)** Medium I, an ordinary medium; Medium II, a Willis medium. **(B)** Both sides are Willis media with parameters that satisfy Eq. 17. **(C)** Both sides are Willis media with parameters that satisfy Eq. 18. In **(A)**, **(B),** and **(C)**, the sources are 5,000-Hz dipoles marked by arrows.

boundaries to each other, so the interface wave can be supported. On the premise that $\rho^{I}_{yy}/\kappa^{I} = \rho^{II}_{yy}/\kappa^{II}$, an existence condition for the interface wave reads

$$\rho^{I}_{yy}/\kappa^{I} = \rho^{II}_{yy}/\kappa^{II} > 0,\quad i\left(S^{I}_{x}\rho^{I}_{yy} - S^{I}_{y}\rho^{I}_{xy}\right) < 0,\quad i\left(S^{II}_{x}\rho^{II}_{yy} - S^{II}_{y}\rho^{II}_{xy}\right) > 0. \tag{17}$$

An FEM example is shown in Figure 7B. For convenience, the parameters of Medium II are obtained by the mirror symmetry operation of Medium I about the y-axis, so if Eq. 17 holds on one side, it also holds on the other side. The parameters are $\boldsymbol{\rho}^{I} = \boldsymbol{\rho}^{II}$ (components are marked in Figure 7B), $\kappa^{I} = \kappa^{II} = \kappa_0$, $S^{I}_{x} = i\sqrt{\kappa_0\rho_0}$, $S^{II}_{x} = -i\sqrt{\kappa_0\rho_0}$, and $S^{I}_{y} = S^{II}_{y} = 0$. Additionally, the parameters in Figure 7B satisfy Eq. 15, so a pure interface wave is excited without bulk leaking.

When the density is isotropic, $\rho > 0$, and $\kappa > 0$, Eq. 17 reduces to

$$\rho^{I}/\kappa^{I} = \rho^{II}/\kappa^{II},\quad W^{I}_{x} < 0, W^{II}_{x} > 0. \tag{18}$$

Similarly, Eq. 18 implies that vectors $\mathbf{W}$ on both sides point away from the interface. An example is shown in Figure 7C. The parameters in Medium I are $\rho^{I} = 5\rho_0$, $\kappa^{I} = 5\kappa_0$, $W^{I} = 1$, and $\phi^{I} = 180°$, and those in Medium II are $\rho^{II} = \rho_0$, $\kappa^{II} = \kappa_0$, $W^{II} = 1$, and $\phi^{II} = 0°$. The density and bulk modulus of the Willis medium on the left side are both five times those on the right side, so the tangential wave vector is continuous on the interface. The coupling vector point away from the interface on both sides. An interface wave is observed as Eq. 18 is satisfied.

5 Conclusion

In this study, unusual wave phenomena relevant to interfaces in the homogeneous acoustic Willis media are studied theoretically. We show that the media exhibit anisotropic features due to the Willis coupling vector terms, and the slowness curve can be tuned between elliptical and hyperbolic shapes. The interface transmittance can be adjusted by the magnitude and direction of the coupling vector, which offers more flexible control in the compared with the traditional acoustic fluids. The Willis acoustic media support edge waves at acoustic hard boundaries and interface waves at interfaces between an ordinary acoustic fluid and a Willis medium or between two Willis media. Particularly, the edge modes may also exist in certain Willis media that do not support bulk modes, in which case they can achieve high transmission.

The study unveils more possibilities for manipulating acoustic waves and may inspire new functional designs with acoustic Willis metamaterials. It should be noted that this theoretical study assumes continuous acoustic media already with Willis coupling. On the experimental side, designing metamaterials with the wanted coupling effect is still an ongoing and challenging task. Especially for those wave phenomena calling for a strong $\mathbf{S}$ vector and negative density or modulus, the experimental demonstration may necessitate a more sophisticated design.

Data availability statement

The original contributions presented in the study are included in the article/Supplementary Material. Further inquiries can be directed to the corresponding author.

Author contributions

HQ wrote the original draft. XL and AZ reviewed and revised the manuscript. XL supervised the work. All authors contributed to the article and approved the submitted version.

Funding

This work was supported by the National Natural Science Foundation of China (Grant no. 11972080) and the Innovation Foundation of Maritime Defense Technologies Innovation Center (Grant no. JJ-2021-719-06). HQ acknowledges the support of the research start-up fund from Shijiazhuang Tiedao University.

Conflict of interest

The authors declare that the research was conducted in the absence of any commercial or financial relationships that could be construed as a potential conflict of interest.

Publisher's note

All claims expressed in this article are solely those of the authors and do not necessarily represent those of their affiliated organizations, or those of the publisher, the editors, and the reviewers. Any product that may be evaluated in this article, or claim that may be made by its manufacturer, is not guaranteed or endorsed by the publisher.

Supplementary material

The Supplementary Material for this article can be found online at: https://www.frontiersin.org/articles/10.3389/fphy.2023.1141129/full#supplementary-material

References

1. Zhang XD, Liu ZY. Negative refraction of acoustic waves in two-dimensional phononic crystals. *Appl Phys Lett* (2004) 85:341–3. doi:10.1063/1.1772854

2. Zhu R, Liu XN, Hu GK, Sun CT, Huang GL. Negative refraction of elastic waves at the deep-subwavelength scale in a single-phase metamaterial. *Nat Commun* (2014) 5: 5510–8. doi:10.1038/ncomms6510

3. Ambati M, Fang N, Sun C, Zhang X. Surface resonant states and superlensing in acoustic metamaterials. *Phys Rev B* (2007) 75:195447. doi:10.1103/physrevb.75.195447

4. Zhang HK, Zhou XM, Hu GK. Shape-adaptable hyperlens for acoustic magnifying imaging. *Appl Phys Lett* (2016) 109:224103. doi:10.1063/1.4971364

5. Chen HY, Chan CT. Acoustic cloaking in three dimensions using acoustic metamaterials. *Appl Phys Lett* (2007) 91:183518. doi:10.1063/1.2803315

6. Chen Y, Liu XN, Hu GK. Latticed pentamode acoustic cloak. *Sci Rep* (2015) 5: 15745. doi:10.1038/srep15745

7. Zhang HK, Chen Y, Liu XN, Hu GK. An asymmetric elastic metamaterial model for elastic wave cloaking. *J Mech Phys Sol* (2020) 135:103796. doi:10.1016/j.jmps.2019.103796

8. Willis JR. Variational principles for dynamic problems for inhomogeneous elastic media. *Wave Motion* (1981) 3:1–11. doi:10.1016/0165-2125(81)90008-1

9. Milton GW, Briane M, Willis JR. On cloaking for elasticity and physical equations with a transformation invariant form. *New J Phys* (2006) 8:248. doi:10.1088/1367-2630/8/10/248

10. Milton GW, Willis JR. On modifications of Newton's second law and linear continuum elastodynamics. *P Roy Soc A* (2007) 463:855–80. doi:10.1098/rspa.2006.1795

11. Muhlestein MB, Sieck CF, Alu A, Haberman MR. Reciprocity, passivity and causality in Willis materials. *P Roy Soc A* (2016) 472:20160604. doi:10.1098/rspa.2016.0604

12. Sieck F, Alù A, Haberman MR. Origins of Willis coupling and acoustic bianisotropy in acoustic metamaterials through source-driven homogenization. *Phys Rev B* (2017) 96:104303. doi:10.1103/physrevb.96.104303

13. Koo S, Cho C, Jeong JH, Park N. Acoustic omni meta-atom for decoupled access to all octants of a wave parameter space. *Nat Commun* (2016) 7:13012. doi:10.1038/ncomms13012

14. Muhlestein MB, Sieck CF, Wilson PS, Haberman MR. Experimental evidence of Willis coupling in a one-dimensional effective material element. *Nat Commun* (2017) 8: 15625. doi:10.1038/ncomms15625

15. Quan L, Ra'di Y, Sounas DL, Alu A. Maximum Willis coupling in acoustic scatterers. *Phys Rev Lett* (2018) 120:254301. doi:10.1103/physrevlett.120.254301

16. Melnikov A, Chiang YK, Quan L, Oberst S, Alù A, Marburg S, et al. Acoustic meta-atom with experimentally verified maximum Willis coupling. *Nat Commun* (2019) 10: 3148. doi:10.1038/s41467-019-10915-5

17. Groby JP, Malléjac M, Merkel A, Romero-García V, Tournat V, Torrent D, et al. Analytical modeling of one-dimensional resonant asymmetric and reciprocal acoustic structures as Willis materials. *New J Phys* (2021) 23:053020. doi:10.1088/1367-2630/abfab0

18. Liu Y, Liang Z, Zhu J, Xia L, Mondain-Monval O, Brunet T, et al. Willis metamaterial on a structured beam. *Phys Rev X* (2019) 9:011040. doi:10.1103/physrevx.9.011040

19. Meng Y, Hao Y, Guenneau S, Wang S, Li J. Willis coupling in water waves. *New J Phys* (2021) 23:073004. doi:10.1088/1367-2630/ac0b7d

20. Qu HF, Liu XN, Hu GK. Mass-spring model of elastic media with customizable Willis coupling. *Int J Mech Sci* (2022) 224:107325. doi:10.1016/j.ijmecsci.2022.107325

21. Merkel A, Romero-García V, Groby JP, Li J, Christensen J. Unidirectional zero sonic reflection in passive PT-symmetric Willis media. *Phys Rev B* (2018) 98:201102. doi:10.1103/physrevb.98.201102

22. Esfahlani H, Mazor Y, Alù A. Homogenization and design of acoustic Willis metasurfaces. *Phys Rev B* (2021) 103:054306. doi:10.1103/physrevb.103.054306

23. Wiest T, Seepersad CC, Haberman MR. Robust design of an asymmetrically absorbing Willis acoustic metasurface subject to manufacturing-induced dimensional variations. *J Acoust Soc Am* (2022) 151:216–31. doi:10.1121/10.0009162

24. Díaz-Rubio A, Tretyakov SA. Acoustic metasurfaces for scattering-free anomalous reflection and refraction. *Phys Rev B* (2017) 96:125409. doi:10.1103/physrevb.96.125409

25. Li J, Shen C, Diaz-Rubio A, Tretyakov SA, Cummer SA. Systematic design and experimental demonstration of bianisotropic metasurfaces for scattering-free manipulation of acoustic wavefronts. *Nat Commun* (2018) 9:1342. doi:10.1038/s41467-018-03778-9

26. Chen Y, Li X, Hu G, Haberman MR, Huang G. An active mechanical Willis meta-layer with asymmetric polarizabilities. *Nat Commun* (2020) 11:3681–8. doi:10.1038/s41467-020-17529-2

27. Craig SR, Su X, Norris A, Shi C. Experimental realization of acoustic bianisotropic gratings. *Phys Rev Appl* (2019) 11:061002. doi:10.1103/physrevapplied.11.061002

28. Quan L, Yves S, Peng Y, Esfahlani H, Alù A. Odd Willis coupling induced by broken time-reversal symmetry. *Nat Commun* (2021) 12:2615–9. doi:10.1038/s41467-021-22745-5

29. Cho C, Wen X, Park N, Li J. Acoustic Willis meta-atom beyond the bounds of passivity and reciprocity. *Commun Phys* (2021) 4:82–8. doi:10.1038/s42005-021-00584-6

30. Zhai Y, Kwon HS, Popa BI. Active Willis metamaterials for ultracompact nonreciprocal linear acoustic devices. *Phys Rev B* (2019) 99:220301. doi:10.1103/physrevb.99.220301

31. Popa BI, Zhai Y, Kwon HS. Broadband sound barriers with bianisotropic metasurfaces. *Nat Commun* (2018) 9:5299. doi:10.1038/s41467-018-07809-3

32. Muhlestein MB, Goldsberry BM, Norris AN, Haberman MR. Acoustic scattering from a fluid cylinder with Willis constitutive properties. *P Roy Soc A* (2018) 474: 20180571. doi:10.1098/rspa.2018.0571

33. Lawrence AJ, Goldsberry BM, Wallen SP, Haberman MR. Numerical study of acoustic focusing using a bianisotropic acoustic lens. *J Acoust Soc Am* (2020) 148: EL365–9. doi:10.1121/10.0002137

34. Qu HF, Liu XN, Hu GK. Topological valley states in sonic crystals with Willis coupling. *Appl Phys Lett* (2021) 119:051903. doi:10.1063/5.0055789

35. Li ZY, Qu HF, Zhang HK, Liu XN, Hu GK. Interfacial wave between acoustic media with Willis coupling. *Wave Motion* (2022) 112:102922. doi:10.1016/j.wavemoti.2022.102922

36. Smith DR, Schurig D. Electromagnetic wave propagation in media with indefinite permittivity and permeability tensors. *Phys Rev Lett* (2003) 90:077405. doi:10.1103/physrevlett.90.077405

37. Bobrovnitskii YI. A Rayleigh-type wave at the plane interface of two homogeneous fluid half-spaces. *Acoust Phys* (2011) 57:595–7. doi:10.1134/s1063771011050046

38. Zhou X, Zhao Y. Unusual one-way edge state in acoustic gyroscopic continuum. *Sci China Phys Mech* (2018) 62:14612–7. doi:10.1007/s11433-018-9268-9

frontiers | Frontiers in Physics

TYPE Methods
PUBLISHED 04 April 2023
DOI 10.3389/fphy.2023.1172536

OPEN ACCESS

EDITED BY
Zhixiong Gong,
Shanghai Jiao Tong University, China

REVIEWED BY
Pierre Grandjean,
Université de Sherbrooke, Canada
Xudong Fan,
Nanjing University of Science and Technology, China

*CORRESPONDENCE
Chenyang Gui,
guichenyang@hrbeu.edu.cn

SPECIALTY SECTION
This article was submitted to Physical Acoustics and Ultrasonics, a section of the journal Frontiers in Physics

RECEIVED 23 February 2023
ACCEPTED 23 March 2023
PUBLISHED 04 April 2023

CITATION
Shi S, Yang B, Guo Q, Li Y and Gui C (2023), Low-frequency sound source localization and identification with spherical microphone arrays extrapolation method.
Front. Phys. 11:1172536.
doi: 10.3389/fphy.2023.1172536

Low-frequency sound source localization and identification with spherical microphone arrays extrapolation method

Shengguo Shi[1,2,3], Boquan Yang[3], Qiang Guo[3], Ying Li[1,2,3] and Chenyang Gui[1,2,3]*

[1]Acoustic Science and Technology Laboratory, Harbin Engineering University, Harbin, China, [2]Key Laboratory of Marine Information Acquisition and Security, Ministry of Industry and Information Technology, Harbin Engineering University, Harbin, China, [3]College of Underwater Acoustic Engineering, Harbin Engineering University, Harbin, China

Beamforming technology with spherical microphone arrays (SMAs) is often applied for localizing and identifying noise sources in airplane cabins, automobiles, and submarines. The performance of a SMA signal processing algorithm depends on its physical characteristics, especially the array aperture. The array aperture limits the frequency range of its application, and the small aperture leads to weak performance at low frequencies. In this paper, a large-aperture virtual SMA is obtained through the virtual SMA extrapolation method. Because the radius of the virtual SMA is larger than that of the actual SMA, an approximate low-frequency signal can be obtained, which may improve the localization effect of the low-frequency noise source of the SMA. Firstly, the paper introduces the extrapolation method of SMA, and through the discussion of several typical parameters such as envelope parameters, SMA aperture and signal-to-noise ratio (SNR), the application scope and conditions of SMA extrapolation method are given. In addition, this paper introduces compressed sensing technology (CS) into the calculation process of virtual SMA extrapolation to improve the accuracy of virtual SMA element data. The generalized inverse beamforming (GIB) algorithm is then used to locate and identify noise sources and verify the benefits of the virtual SMA. Simulation and experimental results show that the virtual SMA can locate and identify noise sources with high spatial resolution in the low frequency range.

KEYWORDS

low-frequency sound source, localization and identification, spherical microphone arrays, array extrapolation, compressed sensing

1 Introduction

Beamforming technology is widely used in detecting marine targets, estimating direction of arrival, localizing and identifying signals, etc., [1, 2]. Beamforming technology with SMA is exceedingly popular in localizing and identifying noise sources in the mid-high-frequency range, because its small-size and full-space directivity [3–5].

SMA with the spherical harmonic beamforming (SHB) algorithm is the most commonly used noise source localization and identification method in the mid-high-frequency range. However, SMA with SHB has two drawbacks. On the one hand, SHB uses the orthogonality of spherical harmonic function to locate the sound source, but it needs to carefully select the

position and number of array elements, and is vulnerable to noise, resulting in serious side lobe. On the other hand, the spatial resolution of low-frequency noise source localization and identification results is poor, because the aperture of the SMA is small [5–8].

In order to narrow main-lobe and suppress side-lobes, and improve the use effect of the array, scholars have also carried out a lot of research. Scholars have improved the beamforming effect using algorithms, for example, DAMAS and its derivative algorithm [9, 10]. Although this algorithm can obtain high-precision noise source localization and identification results in the mid-high-frequency range, it cannot solve the problem of poor spatial resolution in the low-frequency range due to the limitation of small apertures in the array. The concentric dual-radius SMA [11, 12] has a wider application frequency range than the single SMA. In the dual-radius SMA, the large-radius SMA can effectively compensate for the low-frequency application effect of the small-radius SMA. However, in general, the two radii of a dual radius spherical array are fixed values, and the radius cannot be changed according to the application environment.

This paper proposes a high-resolution low-frequency noise source localization and identification method. The advantage of this method is that it can approximately achieve the low-frequency application effect of the dual-radius SMA without changing the actual SMA. The proposed method first obtains a large-aperture virtual SMA through virtual SMA extrapolation [13–16]. The core of virtual SMA extrapolation is to solve the strength of virtual source from ill-posed inverse problem. In this paper, the compressed sensing method (CS) is introduced into the solution process of virtual source strength, which improves the accuracy of source strength [17]. At the same time, through the discussion and analysis of parameters such as the aperture of the envelope surface and the configuration of the virtual source, the radius of the spherical array, the distribution of the array elements, and the signal-to-noise ratio, the parameter configuration scheme of the virtual array method and its application range and conditions are given. Then generalized inverse beamforming (GIB) is introduced into the localization and identification of the noise source of the virtual SMA [16, 18]. This solves the problem of poor spatial resolution of the low-frequency noise source localization and identification results caused by the small aperture of the SMA.

The remainder of this paper is arranged as follows: Section 2 gives the theory of the SMA extrapolation method and discusses several factors that affect SMA extrapolation. Section 3 gives the principle of the GIB algorithm and describes the simulation experiments of low-frequency noise source localization and identification with GIB, verifying the effectiveness of the virtual SMA extrapolation method. Section 4 is devoted to verifying the accuracy of simulation conclusions and the effectiveness of practical applications through noise source localization and identification experiments. The conclusions are provided in Section 5.

2 SMA extrapolation method

2.1 Array extrapolation using the virtual source method

In this paper, the SMA aperture is extrapolated virtually by extrapolating the sound field surrounding the SMA. This method supposes an envelope surface between the sound source and the actual SMA, and there are some virtual sources on the envelope surface S. These virtual sound sources are generated by the actual sound source radiating to the envelope surface S, as shown in Figure 1. After solving the unknown strength of the virtual sources, a virtual SMA with a larger aperture can be obtained by calculating the sound field radiated by the virtual sources in a forward direction [15–17].

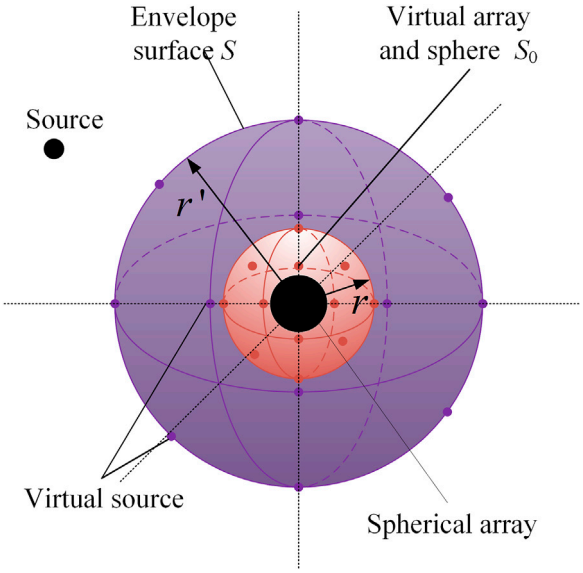

FIGURE 1
Schematic diagram of virtual SMA extrapolation method. The black sphere represents the actual SMA, the red sphere represents the virtual SMA, and the purple sphere represents the envelope surface where the virtual sources are located.

The superposed field generated by the virtual sources can be given by an integral over S:

$$p(a) = \int_S G(a, r')q(r')dS(r') \tag{1}$$

where $p(a)$ is sound pressure, $G(a, r')$ is the free-field Green's function at a field point a (a is the radius of the SMA) caused by the source placed at r', and $q(r')$ is the vector of strengths of the virtual sources, satisfying the Helmholtz equation (the time factor $e^{-i\omega t}$ omitted):

$$\nabla^2 G(a, r') + k^2 G(a, r') = \delta(a - r') \tag{2}$$

where k is wavenumber, and $k = \omega/c$, c is sound speed in the air.

Consider M virtual sources distributed uniformly on S, Eq. 1 can be written as a matrix form:

$$\mathbf{p}(\mathbf{a}_l) = \mathbf{G}(\mathbf{a}_l, \mathbf{r}'_m)\mathbf{q}(\mathbf{r}'_m) \tag{3}$$

where $\mathbf{q}(\mathbf{r}'_m)$ is virtual sources strengths, $\mathbf{G}(a_l, r'_m)$ denotes the transfer function between the mth virtual sources and the lth array elements, $\mathbf{p}(\mathbf{a}_l)$ is the sound pressure vector received by the L array elements SMA. Therefore, $\mathbf{q}(\mathbf{r}'_m)$ can be obtained by solving Eq. 3 and abbreviated as:

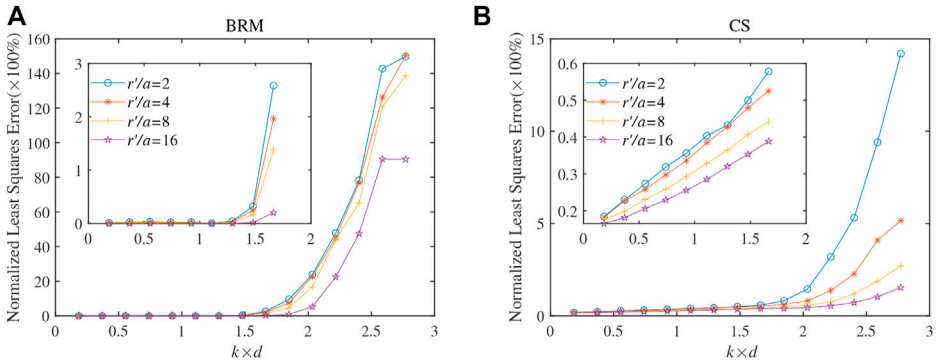

FIGURE 2
The pressure least square errors as a functon of the frequency for different radii of the envelope surfaces. The simulation results of the BRM and CS are shown in **(A)** and **(B)**, respectively.

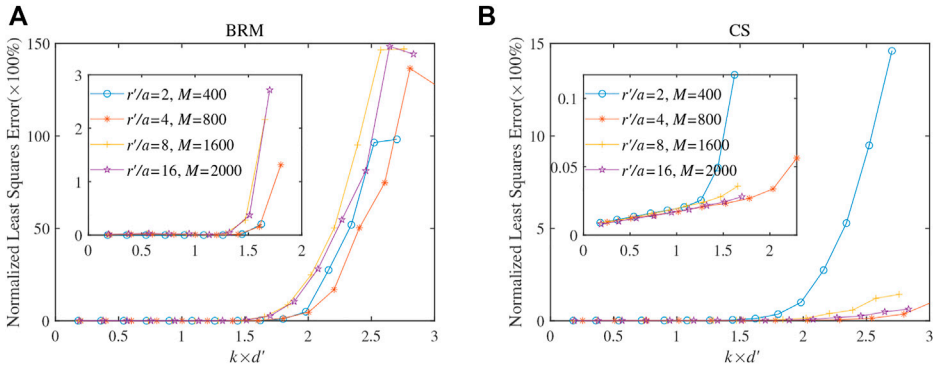

FIGURE 3
The pressure least square errors as a functon of the frequency for different radii of the number of the virtual source at different frequencies. The simulation results of the BRM and CS are shown in **(A)** and **(B)**, respectively.

$$\mathbf{q} = \mathbf{G}^{-1}\mathbf{p} \tag{4}$$

2.1.1 Beamforming regularization matrix method (BRM)

To stabilize the solution of the inverse problem in the presence of measured noise, the Tikhonov regularization is used:

$$\mathbf{q}_{reg} = \arg\min\left\{\|\mathbf{p} - \mathbf{G}\mathbf{q}\|_2^2 + \lambda^2\Omega(\mathbf{q})^2\right\} \tag{5}$$

where λ is the regularization parameter, $\|\bullet\|_2$ represents L_2 norm, and $\Omega(\mathbf{q}) = \|\mathbf{L}\mathbf{q}\|$ is the smoothing norm of $\mathbf{q}$ with $\mathbf{L}$ representing the penalty matrix. For conventional Tikhonov regularization, $\mathbf{L}$ is an identity matrix. When $\mathbf{L}$ is not an identity matrix, the solution is given by:

$$\mathbf{q}_{reg} = \frac{\mathbf{G}^H\mathbf{p}}{\mathbf{G}^H\mathbf{G} + \lambda^2\mathbf{L}^H\mathbf{L}} \tag{6}$$

where $[\bullet]^H$ denotes the complex conjugate transpose. To avoid the lack of information induced by the penalty matrix, the beamforming regularization matrix is adopted Gauthier et al. [13]:

$$\mathbf{L} = \mathrm{diag}\left(\frac{\mathbf{G}^H\mathbf{p}}{\|\mathbf{G}^H\mathbf{p}\|_\infty}\right)^{-1} \tag{7}$$

The virtual sources strengths $\mathbf{q}_{BF}$ solved by the beamforming regularization matrix method is

$$\mathbf{q}_{BF} = \frac{\mathbf{G}^H\mathbf{p}}{\mathbf{G}^H\mathbf{G} + \lambda^2\left[\mathrm{diag}\left(\frac{\mathbf{G}^H\mathbf{p}}{\|\mathbf{G}^H\mathbf{p}\|_\infty}\right)^{-1}\right]^2} \tag{8}$$

2.1.2 Compressed sensing method

According to the above theory, the virtual source is sparse or close to sparse. CS can be used to calculate the source strength of virtual sources. Different from the l_2-norm, the l_1-norm ($\|\bullet\|_1$) can promote sparsity and the sparse virtual source strengths can be obtained. It is preferable to solve the Eq. 4 by minimizing l_1-norm, i.e., [19,20].

$$\arg\min_{\mathbf{q}} \|\mathbf{q}\|_1 \quad \text{subject to} \quad \|\mathbf{p} - \mathbf{G}\mathbf{q}\|_2^2 \le \varepsilon \tag{9}$$

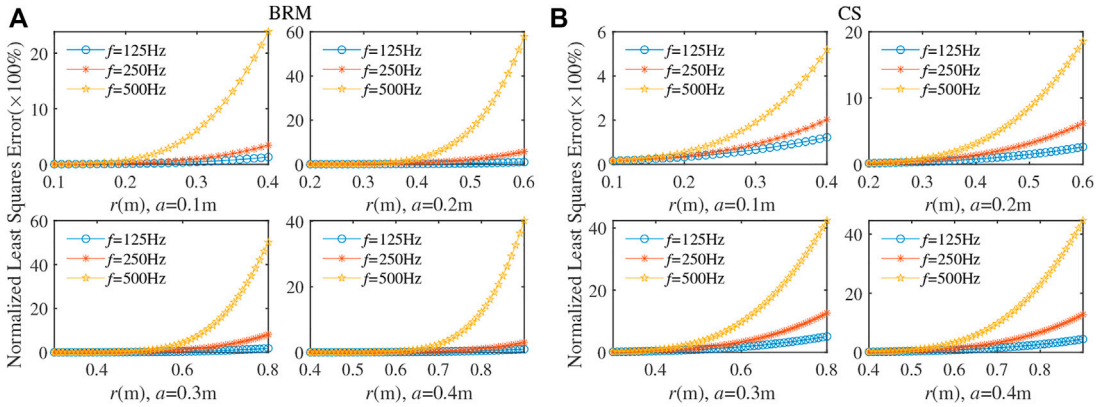

FIGURE 4
The pressure least square errors as a functon of the frequency for different spherical array radius. The simulation results of the BRM and CS are shown in **(A)** and **(B)**, respectively.

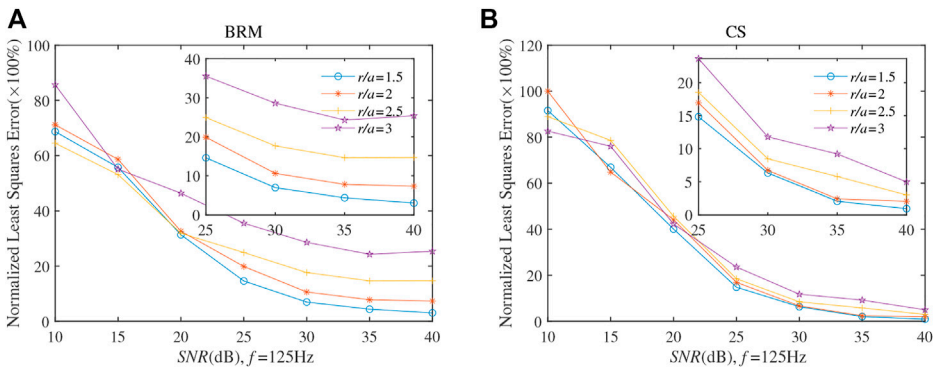

FIGURE 5
The pressure least square errors as a function of SNR at 125 Hz. The simulation results of the BRM and CS are shown in **(A)** and **(B)**, respectively.

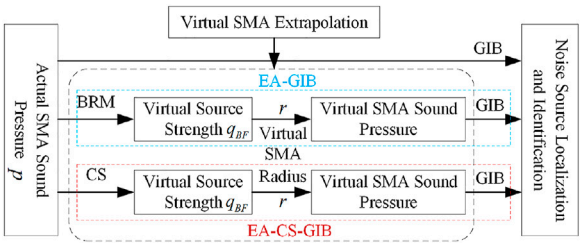

FIGURE 6
Schematic diagram of virtual SMA localization and identification.

where ε is the data fidelity constraint. CS has proved that Eq. 9 can be solved by using a convex optimization algorithm to obtain a well-estimated sparse solution with most elements being zero. In the calculation process, the above CS problem with l_1-norm optimization is solved by the available Matlab CVX package. The result is the source strengths $\mathbf{q}_{BF}$ of the virtual source[21].

2.1.3 Virtual SMA pressure

After solving the strengths of the virtual sources $\mathbf{q}_{BF}$, the sound field in the envelope surface S can be approximately calculated. Assume that a virtual SMA is placed at a surface S_0 (r is the radius of the virtual SMA) as shown in Figure 1. Then, a virtual SMA is used to localize and identify the sound source, the sound pressure $p_v(r_v)$ received at a point r_v on the virtual SMA can be given by:

$$p_v(r_v) = \mathbf{G}(r_v, r')\mathbf{q}_{BF}(r') \tag{10}$$

2.2 Analysis of parameters affecting the SMA extrapolation

Before applying the virtual SMA for noise localization and identification, it is necessary to analyze the factors affecting the accuracy of the extrapolation. This section analyzes the parameter sensitivity of the extrapolation. Here, several dominant parameters

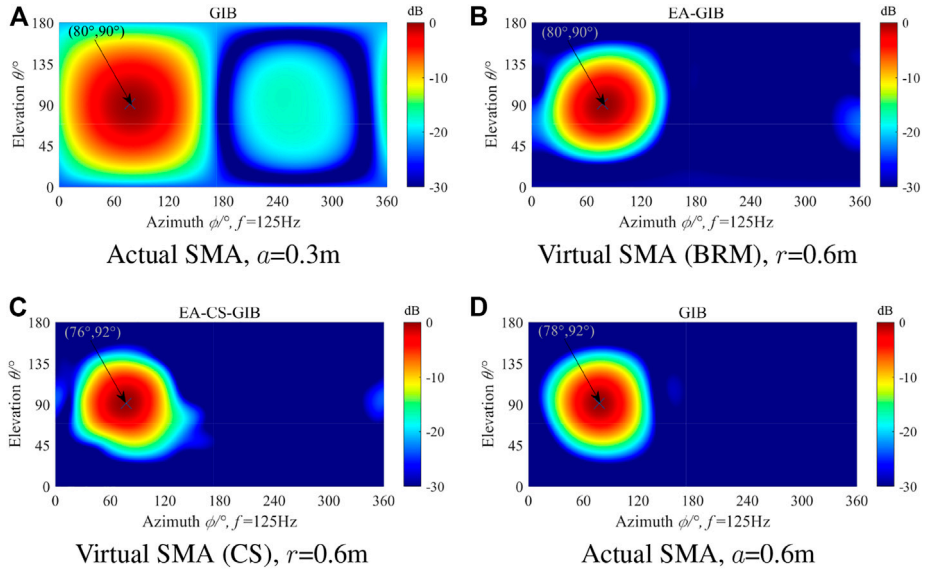

FIGURE 7
The simulation results for single source localization and identification using the virtual SMA in **(B)** and **(C)** at 125 Hz and SNR = 20dB, and using the actual SMA shown in **(A)** and **(D)** for comparison purposes.

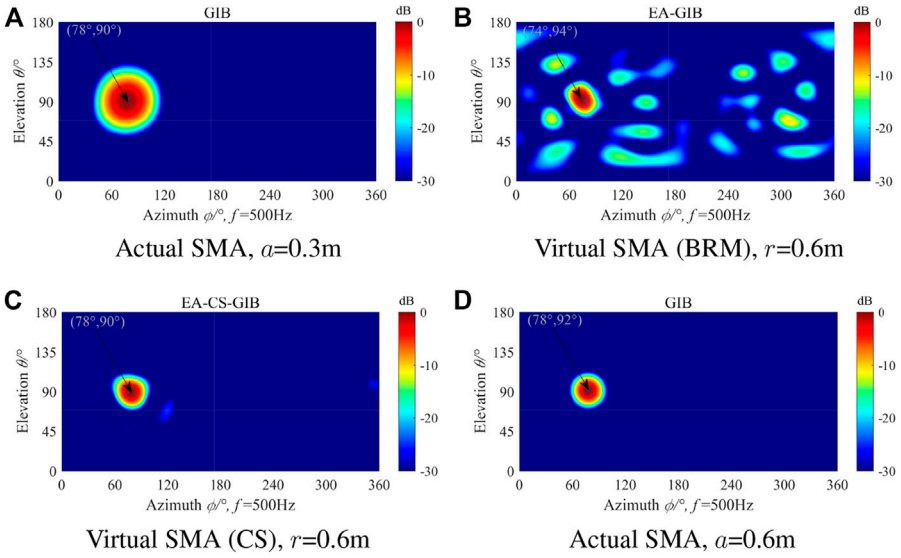

FIGURE 8
The simulation results for single source localization and identification using the virtual SMA in **(B)** and **(C)** at 500 Hz and SNR = 20dB, and using the actual SMA shown in **(A)** and **(D)** for comparison purposes.

were considered, including the configuration of the surface where the virtual source is placed, the aperture of the SMA, and the signal-to-noise ratio (SNR). Unless specified, the default parameters treated in the simulations are given as follows: the sound speed c in the air is 340 m/s, the sound source was placed at (5 m, 56°, 201°) in spherical coordinates, the radius of the open SMA a is 0.3 m, and the number of array elements is 64. In order to evaluate the accuracy of the extrapolation, the least square errors of the pressure are defined as follows Zhang et al. [18]:

$$\eta = \frac{\sum_{i=1}^{Q} \left(\| p_{the}(r, \theta_i, \phi_i) - p_{rec}(r, \theta_i, \phi_i) \|_2 \right)^2}{\sum_{i=1}^{Q} \left(\| p_{the}(r, \theta_i, \phi_i) \|_2 \right)^2} \times 100\% \tag{11}$$

where p_{the} and p_{rec} are the theoretical and approximate values of sound pressure on the spherical reference surface, respectively.

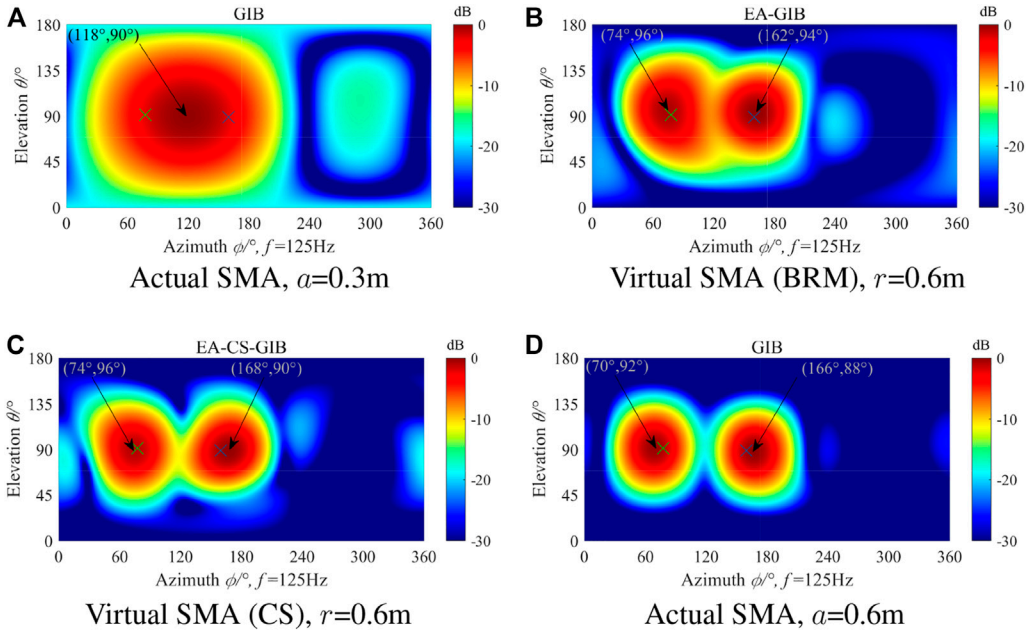

FIGURE 9
The simulation results for double sources localization and identification using the virtual SMA in **(B)** and **(C)** at 125 Hz and SNR = 20dB, and using the actual SMA shown in **(A)** and **(D)** for comparison purposes.

2.2.1 The radius of the envelope surface and the number of the virtual source

Two parameters were considered in the simulations, the radius of the surface where the virtual source is placed and the number of virtual sources used [22, 23]. No noise was added during the simulation process, and the simulation results are shown in Figures 2, 3.

Figure 2 demonstrates the errors at different radii of the virtual source surface *versus* frequency. Here, the radius of virtual source surface r' was set to be 2, 4, 8, and 16 times that of the open SMA (a = 0.3). In Figure 2, the abscissa represents the product of wave number k and minimum array element spacing d, and the ordinate represents the least square error. For a given radius of the virtual source surface, the error remains stable at around 3% before rapidly increasing to a cut-off frequency of $k \times d \approx 2$. The cut-off frequency corresponds to an acoustic wavelength of $2/d$. Thus, an equivalent of the Nyquist criterion for sampling waveforms is violated at the cut-off frequency, where a sudden increase in the error can be seen. In addition, when k is higher than the cut-off frequency, the larger virtual source radius extrpolation error is smaller. Because the smaller the envelope surface, the smaller the distance between the envelope surface and the SMA. Therefore, the correlation of vectors in the transfer matrix is stronger, and the condition number of the transfer matrix becomes larger, resulting in instability of the inverse problem, especially at higher frequencies.

Next, the influence of the number of virtual sources was researched. Figure 3 displays the errors as a function of the number of virtual sources at different frequencies. In the figure, the abscissa represents the product of wave number k and minimum virtual source spacing d'. In this case, the error curves exhibit similar behavior as those for different configurations of virtual sources, significantly decreasing before the number of virtual sources reaches a specific number M and remaining stable afterward. M also corresponds to an equivalent of the Nyquist criterion for virtual sources. This means that the distribution of the virtual sources also needs to satisfy the Nyquist criterion. At the same time, by comparing Figures 3A, B, it can be found that the array extrapolation error of CS method is smaller under the same sampling scheme.

2.2.2 Spherical array aperture

Apart from the virtual source surface configuration, the aperture of the SMA also affects the extrapolation accuracy. This section investigates the influence of the radius of the open SMA. The simulations in this section kept the same default parameters used in Section 2.1.1. Figure 4 shows the error as a function of the radius of the open SMA at 125, 250, and 500 Hz. Four radii, a = 0.1, 0.2, 0.3, and 0.4 m, were considered in the simulations. And the envelope surface parameter at this time is a fixed value (the radius of the virtual source surface and the number of virtual sources are set according to the curve r'/a = 16 in Figure 2). It can be seen from Figure 4 that as r increases, an overall increasing trend of the error curves can be seen at different frequencies. Moreover, the higher the frequency, the larger the increase of error with r. Further, larger radii of the open SMA will cause smaller errors. This coincides with the observation that stable results of the inverse problem can be obtained when the distance between the virtual source surface and the open SMA is far (small condition number of the transfer matrix). At the same time, by comparing Figures 3A, B, under the same conditions, the virtual SMA error obtained by CS method is smaller.

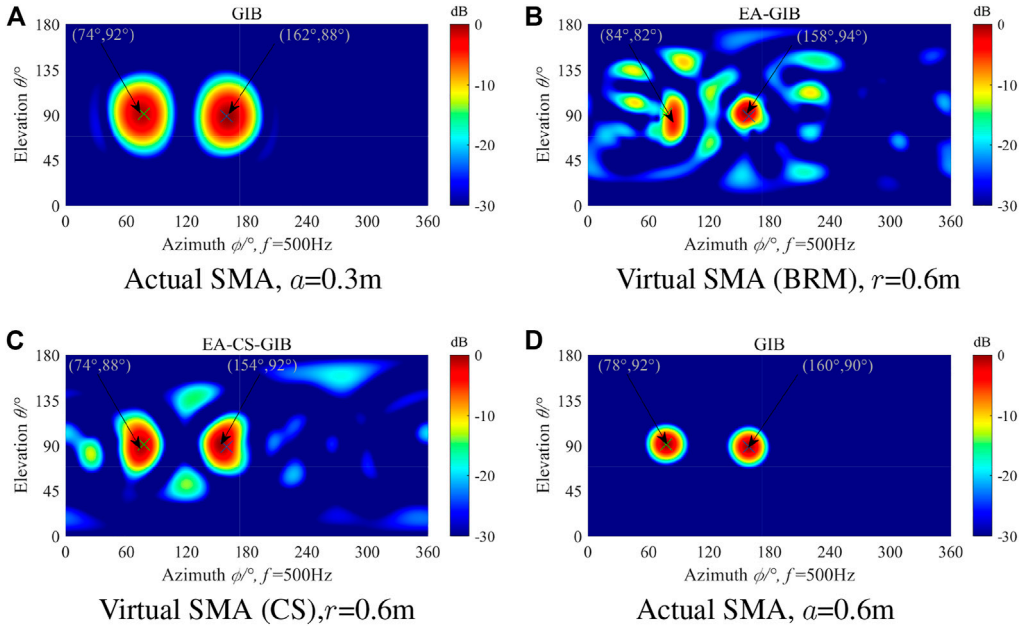

FIGURE 10
The simulation results for double sources localization and identification using the virtual SMA in **(B)** and **(C)**at 500 Hz and SNR = 20dB, and using the actual SMA shown in **(A)** and **(D)** for comparison purposes.

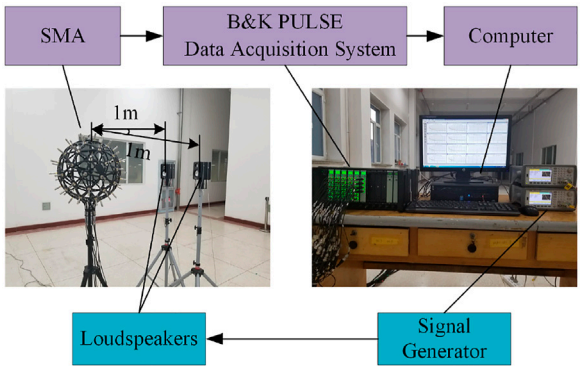

FIGURE 11
Experimental setup.The blue background text at the bottom of the figure represents an experimental signal transmission system consisting of a signal generator and loudspeakers. The purple background text at the top of the figure represents an experimental receiving system consisting of an SMA, data acquisition system, and computer.

2.2.3 Signal-to-noise ratio

In the actual measurement environment, the received data of the SMA contains environment noise. Using the received data with noise could cause the error of the approximate received data of the virtual SMA to become larger, which affects its subsequent application effect.

Figure 5 shows the error results of different virtual SMA radii as the SNR changes at 125 Hz. The radius of the virtual SMA is 1.5, 2, 2.5, and 3 times that of the actual SMA. It can be seen from Figure 5 that the sound pressure extrapolation error at the virtual SMA is high when the signal to noise ratio is low. Therefore, in order to obtain a better application effect of the virtual SMA, it should be ensured that the SNR of the signal received by the actual SMA is high. An SNR value of at least 20 dB was adopted in the subsequent noise source localization simulations. At the same time, by comparing Figures 5A, B, it can be found that the error of CS method is smaller after SNR is greater than 25 dB. In addition, the extrapolation error of the virtual SMA increases as its radius increases at the same SNR.

3 Noise source localization and identification with GIB

To further improve the resolution of source localization using the virtual extrapolated array (EA) in the presence of sound sources in the low-frequency range, GIB is applied in this paper. The GIB algorithm estimates the source information through the data measured by the array and its sound field transfer relationship (Eq. 4). Generally, the number of microphones used is lower than the number of scanning grid points, thus the general solution of the unknown strength can be written as:

$$\mathbf{q}_{\lambda\beta} = \left(\mathbf{L}^H\mathbf{L}\right)^{-1}\mathbf{G}^H\left(\mathbf{G}\left(\mathbf{L}^H\mathbf{L}\right)^{-1}\mathbf{G}^H + \lambda^2\mathbf{I}\right)^{-1}\beta\mathbf{p} \tag{12}$$

where β is the scaling parameter to compensate for reduced source amplitudes caused by over-regularization, with a mathematical expression of $\beta = \|\mathbf{G}\mathbf{L}^{-1}\left(\mathbf{G}\mathbf{L}^{-1}\right)^H + \lambda\mathbf{I}\|_2$ Zhang et al. [18].

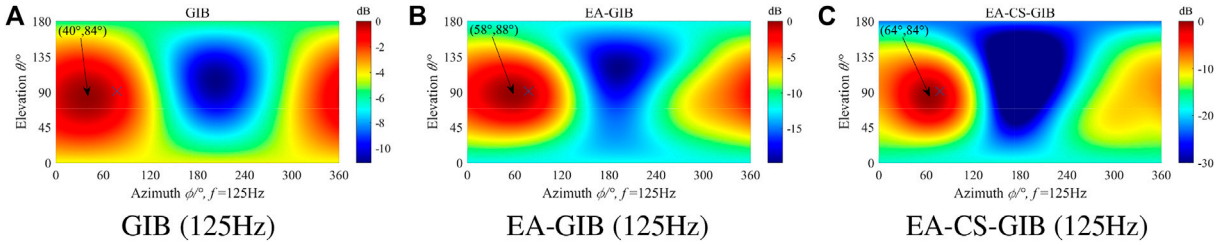

FIGURE 12
The experimental results for single source localization and identification using the actual SMA in **(A)** at 125 Hz, and the virtual SMA shown in **(B)** and **(C)**.

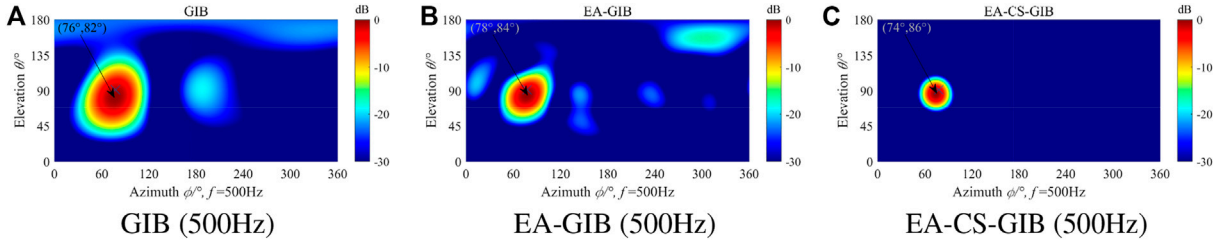

FIGURE 13
The experimental results for single source localization and identification using the actual SMA in **(A)** at 500 Hz, and the virtual SMA shown in **(B)** and **(C)**.

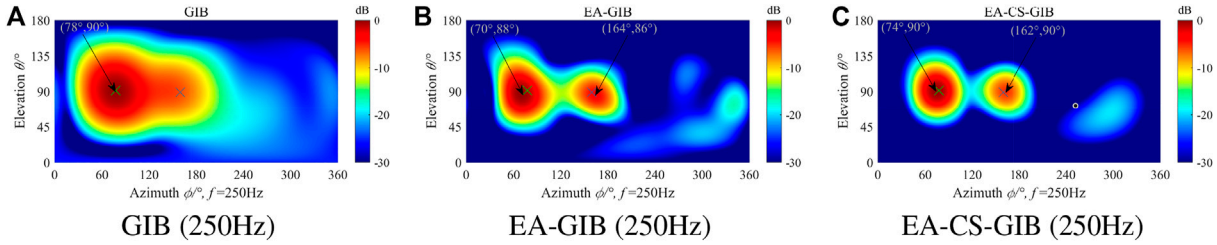

FIGURE 14
The experimental results for double sources localization and identification using the actual SMA in **(A)** at 250 Hz, and the virtual SMA shown in **(B)** and **(C)**.

The actual SMA and virtual SMA data can be substituted into the GIB to realize the noise source localization and identification. Figure 6 shows the schematic diagram of the virtual SMA noise source localization and identification.

3.1 Single source simulation

In the single sound source simulation experiment, the SMA was the same as the array in the simulation parameter analysis. The single sound source was placed at (1m, 91°, 78°) (marked with '×' in the following figures) in the spherical coordinate system where the SMA was located. The sound source position obtained through simulation calculation is marked with an arrow at the upper left corner of the localization result map. During the simulation calculation, the radius of the virtual SMA was equal to 0.6 m, which is two times that of the actual SMA (a = 0.3 m). The simulation results of the actual SMA with the same radius as the virtual SMA (a = 0.6 m) are also displayed for comparison.

Figures 7, 8 show the simulation results for noise source localization and identification using the actual and virtual SMA at 125 and 500 Hz, respectively. Figure 7A shows the localization result of an open SMA with a radius of 0.3 m, Figures 7B, C show the

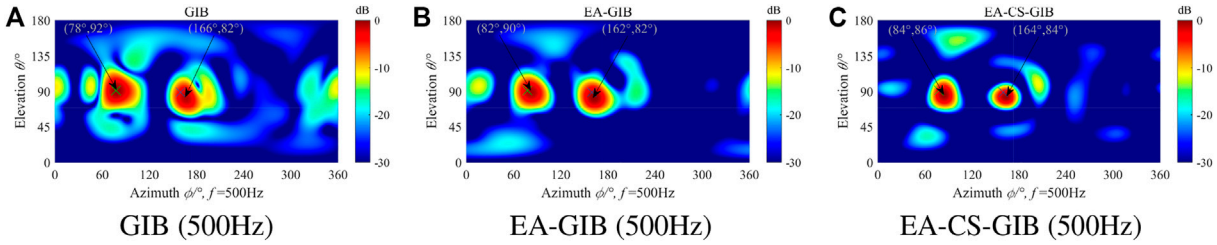

FIGURE 15
The experimental results for double sources localization and identification using the actual SMA in **(A)** at 500 Hz, and the virtual SMA shown in **(B)** and **(C)**.

localization result of a virtual open SMA with a radius of 0.6 m extrapolated from the open SMA, and Figure 7D shows the localization result of an actual open SMA with a radius of 0.6 m. As can be seen from Figure 7, using a virtual open SMA with a radius of 0.6 m at 125 Hz can effectively improve the localization effect of the actual SMA, but the localization effect is slightly worse than a actual SMA with a radius of 0.6 m. It can be found from Figures 7, 8, the virtual SMA extrapolation method has obvious advantages. As can be seen from Figure 4, when the SNR is 20dB, the higher the sound source frequency, the extrapolation error of the SMA becomes larger. Therefore, some interference appears in the localization result graph, but this does not affect the localization result.

3.2 Double sources simulation

The single sound source localization and identification simulations described above proved the advantages of the SMA extrapolation method researched in this paper in the low-frequency range. In the double sound sources simulation experiment, the SMA is the same as that in the single sound source simulation. The sound source position is located at (1 m, 91°, 78°) and (1 m, 89°, 160°) in the spherical coordinate system where the SMA is located, and the virtual SMA radius (0.6 m) is set to be 2 times that of the actual SMA. The simulation results of the actual SMA with the same radius as the virtual SMA are also displayed for comparison and analysis.

Figures 9, 10 show the simulation results of noise source localization and identification using the actual and virtual SMA when SNR = 20 dB at 125 and 500Hz, respectively. It can be seen from Figure 9 that the actual open SMA with a radius of 0.3 m cannot distinguish the two sound sources at 125 Hz, but after the extrapolation method is used to obtain a virtual SMA with a radius of 0.6 m the two sound sources can be clearly distinguished. As can be seen from Figures 9B, C, the virtual SMA obtained by CS method has better resolution effect on two sound sources. But its effect is not as good as the actual SMA with a radius of 0.6 m. It can be seen from Figure 10 that with the increase of sound source frequency, the actual SMA with a radius of 0.3 m can effectively distinguish two sound sources, and the virtual SMA can also distinguish two sound sources. However, due to the increase of the sound source frequency, the SMA extrapolation effect becomes worse, and the sidelobe interference appears in the localization result.

4 Experiments

The simulation experiments of noise source localization and identification in the case of single and double sound sources indicate that the SMA extrapolation method explored in this paper provides some advantages in the low-frequency range. In this section, an experiment with locating loudspeakers based on the open SMA (a = 0.3 m) in an empty room is carried out to verify the accuracy and effectiveness of the extrapolation method in an actual environment. The signal generator (Agilent33522A) in the launching system generates signals to drive the loudspeakers to radiate sound waves. In the receiving system, the sound waves are received by a 64-element randomly and uniformly distributed open SMA (BSWA MPA201 Microphone), collected by the multi-channel data collector (B&K PULSE 3660D) stored in the computer, and then displayed by the computer. Photos of the test site are shown in Figure 11. During the test, the two loudspeakers were located at (1 m, 91°, 78°) and (1 m, 89°, 160°) in the spherical coordinate system, which was established with the center of the open SMA at the origin. In the experiment with the single sound source, only the sound source at position 1 worked. In the experiment with a double sound source, both sound sources worked at the same time.

4.1 Single source experiments

Figures 12, 13 show the experimental data processing results when the sound source frequency is 125 and 500 Hz. It can be seen from the figure that the position of the sound source could be accurately localized with the virtual SMA extrapolation method adopting 125 and 500 Hz. Compared with Figures 12A–C, after adopting the virtual SMA, the width of the mainlobe of the beam in the GIB algorithm is narrower and the sound source localization effect is better. At the same time, through Figures 12B, C, we can see that the virtual SMA obtained by CS method is better. As shown in Figure 13, the increase of the sound source frequency, the transmitting ability of the loudspeaker increases, and the SNR of the signal received by the SMA is higher, the width of the main lobe is narrower and the sound source localization effect is better.

4.2 Double sources experiments

Next, both loudspeakers were switched on in order to conduct the experiment with a double source. Figures 14, 15 show the experimental results for two sound sources at frequencies of 250 Hz (The low frequency emission capability of the loudspeaker used in the experiment is limited, making it difficult to ensure a high SNR at 125 Hz. Therefore, 250 Hz was used as the experimental frequency.) and 500 Hz. It can be seen from the figure that when the sound source frequency is equal to 250 Hz, the actual SMA cannot accurately distinguish the two sound sources, while the virtual SMA can completely distinguish the two sound sources and their positions accurately. And the localization effect of the virtual SMA obtained by CS method is better. When the sound source frequency is equal to 500 Hz, the actual and the virtual SMA can distinguish the two sound sources. And the virtual SMA has higher accuracy, a narrower mainlobe, and a better localization effect than the actual SMA.

5 Conclusion

This paper proposes a low-frequency noise sources localization method based on the virtual SMA extrapolation method and resolves the localization problem of a small-aperture SMA with low-frequency noise sources. Firstly, this paper introduces the method and principle of the virtual SMA extrapolation method and discusses in detail the selection of parameters, the scope of application, and the influence on the array extrapolation of the envelope surface aperture, SMA aperture, and SNR. At the same time, the CS technology is introduced into the extrapolation of the virtual SMA, which further improves the reception accuracy of the virtual SMA. Secondly, the GIB algorithm was introduced into the noise source localization and identification process, and the appropriate virtual SMA radius was selected according to the above parameter discussion. The simulation results show that the error of the virtual SMA obtained by the CS method is smaller, and it also proves the advantages of the virtual SMA extrapolation method in the low-frequency noise source localization and identification. Finally, an experiment with noise source localization and identification of the open SMA was carried out. The experimental results verify the accuracy of the simulation calculation and its effectiveness in an actual environment. The proposed method provides an effective solution for solving the problem of poor low-frequency spatial resolution of small-aperture SMAs and expands the application range of small-aperture SMAs. At the same time, it is proved that the method simultaneously reduces the complexity and cost of the measurement system, which has great engineering application value and prospects.

Data availability statement

The raw data supporting the conclusion of this article will be made available by the authors, without undue reservation.

Author contributions

SS and BY contributed to the conception of the study; BY, QG, and CG carried out experiments; BY performed the data analyses and wrote the manuscript; YL and CG helped to review and revise the manuscript. All authors contributed to the article and approved the submitted version.

Conflict of interest

The authors declare that the research was conducted in the absence of any commercial or financial relationships that could be construed as a potential conflict of interest.

Publisher's note

All claims expressed in this article are solely those of the authors and do not necessarily represent those of their affiliated organizations, or those of the publisher, the editors and the reviewers. Any product that may be evaluated in this article, or claim that may be made by its manufacturer, is not guaranteed or endorsed by the publisher.

References

1. Ginn KB, Haddad K. Noise source identification techniques: Simple to advanced applications. In: Proceedings of the Acoustics; Nantes, France (2012). p. 1781–6.

2. Chiariotti P, Martarelli M, Castellini P. Acoustic beamforming for noise source localization–reviews, methodology and applications. *Mech Syst Signal Process* (2019) 120:422–48. doi:10.1016/j.ymssp.2018.09.019

3. Yang Y, Chu Z, Shen L, Xu Z. Functional delay and sum beamforming for three-dimensional acoustic source identification with solid spherical arrays. *J Sound Vib* (2016) 373:340–59. doi:10.1016/j.jsv.2016.03.024

4. Haddad K, Hald J. 3d localization of acoustic sources with a spherical array. *The J Acoust Soc America* (2008) 123:3311. doi:10.1121/1.2933754

5. Balmages I, Rafaely B. Open-sphere designs for spherical microphone arrays. *IEEE Trans Audio Speech Lang Process* (2007) 15:727–32. doi:10.1109/TASL.2006.881671

6. Rafaely B. Phase-mode versus delay-and-sum spherical microphone array processing. *IEEE Signal Process. Lett* (2015) 12, 713–6.

7. Tiana-Roig E, Torras-Rosell A, Fernandez-Grande E, Jeong C-H, Agerkvist FT. Enhancing the beamforming map of spherical arrays at low frequencies using acoustic holography. In: 5th Berlin Beamforming Conference (2014).

8. Yan S, Sun H, Svensson UP, Ma X, Hovem JM. Optimal modal beamforming for spherical microphone arrays. *IEEE Trans Audio Speech Lang Process* (2011) 19:361–71. doi:10.1109/TASL.2010.2047815

9. Chu Z, Yang Y, He Y. Deconvolution for three-dimensional acoustic source identification based on spherical harmonics beamforming. *J Sound Vib* (2015) 344:484–502. doi:10.1016/j.jsv.2015.01.047

10. Chu Z, Zhao S, Yang Y, Yang Y. Deconvolution using clean-sc for acoustic source identification with spherical microphone arrays. *J Sound Vib* (2019) 440:161–73. doi:10.1016/j.jsv.2018.10.030

11. Parthy A, Jin C, van Schaik A. Measured and theoretical performance comparison of a co-centred rigid and open spherical microphone array. In: 2008 International Conference on Audio, Language and Image Processing (2008). p. 1289–1294. doi:10.1109/ICALIP.2008.4590251

12. Jin CT, Epain N, Parthy A. Design, optimization and evaluation of a dual-radius spherical microphone array. *IEEE/ACM Trans Audio, Speech, Lang Process* (2014) 22:193–204. doi:10.1109/TASLP.2013.2286920

13. Gauthier P-A, Camier C, Pasco Y, Berry A, Chambatte E, Lapointe R, et al. Beamforming regularization matrix and inverse problems applied to sound field measurement and extrapolation using microphone array. *J Sound Vib* (2011) 330:5852–77. doi:10.1016/j.jsv.2011.07.022

14. Gauthier P-A, Chambatte r., Camier C, Pasco Y, Berry A. Beamforming regularization, scaling matrices, and inverse problems for sound field extrapolation and characterization: Part ii–experiments. *J Audio Eng Soc* (2014) 62:207–19. doi:10.17743/jaes.2014.0017

15. Padois T, Gauthier P-A, Berry A. Inverse problem with beamforming regularization matrix applied to sound source localization in closed wind-tunnel using microphone array. *J Sound Vib* (2014) 333:6858–68. doi:10.1016/j.jsv.2014.07.028

16. Yang B, Shi S, Yang D. Acoustic source localization using the open spherical microphone array in the low-frequency range. *MATEC Web of Conf* (2019) 283:04001. doi:10.1051/matecconf/201928304001

17. Ping G, Chu Z, Yang Y, Xu Z. Wideband holography based spherical equivalent source method with rigid spherical arrays. *Mech Syst Signal Process* (2018) 111:303–13. doi:10.1016/j.ymssp.2018.04.006

18. Zhang Z, Chen S, Xu Z, He Y, Li S. Iterative regularization method in generalized inverse beamforming. *J Sound Vib* (2017) 396:108–21. doi:10.1016/j.jsv.2017.02.044

19. Wang Y, Chen K. Compressive sensing based spherical harmonics decomposition of a low frequency sound field within a cylindrical cavity. *J Acoust Soc Am* (2017) 141: 1812–23. doi:10.1121/1.4978247

20. Bi C-X, Liu Y, Xu L, Zhang YB. Sound field reconstruction using compressed modal equivalent point source method. *J Acoust Soc Am* (2017) 141:73–9. doi:10.1121/1.4973567

21. Boyd S. *Cvx: Matlab software for disciplined convex programming*. version 2.2 (2020).

22. He T, Mo S, Fang E, Wang M, Zhang R. Modeling three-dimensional underwater acoustic propagation over multi-layered fluid seabeds using the equivalent source method. *J Acoust Soc Am* (2021) 150:2854–64. doi:10.1121/10.0006663

23. He T, Wang B, Mo S, Fang E. Predicting range-dependent underwater sound propagation from structural sources in shallow water using coupled finite element/equivalent source computations. *Ocean Eng* (2023) 272:113904. doi:10.1016/j.oceaneng.2023.113904

frontiers | Frontiers in Physics

TYPE Original Research
PUBLISHED 07 April 2023
DOI 10.3389/fphy.2023.1163148

OPEN ACCESS

EDITED BY
Zhixiong Gong,
Shanghai Jiao Tong University, China

REVIEWED BY
Youjiang Wang,
Shanghai Jiao Tong University, China
Zou Yucheng,
Harbin Engineering University, China

*CORRESPONDENCE
Yong-Ou Zhang,
zhangyo@whut.edu.cn

SPECIALTY SECTION
This article was submitted to Physical Acoustics and Ultrasonics, a section of the journal Frontiers in Physics

RECEIVED 10 February 2023
ACCEPTED 23 March 2023
PUBLISHED 07 April 2023

CITATION
Qu Y, Zhang Y-O, Li Y-F and Zhang T (2023), Similarity analysis of the flow-induced noise of a benchmark submarine. *Front. Phys.* 11:1163148. doi: 10.3389/fphy.2023.1163148

Similarity analysis of the flow-induced noise of a benchmark submarine

Yao Qu[1], Yong-Ou Zhang[1]*, Yi-Fan Li[1] and Tao Zhang[2]

[1]School of Naval Architecture, Ocean and Energy Power Engineering, Wuhan University of Technology, Wuhan, China, [2]School of Naval Architecture and Ocean Engineering, Huazhong University of Science and Technology, Wuhan, China

As one of the three major noise sources of submarines, flow-induced noise plays a key role for the stealth capability of submarines. Several research studies based on experiment or simulation have evaluated the sound radiation from the scale model; however, it is still a great challenge to efficiently evaluate the flow-induced noise of a large-scale prototype. In order to solve this problem, the flow-induced noise of different scale submarines is analyzed, and both the similarity law and the scale effect are discussed in the dimensionless frequency St = 10–1089. The fully appended DARPA SUBOFF, a famous benchmark submarine model, is used in our research. The relationship between the sound power, scale variables, and the speed and scale variables is obtained using the Buckingham Pi theorem. Then, the sound pressure level and the sound power level of the SUBOFF, with the scale ratio of 1:24 and 1:48 and the speed of 2, 4, and 8 m/s, are calculated based on the large-eddy simulation (LES)/Lighthill hybrid method. Finally, the scale effect between a hypothetical prototype (actually, a benchmark SUBOFF model with a scale ratio of 1:8) and its scale models are discussed at the same speed. The numerical results show that the submarine's sound power level conforms to the similarity relationship of dipole source within the cut-off frequency St = 100. The error of the sound power level is about 20 lg (φ) caused by scale effect when the dimensionless frequency is greater than the cut-off frequency, where φ is the scale ratio from the hypothetical prototype to the model. The scale error of the sound pressure level at different position and different frequency exist differently when extrapolating from model results to prototype according to the similarity law based on dipole source.

KEYWORDS

flow-induced noise, SUBOFF, dipole source, hybrid method, similarity law, scale effect

1 Introduction

There are three main radiated noise sources in submarines, ships, and airplanes, including mechanical noise, propeller noise, and hydrodynamic/aerodynamic noise. Among them, hydrodynamic and aerodynamic noises are divided into flow-induced noise (rigid wall) and flow-excited noise (elastic wall) [1]. The generation mechanism of various noise sources has been comprehensively discussed by scholars. However, due to the large size for those vehicles, noise assessment of the prototype has always been a challenge.

For most studies, noise assessment of the full-scale model is usually based on experiments, for example, measuring different submarines' noise through sea trial [2], monitoring hydrodynamic noise generated by different merchant ships on the fixed channel [3], and determining the location of aerodynamic noise source when the aircraft takes off and

lands on both sides of the airport runway [4]. Although the experiment can obtain accurate values under actual conditions, it is greatly affected by environmental conditions and consumes considerable manpower and financial resources. Evidently, it is difficult to carry out experiments for many design studies.

At present, the main solution is to extrapolate from scale model results to prototype, which requires the similarity law in advance. The International Towing Tank Conference (ITTC) paid attention to similarity studies of the ship noise in previous conferences such as the hydrodynamic noise [5] and propeller noise [6]. During the last decades, there were abundant experimental research studies on similarity of the propeller noise. Lee et al. [7] first verified the similarity law of the propeller tonal noise. Based on the conclusion proposed by the ITTC in 1987, Tani et al. [8] developed and tested a similarity relationship of four conventional propellers of different scales in the cavitation test tunnel. Park et al. [9] established a novel similarity law to estimate propeller tip vortex cavitation noise and obtained more consistent prediction than the results of ITTC. In addition, some scholars also conducted experiments on similarity studies of the flow-induced noise. Arakeri et al. [10] found a similarity law where the flow-induced noise of the axisymmetric body was proportional to the seventh power of inflow velocity. Based on the same simplified landing gear model, Xing et al. [11] obtained the sound pressure level spectrums of the flow-induced noise at different speeds and then normalized the amplitude according to the dipole characteristics and the frequency according to the Helmholtz similarity. The low-speed results are in good agreement with those of high speed, which verified that the acoustic source type of the landing gear is dipole in the low-frequency range.

With the development of computational fluid dynamics and the improvement of computer performance, the numerical prediction method has become a mainstream method [12, 13]. The Lighthill acoustic analogy and the Ffowcs Williams and Hawkings (FW-H) are the main numerical methods for predicting radiated noise. Yang et al. [14] calculated a non-cavitating propeller noise of three different scale models by using the large-eddy simulation (LES)/Lighthill hybrid method and found that the scale effect increased with the increase of the scale ratio. Bosschers et al. [15] proposed a semi-empirical method to predict the hull pressure fluctuation and radiated noise caused by propeller tip vortex cavitation noise, and they compared the predicted results with the measured results using the boundary element method. In the anechoic chamber wind tunnel, Li et al. [16] verified that the frequencies of the different scale cylinders satisfy the similarity of the Strouhal number, and they studied the similarity in different media based on the FW-H numerical method. There were abundant numerical calculations to discuss the submarine performance under small-scale models, including resistance characterization [17], flow characterization [18], radiated noise [19], and self-noise [20]. As for the full-scale model, Sezen et al. [21] analyzed the scale effect of the submarine's hydrodynamic performance based on the Reynolds-averaged Navier–Stokes (RANS) method.

As one can notice, under the general computing resource, most of the numerical methods adopted by scholars only studied the small-scale model. Numerical calculation of the full-scale submarines mainly focused on hydrodynamic performance such as drag and self-propulsion characteristics instead of the radiated noise performance. The radiated noise characteristics of the full-scale model can be effectively obtained by studying the acoustic similarity law. To the best of the authors' knowledge, there are few open research studies on the similarity law of submarine's radiated noise. Moreover, the reduction technology of mechanical noise and propeller noise (non-cavitating) has relatively matured [22, 23]. On this basis, this study is to analyze the similarity of submarine's flow-induced noise based on the numerical method.

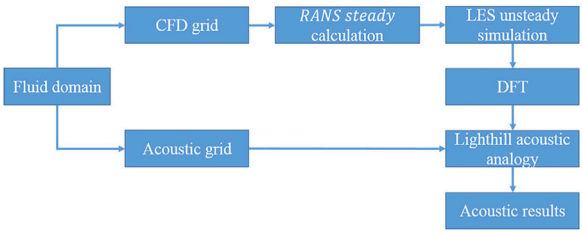

FIGURE 1
Flow chart of the flow-induced noise prediction.

In order to achieve the aforementioned outlined objectives, the fully appended SUBOFF (a benchmark submarine) is selected as the research object, which is fully and deeply submerged by water (i.e., ignoring the influence of wave resistance and free surface on sound propagation). Due to the limitation of computer resources, the similarity of the sound pressure level (SPL) and the sound power level (SWL) in the low-frequency range St = 10–1089 is discussed based on the LES/Lighthill hybrid method. This study is organized as follows: Section 2 introduces numerical methods and numerical models. In Section 3, the similarity conditions and the relationship of the far-field unsteady sound pressure are presented. The obtained similarity laws of the SPL and SWL are verified in Section 4. Section 5 discusses the scale effect of different scale models and the conclusion is included in Section 6.

2 Numerical models

There are two main calculation methods for flow-induced noise: direct method and hybrid method. The direct method is based on the compressible Navier–Stokes equations to calculate the sound pressure field in the whole fluid domain. The hybrid method decouples the flow field and acoustic field for calculation, which ignores the influence of flow on sound propagation. The former is quite difficult for calculating the large-scale and complex models. This paper adopted the LES/Lighthill hybrid method, which had been proved to be effective in predicting flow-induced noise [24, 25].

Figure 1 presents the common flow chart of the coupling algorithm in predicting the submarine's flow-induced noise. First, the SST k-ω turbulence model was used to calculate the steady flow field. Based on the initial steady results, the LES turbulence model was used to predict the transient flow field and then obtain the converged velocity results. The wall-adapting local eddy-viscosity model (WALE) was selected as the sub-grid model. Then, the unsteady results were interpolated to the acoustic grids after DFT transformation. Finally, the acoustic field was calculated based on the variational Lighthill equation under the volume integral [26]. In the flow field calculation of this study, the second-order scheme was

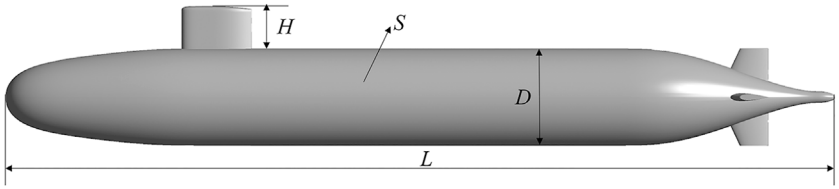

FIGURE 2
Geometric model of DARPA SUBOFF.

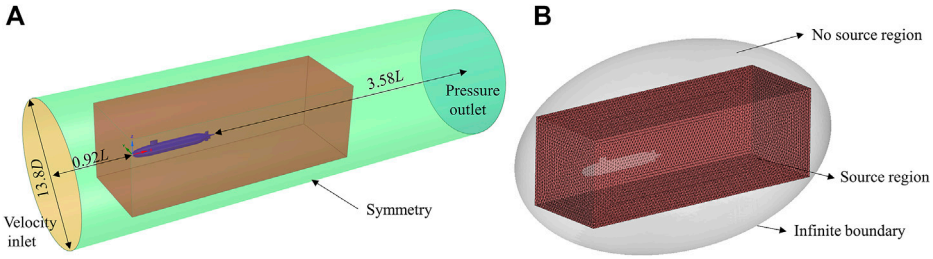

FIGURE 3
Computational domains and boundary conditions of **(A)** flow field and **(B)** acoustic field.

used for spatial discretization, velocity pressure coupling algorithm, for the SIMPLEC algorithm, and the convection scheme was the central difference scheme.

2.1 Computational domains and boundary conditions

A well-known benchmark submarine model named SUBOFF (no propeller) which was introduced by the Defense Advanced Research Projects Agency (DARPA) was selected in this study [27]. The geometric model is shown in Figure 2, the prototype length L = 104.544 m, maximum diameter D = 12.192 m, sail height H = 4.944 m, and the surface area S = 3656 m^2.

The computational domain of the flow field was established around the SUBOFF to calculate different scale model, as shown in Figure 3A. Numerical analysis was performed using the Cartesian coordinate system with the origin at the top of the SUBOFF head. The diameter of the cylinder in the fluid domain was 11D. The upstream of the domain was extended to 0.92 L from the apex of the SUBOFF head, and the downstream of the domain was extended to 3.58 L from the apex of the SUBOFF tail. The inlet boundary condition was identified as velocity inlet, and the outlet boundary condition was defined as pressure outlet. In order to satisfy the kinematic boundary condition, the cylindrical wall was defined as symmetry, and the submarine shell was defined as no-slip wall.

Acoustic calculation needs to establish an independent numerical model, as shown in Figure 3B. The acoustic field was divided into source region, no-source region, and infinite element boundary. The source region was the interpolation region of the stress tensor based on the Lighthill analogy equation. Its boundary usually needs to be far away from the sound source in consideration of the truncation error. In this study, selecting a rectangular domain with the size of 0.92 × 0.92 × 2.75 L as the source region, the wall boundary was 0.23 L away from the SUBOFF head. The infinite element boundary surrounding the sound source domain can make sound propagate to infinity by 1/r. The no-source region was the area connecting the source region and the infinite element boundary with the no-source term in the governing equations.

2.2 Grid generation and verification

The fine element of the fluid domain is the precondition for accurate calculation results, and the element type is structured grid. Similarity analysis needs to generate different scale mesh models, but this paper only introduces the condition that the scale ratio of 1: 24 and the speed U = 4 m/s. Under this condition, the fluid domain was divided into 247 blocks, as shown in Figure 4A. The grids detail can be seen in Figures 4B, C, most grids are concentrated on the SUBOFF surface and the wake of submarine. The boundary-layer grids were encrypted to capture the turbulence details on the surface, the number of prism layer was 15, the growth rate was 1.1, and the height of the first layer was 5 × 10^{-5} m to ensure $Y^+ \approx 1$ under the LES turbulence model. The grids of other scale models which have different number of nodes were produced based on the same blocks.

The resistance coefficient based on the steady SST k-ω turbulence model and SWL based on the LES/Lighthill hybrid method are used as the verification of element convergence. The number of grid models is, respectively, 2.17 million, 5.15 million,

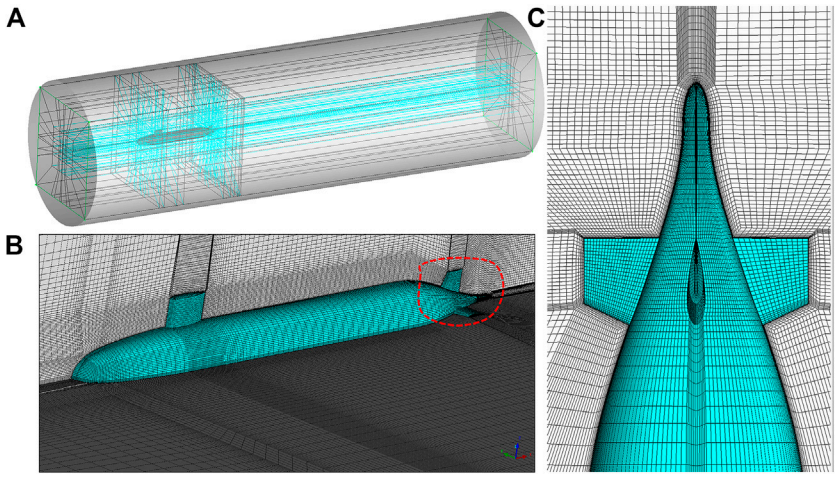

FIGURE 4
Grid model. **(A)** Computational domain blocks, **(B)** grid structure around the SUBOFF, and **(C)** boundary layer grids details.

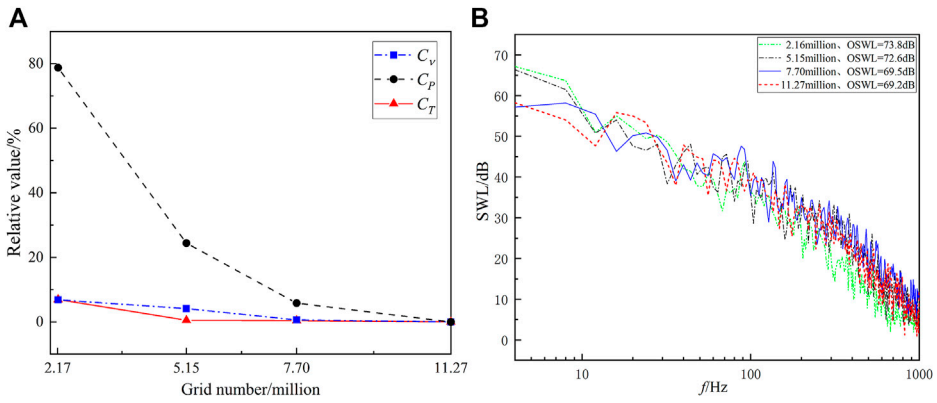

FIGURE 5
Grid convergence verification results. **(A)** Relative value of the resistance coefficient and **(B)** SPL spectrums.

7.7 million, and 11.27 million. Figure 5A shows the relative results of the viscous resistance coefficient (C_v), pressure resistance coefficient (C_P), and total resistance coefficient (C_T) in different grid models. The formula of relative value is $(T - T_m)/T_m \times 100\%$, where T is the resistance coefficient of different mesh models and T_m is the resistance coefficient under the maximum number. Figure 5B shows SWL spectrums and the overall sound power level (OSWL) of different grid models. The calculated results show that the resistance coefficient and OSWL are basically equal when the number of elements reaches 7.7 million, and this grid structure is used for subsequent grid model.

TABLE 1 Comparison between OSPL calculation results and relevant references.

Reference	Model	Method	OSPL/dB
Lu YT [28]	SUBOFF	Simulation	94.5
Yao HL [1]	SUBOFF	Simulation	102.0
Wang XH [29]	SUBOFF	Simulation	103.4
Jiang WC [30]	Water-drop submarine	Experiment	101.3
This study	SUBOFF	Simulation	100.2

2.3 Verification of the numerical method

Due to the lack of public experimental data of SUBOFF's flow-induced noise, calculation results in this paper are compared with those from other references which also used the numerical methods. The conditions are scale ratio, 1:24; speed, 3.0506 m/s; and acoustic measuring point, (2.178, −2 m, 0). The comparison results of the OSPL obtained by the LES/

TABLE 2 Calculational parameters of the SUBOFF.

Parameter	λ = 48			λ = 24		
	1	2	3	4	5	6
L/m	2.178	2.178	2.178	4.356	4.356	4.356
U/ms^{-1}	2	4	8	2	4	8
Re/10^7	0.43	0.86	1.72	0.86	1.72	3.42
Grids/million	3.3	3.3	3.3	7.7	7.7	7.7
Δh/ 10^{-5}m	8	8	8	5	5	5
Δt/ms	0.05	0.05	0.05	0.05	0.05	0.05
n	5,000	2,500	1,250	10,000	5,000	2,500

Lighthill acoustic analogy method in this paper are shown in Table 1. Among them, Ref. [30] is a "water drop" submarine with a small difference from the size of SUBOFF, and acoustic results obtained at the similar measuring points. The calculation results show that OSPL calculated is within the same order of magnitude compared with other references, and the error with OSPL calculated in this paper is within 5.7 dB. This method can be used as the calculation method for the subsequent discussion of submarine similarity.

3 Theoretical analysis on the similarity law

3.1 Dimensional analysis of the sound power

The dimensional analysis method can transform the dimensional relationship into a dimensionless one. Using this method, the similarity conditions between model and prototype can be determined, and then the similarity law can be built to calculate similar models at arbitrary scales. The power spectral density of the flow-induced noise with frequency f and position $\vec{r}$ can be expressed as follows:

$$\langle p_e^2(\vec{r}, f)\rangle = \psi(M, L, T, \rho, \upsilon, g, U, c, k, \vec{r}), \tag{1}$$

where p_e is the effective value of sound pressure, M represents the mass, L represents the length, T represents the time, ρ depicts the fluid density, ν presents the dynamic viscosity coefficient, g presents the acceleration of gravity, U is the flow speed, c is the sound speed, k is the wavenumber, and Ψ represents the functional relationship of a series of variables.

M, L, and T are selected as the basic dimension to obtain the dimensional expression of the remaining physical quantities, as shown in the following equation

$$\begin{aligned}[p_e^2(\vec{r}, f)] = [M^2L^{-2}T^{-3}], [\rho] = [ML^{-3}], [\upsilon] = [L^2T^{-1}],\\ [g] = [LT^{-2}][U] = [LT^{-1}], [c] = [LT^{-1}], [k] = [L^{-1}],\\ [\vec{r}] = [L][\vec{r}\cdot r^{-1}].\end{aligned} \tag{2}$$

Converting the dimensionless relationship into a series of similarity criterion numbers, the results are given as follows:

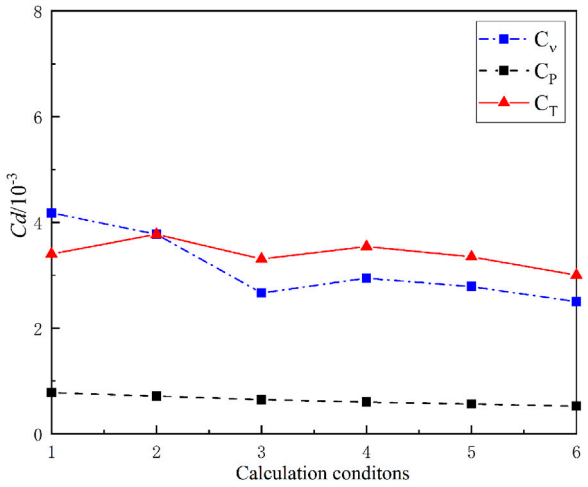

FIGURE 6
Coefficient drag of the SUBOFF models under different conditions.

$$\pi_1 = \frac{\langle p_e^2(\vec{r}, f)\rangle}{M^2L^{-2}T^{-4}T} = \frac{\langle p_e^2(\vec{r}, f)\rangle}{(\rho U^2/2)^2(L/U)}, \pi_2 = \frac{\rho}{ML^{-3}} = \frac{\rho L^2T^{-2}}{ML^{-1}T^{-2}} = \frac{\rho U^2}{P} = \frac{1}{Eu}$$
$$\pi_3 = \frac{\upsilon}{L^2T^{-1}} = \frac{\upsilon}{LU} = \frac{1}{Re}, \pi_4 = \frac{g}{LT^{-2}} = \frac{gL}{U^2} = \frac{1}{Fr^2}$$
$$\pi_5 = \frac{U}{LT^{-1}} = \frac{U}{Lf} = \frac{1}{St}, \pi_6 = \frac{c}{LT^{-1}} = \frac{c}{U} = Ma, \pi_7 = \frac{k}{L^{-1}} = He, \pi_8 = \left(\frac{r}{L}\right)\frac{\vec{r}}{r}. \tag{3}$$

The dimensionless relationship of the sound power spectral density obtained from the Buckingham Pi theorem is as follows:

$$\frac{\langle p_e^2(\vec{r}, f)\rangle}{(\rho U^2/2)^2(L/U)} = \Phi\left(\left(\frac{r}{L}\right)\frac{\vec{r}}{r}, Eu, Fr, Re, St, Ma, He\right), \tag{4}$$

where Φ represents a functional relationship; *Eu* (Euler number), *Fr* (Froude number), *Re* (Reynolds number), *St* (Strouhal number), *Ma* (Mach number), and *He* (Helmholtz number) are similarity criterion numbers.

3.2 Similarity law of the submarine

Converting Eq. 4 into sound power spectral in the bandwidth Δf can be expressed as follows:

$$\langle p_e^2(\vec{r}, f)\rangle\Delta f = \left(\frac{\rho U^2}{2}\right)^2\frac{L}{U}\Delta f\cdot\Phi\left(\left(\frac{r}{L}\right)\frac{\vec{r}}{r}, Eu, Fr, Re, St, Ma, He\right). \tag{5}$$

From Eq. 5, it can be analyzed that the full similarity condition is that all similarity criteria numbers are equal. However, it is almost impossible to satisfy in practice. It is necessary to analyze the similarity conditions and ignore the similarity criterion numbers which have less impact on flow-induced noise. According to the physical meaning of each similarity criterion number, a series of assumptions are made to simplify Eq. 5, as shown in the following section. Assumption (c) and (d) will be further discussed in the next chapter.

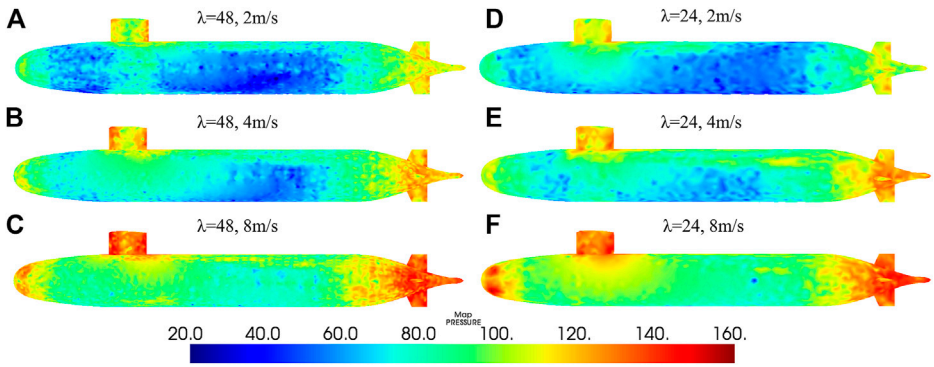

FIGURE 7
SPL of SUBOFF surface with St = 43.56. **(A–C)** is the scale ratio of 1:48 and the speed of 2, 4, and 8 m/s, respectively. **(D–F)** is the scale ratio of 1: 24 and the speed of 2, 4, and 8 m/s respectively.

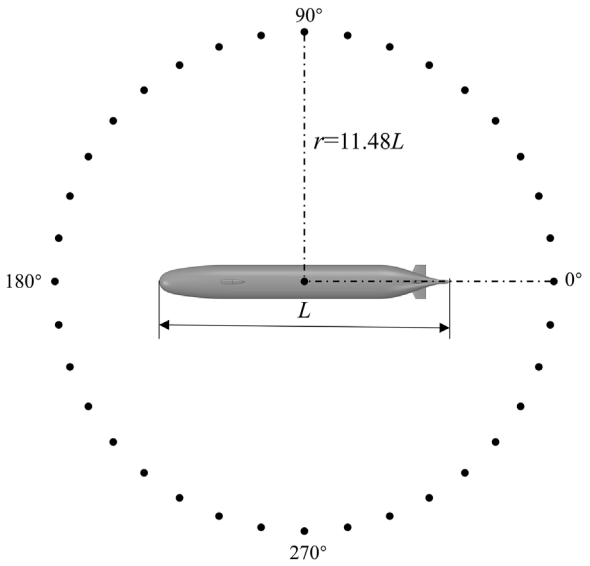

FIGURE 8
Schematic diagram of measuring point location.

(1) Flow-induced noise of the SUBOFF has a non-cavitating phenomenon at low Mach number, and the influence of Euler number can be ignored.
(2) SUBOFF sailing in deep water is far away from the free surface without wave resistance, and the influence of Froude number can be ignored.
(3) There exists a critical Reynolds number, and the influence of Reynolds number for can be ignored when the Reynolds number is greater than the critical Reynolds number.
(4) For the flow-induced noise generated when the fluid flows through the rotating body, and the Strouhal number is related to the Reynolds number under the condition of a high Reynolds number.
(5) Flow-induced noise of the SUBOFF in the low-frequency range is mainly generated by vortex shedding, and the influence of Helmholtz number can be ignored.

Moreover, sound pressure in the free field is inversely proportional to the distance. The simplified similarity relationship is as follows, which ensures the Strouhal number and the Mach number of the model and prototype are equal.

$$\langle p_e^2(\vec{r}, f)\rangle \Delta f = \left(\frac{1}{2}\rho U^2\right)^2 \left(\frac{L}{r}\right)^2 \Delta St \cdot \Phi\left(\frac{\vec{r}}{r}, Ma\right), \tag{6}$$

where ΔSt represents the dimensionless bandwidth, $\Delta St = \Delta f \times L/U$.

Curle [31] equated the sound source of flow-induced noise with monopole source, dipole source, and quadrupole source. This study assumes that the SUBOFF is a rigid body, so the monopole source noise can be ignored. In addition, the Mach number of all the models to be discussed is within a low Mach number range, so the radiated noise of quadrupole source can be ignored. In the scope of this research, it is considered that the sound source of the SUBOFF's flow-induced noise is the dipole type.

Under far-field conditions ($k_0 r \gg 1$), the relationship between sound intensity and variables in the dipole source is shown as follows [31]:

$$I_D \sim \rho_0 \frac{U^6}{c^3} \left(\frac{L}{r}\right)^2 \cos^2\theta, \tag{7}$$

where I_D is the sound intensity of dipole source and θ is the angle.

Equation 8 shows that the sound intensity of flow-induced noise is proportional to the sixth power of inflow velocity, and the radiated sound intensity has the directivity of $\cos^2\theta$. Owing to the SUBOFF's flow-induced noise that is generated by the enclosure and the rudder, this paper considers that SUBOFF is approximately satisfied with the compact sound source in the lower frequency range. Combining with Eq. 8, the relationship of the sound power spectral in the dimensionless bandwidth ΔSt is obtained as follows:

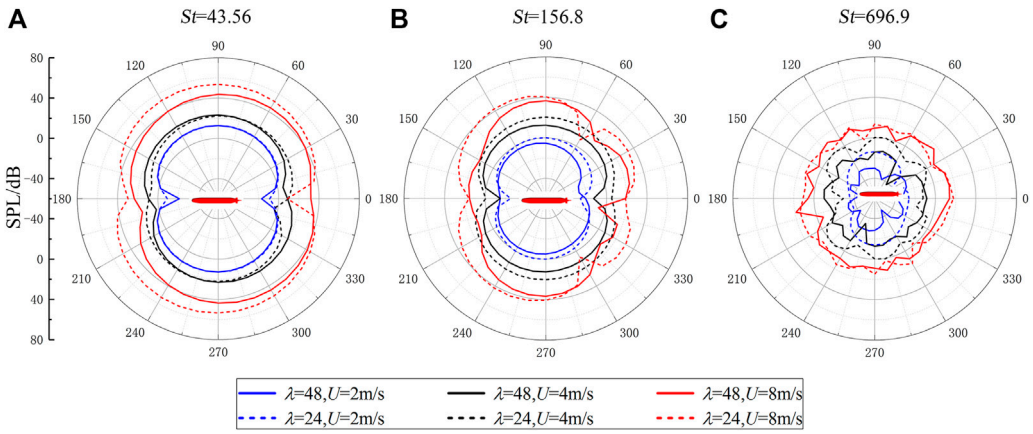

FIGURE 9
Acoustic directivity of Z = 0 plane at **(A)** St = 43.56, **(B)** St = 156.8, and **(C)** St = 696.9 in the range of St = 10–1089.

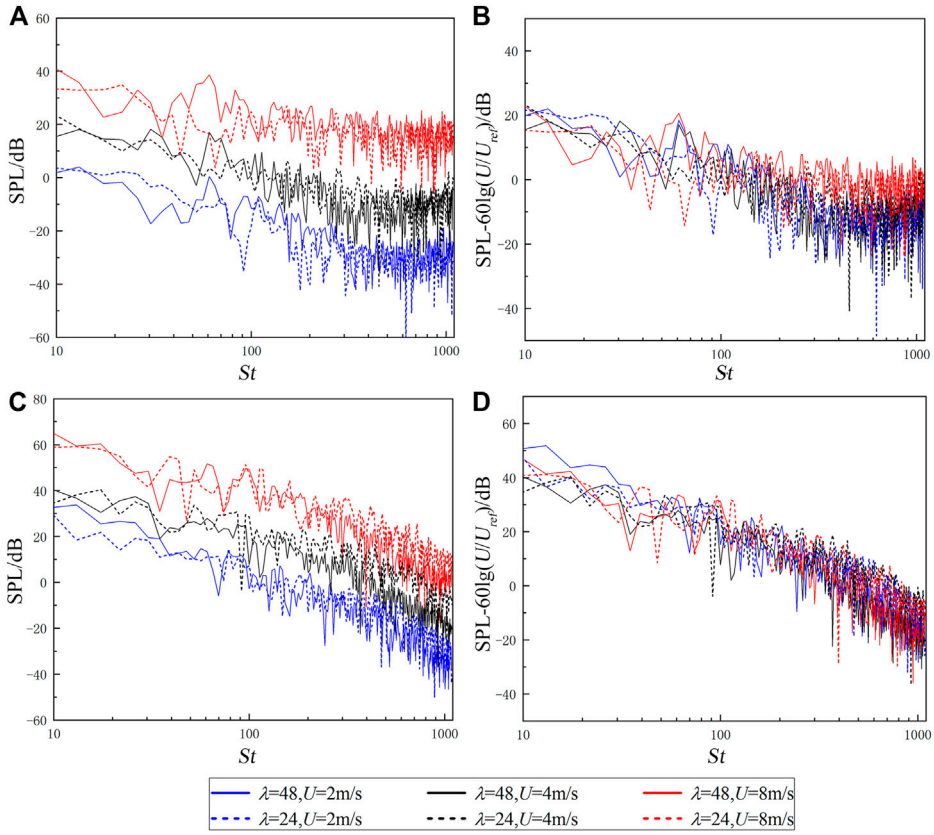

FIGURE 10
SPL spectrums of Z = 0 plane under different conditions. **(A,B)** Calculated results and normalized results of the 0° measuring point. **(C,D)** Calculated results and normalized results of the 90° measuring point.

$$\langle p_e^2(\vec{r}, f)\rangle_D \Delta f = \langle p_e^2(\vec{r}, St)\rangle_D \Delta St = \left(\frac{1}{2}\rho U^2\right)^2 \left(\frac{L}{r}\right)^2 \left(\frac{U}{c}\right)^2 \Delta St \cdot \cos^2\theta, \quad (8)$$

where $\langle p_e^2(\vec{r}, f)\rangle_D$ represents the sound power spectral density of the dipole source.

4 Verification of the similarity law

4.1 Calculational parameters

Under the same medium condition, the calculational parameters are designed as shown in Table 2 to verify the similarity of the speed

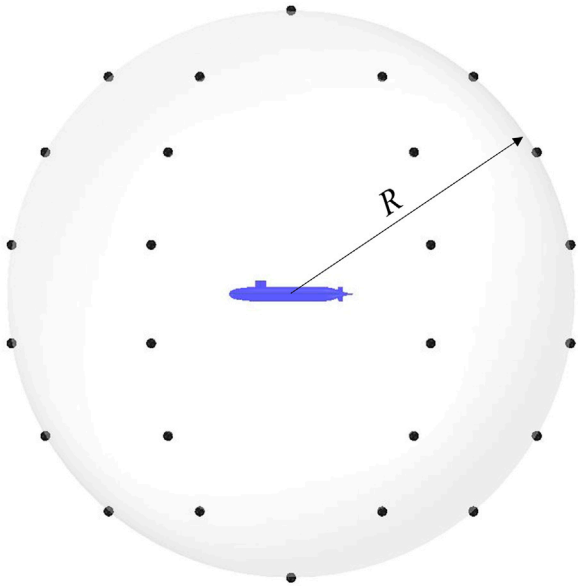

FIGURE 11
Measuring point location of radiated sound power under ISO3744.

and scale. There are six groups of calculational conditions, including the scale ratio of 1:24 and 1:48 and the speed of 2, 4, and 8 m/s, respectively. To facilitate the analysis, the calculated models are numbered from 1–6. Fluid material of all calculated models are water, where $\rho = 998.2\text{kg}/m^3$ and $c = 1500$ m/s. In order to ensure that the frequency range and frequency resolution are consistent after spectrum normalization, time step Δt and step number n need to be controlled before calculation. The calculated dimensionless frequency range St = 10–1089 and the dimensionless bandwidth $\Delta St = 4.356$.

4.2 Discussion of the similarity conditions

Similarity conditions of the submarine's flow-induced noise are simplified in Section 3.2, and part of them are discussed in this section. The assumption (a) and (b) in Section 3.2 are satisfied within the scope of this study and do not need verification; the assumption (e) can be reflected in the normalized spectrum of the subsequent section, where it only discusses the assumption (c) and (d). Evidently, the common premise of the two assumptions is whether the similarity conditions are met when the Reynolds number is greater than the critical Reynolds number.

The Reynolds number represents the ratio of inertial force to viscous force; the higher it is, the less influence of viscous force is. Therefore, this section first judges the Reynolds similarity from the viscosity force of models under different cases, Section 4.3 will further explain that Reynolds number meets similar conditions from the acoustic spectrum results. The resistance coefficients of each model in Table 2 were calculated based on the SST $k-\omega$ turbulence model of steady state, as shown in Figure 6. The results show that all resistance coefficients change slightly, which indicates that Reynolds number has little influence on viscous force.

Ahlborn et al. [32] obtained the relationship between the Strouhal number and the drag coefficient of the cylinder with a high Reynolds number; the equation is given as follows:

$$St_{\infty}^{\triangle} \approx \frac{1}{2^{3/4}\pi}\sqrt{C_{d,\infty}+1}, \tag{9}$$

where $St_{\infty}^{\triangle}$ represents the universal Strouhal number at a high Reynolds number and $C_{d,\infty}$ represents the drag coefficient at high Reynolds number.

Under different conditions, Figure 7 shows SPL of the SUBOFF surface at the dimensionless frequency of $St = 43.56$. It can be found that flow-induced noise of the SUBOFF is mainly caused by shedding vortex of the enclosure and the tail rudder. Combining the conclusion of Figure 6, it can be found that the Strouhal number in this study is basically equal. In the process of similarity prediction, frequency can be converted by the Strouhal number.

4.3 Verification of the SPL similarity law

In this section, the dimensionless SPL of far-field measuring points under different cases were calculated to verify the similarity relationship of submarine's flow-induced noise obtained in Chapter 3. Acoustic radiation in the horizontal direction is more important when the submarine is sailing underwater. The schematic diagram of the measuring point position in the Z = 0 plane is shown in Figure 8. Taking the coordinate (0.5 L, 0, 0) as the center of the circle, the radius $r = 11.48\ L$, and the positive direction of the X axis is regarded as the starting angle. SPL results of different measuring points in Figure 8 were calculated based on the numerical method introduced in Chapter 2, where the computing formula of SPL at dimensionless frequency is given as follows:

$$\text{SPL}(\vec{r}, f_n)\big|_{\Delta f} = \text{SPL}(\vec{r}, St_n)\big|_{\Delta St} = 10\lg\left(\frac{p_e^2(\vec{r}, St_n)}{p_{ref}^2}\right), \tag{10}$$

where $\vec{r}$ shows the point position, f_n is the center frequency, St_n is the center dimensionless frequency, Δf represents the bandwidth, p_e is the effective value of sound pressure, and p_{ref} is the reference value of sound pressure, which is 1×10^{-6} Pa in water.

Before the verification of the SPL similarity law, this paper made acoustic directivity of Z = 0 plane at three different dimensionless frequencies so as to analyze the radiation type of sound source in the frequency band St = 10–1089 and provide guidance for the subsequent verification of the similarity law. The SPL directivity results of $St = 43.56$, 156.8, and 696.9 are established in Figure 9, and the following analysis can be obtained. First, at the lower frequency $St = 43.56$, it has notable radiation characteristics of dipole "8." The radiated direction is perpendicular to the inflow direction, and SPL in the direction of incoming flow and wake is lower than that on both sides of the SUBOFF. At higher frequency St = 156.8 and St = 696.9, especially the latter, the dipole radiation characteristics become less evident with the increase of frequency. The possible reasons are the increase in the proportion of quadrupole source at high frequencies or the gradual change of sound source from compact to non-compact. Second, under the same dimensionless frequencies, the directivity at the same speed is in good agreement, and all acoustic directivity shapes are similar with different speed

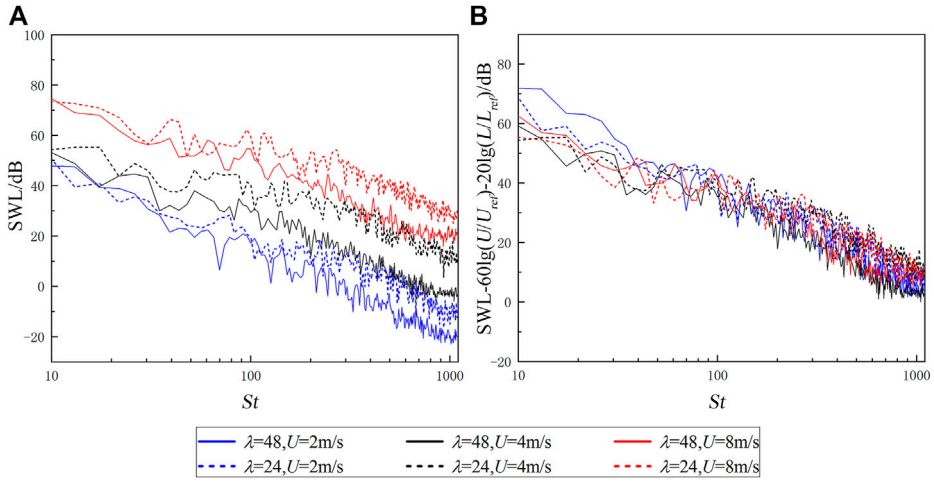

FIGURE 12
Radiated SWL of **(A)** calculated results and **(B)** normalized results under different conditions.

TABLE 3 Calculation parameters of different scales.

Parameter	Model1	Model2	Model3	Prototype
λ	48	24	12	8
φ	6	3	1.5	1
L/m	2.178	4.356	8.712	13.068
U/ms^{-1}	4	4	4	4
f_{max}/Hz	2000	1000	500	334
Δf	8	4	2	1.33

condition. This shows that SPL of the SUBOFF has a certain linear relationship with the speed, and the relationship is easier to find in the lower frequency range.

Then, the spectrum results of a single measuring point at different speeds were analyzed. Assuming that there is a reference model whose condition L_{ref} = 4.356 m and speed U_{ref} = 4 m/s. Combined with Eqs 8, 10, under the same medium and dimensionless frequency, the normalized formula of SPL at similar measuring points can be written as follows:

$$\mathrm{SPL}_{ref}(St) = \mathrm{SPL}(St) - 60\lg\left(\frac{U}{U_{ref}}\right), \tag{11}$$

where SPL_{ref} represents the reference of the sound pressure level; U and U_{ref} is the speed of calculated models and reference model, respectively.

SPL spectrums of 0° and 90° measuring points in the $Z = 0$ plane are shown in Figure 10, which includes the direct calculation results and its normalization results of SPL at dimensionless frequency. From the calculation results, as shown in Figures 10A, C, SPL spectrum curves with the same speed but different scales coincide well, and all of them have the same trend but merely different values, this indicates that the spectrum has the same conclusion as the directivity. Figures 10B, D are the normalized spectrum result, according to Eq. 11. At the 0° measuring point, OSPL of cases 1–6 are, respectively, 34.6, 32.8, 35.3, 34.2, 31.9, and 31.7 dB, and the error value with the reference model (case 5) is within 3.4 dB. At the 90° measuring point, OSPL of cases 1–6 are, respectively, 60.2, 50.6, 54.6, 54.2, 52.3, and 53.7 dB, and the error value with the reference model is within 7.9 dB. The results show that SPL of the SUBOFF's flow-induced noise conforms to the similarity law under the dipole source. However, we concurrently note that the error of the normalized results is different at different directions and frequencies, this paper will analyze the scale error of the SUBOFF model in Chapter 4.

4.4 Verification of the SWL similarity law

Section 4.3 only reflects that the sound power in a certain direction meets the established SPL similarity law; this section further verifies the SUBOFF's SWL similarity law to reflect the total radiation characteristics in different frequency. As shown in Figure 11, the layout of SWL measuring points is ISO3744, the central coordinate is (0.5 L, 0, 0), and the radius R = 2.75 L. The formula of SWL at dimensionless frequency is shown as follows:

$$\mathrm{SWL}(\vec{r}, St_n)|_{\Delta St} = 10\lg\left(\frac{P}{P_{ref}}\right), P = \frac{4\pi R^2 \cdot \frac{1}{N}\sum_{i=1}^{N}\left[p_e^2(\vec{r}, St_n)\right]}{\rho_0 c_0}, \tag{12}$$

where P shows the mean sound power; P_{ref} is the reference of sound power; which is 10^{-12} W in water; R is the radio of the measuring points; N is the number of measuring points; and p_e^i is the effective sound pressure of measuring points.

Combined with Eqs 8, 12, under the same medium and dimensionless frequency, the normalized formula of SWL at similar measuring points can be written as follows:

$$\mathrm{SWL}_{ref}(St) = \mathrm{SWL}(St) - 60\lg\left(\frac{U_P}{U_{ref}}\right) - 20\lg\left(\frac{L_P}{L_{ref}}\right), \tag{13}$$

where SWL_{ref} represents the reference value of the sound power level.

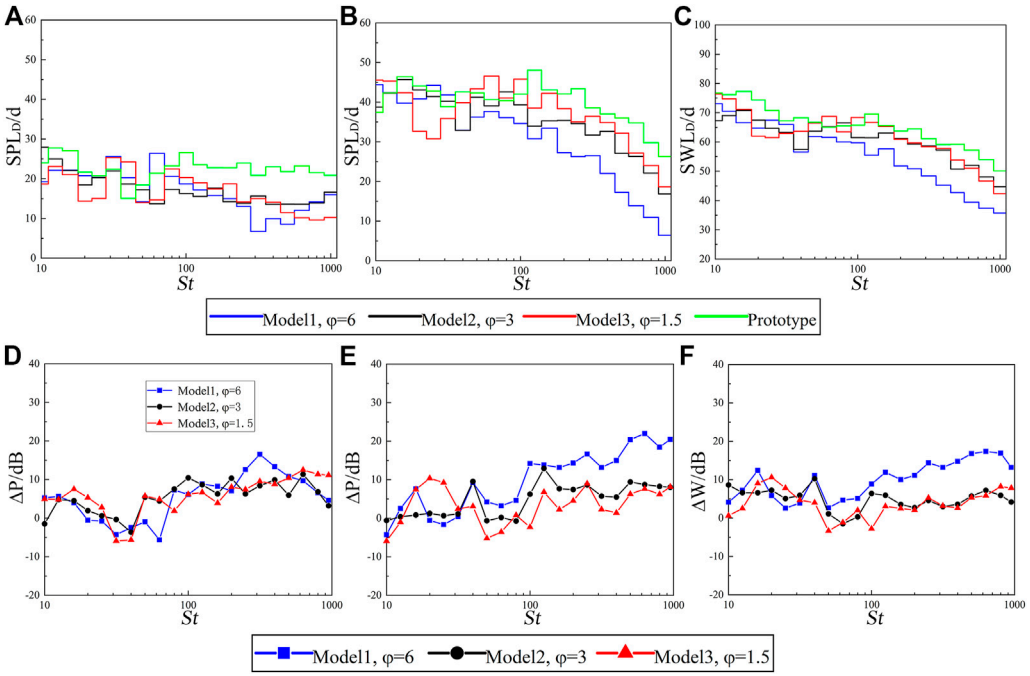

FIGURE 13
Extrapolated results and error value between scale models and hypothetical prototype. **(A,D)** SPL of the 0° mearing point. **(B,E)** SPL of the 90° mearing point. **(C,F)** SWL of the ISO3744 mearing point.

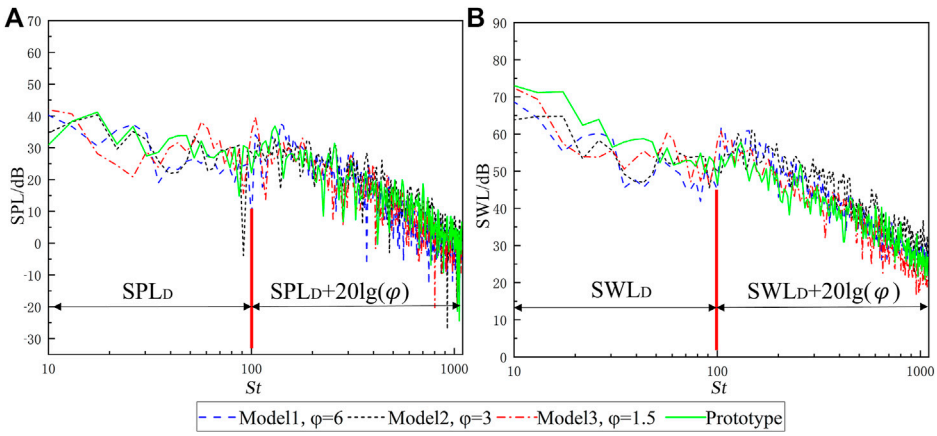

FIGURE 14
Comparison between extrapolated results which added the modified value and hypothetical prototype. **(A)** SPL of the 90° mearing point. **(B)** SWL of the ISO3744 mearing point.

The simulation results and normalization results of SWL are, respectively, shown in Figures 12A, B. The latter shows that SWL spectrum curves under different cases are in good agreement, meeting the SWL similarity law under dipole source. In addition, SWL spectrum curves at the same scale but different speeds are relatively consistent, while at different scales are slightly worse especially $St \geq 100$. In this paper, this frequency is called the cut-off frequency of the similarity law. Above the cut-off frequency, the error is evidently caused by scale effect, which will be analyzed in the next chapter.

5 Scale effect analysis

The similarity analysis in Chapter 4 verifies that the SUBOFF satisfies the similarity law of dipole source in the low-frequency

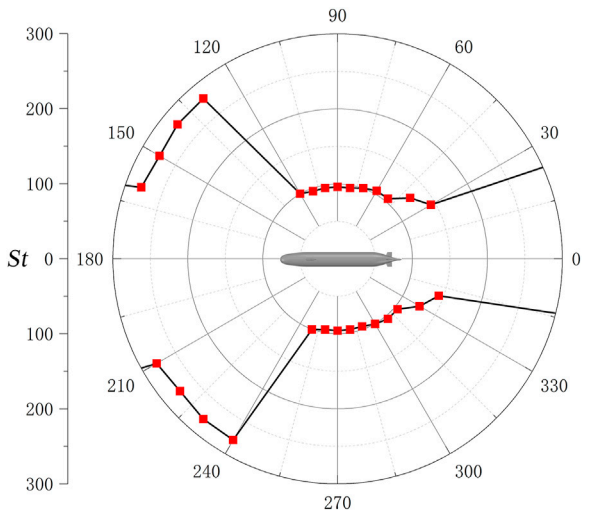

FIGURE 15
Cut-off frequencies of the Z = 0 plane in different directions.

range, that is, the SPL similarity law of Eq. 11 and the SWL similarity law of Eq. 13. This chapter analyzes the scale effect generated by the prediction of the SUBOFF prototype based on the similarity law. All models and prototype have the same speed, which can ensure that the Strouhal number and the Helmholtz number meet similar conditions at the same time. Converting Eqs 11, 13 into the following formulas

$$\mathrm{SPL}_p(St) = \mathrm{SPL}_m(St) + \Delta P = \mathrm{SPL}_\mathrm{D}(St) + \Delta P$$
$$\mathrm{SWL}_p(St) = \mathrm{SWL}_m(St) + 20\lg\left(\frac{L_p}{L_m}\right) + \Delta W = \mathrm{SWL}_\mathrm{D}(St) + \Delta W, \quad (14)$$

where SPL_D and SWL_D, respectively, represent the sound pressure level and the sound power level extrapolated from model to prototype according to the similarity law of dipole source; ΔP is the SPL error; ΔW is the SWL error; and p and m represent prototype and model, respectively.

Due to the lack of experimental data, a SUBOFF model with the scale radio of 1:8 is taken as a hypothetical prototype, and its calculation results are regarded as the actual results of the prototype. φ ($\varphi = L_P/L_m$) is the scale ratio between the scale model and the hypothetical prototype, and the related parameters are shown in Table 3.

The scale effect is discussed under the SPL similarity law of 0° and 90° measuring points in the Z = 0 plane and the SWL similarity law of ISO3744 measuring points. In order to reduce the numerical error of a single frequency, the simulation results are converted to 1/3 octave results, as show in Figures 13A–C. Then, calculating the error value in each frequency band, respectively, the error results are shown in Figures 13D–F. The error curves of the 0° measuring points between models and hypothetical prototype are in good agreement, which indicates that the extrapolated results parallel to the inflow direction are less affected by the scale effect within St = 10–1089. At the 90° measuring point, the scale effect increases with the increase of scale radio φ when $St > 100$. The possible reason is that the radiated sound is mainly caused by the enclosure and tail rudder, which has different sizes in the 0° and 90° directions, so the sound propagation in the 90° direction is more affected due to SUBOFF scattering. Thus, compared with SPL spectrums of the measuring points in the direction of 90° and 0°, the frequency range of the former meeting the established similarity law is smaller. Owing to the radiated sound energy is mainly perpendicular to the inflow direction, and the scale effect of sound power is similar as the sound pressure at the 90° measuring point.

From the results of $St > 100$ in 1/3 octave, it can be clearly seen that SPL of the 90° mearing point and SWL of ISO3744 mearing points have similar trend. Comparing the data in the dimensionless frequency range, the error value is about $20\lg(\varphi)$, it shows that the ratio of the real value of the sound pressure at the prototype measuring point to the predicted value is φ. The corrected spectrums are shown in Figure 14 after adding the modified value.

In the $Z = 0$ plane, the SPL spectrum of all measuring points is analyzed similar to that in Figure 13 to obtain the dimensionless cut-off frequencies in different directions, as shown in Figure 15. On both sides of the SUBOFF, the dimensionless cut-off frequencies are about St = 100. In the head and tail directions, due to the SPL spectrum having better coincidence within St = 10–1089, the cut-off frequencies near these directions are greater than the highest dimensionless frequency within the scope of this study. This shows that in the similarity prediction based on the dipole source, the SPL spectrum in different directions has different dimensionless cut-off frequencies. The cut-off frequencies in the figure are obtained by observing the normalized spectrum, and there is no specific calculation method and accurate value, which is only for readers' reference. The evaluation method and accurate value of cut-off frequency need further study.

6 Conclusion

In this study, the LES/Lighthill hybrid method was used to verify the similarity conditions and similarity laws of the SUBOFF's flow-induced noise within the test speed range, and the scale effect under the similarity law was analyzed. The frequency range of analysis is St = 10–1089, and the maximum scale ratio is 1:6; certain conclusions are described as follows:

(1) With the dimensionless frequency in the range of St = 10–1089, SPL directivity in the Z = 0 plane conform to the dipole characteristics, and the major radiation direction is perpendicular to the inflow direction.
(2) When the Reynolds number is greater than the critical Reynolds number, the submarine's flow-induced noise meets the similarity condition, and the frequencies are normalized according to the Strouhal number. At the same dimensionless measuring point distance, SPL is proportional to the sixth power of the speed, and SWL is proportional to the sixth power of the speed and second power of the scale.
(3) The established similarity law is affected by the scale. At the same scale, the predicted SPL and SWL spectral curves with different inflow speeds are generally in good agreement. Under different scales but the same speed, there exists a dimensionless cut-off frequency St = 100, below which the SWL spectrums predicted are

in good agreement; otherwise, the scale error is about 20 lg (φ) when the dimensionless frequency is greater than it.

(4) The cut-off frequency of SPL similarity law is related to the angle of the measuring points, which, perpendicular to the incoming flow direction, is St = 100 (the same as the cut-off frequency of the SWL similarity law), but the cut-off frequency parallel to the incoming direction is greater than St = 100.

Data availability statement

The original contributions presented in the study are included in the article/Supplementary Material; further inquiries can be directed to the corresponding author.

Author contributions

YQ: writing (original draft), methodology, theoretical model analysis, and data. Y-OZ and TZ: idea, conceptualization, writing and reviewing of the manuscript, structural scheme design, theoretical model analysis, supervision, and funding. Y-FL: investigation and review of the manuscript. All authors contributed to the article and approved the submitted version.

Funding

This study is supported by the Innovative Research Foundation of Ship General Performance of China (No. 33122233) and the Open Fund of Science and Technology on Thermal Energy and Power Laboratory (No. TPL2021B03).

Conflict of interest

The authors declare that the research was conducted in the absence of any commercial or financial relationships that could be construed as a potential conflict of interest.

Publisher's note

All claims expressed in this article are solely those of the authors and do not necessarily represent those of their affiliated organizations, or those of the publisher, the editors, and the reviewers. Any product that may be evaluated in this article, or claim that may be made by its manufacturer, is not guaranteed or endorsed by the publisher.

References

1. Yao H, Zhang H, Liu H, Jiang W. Numerical study of flow-excited noise of a submarine with full appendages considering fluid structure interaction using the boundary element method. *Eng Anal Bound Elem* (2017) 77:1–9. doi:10.1016/j.enganabound.2016.12.012

2. Liu Z. X., Song Y., Yang Q. X., Liu Y., et al. Research on foreign free manoeuvring submarine models experiment. *Ship Sci Tech* (2017) 39(17):194–9. (In Chinese). doi:10.3404/j.issn.1672-7649.2017.09.039

3. Jiang PF, Lin JH, Sun JP, Yi X, Shan Y. Source spectrum model for merchant ship radiated noise in the Yellow Sea of China. *Ocean Eng* (2020) 216:107607. doi:10.1016/j.oceaneng.2020.107607

4. Merino Martinez R, Neri E, Snellen M, Kennedy J, Simons D, Bennett GJ. Comparing flyover noise measurements to full-scale nose landing gear wind tunnel experiments for regional aircraft. *AIAA J* (2017) 2017–3006. doi:10.2514/6.2017-3006

5. Breeding J. E., Pflug L. A., Bradley M., Walrod M. H. (1996) *Research ambient noise DIrectionality (RANDI) 3.1 Physics description*. Naval Research Lab Stennis Space Center MS. Available at: https://apps.dtic.mil/sti/pdfs/ADA316034.pdf.

6. Bark G. Prediction of propeller cavitation noise from model tests and its comparison with full scale data. *J Fluids Eng* (1985) 107(1):112–9. doi:10.1115/1.3242424

7. Lee S. B., Kim K. Y., Kim J. Y., Yang G. C. A study on the effects of non-uniform inlet flows upon performance and tonal radiation from a propeller fan. In: Proceedings of ASME Fluid Engineering Division Summer Meeting (1998). p. 3245–3253. Available at: https://www.researchgate.net/publication/283010594_A_Study_on_the_Effects_of_Non_Uniform_Inlet_Flows_upon_Performance_and_Tonal_Radiation_from_A_Propeller_Fan.

8. Tani G, Viviani M, Hallander J, Johansson T, Rizzuto E. Propeller underwater radiated noise: A comparison between model scale measurements in two different facilities and full scale measurements. *Appl Ocean Res* (2016) 56:48–66. doi:10.1016/j.apor.2016.01.007

9. Park J, Seong W. Novel scaling law for estimating propeller tip vortex cavitation noise from model experiment. *J Hydrodyn* (2017) 29:962–71. doi:10.1016/S1001-6058(16)60810-7

10. Arakeri VH, Satyanarayana SG, Mani K, Sharma S. Studies on scaling of flow noise received at the stagnation point of an axisymmetric body. *J Sound Vibr* (1991) 146(3):449–62. doi:10.1016/0022-460X(91)90701-K

11. Xing Y., Liu P. Q., Guo H., Xu L., Li L. Similarity rule and Mach number scaling law for simplified landing gear noise. *Hangkong Xuebao* (2017) 38(06):72–9. (In Chinese) doi:10.7527/S1000-6893.2016.0290

12. Kaltenbacher M, Escobar M, Becker S, Ali I. Numerical simulation of flow-induced noise using LES/SAS and Lighthill's acoustic analogy. *Int J Numer Methods Fluids* (2010) 63(9):1103–22. doi:10.1002/fld.2123

13. Han T, Wang L, Cen K, Song B, Shen R, Liu H, et al. Flow-induced noise analysis for natural gas manifolds using LES and FW-H hybrid method. *Appl Acoust* (2020) 159:107101. doi:10.1016/j.apacoust.2019.107101

14. Yang QF, Wang YS, Zhang MM. Scale effects on non-cavitation hydrodynamics and noise of highly-skewed propeller in wake flow. *J Southeast Univ* (2013) 29(2):162–9. doi:10.3969/j.issn.1003-7985.2013.02.010

15. Bosschers J. A semi-empirical prediction method for broadband hull-pressure fluctuations and underwater radiated noise by propeller tip vortex cavitation. *J Mar Sci Eng* (2018) 6(2):49. doi:10.3390/jmse6020049

16. Li D. Y., Fang B., Li Y. M., Guan H. R., et al. Study on the similarity of characteristic frequency of flow around cylinder. *Ship Electron Eng* (2022) 42(03):197–202. (In Chinese) doi:10.3969/j.issn.1672-9730.2022.03.043

17. Bhushan S, Alam MF, Walters DK. Evaluation of hybrid RANS/LES models for prediction of flow around surface combatant and Suboff geometries. *Comput Fluids* (2013) 88:834–49. doi:10.1016/j.compfluid.2013.07.020

18. Paredes RJ, Quintuña MT, Arias-Hidalgo M, Datla R. Numerical flow characteriza-tion around a type 209 submarine using OpenFOAM. *Fluids* (2021) 6(2):66. doi:10.3390/fluids6020066

19. Wang XH, Huang Q, Pan G. Numerical research on the influence of sail leading edge shapes on the hydrodynamic noise of a submarine. *Appl Ocean Res* (2021) 117:102935. doi:10.1016/j.apor.2021.102935

20. Jie P, Chen N, Qu JC, Liu Y, Shang D. The suppression of hydrodynamic noise from underwater sonar domes by flow control. *MATEC Web Conf* (2019) 283:08008. doi:10.1051/matecconf/201928308008

21. Sezen S, Delen C, Dogrul A, Atlar M. An investigation of scale effects on the self-propulsion characteristics of a submarine. *Appl Ocean Res* (2021) 113:102728. doi:10.1016/j.apor.2021.102728

22. Howard CQ. Recent developments in submarine vibration isolation and noise control. In: Proceedings of the 1st Submarine Science Technology and Engineering Conference (2011). p. 1–7.

23. Liu ZH, Xiong Y, Tu CX. Method to control unsteady force of submarine propeller based on the control of horseshoe vortex. *J Ship Res* (2012) 56(01):12–22. doi:10.5957/jsr.2012.56.1.12

24. Zhang YO, Zhang T, Li TY. Flow-induced noise simulation based on LES/Lighthill hybrid method. *ICMECS* (2014) 614:428–31. doi:10.4028/www.scientific.net/amm.614.428

25. Zhang YO, Zhang T, Ouyang H, Li T. Flow-induced noise analysis for 3D trash rack based on LES/Lighthill hybrid method. *Appl Acoust* (2014) 79:141–52. doi:10.1016/j.apacoust.2013.12.016

26. Oberai AA, Roknaldin F, Hughes TJR. Computational procedures for determining structural-acoustic response due to hydrodynamic sources. *Comput Meth Appl Mech Eng* (2000) 190(3-4):345–61. doi:10.1016/S0045-7825(00)00206-1

27. Liu HL, Huang T. *Summary of DARPA SUBOFF experimental program data*. Report No CRDKNSWC/HD-1298-11 (1998). doi:10.21236/ada359226

28. Lu YT, Zhang HX, Pan XJ. Numerical simulation of flow-field and flow-noise of a fully appended submarine. *J Vibration Shock* (2008) 09:142–6+189. doi:10.13465/j.cnki.jvs.2008.09.009

29. Wang XH, Hang QG, Pan G. Numerical research on influence of fairwater shape on flow-induced noise of submarine. *SHIPBUILDING OF CHINA* (2020) 61(S2):262–72. doi:10.3969/j.issn.1000-4882.2020.z2.029

30. Jiang WC, Zhang HX, Meng KY. Research on the flow noise of underwater submarine based on boundary element method. *Chin J Hydrodynamics* (2013) 28(04):453–9. doi:10.3969/j.issn1000-4874.2013.04.011

31. Curle N. The influence of solid boundaries upon aerodynamic sound. *Proc R Soc Lond Ser A* (1955) 231(1187):505–14. doi:10.1098/rspa.1955.0191

32. Ahlborn B, Seto ML, Noack B. On drag, Strouhal number and vortex-street structure. *Fluid Dyn Res* (2002) 30(6):379–99. doi:10.1016/s0169-5983(02)00062-x

frontiers | Frontiers in Physics

TYPE Original Research
PUBLISHED 21 April 2023
DOI 10.3389/fphy.2023.1182532

OPEN ACCESS

EDITED BY
Zhixiong Gong,
Shanghai Jiao Tong University, China

REVIEWED BY
Junjun Lei,
Guangdong University of Technology, China
Glauber T. Silva,
Federal University of Alagoas, Brazil
Philippe Brunet,
UMR7057 Laboratoire Matière et Systèmes Complexes (MSC), France

*CORRESPONDENCE
Alen Pavlic,
apavlic@ethz.ch

†These authors have contributed equally to this work

RECEIVED 08 March 2023
ACCEPTED 03 April 2023
PUBLISHED 21 April 2023

CITATION
Pavlic A, Roth L, Harshbarger CL and Dual J (2023), Efficient modeling of sharp-edge acoustofluidics.
Front. Phys. 11:1182532.
doi: 10.3389/fphy.2023.1182532

Efficient modeling of sharp-edge acoustofluidics

Alen Pavlic[1*†], Lukas Roth[1†], Cooper Lars Harshbarger[1,2,3] and Jürg Dual[1]

[1]Institute for Mechanical Systems, Swiss Federal Institute of Technology Zurich, Zurich, Switzerland, [2]Department of Orthopedics, Balgrist University Hospital Zurich, University of Zurich, Zurich, Switzerland, [3]Institute for Biomechanics, Swiss Federal Institute of Technology Zurich, Zurich, Switzerland

Sharp-edge structures exposed to acoustic fields are known to produce a strong non-linear response, mainly in the form of acoustic streaming and acoustic radiation force. The two phenomena are useful for various processes at the microscale, such as fluid mixing, pumping, or trapping of microparticles and biological cells. Numerical simulations are essential in order to improve the performance of sharp-edge-based devices. However, simulation of sharp-edge structures in the scope of whole acoustofluidic devices is challenging due to the thin viscous boundary layer that needs to be resolved. Existing efficient modeling techniques that substitute the need for discretization of the thin viscous boundary layer through analytically derived limiting velocity fail due to large curvatures of sharp edges. Here, we combine the Fully Viscous modeling approach that accurately resolves the viscous boundary layer near sharp edges with an existing efficient modeling method in the rest of a device. We validate our Hybrid method on several 2D configurations, revealing its potential to significantly reduce the required degrees of freedom compared to using the Fully Viscous approach for the whole system, while retaining the relevant physics. Furthermore, we demonstrate the ability of the presented modeling approach to model high-frequency 3D acoustofluidic devices featuring sharp edges, which will hopefully facilitate a new generation of sharp-edge-based acoustofluidic devices.

KEYWORDS

acoustofluidics, microfluidics, acoustic streaming, acoustic sharp edges, finite-element method (FEM), numerical simulation

1 Introduction

Acoustofluidic devices commonly exploit two phenomena, namely, acoustic streaming (AS) and acoustic radiation force (ARF), for an increasing variety of tasks due to their ability to precisely manipulate fluids and objects on the microscale and in a contactless manner [1]. A particular type of acoustofluidic device features sharp-edge structures inside an acoustically excited device. In such a configuration, sharp edges produce a strong response in the form of AS [2–5] and ARF [6, 7], as illustrated in Figure 1. The literature indicates that in most 2D cases, the AS around a single sharp edge manifests itself in the form of two counter rotating vortices, one on each side of the tip of the sharp edge, with the flow above the apex directed away from the edge tip [4]. As for the ARF, it has been shown that "heavy" microparticles get attracted to the excited sharp edge, whereas "light" particles get repelled from the edge [7].

Acoustically excited sharp edges can be used for micropumping [8, 9], trapping of biological cells [6, 10, 11], and powerful mixing [12–14]. Numerical models capable of predicting the behavior inside such devices and, thus, their performance are a valuable tool

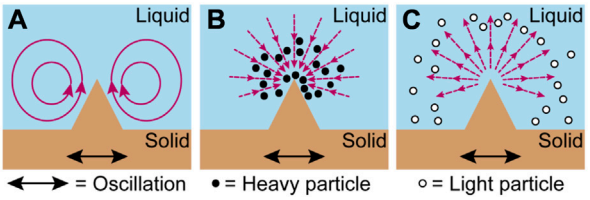

FIGURE 1
Illustration of the main phenomena driven by the oscillations of a sharp edge relative to the surrounding fluid: **(A)** the sharp-edge-driven acoustic streaming [4], **(B)** the attraction of "heavy" particles to the tip of the sharp edge due to the ARF [7], and **(C)** the ARF-based repulsion of "light" particles by the sharp edge [7].

for design optimization. Especially, since the production of most acoustofluidic devices requires a cleanroom environment, making prototyping laborious and expensive. Furthermore, numerical simulations can give deeper insight into the underlying physics [2, 4, 5].

The modeling of harmonic acoustic fields at the scale of a typical acoustofluidic device for micromanipulation requires the modeling of one-half to several acoustic wavelengths $\lambda = c_0/f$, with the speed of sound in the fluid c_0 and the driving frequency f. Each wavelength is normally discretized with several tens of elements, making such a device possible to simulate as a whole 3D multiphysics problem. However, when analyzing higher-order steady phenomena in viscous fluids, such as AS, another characteristic length needs to be discretized-the viscous boundary layer thickness $\delta = \sqrt{\eta/(\pi\rho_0 f)}$, with the dynamic fluid viscosity η and the density of the fluid ρ_0. In a typical acoustofluidic device, filled with water and driven at f = 1 MHz, we have $\lambda \approx 1.5$ mm and $\delta = 0.56$ µm. This indicates a large separation of length scales, with the device being $\mathcal{O}(\lambda)$, whereas the discretization at boundaries is required to resolve $\mathcal{O}(\delta)$. Muller et al. [15] introduced a Fully Viscous modeling approach based on the perturbation theory that resolves both λ and δ, requiring significant computational effort and is, thus, in most cases limited to simplified 2D models. Over the years, alternative approaches were developed that analytically solve AS in the viscous boundary layer and use the solution as a boundary condition for the flow in the fluid bulk. This so-called limiting velocity method (LVM) was already used in [16], [17, 18], [19], [20, 21], and others. Recently, [22] and [23] improved the LVM by accounting for the Stokes drift and thermal boundary layer, respectively. The LVM approach has already enabled 3D simulations of AS in a whole acoustofluidic device [19, 21, 24]. There is, however, a general limitation of the LVM, in which the radius of the curvature of boundaries in the system needs to be much larger than δ. This makes LVM as such unusable for the simulation of AS in acoustofluidic devices featuring sharp edges, since the behavior in such devices is greatly influenced by the behavior near the tips of sharp edges [5].

Sharp-edge acoustofluidics has been successfully modeled in several studies using the Fully Viscous approach, but typically in 2D [4, 13, 25, 26] and under further simplifications, such as assuming a periodicity across the device [3], using systems at low frequencies with the acoustic wavelength larger than the system (subwavelength system) [2, 5, 27], or exploiting symmetries [28]. Under these simplified conditions, a few studies featured the direct numerical simulations that revealed the threshold amplitude of the oscillatory excitation velocity at which the perturbation-based computation of the acoustic streaming near a sharp edge fails [2, 5, 29].

Here, we introduce a Hybrid modeling approach that fully resolves the viscous boundary layers in the vicinity of sharp edges, analogous to the approach of [15], while the rest of the acoustofluidic device is modeled using LVM-based approach derived by [22]. First, we validate the Hybrid approach against the Fully Viscous approach on a simple single-sharp-edge geometry, which is used in several previous studies [4, 5, 26]. Second, we apply the Hybrid approach to model a more complex acoustofluidic device that features a pair of sharp edges and is capable of pumping, as introduced recently in [9]. At last, we apply the Hybrid approach to model high-frequency sharp-edge acoustofluidics in 3D. The developed approach, depending on the complexity of the device, significantly decreases the required degrees of freedom (DOF) in the model compared to fully resolving the viscous boundary layer.

2 Methodology

In the current work, we model only the behavior of fluids within microfluidic channels, whereas the solids typically bounding such channels are replaced by suitable boundary conditions.

We assume a viscous fluid, the motion of which can be described by the compressible Navier–Stokes equations

$$\rho\left[\frac{\partial \boldsymbol{v}}{\partial t} + (\boldsymbol{v}\cdot\boldsymbol{\nabla})\boldsymbol{v}\right] = -\boldsymbol{\nabla}p + \eta\nabla^2\boldsymbol{v} + \left(\eta_B + \frac{\eta}{3}\right)\boldsymbol{\nabla}(\boldsymbol{\nabla}\cdot\boldsymbol{v}), \tag{1}$$

and the continuity equation

$$\frac{\partial \rho}{\partial t} = -\boldsymbol{\nabla}\cdot(\rho\boldsymbol{v}), \tag{2}$$

with the velocity $\boldsymbol{v}$, the dynamic viscosity η, and the bulk viscosity η_B. The fluid is assumed to be barotropic, and the density ρ, therefore, depends only on the pressure p, namely,

$$\rho = \rho(p). \tag{3}$$

The equations are linearized using the regular perturbation approach [30]. Accordingly, the physical fields are expanded in a series $\square = \square_0 + \square_1 + \square_2 + \ldots$, where $\square$ represents the field and the subscript denotes the respective order. The amplitude of the first-order velocity v_1 is, therefore, assumed to be small with respect to the speed of sound c_0—small Mach number assumption.

2.1 First-order (acoustic) problem

For a fluid quiescent at the zeroth order ($\boldsymbol{v}_0 = \boldsymbol{0}$), the substitution of the first-order perturbed fields into governing Eqs. 1, 2 yields the set of first-order equations

$$\rho_0\frac{\partial \boldsymbol{v}_1}{\partial t} = -\boldsymbol{\nabla}p_1 + \eta\nabla^2\boldsymbol{v}_1 + \left(\eta_B + \frac{\eta}{3}\right)\boldsymbol{\nabla}(\boldsymbol{\nabla}\cdot\boldsymbol{v}_1), \tag{4}$$

$$\frac{\partial \rho_1}{\partial t} = -\rho_0\boldsymbol{\nabla}\cdot\boldsymbol{v}_1, \tag{5}$$

with the equilibrium density ρ_0. The equation of state, namely Eq. 3, translates to

$$\rho_1 = \frac{1}{c_0^2} p_1 \tag{6}$$

and connects the first-order density with the first-order pressure. The first-order fields are assumed to have a harmonic time dependency through the factor $e^{i\omega t}$, with the angular frequency $\omega = 2\pi f$ and the imaginary unit i.

2.2 Second-order (streaming) problem

Applying the perturbation theory to the governing equations up to second order and taking the time average $\langle \square \rangle = \frac{1}{T}\int_T \square \, dt$ over an oscillation period T lead to the equations of acoustic streaming [31]

$$\boldsymbol{\nabla}\langle p_2 \rangle - \eta \nabla^2 \langle \boldsymbol{v}_2 \rangle = -\rho_0 \boldsymbol{\nabla} \cdot \langle \boldsymbol{v}_1 \boldsymbol{v}_1 \rangle, \tag{7}$$

$$\boldsymbol{\nabla} \cdot \langle \boldsymbol{v}_2 \rangle = 0. \tag{8}$$

The time average of a product of first-order fields $\square_1 = \tilde{\square}_1 e^{i\omega t}$, with the spatially-dependent and time-independent complex amplitude $\tilde{\square}_1$, is computed as $\langle \square_1 \blacksquare_1 \rangle = \frac{1}{2}\mathrm{Re}[\tilde{\square}_1 \tilde{\blacksquare}_1^*]$ with $\square^*$ denoting a complex conjugate of $\square$ [32]. For $\langle \boldsymbol{v}_1 \boldsymbol{v}_1 \rangle$ in Eq. 7, the tensor product is implied. In Eqs 7, 8, the streaming field is considered to be incompressible, which is in line with related studies [33–36].

At the second order, the no-slip boundary condition is imposed on the Lagrangian velocity of the fluid at the fluid boundary. The Lagrangian velocity is defined as the sum of the Eulerian streaming velocity $\langle \boldsymbol{v}_2 \rangle$ and the Stokes drift [37, 38]

$$\boldsymbol{v}_{\mathrm{SD}} = \left\langle \left(\int \boldsymbol{v}_1 dt \cdot \boldsymbol{\nabla} \right) \boldsymbol{v}_1 \right\rangle, \tag{9}$$

leading to the boundary condition on the Eulerian streaming velocity

$$\langle \boldsymbol{v}_2 \rangle = -\boldsymbol{v}_{\mathrm{SD}} \quad \text{at the boundary.} \tag{10}$$

For rigid boundaries that we assume in this work, $\boldsymbol{v}_{\mathrm{SD}}$ reduces to zero.

This theoretical framework is only applicable as long as the perturbation theory is valid and as long as the streaming remains laminar. The validity of the perturbation theory approach in the context of sharp-edge streaming is further discussed in [2], [5].

2.3 Limiting velocity method

To compute the acoustic streaming one needs to solve the first- and the second-order problems outlined in the previous sections. Based on the complexity of the formulation, analytical solutions are rare and rely on basic geometries, simplified boundary conditions, and various assumptions regarding the relevant characteristic lengths, as, for example, performed in [16], [39], [34], [40]. However, under additional assumptions, the so-called limiting velocity method has been developed by [18], [38], [22], wherein the aforementioned equations are solved separately in the vicinity of boundaries, where the viscous boundary layer develops. The main assumption of the LVM is the smallness of the viscous boundary layer thickness δ relative to the acoustic wavelength $\lambda = c_0/f$ and relative to the curvature R of the boundary surface. Additionally, the displacement of a moving boundary surface tangential to the boundary surface needs to be small relative to R, while the displacement normal to the boundary surface needs to be small relative to δ. The derivation of the fields in the boundary layer assumes a solenoidal first-order velocity field, and the resulting (limiting) streaming velocity is then applied to a simplified streaming problem originating from Eqs 7, 8 as a slip velocity at certain small distance from the boundary [18] or at the boundary itself [22], depending on the formulation. It is important to note that the derivations in [22] are developed for $e^{-i\omega t}$ time dependence, whereas the interfaces of the Acoustics Module of COMSOL Multiphysics that we use for implementation assume $e^{i\omega t}$. In the continuation, the formulation from [22] is, therefore, adapted to the COMSOL Multiphysics-compatible $e^{i\omega t}$.

The first-order problem, in the scope of the LVM, is simplified by assuming that the velocity field in the fluid bulk is irrotational, which leads to the Helmholtz equation

$$\nabla^2 p_1 + k_c^2 p_1 = 0, \tag{11}$$

with p_1 as the only unknown variable and with the viscous compressional wavenumber

$$k_c = \left(1 - i\frac{\Gamma}{2}\right)\frac{\omega}{c_0}, \tag{12}$$

with the damping coefficient

$$\Gamma = \left(\eta_B + \frac{4}{3}\eta\right)\frac{\omega}{\rho_0 c_0^2}. \tag{13}$$

The first-order velocity is separated as

$$\boldsymbol{v}_1 = \boldsymbol{v}_1^{\mathrm{b}} + \boldsymbol{v}_1^{\delta}, \tag{14}$$

into a sum of the irrotational ($\nabla \times \square = 0$) long-range velocity in the bulk of the fluid $\boldsymbol{v}_1^{\mathrm{b}}$ and the solenoidal ($\boldsymbol{\nabla} \cdot \square = 0$) short-range velocity in the viscous boundary layer $\boldsymbol{v}_1^{\delta}$. The velocity in the bulk is connected to the pressure through

$$\boldsymbol{v}_1^{\mathrm{b}} = \frac{i - \Gamma}{\omega \rho_0} \boldsymbol{\nabla} p_1. \tag{15}$$

To account for the damping of the viscous boundary layer, the following condition needs to be applied at the boundary:

$$\begin{aligned} \boldsymbol{n} \cdot \boldsymbol{\nabla} p_1 = {} & \frac{\omega \rho_0}{i - \Gamma}\left[\boldsymbol{n} \cdot \boldsymbol{V}_1^0 - \frac{i}{k_s}\boldsymbol{\nabla} \cdot \boldsymbol{V}_1^0\right] \\ & - \frac{i}{k_s}\left[\frac{\omega^2}{c_0^2(1 + i\Gamma)} p_1 + (\boldsymbol{n} \cdot \boldsymbol{\nabla})^2 p_1\right], \end{aligned} \tag{16}$$

with the outward pointing normal of the unit length $\boldsymbol{n}$, the velocity of the harmonic boundary $\boldsymbol{V}_1^0$, and the shear wavenumber

$$k_s = \frac{1 - i}{\delta}. \tag{17}$$

The second-order problem for the streaming in the bulk of the fluid is in LVM governed by

$$\boldsymbol{\nabla} \cdot \boldsymbol{v}_2^{\mathrm{b}} = 0, \tag{18}$$

$$\boldsymbol{\nabla}\langle p_2^{\mathrm{b}} \rangle - \eta \nabla^2 \langle \boldsymbol{v}_2^{\mathrm{b}} \rangle = \boldsymbol{\nabla}\langle \mathcal{L}_{\mathrm{ac}}^{\mathrm{b}} \rangle + \frac{\Gamma \omega}{c_0^2}\langle \boldsymbol{S}_{\mathrm{ac}}^{\mathrm{b}} \rangle, \tag{19}$$

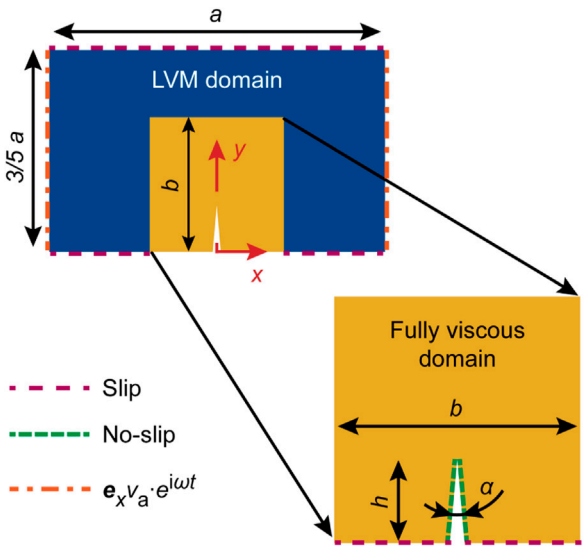

FIGURE 2
Geometry of the Hybrid model of a single sharp edge in a rectangular channel. The model is divided into a Fully Viscous domain (yellow) and a limiting velocity method domain (dark blue). The boundary conditions of the first-order problem are graphically indicated. The system is excited by an oscillatory velocity boundary condition along the x-axis, at $x = \pm a/2$ (dash-dotted line) with the velocity amplitude v_a. All walls of the LVM domain, including the driving wall, have an additional artificial velocity imposed according to [22] that accounts for damping inside the viscous boundary layer δ. The sharp edge in the Fully Viscous domain is modeled using the no-slip boundary condition, while the walls at the bottom of the edge are constrained with a slip boundary condition to improve the fully viscous-LVM interface. The geometric parameters describing the model are the channel width a, the Fully Viscous domain width b, the sharp-edge tip height h, the apex angle of the sharp edge α, and the radius of the rounding of the sharp-edge tip that is defined as $\delta/2$, unless specified otherwise.

with the bulk Lagrangian density

$$\langle \mathcal{L}_{ac}^{b} \rangle = \frac{1}{2}\frac{1}{\rho_0 c_0^2}\langle p_1^2 \rangle - \frac{1}{2}\rho_0 \langle \boldsymbol{v}_1^{b} \rangle \tag{20}$$

and the energy-flux density

$$\langle \boldsymbol{S}_{ac}^{b} \rangle = \langle p_1 \boldsymbol{v}_1^{b} \rangle. \tag{21}$$

The boundary condition that constrains the second-order problem is given in a form of a slip velocity

$$\boldsymbol{v}_2^{b0} = (\boldsymbol{A}\cdot\boldsymbol{t}_1)\boldsymbol{t}_1 + (\boldsymbol{A}\cdot\boldsymbol{t}_2)\boldsymbol{t}_2 + (\boldsymbol{B}\cdot\boldsymbol{n})\boldsymbol{n}, \tag{22}$$

with orthogonal unit vectors $\boldsymbol{t}_1$ and $\boldsymbol{t}_2$ that are tangential to the boundary surface and with

$$\begin{aligned}\boldsymbol{A} = -\frac{1}{2\omega}\mathrm{Re}\Big\{ & \boldsymbol{v}_1^{\delta 0*}\cdot\nabla\Big(\frac{1}{2}\boldsymbol{v}_1^{\delta 0} - \mathrm{i}\boldsymbol{V}_1^{0}\Big) \\ & + \mathrm{i}\boldsymbol{V}_1^{0*}\cdot\nabla\boldsymbol{v}_1^{b} + \Big[\frac{2-\mathrm{i}}{2}\nabla\cdot\boldsymbol{v}_1^{\delta 0*} \\ & + \mathrm{i}\big(\nabla\cdot\boldsymbol{V}_1^{0*} - (\boldsymbol{n}\cdot\nabla)v_{1n}^{b*}\big)\Big]\boldsymbol{v}_1^{\delta 0}\Big\},\end{aligned} \tag{23}$$

$$\boldsymbol{B} = \frac{1}{2\omega}\mathrm{Re}\big\{\mathrm{i}\boldsymbol{v}_1^{b0*}\cdot\nabla\boldsymbol{v}_1^{b}\big\}, \tag{24}$$

with $v_{1n}^{b*} = \boldsymbol{n}\cdot\boldsymbol{v}_{1n}^{b*}$; $\boldsymbol{v}_1^{\delta 0}$ follows from the no-slip boundary condition at the first order as

$$\boldsymbol{v}_1^{\delta 0} = \boldsymbol{V}_1^{0} - \boldsymbol{v}_1^{b0}. \tag{25}$$

The superscript $\square^0$ indicates that $\square$ is evaluated at the boundary.

2.4 Numerical model

The numerical models implementing the first- and the second-order problems are developed in the finite-element method framework of COMSOL Multiphysics 5.6 [41]. In the analysis that follows, we use three kinds of numerical models, namely, **(I)** the Fully Viscous model that numerically solves Eqs. 4–8, 10 in line with the approach introduced in [15] and used in many studies since [5, 9, 28, 42], **(II)** the Full Limiting Velocity Method (FLVM) model that is based on the LVM of [22] and incorporates Eqs. 11, 16, 18, 19, and 22, and **(III)** the Hybrid model that uses the formulation of the Fully Viscous model in the vicinity of sharp edges and the LVM formulation in the rest of the fluid domain, as illustrated in Figure 2.

2.4.1 Fully viscous model

The Fully Viscous model is implemented in COMSOL Multiphysics by using the adiabatic form of the Thermoviscous Acoustics interface for the first-order problem, which is then solved with a Frequency Domain study. The second-order problem is implemented using the Creeping Flow interface, with the streaming source term $-\rho_0\nabla\cdot\langle \boldsymbol{v}_1\boldsymbol{v}_1\rangle$ from Eq. 7, which is the spatial variation of the Reynolds stress, and added to the governing equations of the Creeping Flow interface as a volume force. The second-order problem is solved with the Stationary study.

The boundary conditions in the Fully Viscous model at the first order are the no-slip condition applied on all the non-moving (rigid) walls; specifically,

$$\boldsymbol{v}_1 = \boldsymbol{0} \quad \text{at the non-moving walls,} \tag{26}$$

while at the moving walls, the applied wall velocity is imposed as

$$\boldsymbol{v}_1 = \boldsymbol{v}_{\mathrm{wall}} \quad \text{at the moving walls,} \tag{27}$$

with the velocity $\boldsymbol{v}_{\mathrm{wall}}$ defined on the case-by-case basis. At the second order, the no-slip boundary condition is applied to all the walls, but on the Lagrangian velocity, as in Eq. 10. However, the Stokes drift that appears in Eq. 10 only at the moving walls.

2.4.2 Full Limiting Velocity Method model

The first-order problem of the FLVM model is implemented through the Pressure Acoustics interface, with the boundary condition on the pressure gradient from Eq. 16 that accounts for viscous boundary layer damping imposed as an inward velocity at all boundaries. The first-order problem is solved with a Frequency Domain study. The second-order problem is implemented via the Creeping Flow interface, same as for the Fully Viscous model. The source term from Eq. 19 is implemented as a volume force.

The boundary conditions of the FLVM model at the first order are the slip condition with the additional artificial velocity in the

direction normal to the wall that imposes viscous damping resulting from the viscous boundary layer; specifically,

$$\boldsymbol{n}\cdot\boldsymbol{v}_1 = \frac{\boldsymbol{n}\cdot\boldsymbol{\nabla}p_1}{\mathrm{i}\omega\rho_0} \quad \text{at the walls,} \tag{28}$$

where $\boldsymbol{n}\cdot\boldsymbol{\nabla}p_1$ is defined in Eq. 16. The case-specific oscillatory velocity of the moving walls is imposed directly in the expression from Eq. 16, by setting $\boldsymbol{V}_1^0 = \boldsymbol{v}_{\mathrm{wall}}$, with the case-specific $\boldsymbol{v}_{\mathrm{wall}}$. At the second order, the slip velocity defined in Eq. 22 is imposed to the fluid at the walls. Specifically,

$$\langle\boldsymbol{v}_2\rangle = \boldsymbol{v}_2^{\mathrm{b0}} \quad \text{at the walls.} \tag{29}$$

For the 2D cases, the boundary condition in Eq. 29 simplifies as $\boldsymbol{t}_2 = \boldsymbol{0}$.

2.4.3 Hybrid model

In the Hybrid model, the Fully Viscous domain is implemented analogously to the implementation of the Fully Viscous model, whereas the LVM domain is implemented analogously to the FLVM model. The Thermoviscous Acoustics interface and the Pressure Acoustics interface are coupled through the Acoustic-Thermoviscous Acoustic Boundary interface. In the Creeping Flow interface, the gradient of the Lagrangian density ($\boldsymbol{\nabla}\mathcal{L}_{\mathrm{ac}}$) is omitted from the LVM domain for numerical stability, since it does not contribute to the streaming [43]. Consequently, the gradient of the Lagrangian density needs to be subtracted from the streaming source term $-\rho_0\boldsymbol{\nabla}\cdot\langle\boldsymbol{v}_1\boldsymbol{v}_1\rangle$ in the Fully Viscous domain, to avoid a non-physical source of streaming at the interface of the LVM and the Fully Viscous domains. In the LVM domain, we also omit the streaming source $\frac{\Gamma\omega}{c_0^2}\langle\boldsymbol{S}_{\mathrm{ac}}^{\mathrm{b}}\rangle$ from Eq. 19 for numerical stability, as it contributes to bulk-driven streaming, which is insignificant in the cases analyzed here, but might be important in some other configurations [44].

The boundary conditions in the Fully Viscous domain of the Hybrid model resemble the boundary conditions applied in the Fully Viscous model, while the boundary conditions imposed in the LVM domain of the Hybrid model resemble those in the FLVM model. There are two exceptions to this at the first order: The walls in the Fully Viscous domain are coupled to the LVM domain, where the slip velocity is applied (indicated in Figure 2) through the following conditions:

$$\boldsymbol{n}\cdot\boldsymbol{v}_1 = \boldsymbol{0} \quad \text{at the slip walls,} \tag{30}$$

$$\boldsymbol{\sigma}_n - (\boldsymbol{\sigma}_n\cdot\boldsymbol{n})\boldsymbol{n} = \boldsymbol{0} \quad \text{at the slip walls,} \tag{31}$$

with

$$\boldsymbol{\sigma}_n = \left(-p_1\boldsymbol{I} + \eta\left[\boldsymbol{\nabla}\boldsymbol{v}_1 + (\boldsymbol{\nabla}\boldsymbol{v}_1)^T\right] - \left(\frac{2}{3}\eta - \eta_{\mathrm{B}}\right)(\boldsymbol{\nabla}\cdot\boldsymbol{v}_1)\boldsymbol{I}\right)\boldsymbol{n}, \tag{32}$$

with the identity tensor $\boldsymbol{I}$; the second exception is at the coupling boundary between the Fully Viscous domain and the LVM domain, where the following coupling conditions are applied:

$$\frac{\boldsymbol{n}\cdot\boldsymbol{\nabla}p_1}{\mathrm{i}\omega\rho_0}\Big|_{\mathrm{LVM}} = \boldsymbol{n}\cdot\boldsymbol{v}_1|_{\mathrm{Full.\ visc.}} \quad \text{at the coupling boundary,} \tag{33}$$

$$\boldsymbol{n}p_1|_{\mathrm{LVM}} = \boldsymbol{\sigma}_n|_{\mathrm{Full.\ visc.}} \quad \text{at the coupling boundary,} \tag{34}$$

with the left-hand side evaluated in the LVM domain and the right-hand side in the Fully Viscous domain, at the coupling boundary. At the second order, there is no special coupling between the two domains, except for the volume force accounting for the spatial variation of the Reynolds stress on the right-hand side of Eq. 7, which is applied only in the Fully Viscous domain and not in the LVM domain.

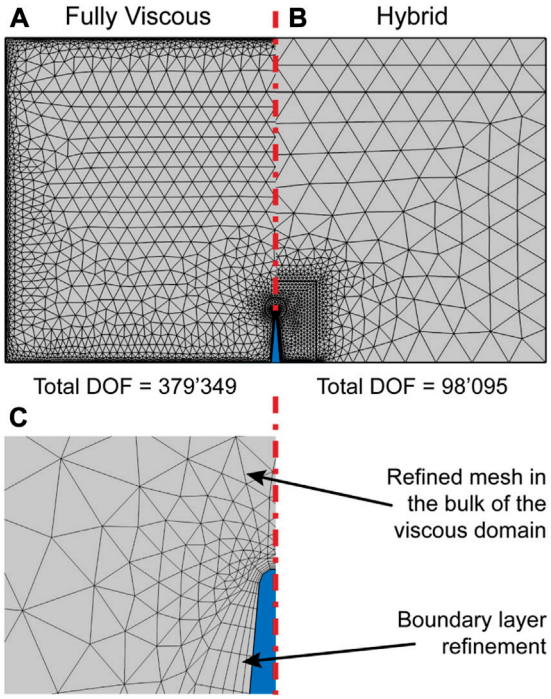

FIGURE 3
Comparison of the converged meshes of **(A)** the Fully Viscous model with the total DOF of 379′349 and **(B)** the Hybrid model with the total DOF of 98′095 at f = 720 kHz in water, with a = 1 mm, h = 100 μm, $\alpha = 10^{\circ}$, and b = 150 μm; **(C)** closeup of the mesh of the Hybrid model near the sharp-edge tip, where the viscous boundary layer mesh is distinguishable.

The size of the LVM domain in the Hybrid model, here defined through the length b in Figure 2, should be chosen such that it surrounds the region of the high curvature of the boundary, satisfying the condition $b \gg \delta$ under the assumption that $\delta \gtrsim 1/R$.

For all the models, the Creeping Flow interface contains a pressure constraint in the form of a zero average across the whole fluid domain. All the studied 2D cases were solved with the default solvers, suggested by COMSOL Multiphysics. For the 3D cases featured here, the solver had to be manually switched to a Direct solver.

It is important to note that the first-order problem implemented using COMSOL Multiphysics through the native Thermoviscous Acoustics or Pressure Acoustics interfaces needs to be consistent with the time dependency with a factor of $e^{\mathrm{i}\omega t}$, whereas the acoustofluidic theories often assume $e^{-\mathrm{i}\omega t}$, as, for example, assumed in [22], [23].

For all the studies herein, we assume the fluid to be water with ρ_0 = 1000 kg m^{-3}, c_0 = 1481 m s^{-1}, η = 1.02 mPa s, and η_{B} = 3.09 mPa s [45].

Exemplary 2D meshes for the Fully Viscous model and the Hybrid model are compared in Figure 3. The inherently larger bulk element size of the Hybrid model and the absence of mesh refinements at the boundaries promise a substantial reduction in the computational effort for the Hybrid model compared to the

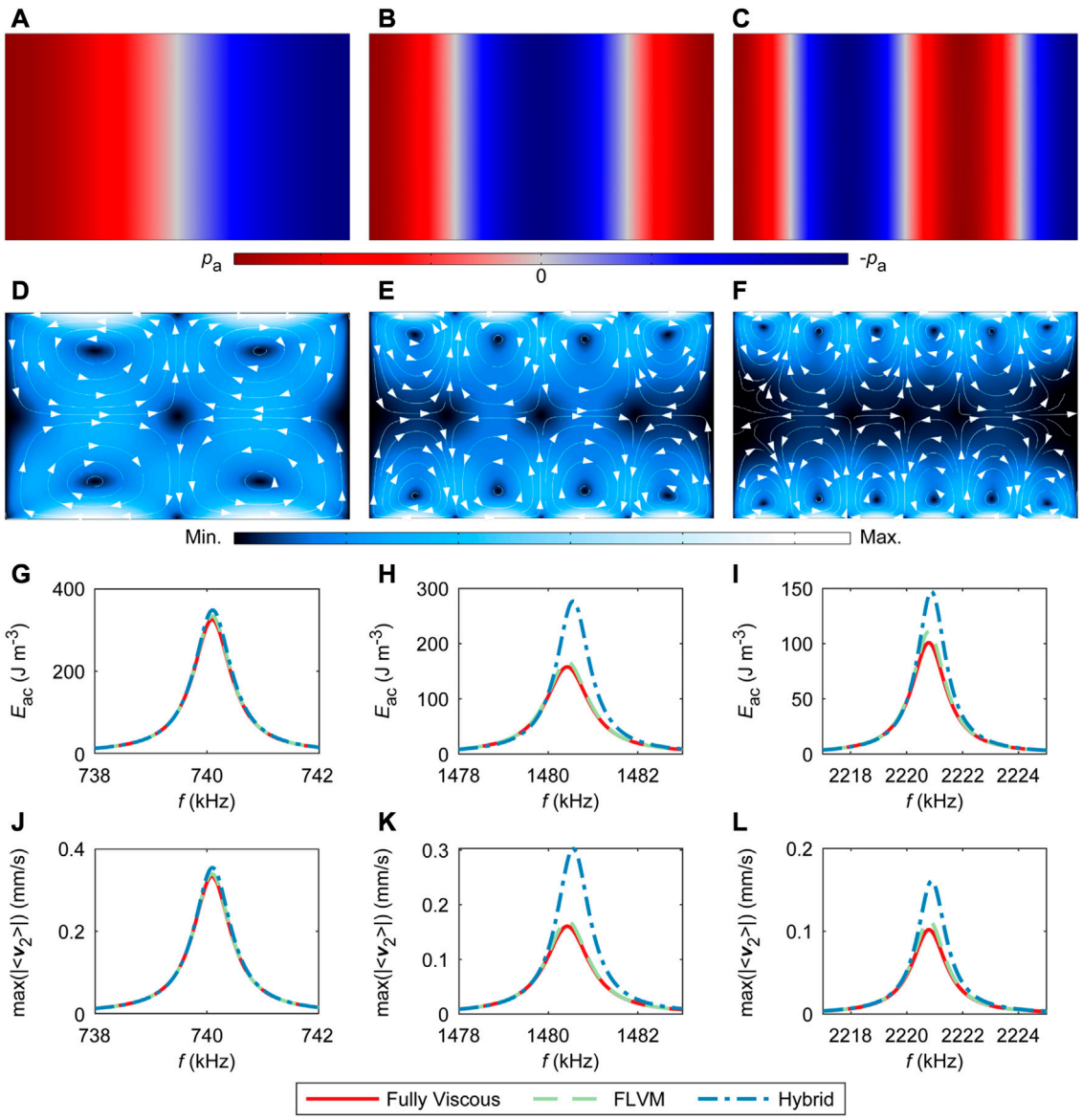

FIGURE 4
Different modeling approaches validated with a rectangular channel without the presence of a sharp edge. We compare the performance of the Fully Viscous model according to [15], the FLVM model from [22], and the Hybrid model outlined in Figure 2 that combines the two former approaches. The comparison is made for the first three resonance modes in water along the channel width a = 1 mm, with b = 200 μm; mode 1 is shown in **(A)**, **(D)**, **(G)**, and **(J)**; mode 2 in **(B)**, **(E)**, **(H)**, and **(K)**; and mode 3 in **(C)**, **(F)**, **(I)**, and **(L)**. The first row shows representative acoustic pressure fields (FLVM), the second row shows representative Eulerian streaming velocity fields (FLVM) with streamlines and arrows revealing the direction of the velocity, the third row shows the average acoustic energy density E_{ac}, and the fourth row shows the maximal magnitude of the Eulerian streaming velocity $|\langle \boldsymbol{v}_2 \rangle|$. To support the build-up of the corresponding resonances, the excitation at $x = \pm a/2$ with v_a = 1 mm s^{-1} is imposed in the same direction (in phase) for modes 1 and 3 and in the opposing directions (π phase shift) for mode 2.

Fully Viscous model, especially for larger problems. The larger bulk element size admissible in the LVM domain, compared to the Fully Viscous domain, stems from the lack of the divergence of the Reynolds stress in Eq. 19 that requires a refined mesh [22]. The difference in the total DOF is further increased due to the Fully Viscous model solving the velocity field and the pressure field in the fluid bulk in the first-order problem, whereas the hybrid model only solves for the pressure field in the fluid bulk.

The convergence of representative models with respect to the mesh element size is discussed in Supplementary Material.

In the Fully Viscous model, the first-order pressure and velocity were discretized using cubic Lagrange and quartic Lagrange elements, respectively. The second-order pressure and velocity were discretized with quadratic and cubic elements, respectively. In the Hybrid model, cubic Lagrange elements were used for the first-order pressure in the LVM domain, while the pressure and velocity in the Fully Viscous domain were discretized with quadratic and cubic Lagrange elements, respectively. At the second order, the discretization was quadratic and cubic for pressure and velocity, respectively.

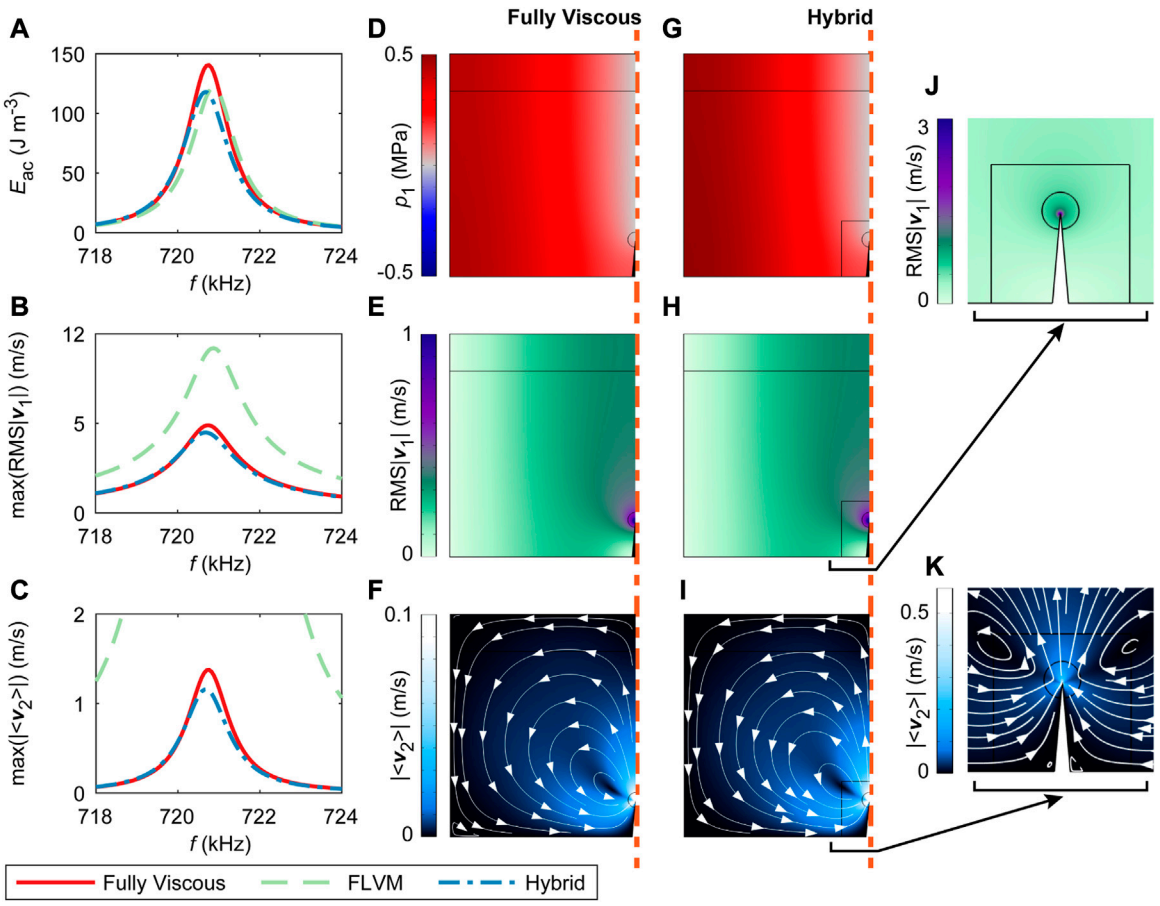

FIGURE 5
Different modeling approaches validated with a rectangular channel containing a sharp-edge structure. We compare the performance of the Fully Viscous model according to Muller et al. [15], the FLVM model from [22], and the Hybrid model outlined in Figure 2 that combines the two former approaches. The comparison is made for the first resonance mode in water along the channel width a = 1 mm, with h = 100 μm, b = 150 μm, and α = 10°. **(A)** Average acoustic energy density E_{ac}, **(B)** maximal root-mean-square acoustic velocity RMS|$\boldsymbol{v}_1$|, and **(C)** maximal Eulerian streaming velocity magnitude |⟨$\boldsymbol{v}_2$⟩|. **(D), (G)** Half of the acoustic pressure fields that are otherwise antisymmetric. **(E), (H)** Half of the root-mean-square acoustic velocity magnitudes that are otherwise symmetric. **(F), (I)** Half of the Eulerian streaming velocity fields that are otherwise symmetric. **(J), (K)** Zoomed-in fields corresponding to **(H)** and **(I)**, respectively. **(D)**–**(F)** From the Fully Viscous model; **(G)**–**(K)** from the Hybrid model. All the displayed fields correspond to f = 720 kHz. The fields from the FLVM model are omitted, since they are erroneous due to the inherent assumptions of the model (as a note, the direction of the streaming velocity from the FLVM model is inverted relative to the actual pattern). The excitation is imposed in the same direction (in phase) at $x = \pm a/2$ with v_a = 1 mm s^{-1}.

The results of numerical simulations are evaluated through the base variables (p_1, $\boldsymbol{v}_1$, and ⟨$\boldsymbol{v}_2$⟩) as well as through the time- and space-averaged acoustic energy density [46]

$$E_{ac} = \frac{1}{\Omega}\int_{\Omega}\left\langle \frac{1}{2\rho_0 c_0^2}p_1^2 + \frac{\rho_0}{2}(\boldsymbol{v}_1\cdot\boldsymbol{v}_1)\right\rangle \mathrm{d}\Omega, \tag{35}$$

within a spatial domain Ω that corresponds to the volume in a 3D or the area in a 2D configuration. The first term within ⟨□⟩ in Eq. 35 represents the potential energy density, while the second term represents the kinetic energy density. In the LVM subdomains of Ω, $\boldsymbol{v}_1$ is computed from Eq. 15.

3 Results

We study several cases using the described numerical models, which validate the Hybrid model on various 2D geometries in combination with fluidic channel resonances. In the last part, the benefit of the Hybrid model is demonstrated on the analysis of an exemplary 3D case that would have been very difficult if not impossible to model using preexisting approaches.

3.1 Rectangular channel in 2D

We first analyze a simple case of a 2D rectangular fluidic channel that is geometrically equivalent to the case presented in Figure 2, but without the sharp edge. The analysis, presented in Figure 4, compares the FLVM model and the Hybrid model against the Fully Viscous model, in order to validate the implementation in COMSOL Multiphysics and to estimate the baseline error caused by the coupling of Fully Viscous and LVM domains within the Hybrid model. In the Hybrid

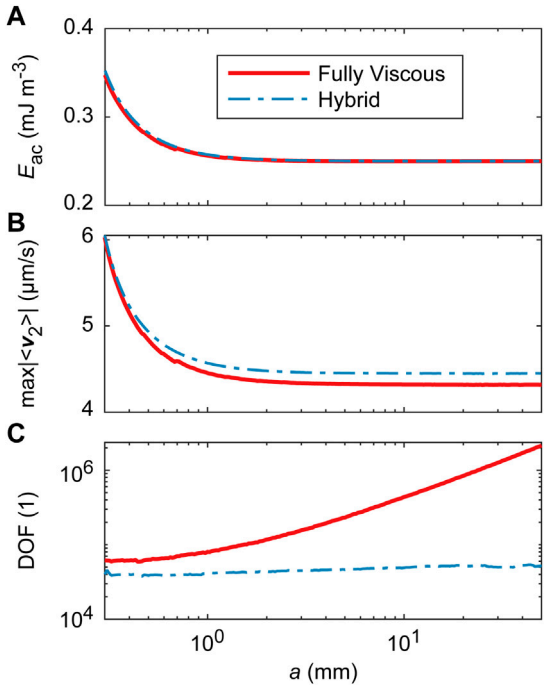

FIGURE 6
Influence of the channel width a on the performance of the Fully Viscous model and the Hybrid model for a subwavelength system with a sharp edge. The channel width is varied in the range of 0.3 mm ≤ a ≤ 50 mm at a fixed low frequency of f = 10 kHz to avoid channel resonances. The channel contains a single sharp edge, as indicated in Figure 2, with h = 100 μm, b = 150 μm, $\alpha = 10^{\circ}$, and the sharp-edge rounding radius of 0.3 μm. **(A)** Average acoustic energy density E_{ac}, **(B)** maximal Eulerian streaming velocity magnitude $|\langle \boldsymbol{v}_2 \rangle|$, and **(C)** scaling of the DOF with the channel width. The excitation is imposed in the same direction (in phase) at $x = \pm a/2$, with a channel-width-dependent amplitude $v_a = v_{mid} \cos[2xf\pi/c_0]$ that enforces a constant acoustic velocity amplitude v_{mid} = 1 mm s^{-1} in the middle of the channel at the sharp edge.

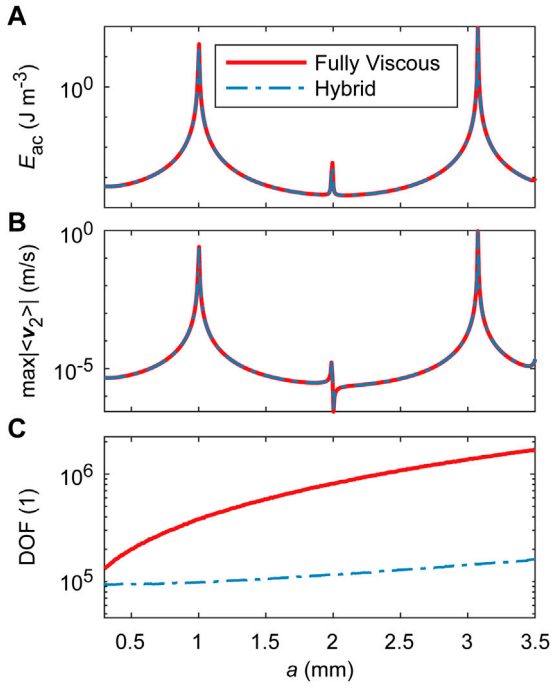

FIGURE 7
Influence of the channel width a on the performance of the Fully Viscous model and the Hybrid model for a resonant system with a sharp edge. Channel width is varied in the range of 0.3 mm ≤ a ≤ 3.5 mm at a fixed frequency of f = 720 kHz to induce channel resonances. The channel contains a single sharp edge, as indicated in Figure 2, with h = 100 μm, b = 150 μm, $\alpha = 10^{\circ}$, and the sharp-edge rounding radius of $\delta/2$. **(A)** Average acoustic energy density E_{ac}, **(B)** maximal Eulerian streaming velocity magnitude $|\langle \boldsymbol{v}_2 \rangle|$, and **(C)** scaling of the DOF with the channel width. The excitation is imposed in the same direction (in phase) at $x = \pm a/2$, with a fixed amplitude v_a = 1 mm s^{-1}. The imposed excitation supports the odd resonances (modes 1, 3, ...) that have a symmetric acoustic velocity field about the plane of the symmetry x =0 at the sharp edge.

model, the Fully Viscous domain is defined with length b, while the LVM formulation is applied to the rest of the rectangular domain defined with length a, as specified in Figure 2.

The 2D geometry of the rectangular fluidic channel in Figure 4 is frequently used for studies in acoustofluidics [15, 25, 39, 46, 47]. The geometry is defined through the lengths a = 1 mm and b = 200 μm. Predictions of the three models are compared around the first three resonance modes across the width of the rectangular channel in the x-direction. We apply the excitation at $x = \pm a/2$ with v_a = 1 mm s^{-1} imposed in the same direction at both sides of the channel (in phase) to support the build-up of the resonance modes 1 (Figure 4A) and 3 (Figure 4C) across the channel width. For the resonance mode 2 in Figure 4B, the velocity v_a = 1 mm s^{-1} is imposed in the opposing directions (π phase shift) at the two sides of the channel.

Qualitatively, the first- and second-order fields look the same for all models and modes; therefore, only reference normalized fields are shown in Figures 4A-F. The frequency sweeps around the three resonance frequencies in Figures 4G-L, which further validate our COMSOL Multiphysics implementation of the LVM, as particularly the FLVM model matches the Fully Viscous model perfectly. While the Hybrid model matches the Fully Viscous model well for all three modes in terms of the corresponding resonance frequency, it overestimates the acoustic energy density E_{ac} and maximal streaming velocity max($|\langle \boldsymbol{v}_2 \rangle|$). The error for the first mode is 7% and 6% for E_{ac} and max($|\langle \boldsymbol{v}_2 \rangle|$), respectively. In the case of the two higher modes, the errors reach up to 76%. The error comes from the coupling of the LVM with Fully Viscous domains and can be minimized by reducing the length of the boundary section that assumes a Fully viscous formulation and by positioning the Fully Viscous domain close to the pressure node (see Supplementary Material for further analysis). However, for frequencies away from the center of the resonance peak, the errors are minimized and all three models agree well.

3.2 Rectangular channel with a sharp-edge structure in 2D

In Figure 5, we look at the same 2D rectangular fluidic channel as in Figure 4, whereas a sharp edge has been added. A comparable

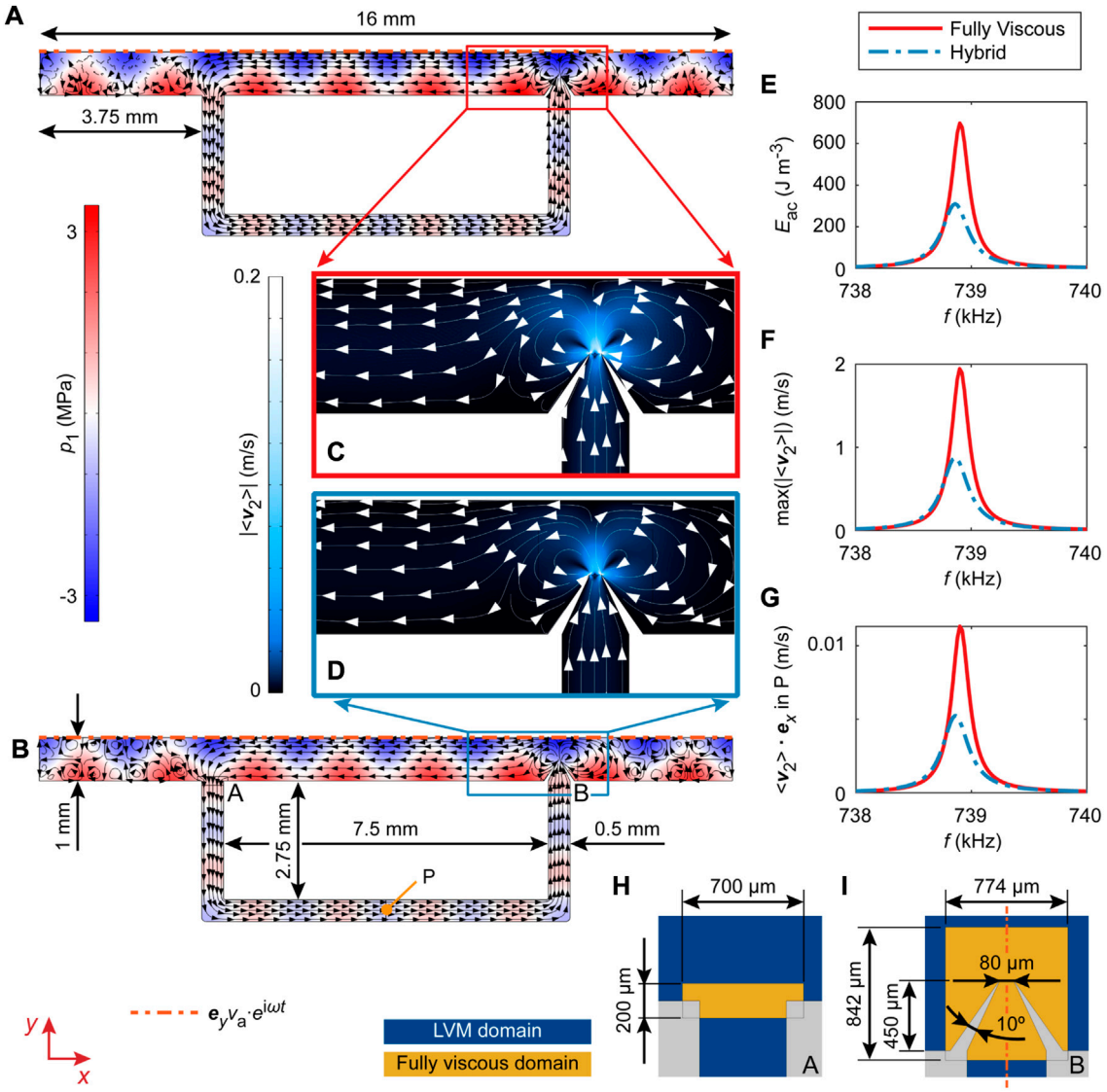

FIGURE 8
Different modeling approaches validated on a complex 2D geometry containing a pair of sharp edges that can facilitate pumping. The geometry is inspired by the experimental device from [9]. We compare the performance of the Fully Viscous model and the Hybrid model that combines the Fully Viscous domain with the limiting velocity method domain. The comparison is made for one of the resonance modes in water with the dimensions of the rigid channels defined in **(A)**, **(B)**, **(H)**, and **(I)**, where **(H)** and **(I)** show the Fully Viscous domains. The acoustic pressure and the streamlines of the Eulerian streaming velocity are shown in **(A)** for the Fully Viscous model and in **(B)** for the Hybrid model and **(C)** and **(D)** show the respective zoomed-in Eulerian streaming fields near the pair of sharp edges. The compared fields correspond to f = 738.85 kHz, where **(E)** shows the average acoustic energy density E_{ac}, **(F)** shows the maximal Eulerian streaming velocity magnitude $|\langle \boldsymbol{v}_2 \rangle|$, and **(G)** shows the x-component of the Eulerian streaming velocity in point P, defined in **(B)**. The excitation in a form of an oscillatory velocity in the y-direction with an amplitude v_a = 1 mm s^{-1} is imposed on the whole uppermost boundary.

geometry is featured in several prior experimental [2, 4, 7, 14] and numerical [2, 5, 25, 26] studies of sharp-edge acoustofluidics.

We apply the excitation at $x = \pm a/2$ with v_a = 1 mm s^{-1} imposed in the same direction at both sides of the channel (in phase) to facilitate the build-up of the first resonance mode across the channel width. The first resonance mode was chosen for the analysis as it induces a pressure node and, thus, a velocity antinode at the location of the sharp-edge tip, producing strong sharp-edge phenomena.

The presence of the sharp edge shifts the resonance frequency of the first mode in Figure 5 from ~ 740.1 kHz down to ~ 720.8 kHz, when compared to a channel without the sharp edge in Figure 4. The lower resonance frequency in the rectangular fluidic channel featuring a sharp edge, compared to the channel without the sharp edge, was already observed in simulations in [26]. This frequency shift might be due to the increased path of waves, as they have to circumvent the sharp edge, analogously to the presence of other objects dispersed in an acoustic field that decrease the resonance frequency, for instance, bubbles [30].

Figure 5 reveals a good agreement between the Hybrid model and the Fully Viscous model, whereas the FLVM model

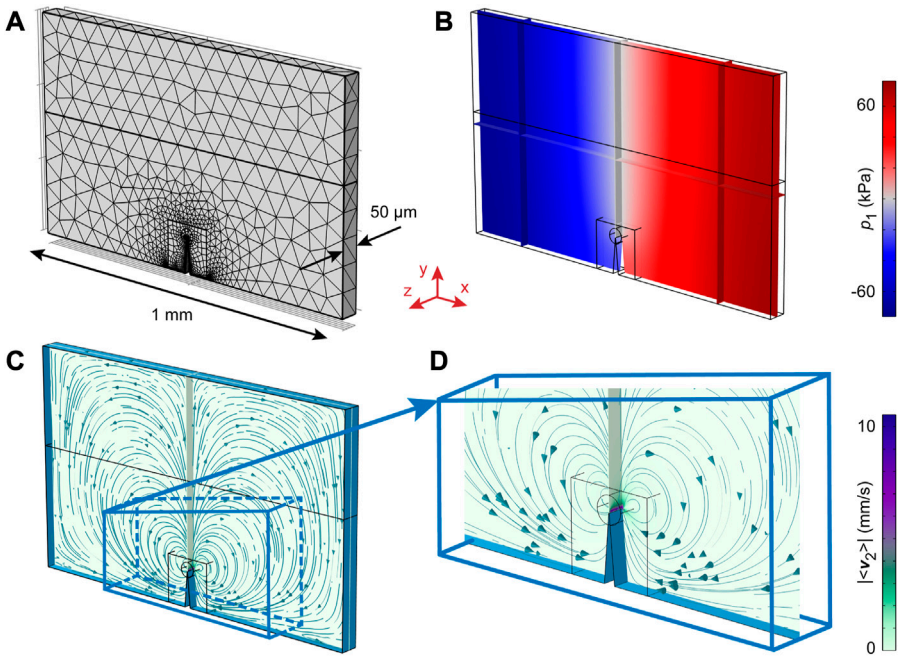

FIGURE 9
The Hybrid model of a rectangular channel containing a sharp-edge structure in 3D. An analysis is performed near the first resonance mode in water along the channel width a = 1 mm, with h = 100 μm, b = 150 μm, d = 50 μm, and α = 10°. **(A)** The mesh, **(B)** the first-order pressure p_1, **(C)** the Eulerian streaming velocity pattern, and **(D)** the zoomed-in streaming field corresponding to **(C)**. The analysis of the pressure and streaming velocity fields in **(B)**–**(D)** is performed at the middle xy-plane (at $z = d/2$), with some additional xz- and yz-planes for orientation. All the displayed fields correspond to f = 720 kHz. The excitation is imposed in the same direction (in phase) at $x = \pm a/2$ with v_a = 1 mm s^{-1}.

quantitatively and qualitatively disagrees with the Fully Viscous model. The latter is expected based on the underlying assumptions of the LVM, and the FLVM model is, therefore, omitted from further analysis. At the resonance peak, the Hybrid model slightly underestimates the magnitude of the first-order fields, reflected in ~16% lower E_{ac} maximum compared to the Fully Viscous model. Similarly, the maximal magnitude of the Eulerian streaming velocity is underestimated by ~16% at the resonance peak. However, the agreement between the Hybrid model and the Fully Viscous model is very good away from the center of the resonance peak. Specifically, the difference in E_{ac} and $\max(|\langle \boldsymbol{v}_2 \rangle|)$ is $< 5\%$ for frequencies $> |\pm 2$ kHz $|$ from the center frequency of the peak.

In order to understand how the newly developed Hybrid model is compared to the Fully Viscous model in terms of the computational demand relative to an increasing size of the domain, we keep track of the DOF as the channel width a is increased. The results shown in Figure 6 present E_{ac}, $\max(|\langle \boldsymbol{v}_2 \rangle|)$, and the DOF for the rectangular channel with a sharp edge from Figure 2 at f = 10 kHz and across the channel width range of 0.3 mm $\leq a \leq$ 50 mm, making this a subwavelength problem ($\lambda \approx$ 150 mm). The results indicate a good agreement between the two models in terms of E_{ac} and $\max(|\langle \boldsymbol{v}_2 \rangle|)$ across the whole range of a. Interestingly, the behavior below $a \approx$ 1 mm depends on a, while it remains independent of a for larger domain sizes. The DOF in the Fully Viscous model, however, significantly exceeds the DOF in the Hybrid model, with the DOF reaching $>$40-fold reduction as the domain size is increased, indicating the benefit of the Hybrid model.

To compare the scaling of the Hybrid model and the Fully Viscous model at higher frequencies, we vary a from 0.3 mm to 3.5 mm at f = 720 kHz. The results in Figure 7 reveal three resonances in the channel across the investigated range of a, with the first peak at $a \approx$ 1 mm corresponding to the resonance peak previously analyzed in Figure 5. The two models match very well in terms of E_{ac} and $\max(|\langle \boldsymbol{v}_2 \rangle|)$. The DOF generally exceed those from Figure 6 due to the higher frequency, and the DOF in the Hybrid model again show a significant up to ~ 11-fold decrease relative to the DOF in the Fully Viscous model.

3.3 Sharp-edge-based micropump in 2D

The main advantage of the developed Hybrid model is the ability to model larger systems that feature sharp-edge structures. We analyze the performance of the Hybrid model for a larger system in Figure 8, in the case of a 2D acoustofluidic micropump inspired by [9] that is capable of fluid pumping and mixing due to the sharp-edge streaming, as well as microparticle/cell focusing and trapping by the acoustic radiation force due to the fluidic channel resonances.

Similar to the previous results, the behavior predicted by the Fully Viscous model and the Hybrid model matches qualitatively and quantitatively, except for the resonance peak, where the Hybrid model underestimates the magnitude of acoustic fields.

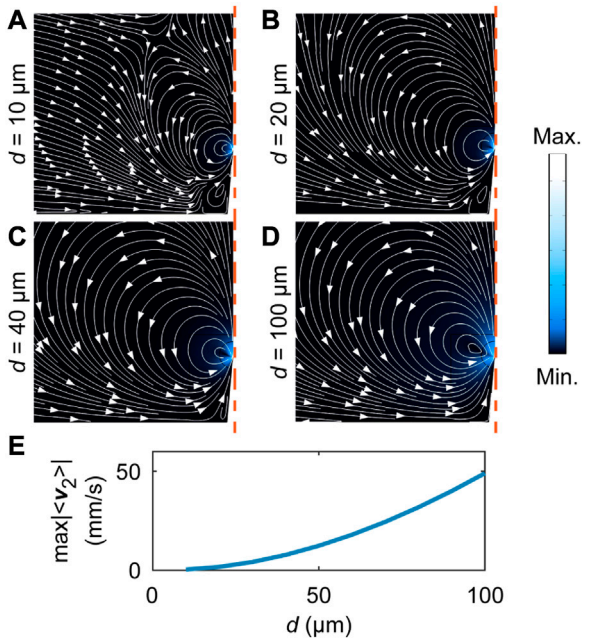

FIGURE 10
Influence of the channel depth d on the sharp-edge streaming pattern at the middle xy-plane (at $z = d/2$), studied with the Hybrid 3D model. The channel depth is varied from d = 10 µm in **(A)** to d = 100 µm in **(D)** at a fixed frequency of f = 720 kHz. The corresponding maximal Eulerian streaming velocity $|\langle \boldsymbol{v}_2 \rangle|$ is shown in **(E)**. The channel contains a single sharp edge, as indicated in Figure 2, with h = 100 µm, b = 150 µm, $\alpha = 10^{\circ}$, and the sharp-edge rounding radius of $\delta/2$. **(A)**–**(D)** Eulerian streaming velocity magnitude $|\langle \boldsymbol{v}_2 \rangle|$. The excitation is imposed in the same direction (in phase) at $x = \pm a/2$, with an amplitude of v_a = 1 mm s^{-1}.

3.4 Rectangular channel with a sharp-edge structure in 3D

Finally, we demonstrate the capability of our efficient modeling approach by solving a high-frequency acoustic streaming problem in 3D using a Hybrid model with the geometry from Figure 2 extruded to a depth of d. The exemplary mesh and results are shown in Figure 9.

We apply the 3D model to study the influence of the depth d on the Eulerian streaming pattern on the xy-plane at $z = d/2$ in Figure 10. The results show that the pattern is visibly affected by the presence of the front ($z = d$) and back ($z = 0$) covers when d = 10 µm in Figure 10A, but the pattern gradually converges to the streaming pattern in the 2D model from Figure 5 as d is increased to 100 µm in Figure 10D. However, as shown in Figure 10E, the maximal Eulerian streaming velocity magnitude remains impaired by the 3D effects even at d = 100 µm, when compared to the magnitudes from a comparable 2D configuration at f = 720 kHz from Figure 5C.

4 Discussion

We have demonstrated that the novel Hybrid model, combining the Fully Viscous modeling of the acoustic phenomena [15] near sharp edges with the efficient modeling of the viscous boundary layers according to [22] in the rest of the device, provides up to > 40-fold reduction in the required DOF in 2D validation studies while capturing the relevant physics. Furthermore, this approach enables the modeling of 3D sharp-edge phenomena at high frequencies, where the viscous boundary layer thickness δ reduces to the rounding radius of sharp edges or below.

While the novel Hybrid model introduces a quantitative error on the estimated magnitude of fields at the resonance peaks, it correctly predicts the qualitative behavior throughout the modeled device. This is of no concern for problems that do not involve resonances in the fluidic channels, e.g., the configurations from [2, 5, 14]. Sharp-edge-based devices operating at higher frequencies, such as the multifunctional chip reported by [9], can still be effectively modeled, as demonstrated in Figure 8. Shortcomings in terms of erroneous magnitudes at resonances are not too important, since the underlying total damping defining the quality of a given resonance is generally difficult to model anyway and can vary due to a plethora of experimental conditions [19], such as the temperature, material damping, damping in the connecting glue layers, and many more.

The relative error of the Hybrid model is for a given resonance similar for both analyzed quantities, E_{ac} and max ($|\langle \boldsymbol{v}_2 \rangle|$). This implies that the error originates from the computation of the first-order fields, since both quantities rely on the square of a first-order quantity—E_{ac} directly, while max ($|\langle \boldsymbol{v}_2 \rangle|$) depends the square of the first-order velocity as a source term in Eq. 7 and as a boundary condition through Eq. 9.

Our Hybrid model allows the study of 3D sharp-edge effects, as demonstrated in Figure 10, where we showed that the 3D effects in the quasi-2D geometry are limited to a certain depth, as previously hypothesized in [5]. This provides the justification for the use of 2D models when modeling quasi-2D channels of lab-on-a-chip devices that typically exceed the depth of 100 µm.

The herein introduced Hybrid modeling approach can be used to aid the emerging field of sharp-edge acoustofluidics. In the latter, sharp-edge structures such as needles or wedges in microfluidic devices are excited with ultrasound for a wide range of applications, ranging from propulsion of microrobots [48–50] and enhanced drug delivery [27] to advanced lab-on-a-chip technology involving sharp-edge-based micropumps and micromixers [3, 8, 9, 12–14, 51].

Data availability statement

The original contributions presented in the study are included in the article/Supplementary Material; further inquiries can be directed to the corresponding author.

Author contributions

AP and LR implemented the numerical models and carried out the numerical studies. AP and CH supervised LR. AP provided the initial draft of the manuscript. JD supervised the project. All authors contributed substantially to scientific discussion and to the writing of the manuscript.

Funding

The authors gratefully acknowledge the financial support of the Swiss Federal Institute of Technology Zurich (ETH Zurich) and open-access funding by ETH Zurich.

Acknowledgments

The authors would like to thank COMSOL AB and Jonas H. Jørgensen for their support. They would also like to thank Luca Rosenthaler for his work on the implementation of the limiting velocity method in COMSOL Multiphysics.

Conflict of interest

The authors declare that the research was conducted in the absence of any commercial or financial relationships that could be construed as a potential conflict of interest.

Publisher's note

All claims expressed in this article are solely those of the authors and do not necessarily represent those of their affiliated organizations, or those of the publisher, the editors, and the reviewers. Any product that may be evaluated in this article, or claim that may be made by its manufacturer, is not guaranteed or endorsed by the publisher.

Supplementary material

The Supplementary Material for this article can be found online at: https://www.frontiersin.org/articles/10.3389/fphy.2023.1182532/full#supplementary-material

References

1. Bruus H, Dual J, Hawkes J, Hill M, Laurell T, Nilsson J, et al. Forthcoming lab on a chip tutorial series on acoustofluidics: Acoustofluidics—Exploiting ultrasonic standing wave forces and acoustic streaming in microfluidic systems for cell and particle manipulation. *Lab Chip* (2011) 11:3579–80. doi:10.1039/c1lc90058g

2. Ovchinnikov M, Zhou J, Yalamanchili S. Acoustic streaming of a sharp edge. *The J Acoust Soc America* (2014) 136:22–9. doi:10.1121/1.4881919

3. Nama N, Huang PH, Huang TJ, Costanzo F. Investigation of acoustic streaming patterns around oscillating sharp edges. *Lab Chip* (2014) 14:2824–36. doi:10.1039/c4lc00191e

4. Doinikov AA, Gerlt MS, Pavlic A, Dual J. Acoustic streaming produced by sharp-edge structures in microfluidic devices. *Microfluidics and Nanofluidics* (2020) 24:32. doi:10.1007/s10404-020-02335-5

5. Zhang C, Guo X, Royon L, Brunet P. Unveiling of the mechanisms of acoustic streaming induced by sharp edges. *Phys Rev E* (2020) 102:043110. doi:10.1103/physreve.102.043110

6. Leibacher I, Hahn P, Dual J. Acoustophoretic cell and particle trapping on microfluidic sharp edges. *Microfluidics and Nanofluidics* (2015) 19:923–33. doi:10.1007/s10404-015-1621-1

7. Doinikov AA, Gerlt MS, Dual J. Acoustic radiation forces produced by sharp-edge structures in microfluidic systems. *Phys Rev Lett* (2020) 124:154501. doi:10.1103/physrevlett.124.154501

8. Huang PH, Nama N, Mao Z, Li P, Rufo J, Chen Y, et al. A reliable and programmable acoustofluidic pump powered by oscillating sharp-edge structures. *Lab Chip* (2014) 14:4319–23. doi:10.1039/c4lc00806e

9. Pavlic A, Harshbarger CL, Rosenthaler L, Snedeker JG, Dual J. Sharp-edge-based acoustofluidic chip capable of programmable pumping, mixing, cell focusing and trapping. *Phys Fluids* (2023) 35:022006. doi:10.1063/5.0133992

10. Nivedita N, Garg N, Lee AP, Papautsky I. A high throughput microfluidic platform for size-selective enrichment of cell populations in tissue and blood samples. *Analyst* (2017) 142:2558–69. doi:10.1039/c7an00290d

11. Garg N, Westerhof TM, Liu V, Liu R, Nelson EL, Lee AP. Whole-blood sorting, enrichment and *in situ* immunolabeling of cellular subsets using acoustic microstreaming. *Microsystems and Nanoengineering* (2018) 4:17085. doi:10.1038/micronano.2017.85

12. Huang PH, Xie Y, Ahmed D, Rufo J, Nama N, Chen Y, et al. An acoustofluidic micromixer based on oscillating sidewall sharp-edges. *Lab Chip* (2013) 13:3847–52. doi:10.1039/c3lc50568e

13. Nama N, Huang PH, Huang TJ, Costanzo F. Investigation of micromixing by acoustically oscillated sharp-edges. *Biomicrofluidics* (2016) 10:024124. doi:10.1063/1.4946875

14. Zhang C, Guo X, Brunet P, Costalonga M, Royon L. Acoustic streaming near a sharp structure and its mixing performance characterization. *Microfluidics and Nanofluidics* (2019) 23:104. doi:10.1007/s10404-019-2271-5

15. Muller PB, Barnkob R, Jensen MJH, Bruus H. A numerical study of microparticle acoustophoresis driven by acoustic radiation forces and streaming-induced drag forces. *Lab Chip* (2012) 12:4617–27. doi:10.1039/c2lc40612h

16. Rayleigh L. On the circulation of air observed in Kundt's tubes, and on some allied acoustical problems. *Phil Trans R Soc Lond* (1884) 175:1–21. doi:10.1098/rstl.1884.0002

17. Nyborg WL. Acoustic streaming due to attenuated plane waves. *The J Acoust Soc America* (1953) 25:68–75. doi:10.1121/1.1907010

18. Nyborg WL. Acoustic streaming near a boundary. *J Acoust Soc America* (1958) 30:329–39. doi:10.1121/1.1909587

19. Hahn P, Leibacher I, Baasch T, Dual J. Numerical simulation of acoustofluidic manipulation by radiation forces and acoustic streaming for complex particles. *Lab Chip* (2015) 15:4302–13. doi:10.1039/c5lc00866b

20. Lei J, Glynne-Jones P, Hill M. Acoustic streaming in the transducer plane in ultrasonic particle manipulation devices. *Lab Chip* (2013) 13:2133–43. doi:10.1039/c3lc00010a

21. Lei J, Hill M, Glynne-Jones P. Numerical simulation of 3d boundary-driven acoustic streaming in microfluidic devices. *Lab Chip* (2014) 14:532–41. doi:10.1039/c3lc50985k

22. Bach JS, Bruus H. Theory of pressure acoustics with viscous boundary layers and streaming in curved elastic cavities. *J Acoust Soc America* (2018) 144:766–84. doi:10.1121/1.5049579

23. Joergensen JH, Bruus H. Theory of pressure acoustics with thermoviscous boundary layers and streaming in elastic cavities. *J Acoust Soc America* (2021) 149:3599–610. doi:10.1121/10.0005005

24. Skov NR, Bach JS, Winckelmann BG, Bruus H. 3d modeling of acoustofluidics in a liquid-filled cavity including streaming, viscous boundary layers, surrounding solids, and a piezoelectric transducer. *Aims Math* (2019) 4:99–111. doi:10.3934/math.2019.1.99

25. Lei J, Hill M, de León Albarrán CP, Glynne-Jones P. Effects of micron scale surface profiles on acoustic streaming. *Microfluidics and Nanofluidics* (2018) 22:140–14. doi:10.1007/s10404-018-2161-2

26. Zhou Y. Effect of microchannel protrusion on the bulk acoustic wave-induced acoustofluidics: Numerical investigation. *Biomed Microdevices* (2022) 24:7–12. doi:10.1007/s10544-021-00608-6

27. Perra E, Hayward N, Pritzker KP, Nieminen HJ. An ultrasonically actuated needle promotes the transport of nanoparticles and fluids. *J Acoust Soc America* (2022) 152:251–65. doi:10.1121/10.0012190

28. Pavlic A, Nagpure P, Ermanni L, Dual J. Influence of particle shape and material on the acoustic radiation force and microstreaming in a standing wave. *Phys Rev E* (2022) 106:015105. doi:10.1103/physreve.106.015105

29. Orosco J, Friend J. Modeling fast acoustic streaming: Steady-state and transient flow solutions. *Phys Rev E* (2022) 106:045101. doi:10.1103/physreve.106.045101

30. Hamilton MF, Blackstock DT. *Nonlinear acoustics*. San Diego: Academic press San Diego (1998).

31. Lighthill J. Acoustic streaming. *J Sound Vibration* (1978) 61:391–418. doi:10.1016/0022-460x(78)90388-7

32. Bruus H. *Theoretical Microfluidics*, 18. Oxford University Press (2007).

33. Nyborg WLM. Acoustic streaming. In: *Physical acoustics*, 2. Elsevier (1965). p. 265–331.

34. Doinikov AA, Thibault P, Marmottant P. Acoustic streaming in a microfluidic channel with a reflector: Case of a standing wave generated by two counterpropagating leaky surface waves. *Phys Rev E* (2017) 96:013101. doi:10.1103/physreve.96.013101

35. Doinikov AA, Thibault P, Marmottant P. Acoustic streaming induced by two orthogonal ultrasound standing waves in a microfluidic channel. *Ultrasonics* (2018) 87:7–19. doi:10.1016/j.ultras.2018.02.002

36. Baasch T, Doinikov AA, Dual J. Acoustic streaming outside and inside a fluid particle undergoing monopole and dipole oscillations. *Phys Rev E* (2020) 101:013108. doi:10.1103/physreve.101.013108

37. Andrews DG, McIntyre M. An exact theory of nonlinear waves on a Lagrangian-mean flow. *J Fluid Mech* (1978) 89:609–46. doi:10.1017/s0022112078002773

38. Vanneste J, Bühler O. Streaming by leaky surface acoustic waves. *Proc R Soc A: Math Phys Eng Sci* (2011) 467:1779–800. doi:10.1098/rspa.2010.0457

39. Hamilton MF, Ilinskii YA, Zabolotskaya EA. Acoustic streaming generated by standing waves in two-dimensional channels of arbitrary width. *J Acoust Soc America* (2003) 113:153–60. doi:10.1121/1.1528928

40. Pavlic A, Dual J. On the streaming in a microfluidic Kundt's tube. *J Fluid Mech* (2021) 911:A28. doi:10.1017/jfm.2020.1046

41. Comsol AB. *COMSOL Multiphysics 5.6* (2020). Available at: www.comsol.com (March 08, 2023).

42. Baasch T, Pavlic A, Dual J. Acoustic radiation force acting on a heavy particle in a standing wave can be dominated by the acoustic microstreaming. *Phys Rev E* (2019) 100:061102. doi:10.1103/physreve.100.061102

43. Riaud A, Baudoin M, Matar OB, Thomas JL, Brunet P. On the influence of viscosity and caustics on acoustic streaming in sessile droplets: An experimental and a numerical study with a cost-effective method. *J Fluid Mech* (2017) 821:384–420. doi:10.1017/jfm.2017.178

44. Bach JS, Bruus H. Bulk-driven acoustic streaming at resonance in closed microcavities. *Phys Rev E* (2019) 100:023104. doi:10.1103/physreve.100.023104

45. Holmes M, Parker N, Povey M. Temperature dependence of bulk viscosity in water using acoustic spectroscopy. *J Phys Conf Ser* (2011) 269:012011. doi:10.1088/1742-6596/269/1/012011

46. Muller PB, Bruus H. Theoretical study of time-dependent, ultrasound-induced acoustic streaming in microchannels. *Phys Rev E* (2015) 92:063018. doi:10.1103/physreve.92.063018

47. Bruus H. Acoustofluidics 2: Perturbation theory and ultrasound resonance modes. *Lab Chip* (2012) 12:20–8. doi:10.1039/c1lc20770a

48. Kaynak M, Ozcelik A, Nama N, Nourhani A, Lammert PE, Crespi VH, et al. Acoustofluidic actuation of *in situ* fabricated microrotors. *Lab Chip* (2016) 16:3532–7. doi:10.1039/c6lc00443a

49. Kaynak M, Ozcelik A, Nourhani A, Lammert PE, Crespi VH, Huang TJ. Acoustic actuation of bioinspired microswimmers. *Lab Chip* (2017) 17:395–400. doi:10.1039/c6lc01272h

50. Dillinger C, Nama N, Ahmed D. Ultrasound-activated ciliary bands for microrobotic systems inspired by starfish. *Nat Commun* (2021) 12:6455. doi:10.1038/s41467-021-26607-y

51. Chen Z, Liu P, Zhao X, Huang L, Xiao Y, Zhang Y, et al. Sharp-edge acoustic microfluidics: Principles, structures, and applications. *Appl Mater Today* (2021) 25:101239. doi:10.1016/j.apmt.2021.101239

frontiers | Frontiers in Physics

TYPE Original Research
PUBLISHED 21 April 2023
DOI 10.3389/fphy.2023.1128265

OPEN ACCESS

EDITED BY
Zhixiong Gong,
Shanghai Jiao Tong University, China

REVIEWED BY
Kuo-Chih Chuang,
Zhejiang University, China
Zhichao Ma,
Shanghai Jiao Tong University, China

*CORRESPONDENCE
Shengzeng Zhou,
13501870217@139.com

SPECIALTY SECTION
This article was submitted to Physical Acoustics and Ultrasonics, a section of the journal Frontiers in Physics

RECEIVED 20 December 2022
ACCEPTED 24 February 2023
PUBLISHED 21 April 2023

CITATION
Ye T, Zhou S, Du X and Liu J (2023), Focusing higher-order Lamb waves based on the Luneburg lens. *Front. Phys.* 11:1128265. doi: 10.3389/fphy.2023.1128265

Focusing higher-order Lamb waves based on the Luneburg lens

Tianming Ye[1,2], Shengzeng Zhou[1,2]*, Xuanmin Du[1,2] and Jiaqi Liu[1,2]

[1]Shanghai Marine Electronic Equipment Research Institute, Shanghai, China, [2]National Key Laboratory of Science and Technology on Underwater Acoustic Antagonizing, Shanghai, China

In order to improve the spatial resolution and the signal-to-noise ratio of Lamb waves in structural health monitoring systems or non-destructive testing techniques, this study presents the construction of Luneburg lenses for focusing higher-order Lamb waves based on the thickness variation. The dispersion curves of Lamb waves are calculated firstly, from which the relation between the phase velocity of a specific mode and the plate thickness is quantified. After that, the plate thickness is determined via the refractive index variation. To demonstrate the generality of this design scheme, two lenses, i.e., the A1-wave-based Luneburg lens and the S2-wave-based Luneburg lens are constructed, and their focusing abilities are examined via numerical simulations in both the time domain and frequency domain. It is revealed that the A1 wave and S2 wave can be focused with a focusing size smaller than one wavelength. The design methodology is easy to realize and can be used to control higher-order Lamb waves efficiently, which also provides potential application values in wave detections and energy collections.

KEYWORDS

higher-order Lamb waves, Luneburg lens, refractive index, wave focusing phenomenon, ultrasound

1 Introduction

Lamb waves, propagating in a plate-type structure with two traction-free surfaces, have been widely applied in structural health monitoring (SHM) systems and non-destructive testing (NDT) techniques [1–3], which dues to their unique characteristics for long-distance and large-area detection. During the engineering application, efficiently receiving the Lamb wave signals and improving the signal-to-noise ratio (SNR) poses a considerable challenge. Accompanying that, wave focusing is viewed as the effective method to overcome it, as the wave energy is increased to improve the defect detection ability. Many methods have been proposed to focus Lamb waves, e.g., using the phased array transducer [4–6], forming the laser arc-array based on the arc-slit [7, 8], etc. With the development of microfabrication techniques, such as 3D printing, composite structures with multiple components or complex shapes have already been realized, which allows us to focus Lamb waves with the aid of phononic crystals (PCs) and metamaterials.

Generally speaking, PCs and metamaterials are artificial structures that assemble multiple elements or fabricate with a complex configuration, aiming to manipulate the propagation of structural and acoustic waves. Wave velocity can be easily controlled by introducing PCs and metamaterials into SHM systems and NDT techniques, such as the Lamb-wave-based gradient-index (GRIN) lens. The phase velocity and group velocity can be reduced and controlled by the additional artificial sub-component, which makes the Lamb wave propagate in a specified route designed previously. The refractive index of a typical GRIN-PC lens for focusing A0 mode Lamb waves satisfies a hyperbolic secant. For example,

Yan and Zhu et al. [9] achieved the hyperbolic secant distribution by using the surface bonded metamaterials with different heights, Tol and Degertekin et al. [10] formed the distribution by an array of blind holes with different diameters, Tian and Tan et al. [11] proposed rotating three-petal epoxy cylinders to satisfy a hyperbolic secant profile. However, the focusing ability of a hyperbolic secant lens is dependent on the orientation of the incident plane wave. A PC Luneburg lens, due to its omnidirectional focusing characteristics, has gained increasing attention from researchers. Tol and Degertekin et al. [12] presented a phononic crystal Luneburg lens numerically and experimentally, and the focusing performance of the A0 mode Lambs waves at different angles are confirmed. Jin and Torrent et al. [13] achieved controlling A0 and S0 Lamb waves simultaneously via graded phononic crystal plates of a circular Luneburg lens.

As we know, the A0 mode of Lamb waves in low-frequency regions can be approximated as the bending wave, with its phase velocity directly related to the plate thickness. Therefore, a relatively simple design methodology, i.e., adopting the thickness variation according to dispersion curves, is proposed to achieve the focusing and guiding of A0 waves [14–16]. Such as the Luneburg lens [14, 17] for focusing a plane wave and the Maxwell Fish-Eye lens [14, 15] for focusing the wave from a point source. The structure designed consists of only single-phase material with no joints and conjunctions between different components, which is beneficial for the fabrication and service life. To the authors' knowledge, the existing investigations concentrate on the A0 and S0 mode Lamb waves and focusing the higher-order Lamb waves has rarely been studied. However, the higher-order Lamb wave plays an important role in the NDT technique. To be more specific, the abundant higher-order modes provide various displacement and stress patterns for different detecting situations [18, 19]. Moreover, the non-linear effect of the higher-order Lamb waves provides high detecting sensitivity to micro defects, attracting much attention from scientists for damage detections [20–24]. To some extent, focused higher-order Lamb waves can further efficiently improve their performance in NDT and SHM.

This paper proposes two Luneburg lenses for focusing the higher-order Lamb waves, A1 and S2 modes, based on the thickness variation. These lenses are constructed according to the variation principle of the refractive index and the dispersion relationship of the higher-order Lamb waves. After the detailed demonstration of the present design scheme, some finite element simulations are conducted in both time and frequency domains, which prove the excellent focusing ability of the Luneburg lens for A1 and S2 waves. Not limited by A1 and S2 waves, the present design methodology is general and suitable for other higher-order modes of Lamb waves.

2 Design of the Luneburg lens for higher-order Lamb waves

Before designing a Luneburg lens for focusing the higher-order Lamb waves, calculating the frequency spectrum of Lamb waves is the prerequisite. For a plate with its upper and bottom surfaces

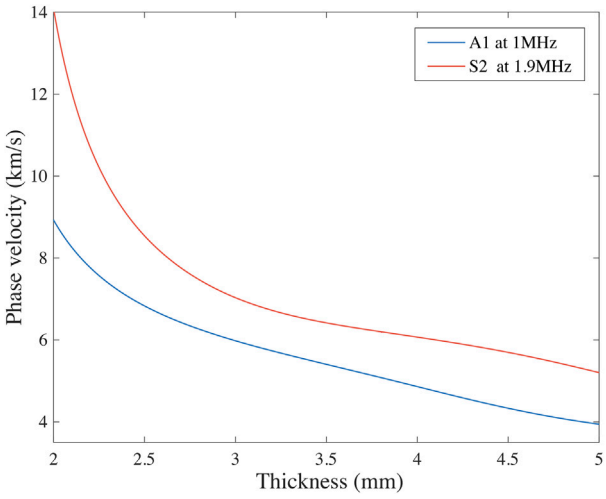

FIGURE 1
The phase velocity variation of the A1 and S2 modes with the plate thickness at some specific frequencies.

traction-free, the phase velocity of Lamb waves can be obtained from the dispersion relationship by solving the following Rayleigh-Lamb equations [25]:

$$\frac{\tan(qh)}{\tan(ph)} = -\frac{4k^2pq}{(q^2-k^2)^2}, \text{for symmetric modes,} \tag{1}$$

and

$$\frac{\tan(qh)}{\tan(ph)} = -\frac{(q^2-k^2)^2}{4k^2pq}, \text{for anti}-\text{symmetric modes.} \tag{2}$$

Here, the plate thickness is represented by $2h$. k is the wavenumber along the wave propagation direction and p and q are wavenumbers along the plate thickness with $p = \sqrt{\frac{\omega^2}{c_L^2} - k^2}$, $q = \sqrt{\frac{\omega^2}{c_T^2} - k^2}$, where $c_L = \sqrt{(\lambda + 2\mu)/\rho}$ and $c_T = \sqrt{\mu/\rho}$ are the longitude and transverse velocities, respectively. ω is the angular frequency, λ and μ are Lamé coefficients, and ρ is the mass density. These equations show that the dispersion relationship depends on the material parameters, frequency, and plate thickness, from which the phase velocities of different modes versus the plate thickness can be calculated. Taking an aluminum plate as an example, the corresponding Young's modulus, Poisson's ratio, and mass density of the aluminum plate are 70 GPa, 0.33, and 2,700 kg/m^3, respectively. Figure 1 shows the phase velocity variation with the plate thickness of the A1 and S2 modes at some specific frequencies by solving Eqs 1, 2. These two modes exhibit a similar tendency, i.e., the phase velocity decreases as the plate thickness increases, allowing us to control them using thickness variation.

Reviewing the Luneburg lens, its refractive index requires [12, 26–28]

$$n(r) = \sqrt{2 - (r/R)^2}, \tag{3}$$

where R is the lens radius and $n(r)$ is the refractive index as a function of the distance r to the center lens. Here, the refractive index can be calculated via $n = c_0/c$, where c_0 is the phase velocity of

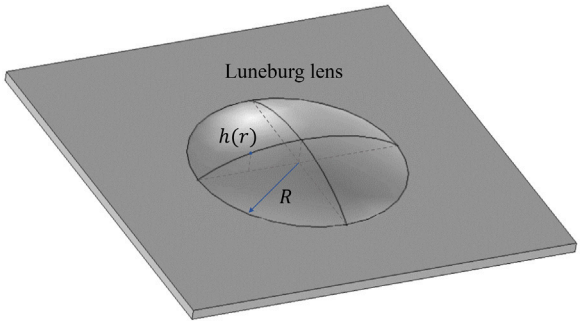

FIGURE 2
Schematic of the Luneburg lens designed for focusing the higher-order Lamb waves.

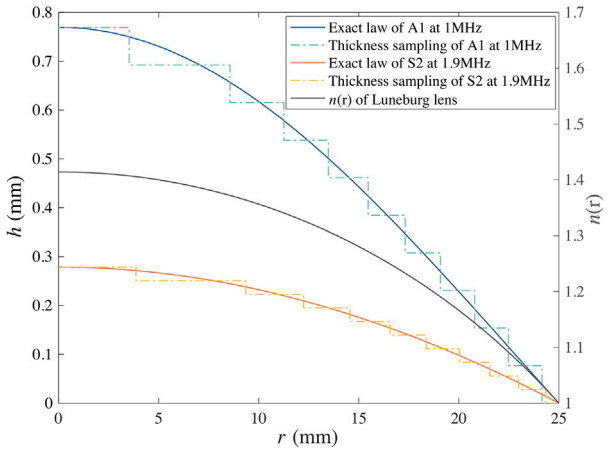

FIGURE 3
The variations of the refractive index and the thickness of the A1-wave-based Luneburg lens and S2-wave-based Luneburg lens along the radius direction. The black curve is the refractive index of the Luneburg lens. Blue and orange curves are the theoretical thickness profiles of the A1-wave-based Luneburg lens at 1 MHz and the S2-wave-based Luneburg lens at 1.9 MHz, respectively, and the discretized profiles are represented by the green and yellow dot-lines.

the specific Lamb wave in the base plate and c is that in the lens. According to Eq. 3, the center of the Luneburg has a relatively higher refractive index, and if a Luneburg lens for controlling higher-order modes with the refractive index satisfying Eq. 3 needs to be designed, the lens will possess a protruding surface with the lens center highest, such as Figure 2, where $h(r)$ is the thickness of the lens at distance r to the center lens.

To be noticed that the higher-order modes of the Lamb waves are converged to the transverse velocity as the frequency-thickness product increase so that there will be a range suitable for the method. The phase velocity of the mode at the working frequency should be higher than $\sqrt{2}c_T$, so that the effective frequency-thickness product range for this aluminum plate is from the cut-off frequency to 4.40, 8.84, 6.60, and 11.04 MHz-mm for A1 mode, A2 mode, S1 mode, and S2 mode, respectively.

In this paper, two Luneburg lenses for focusing the A1 wave at 1 MHz and the S2 wave at 1.9 MHz in a 2 mm aluminum plate, with a radius of 25 mm are designed. In that case, the phase velocity of A1 and S2 waves are 8.9275 km/s and 14.0845 km/s, respectively. With the help of Eq. 3 and the quantitative relations between the phase velocity and the plate thickness shown in Figure 1, the thickness variation of the lens with the radius can be calculated. The refractive index and the corresponding thickness variations of A1 and S2 modes along the radius direction are shown in Figure 3. To simplify the modeling, also facilitate the specimen preparation, continuous thickness variation of the theoretically designed Luneburg lens is discretized into ten sections with equal height variation in the radius direction. The phase velocity of the S2 wave at 1.9 MHz in Figure 1 has a more dramatic variation tendency with the plate thickness than the A1 wave at 1 MHz. Therefore, the thickness of the S2-wave-based Luneburg lens is smaller than that of the A1-wave-based Luneburg lens.

3 Numerical simulation and results

To validate the focusing ability of the Luneburg lenses designed, the FEM simulations in the time and frequency domains are carried out with the aid of COMSOL Multiphysics software. The schematic of the computational model used for the analysis is shown in Figure 4, where Figure 4A is the schematic model for the time domain analysis, and Figure 4B is the schematic model for the frequency domain analysis. The S2-wave-based Luneburg lens or the A1-wave-based Luneburg lens, constructed by ten concentric cylinders according to Figure 3, is built with its center at (0,0,0), with the same material as the aluminum plate. The calculation region of the plate is divided into finite elements, and to obtain reliable results, the element size is set to be smaller than one-eighth of the minimum wavelength of the designed higher-order mode. The time step is set according to the mesh size and time step length (Courant–Friedrichs–Lewy number lower than 0.2) to obtain the optimal solution. Low reflection boundary conditions are applied to the edge of the plate in the time domain analysis, and perfectly matched layers (PMLs) of length 2λ are connected to the edge in the frequency domain analysis to eliminate unwanted reflected waves from the boundaries.

To observe the focusing ability of the Luneburg lens for the designed modes at a specific frequency, the pure mode of the Lamb wave is generated by implementing a comb transducer. A typical comb transducer is an acoustic buffer with periodic teeth applied to the test samples, a spatial modulation technique. The activated mode lies on the intersecting points between the dispersion curves of Lamb waves and the line, where the slope of the line depends on the element spacing. The detailed feature of a comb transducer has been studied by Viktorov [29] and Rose [30–33], and according to the principle that the comb transducer requires, the element spacing l_s can be calculated according to the phase velocity c of the generated mode and the excitation frequency f_0 of the comb transducer, i.e.,

$$l_s = c/f_0 \tag{4}$$

Based on the lenses designed in this paper, the element spacing l_s of the comb transducer used for generating A1 mode at 1 MHz is

10.3389/fphy.2023.1128265

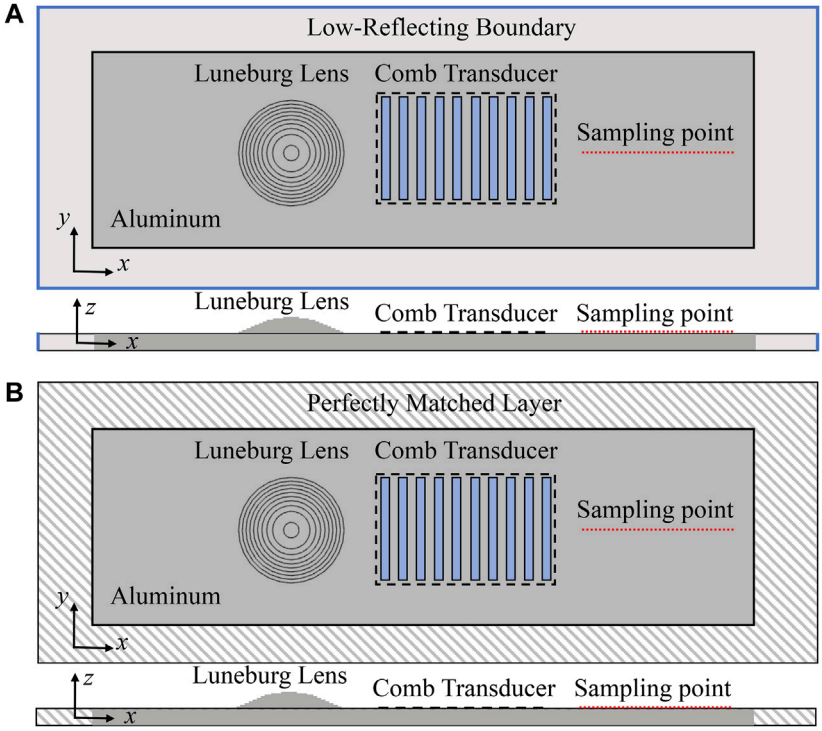

FIGURE 4
Schematic of the FEM model in a top view and side view: **(A)** the time domain analysis, **(B)** the frequency domain analysis.

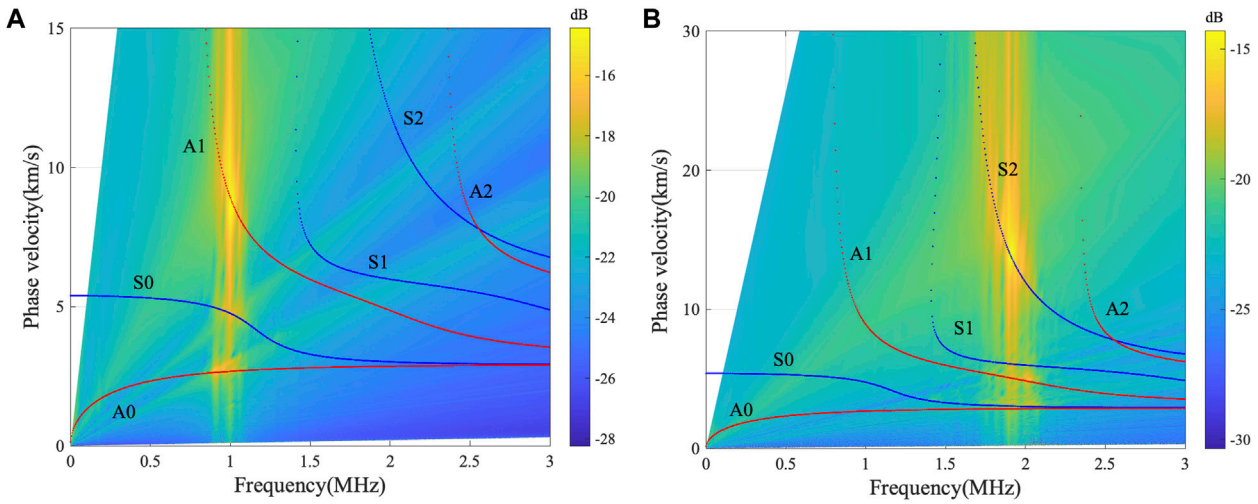

FIGURE 5
The dispersion curves and the two-dimensional Fourier transform results from FEM models: **(A)** the A1 wave at 1 MHz, **(B)** the S2 wave at 1.9 MHz. The red and blue curves are corresponding to the anti-symmetric modes and symmetric modes of the Lamb wave, respectively.

8.93 mm, and S2 mode at 1.9 MHz is 7.41 mm. Ten elements located 50 mm away from the Luneburg lens center are implemented, such as in Figure 4. Moreover, the duty ratio of the comb transducer is set at 0.5 to achieve the maximal excitation efficiency. The boundary load with 15 cycles of Gaussian windowed tone-burst signal is applied at the transducer region with the direction vertical to the plate surface, which is used to simulate the excitation of the comb transducer.

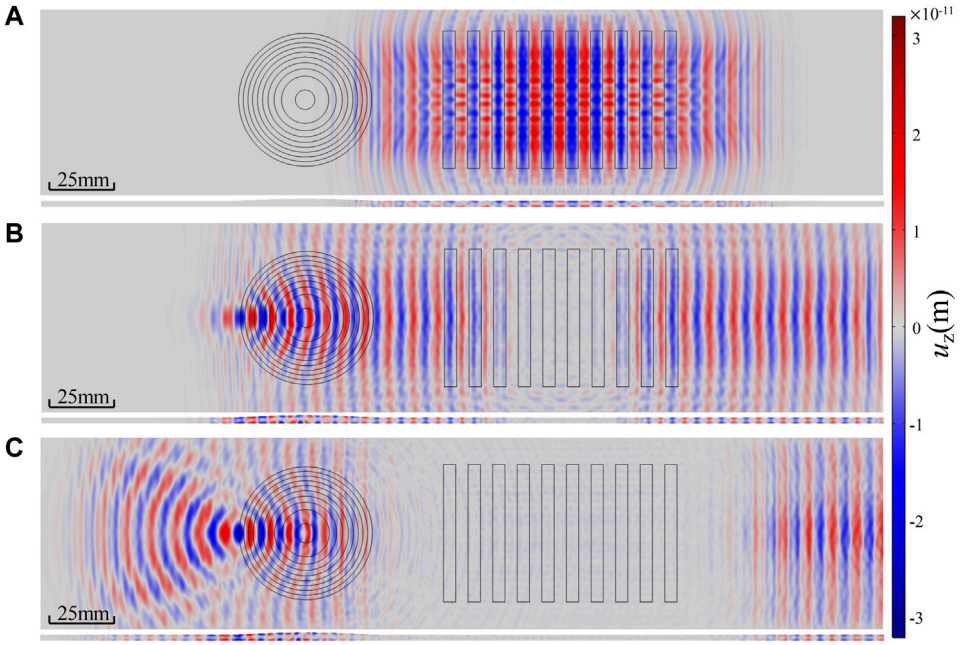

FIGURE 6
The focusing phenomenon of the A1-wave-based Luneburg lens at 1 MHz: **(A)** t = 15 μs, **(B)** t = 30 μs and **(C)** t = 45 μs.

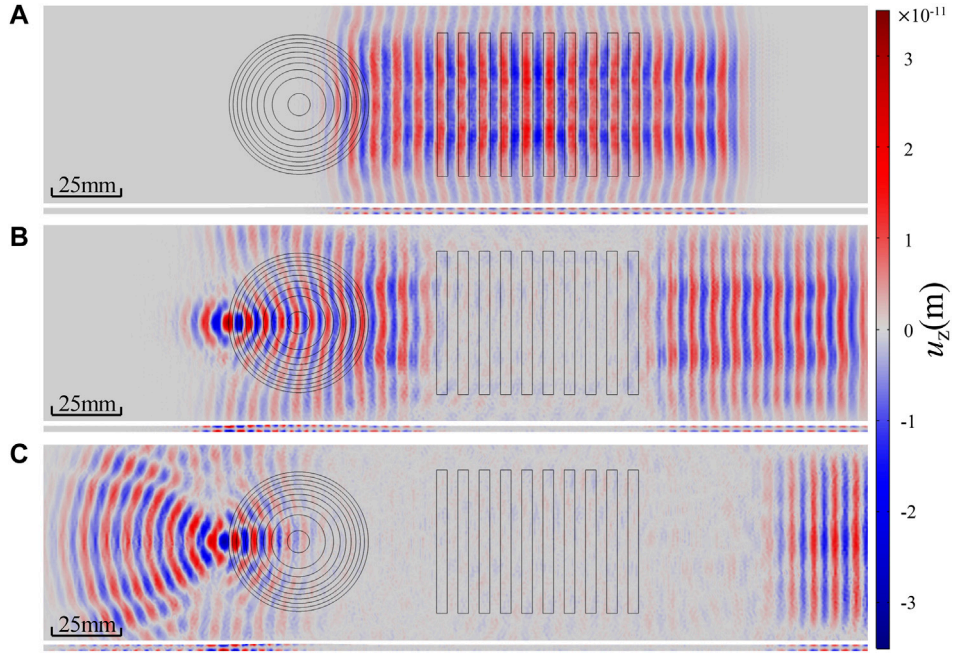

FIGURE 7
The focusing phenomenon of the S2-wave-based Luneburg lens at 1.9 MHz: **(A)** t = 15 μs, **(B)** t = 30 μs and **(C)** t = 45 μs.

Here, to prove the generation efficiency for pure A1 and S2 waves from the comb transducer, the two-dimensional Fourier transform is applied to the out-of-plane displacements, sampling from 512 points at the plate surface with the sampling interval 0.1 mm on the right side of the comb transducer. The numerical data in the f-c domain with the theoretical dispersion curves of

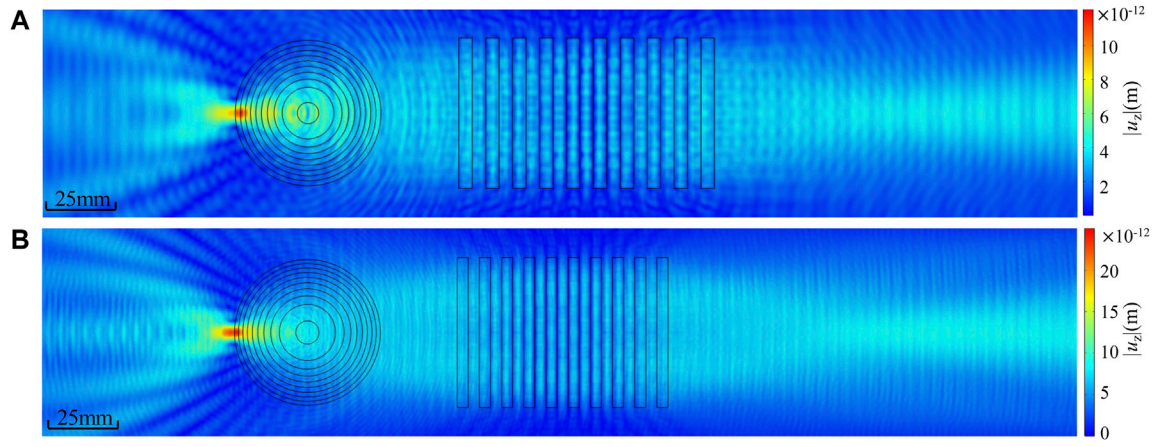

FIGURE 8
Spatial energy distribution represented by $|u_z|$ of **(A)** the A1-wave-based Luneburg lens at 1 MHz, and **(B)** the S2-wave-based Luneburg lens at 1.9 MHz.

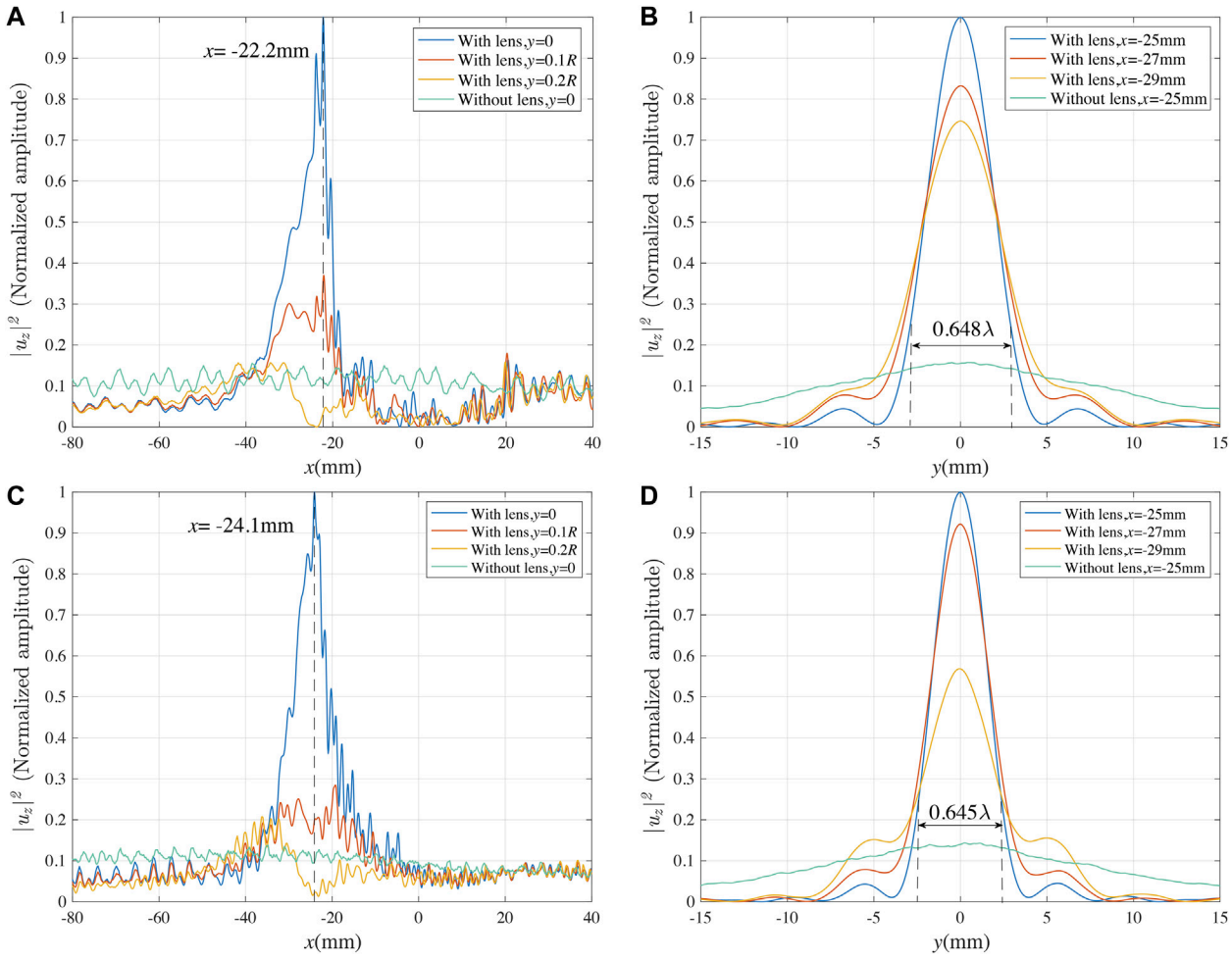

FIGURE 9
The spatial distribution of $|u_z|^2$ along the *x* and *y* directions: **(A)** and **(B)** correspond to the A1-wave-based Luneburg lens at 1 MHz; **(C)** and **(D)** correspond to the S2-wave-based Luneburg lens at 1.9 MHz.

the Lamb wave in an aluminum plate are shown in Figure 5. The highlighted part in the *f-c* spectrum represents the generated mode, showing that the narrowband Lamb mode of the desired mode is generated successfully with the help of the comb transducer and the 15 cycles Gaussian windowed tone-burst signal. Although other modes with small amplitudes near the center frequency are generated, A1 or S2 wave is still the dominant mode propagating in the plate, and the effect of other modes can be ignored.

Out-of-plane displacement wave fields at some specific time instants are displayed to observe the focusing phenomenon, such as the A1-wave-based Luneburg lens at 1 MHz in Figure 6 and the S2-wave-based Luneburg lens at 1.9 MHz in Figure 7. As shown in Figure 6A and Figure 7A, the plane A1 wave or S2 wave with a tiny and ignorable disturbance propagates along both $+x$ and $-x$ directions. Waves propagating near the lens edge region are faster than that across the lens center, which makes the wavefront bend towards the lens center and finally focus at the opposite point on edge, such as Figures 6B, 7B. After that, the A1 wave or S2 wave will emit from the focusing point, e.g., the out-of-plane displacement distribution in Figures 6C, 7C. The A1 or S2 wave propagation process clearly shows the focusing phenomenon of the Luneburg lenses designed.

The frequency domain analysis is also performed for quantitative investigations and further checking the focusing ability of the Luneburg lens for higher-order Lamb waves. The boundary load with the force of 100 N/m^2 is applied at the transducer region with the direction vertical to the plate surface to simulate the comb transducer excitation. Figures 8A, B show the spatial energy distribution represented by $|u_z|$ of the A1-wave-based Luneburg lens at 1 MHz and the S2-wave-based Luneburg lens at 1.9 MHz, respectively, from which the wave energy focusing phenomenon is extremely evident, i.e., the energy is successfully focused at the lens edge as expected. Also, the amplitude is greatly amplified compared with the corresponding regions on the right of the comb transducer.

Near the focusing point, the $|u_z|^2$ value is extracted, and its spatial variations along the x and y directions are illustrated in Figures 9A,C and B,D, respectively. By contrast, the $|u_z|^2$ value in the right regions of the comb transducers without lenses is mirrored and also displayed in Figure 9. Generally speaking, the wave focusing phenomenon is validated once again. Theoretically, the A1 or S2 wave focuses at (−25 mm, 0) after it travels across the lens. However, the $|u_z|^2$ value achieves the maximum, respectively at (−22.2 mm, 0) for the A1 wave and (−24.1 mm, 0) for the S2 wave, a little deviated from the theoretical prediction. Two main issues may lead to the slight difference. One is the discretized variation of the lens thickness, and the other is the incident quasi-plane wave generated by the comb transducers. Even though the deviation, smaller than one wavelength, is acceptable.

The focusing size in the y direction is evaluated by using the −3 dB attenuation of the displacement amplitude $|u_z|$, the quarter of maximal $|u_z|^2$ [27], and shown in Figures 9B, D. Specifically, the focusing sizes for the A1-wave-based Luneburg lens and the S2-wave-based Luneburg lens are 0.648λ and 0.645λ, respectively, both smaller than one corresponding wavelength, which efficiently proves the excellent focusing ability of the Luneburg lens for the higher-order Lamb waves at the designed frequency.

4 Conclusion and perspectives

In conclusion, a design scheme for focusing the higher-order Lamb waves, based on the sensitivity of the phase velocity with the plate thickness, is introduced. To examine the feasibility of this methodology, two lenses, i.e., the A1-wave-based Luneburg lens and the S2-wave-based Luneburg lens, are designed via different thickness variations. The analysis in the time and frequency domains clearly shows the excellent focusing phenomenon for higher-order Lamb waves. This design method and the outcomes in this paper provide theoretical foundations for wave manipulation and energy harvesting, as well as the receiving and application of higher-mode Lamb waves in SHM.

As a final remark, this paper presents a general design scheme for focusing higher-order Lamb waves, although the Luneburg lens is designed for a single and fixed working frequency. Any higher-order mode, not limited by A1 and S2 waves, can be focused using this method as long as its phase velocity is sensitive to the plate thickness. For example, this method is suitable for all higher-order modes if the operating frequency is near their cut-off frequencies. However, if the working frequency is far from the cut-off frequencies, the phase velocities of these modes approach the inherent shear wave, insensitive to the thickness, and thus not be adopted for the lens design. It should be pointed out that other lenses can also be constructed using the present method, such as Maxwell's fisheye lens, the concentrator lens, and other gradient index lenses. We expect this method and the Luneburg lenses designed for high-order Lamb waves will stimulate future experimental work and extend their practical engineering applications.

Data availability statement

The raw data supporting the conclusion of this article will be made available by the authors, without undue reservation.

Author contributions

TY: Methodology (lead); Formal analysis (lead); validation (lead); Writing—original draft (lead). SZ: Project administration (lead); Writing-review and editing (equal). XD: supervision (lead); JL: funding acquisition (lead); Writing-review and editing (equal). All authors contributed to the article and approved the submitted version.

Funding

Sponsored by Shanghai Pujiang Program.

Conflict of interest

The authors declare that the research was conducted in the absence of any commercial or financial relationships that could be construed as a potential conflict of interest.

Publisher's note

References

1. Cawley P, Alleyne D. The use of Lamb waves for the long range inspection of large structures. *Ultrasonics* (1996) 34:287–90. doi:10.1016/0041-624X(96)00024-8

2. Wilcox PD, Lowe MJS, Cawley P. Mode and transducer selection for long range lamb wave inspection. *J Intell Mater Syst Struct* (2001) 12:553–65. doi:10.1177/10453890122145348

3. Rose JL. A baseline and vision of ultrasonic guided wave inspection potential. *J Press Vessel Technol* (2002) 124:273–82. doi:10.1115/1.1491272

4. Kudela P, Radzienski M, Ostachowicz W, Yang Z. Structural Health Monitoring system based on a concept of Lamb wave focusing by the piezoelectric array. *Mech Syst Signal Process* (2018) 108:21–32. doi:10.1016/j.ymssp.2018.02.008

5. Malinowski P, Wandowski T, Trendafilova I, Ostachowicz W. A phased array-based method for damage detection and localization in thin plates. *Struct Health Monit* (2009) 8:5–15. doi:10.1177/1475921708090569

6. Deutsch WAK, Cheng A, Achenbach JD. Self-focusing of Rayleigh waves and lamb waves with a linear phased array. *Res Nondestructive Eval* (1997) 9:81–95. doi:10.1080/09349849709409609

7. Kim H, Jhang K, Shin M, Kim J. A noncontact NDE method using a laser generated focused-Lamb wave with enhanced defect-detection ability and spatial resolution. *NDT E Int* (2006) 39:312–9. doi:10.1016/j.ndteint.2005.09.001

8. Jhang KY, Shin MJ, Lim BO. Application of the laser generated focused-Lamb wave for non-contact imaging of defects in plate. *Ultrasonics* (2006) 44:1265–8. doi:10.1016/j.ultras.2006.05.080

9. Yan X, Zhu R, Huang G, Yuan F-G. Focusing guided waves using surface bonded elastic metamaterials. *Appl Phys Lett* (2013) 103:121901. doi:10.1063/1.4821258

10. Tol S, Degertekin FL, Erturk A. Gradient-index phononic crystal lens-based enhancement of elastic wave energy harvesting. *Appl Phys Lett* (2016) 109:063902. doi:10.1063/1.4960792

11. Tian Y, Tan Z, Han X, Li W. Phononic crystal lens with an asymmetric scatterer. *J Phys D Appl Phys* (2019) 52:025102. doi:10.1088/1361-6463/aae679

12. Tol S, Degertekin FL, Erturk A. Phononic crystal Luneburg lens for omnidirectional elastic wave focusing and energy harvesting. *Appl Phys Lett* (2017) 111:013503. doi:10.1063/1.4991684

13. Jin Y, Torrent D, Pennec Y, Pan Y, Djafari-Rouhani B. Simultaneous control of the S 0 and A 0 Lamb modes by graded phononic crystal plates. *J Appl Phys* (2015) 117:244904. doi:10.1063/1.4923040

14. Climente A, Torrent D, Sánchez-dehesa J. *Sound focusing by gradient index sonic* (2016) 104103. doi:10.1063/1.3488349

15. Lefebvre G, Dubois M, Beauvais R, Achaoui Y, Ing RK, Guenneau S, et al. Experiments on Maxwell's fish-eye dynamics in elastic plates. *Appl Phys Lett* (2015) 106:024101. doi:10.1063/1.4905730

16. Tian Z, Yu L Rainbow trapping of ultrasonic guided waves in chirped phononic crystal plates. *Sci Rep* (2017) 1:1–7.

17. Wang DF, Wang YH, Chuang KC. Nearly-isotropic adjustable phononic crystal lenses using concentrated balls with Hertz contacts. *Phys Lett A* (2021) 396:127240. doi:10.1016/J.PHYSLETA.2021.127240

18. Ren B, Lissenden CJ. Ultrasonic guided wave inspection of adhesive bonds between composite laminates. *Int J Adhes Adhes* (2013) 45:59–68. doi:10.1016/j.ijadhadh.2013.04.001

19. Lanza di Scalea F, Rizzo P, Marzani A. Propagation of ultrasonic guided waves in lap-shear adhesive joints: Case of incident a0 Lamb wave. *J Acoust Soc Am* (2004) 115:146–56. doi:10.1121/1.1630999

20. Lee T, Choi I, Jhang K. The nonlinearity of guided wave in an elastic plate. *Mod Phys Lett B* (2008) 22:1135–40. doi:10.1142/S0217984908015966

21. Lissenden C. *Use of non-linear ultrasonic guided waves for early damage detection Use of non-linear ultrasonic guided waves for early damage detection* (2015). doi:10.1784/insi.2015.57.4.206

22. Hong M, Su Z, Wang Q, Cheng L, Qing X. Modeling nonlinearities of ultrasonic waves for fatigue damage characterization: Theory, simulation, and experimental validation. *Ultrasonics* (2014) 54:770–8. doi:10.1016/j.ultras.2013.09.023

23. Wang Y, Guan R, Lu Y *Nonlinear Lamb waves for fatigue damage identification in FRP- reinforced steel plates*, 80 (2017). p. 87–95. doi:10.1016/j.ultras.2017.05.004

24. Ye T, Biwa S, Mori N. Second-harmonic generation of the lowest-order antisymmetric Lamb wave at a closed parallel crack. *J Acoust Soc Am* (2020) 148:2073–85. doi:10.1121/10.0002171

25. Rose JL. *Ultrasonic guided waves in solid media*. Cambridge University Press (2014).

26. Climente A, Torrent D, Sánchez-Dehesa J. Gradient index lenses for flexural waves based on thickness variations. *Appl Phys Lett* (2014) 105:064101. doi:10.1063/1.4893153

27. Li P, Biwa S. The SH0 wave manipulation in graded stubbed plates and its application to wave focusing and frequency separation. *Smart Mater Struct* (2019) 28:115004. doi:10.1088/1361-665x/ab3ef0

28. Fuentes-Domínguez R, Yao M, Colombi A, Dryburgh P, Pieris D, Jackson-Crisp A, et al. Design of a resonant Luneburg lens for surface acoustic waves. *Ultrasonics* (2021) 111:106306. doi:10.1016/j.ultras.2020.106306

29. Viktorov IA, Mason WP. *Rayleigh and Lamb waves: Physical theory and applications*. New York: Plenum Press (1967).

30. Rose JL. Ultrasonic comb transducer for smart materials. in, Proceedings Volume 3321, 1996 Symposium on Smart Materials, Structures, and MEMS; (1998) (1998), V. K. Aatre, V. K. Varadan, V. v. Varadan, 636–43. doi:10.1117/12.305600

31. Rose JL, Pelts SP, Quarry MJ. A comb transducer model for guided wave NDE. *Ultrasonics* (1998) 36:163–9. doi:10.1016/S0041-624X(97)00042-5

32. Pelts SP, Jiao D, Rose JL. Comb transducer for guided wave generation and mode selection. *Proc IEEE Ultrason Symp* (1996) 2:857–60. doi:10.1109/ULTSYM.1996.584128

33. Rose JL, Pelts SP, Barshinger JN, Quarry MJ. An ultrasonic comb transducer for guided wave mode selection in materials characterization. In: *Nondestructive characterization of materials VIII*. Boston, MA: Springer US (2023). p. 695–700. doi:10.1007/978-1-4615-4847-8_109

frontiers | Frontiers in Physics

TYPE Original Research
PUBLISHED 30 May 2023
DOI 10.3389/fphy.2023.1191160

OPEN ACCESS

EDITED BY
Feiyan Cai,
Chinese Academy of Sciences (CAS), China

REVIEWED BY
Ould El Moctar,
University of Duisburg-Essen, Germany
A-Man Zhang,
Harbin Engineering University, China

*CORRESPONDENCE
Yong-Ou Zhang,
zhangyo@whut.edu.cn

RECEIVED 21 March 2023
ACCEPTED 17 May 2023
PUBLISHED 30 May 2023

CITATION
Li Y-F, Zhang Y-O, Qu Y and Zhang T (2023), A numerical approach for acoustic radiation and scattering of moving bubbles at low frequencies. *Front. Phys.* 11:1191160. doi: 10.3389/fphy.2023.1191160

A numerical approach for acoustic radiation and scattering of moving bubbles at low frequencies

Yi-Fan Li[1], Yong-Ou Zhang[1]*, Yao Qu[1] and Tao Zhang[2]

[1]School of Naval Architecture, Ocean, and Energy Power Engineering, Wuhan University of Technology, Wuhan, China, [2]School of Naval Architecture and Ocean Engineering, Huazhong University of Science and Technology, Wuhan, China

The acoustic radiation and scattering of underwater bubbles play an important role in ocean exploration, target localization, acoustic measurements, *etc.* The two-phase fluid flow and moving boundary result in the lack of means to predict the sound field, which limits the exploration of relevant characteristics and mechanisms. The present work is intended to introduce a numerical approach for acoustic radiation and scattering of moving bubbles at low frequencies with CFD-BEM coupling method. The two-phase interface is captured with the volume of fluid scheme and the sound field is solved with the boundary element method. After that, some benchmark problems are solved and the results are compared with data from literatures. Finally, the radiation and scattering of moving bubbles at low frequencies are predicted with our approach. The acoustic radiation pressure of bubbles shows a slight increase trend during deformation. As the *ka* value increases, both the acoustic directionality of radiation and scattering exhibit main and side lobes, and the scattering energy gradually concentrates in the positive direction of the incident wave. For a moving bubble, its displacement and velocity of moving have a significant impact on the directionality of the scattered sound field. Therefore, the problem of bubble localization can be studied based on directionality shift.

KEYWORDS

moving bubble, computational fluid dynamics, boundary element method, acoustic scattering, acoustic radiation

1 Introduction

The research of acoustic radiation in gas-liquid two-phase medium is the theoretical basis for the development of technologies such as ocean exploration, target localization and acoustic measurement. For decades, researchers have conducted extensive and in-depth research on the acoustic radiation and scattering properties of bubbles.

The research of acoustic propagation of bubbles can be traced back to 1917, Rayleigh [1] derived the pressure equation during collapsing bubble based on the phenomenon of sound generated by bubble breakage in boiling water. Then the motion equation of a spherical bubble under incompressible flow conditions was established. Since the Rayleigh's equation tended to be idealized and cannot accurately describe the behavior of bubbles in reality, many researchers subsequently modified the equation under different conditions [2–5]. Zhang et al. [6] have proposed a bubble dynamic equation that can simultaneously consider the effects of boundary, bubble interaction, environmental flow field, gravity, bubble migration, fluid compressibility, viscosity and surface tension, and achieved good results. Minnaert [7] was the first to study the vibration of bubbles separated from the nozzle He analyzed the

small oscillation of a single spherical bubble, and gave an expression for the intrinsic frequency of the bubble. Some researchers paid attention to the violent bubbles with large amplitude vibration, such as bubbles generated by underwater explosion, they analyzed the pulsating pressure and radiation noise produced by collapsing bubble [8–10]. Twersky [11] used the Bessel-Lejeuneade series to characterize the acoustic scattering at a relatively small equivalent frequency (*ka*) and derived a theoretical solution for the sound scattering of a small sphere. Subsequently, the results of the scattering problem of elastic spheres in fluids were also discussed [12], and these theoretical predictions were confirmed by a large number of experiments [13]. In 1994, Leighton [14] summarized the contents of previous studies on bubble acoustics in different fields and published the book *The Acoustic Bubble*, and the theoretical system of bubble acoustics was basically established.

Before the 21st century, due to the incomplete understanding of bubbles, the research on the acoustic field of bubbles was mainly focused on the theoretical model. With the rapid development of computers, the improvement of computational efficiency and accuracy has provided great convenience for the numerical simulation of bubble acoustics. Using CFD commercial software to calculate the motion and acoustics of bubbles has been a widely used means [15], such as ANSYS Fluent and COMSOL Multiphysics. The main methods for predicting the acoustic field include the integral equation method [16], the T-matrix method [17], the finite element method (FEM) [18], and the boundary element method (BEM) [19].

The BEM can reduce the computational dimension and improve the computational efficiency, so it was suitable for the calculation of acoustic radiation problems [20]. Chen [21] used the BEM to simulate the underwater acoustic radiation and scattering of multiple stationary objects. Fan [22] studied the acoustic scattering problems of stationary bubbles based on the BEM, and obtained accurate results. Many researchers have also taken different approaches to calculate the acoustic field in the frequency and time domains. Liu [23] combined large eddy simulation and acoustic analogy to predict the acoustic characteristics of bubble formation at the nozzle. Zhang et al. [24] combined radial point interpolation with implicit time integration to analyze the underwater acoustic propagation problem. Cong [25] combined experiments and numerical simulations to analyze the flow pattern and acoustic properties of the bubble. In addition, Chai et al. [26, 27] used FEM and the meshless method to study the distribution of the acoustic field.

With the deeper understanding of bubble acoustics, the research of bubble acoustic radiation and scattering has been gradually improved. However, due to the complexity of flow-acoustic coupling analysis, most of the current studies on acoustic scattering were about stationary objects [28], and there were few studies on the acoustic scattering of moving bubbles. Therefore, this paper calculated the acoustic radiation and scattering of moving bubbles at low frequencies based on the coupled CFD-BEM method. The research is as follows: the calculation method of flow field and the acoustic BEM are introduced in Chapter 2, the calculation procedure of acoustic field used in this paper is verified in Chapter 3, the results with analysis of acoustic radiation and scattering about moving bubbles are shown in Chapter 4 and Chapter 5 respectively, and the conclusions are included in Chapter 6.

2 Numerical model

The motion and acoustic scattering of bubbles in water involve two-phase fluid flow and flow-acoustic coupling process. In this work, the flow field was predicted by the CFD commercial software, which captured the boundary information during the bubble motion based on the volume of fluid method (VOF). Then, the boundary information is used as the initial condition for BEM to calculate the acoustic field. The pressure and velocity at the boundary of a bubble during its movement can be calculated in the flow field, which are transformed into pulsating pressure and vibration velocity that can be used for acoustic calculations through Fourier transform. This CFD-BEM coupling calculation belongs to the one-way coupling and is an explicit algorithm.

2.1 VOF for flow field

The prediction of flow field in present work is based on the Navier-Stokes (N-S) equation, which is based on the following assumptions: 1) the moving of bubble is isothermal and adiabatic, there is no heat transfer occurs with the external environment, 2) the gas and liquid in the model are incompressible Newtonian fluids, 3) the interaction between the gas and liquid happens only at the interface. According to the law of conservation of mass, the continuity equation of fluid motion is deduced as

$$\nabla \boldsymbol{u} = 0 \tag{1}$$

in which $\boldsymbol{u}$ represents the velocity of the fluid flow, ∇ is the Laplace operator.

$$\nabla = \frac{\partial}{\partial x} + \frac{\partial}{\partial y} + \frac{\partial}{\partial z} \tag{2}$$

According to Newton's second law, the momentum equation for an incompressible viscous fluid is derived as

$$\frac{\partial \rho \boldsymbol{u}}{\partial t} + \nabla \cdot \rho \boldsymbol{u}\boldsymbol{u} = -\nabla \rho + \nabla \cdot \left[\mu (\nabla \boldsymbol{u})^T\right] + \rho \boldsymbol{g} \tag{3}$$

in which ρ denotes the density of the liquid, t is the time of moving μ is the viscosity coefficient of the fluid; $\boldsymbol{g}$ is the acceleration of gravity.

Due to the shape of the bubble is changeable, the interface change has a great influence on the movement of bubbles. Various complex phenomena in the movement of bubbles are also related to the interaction of gas-liquid phase at the interface. Therefore, the VOF model is used for the prediction of the bubble surface, tracking the moving interface on the basis of a fixed Eulerian grid. Because the VOF method does not track the movement of fluid particles, it has the advantages of implementation, the amount of calculation and accuracy.

The VOF method is proposed by Hirt [29] in 1981, which is based on the principle that the fluid is divided into target fluid and non-target fluid. Then the fluid is tracked by calculating the volume

fraction of each phase in the grid, so as to determine the interface of two phases. The volume function can be obtained as follows.

$$C = \frac{\alpha}{Q} \tag{4}$$

in which α is the volume of the target fluid in the grid, α represents the volume of gas in this work, Q is the grid volume.

There are three types of results.

(1) $C = 0$: there is no target fluid in the grid,
(2) $0 < C < 1$: the interior of the grid contains both the target fluid and the non-target fluid, which represented as an interface,
(3) $C = 1$: the interior of the grid is target fluid.

The prediction of the flow field of the bubble in this paper was based on the commercial CFD software ANSYS Fluent. The VOF model and the SIMPLE algorithm was used to solve the N-S equation, the Euler scheme was adopted for the time discretization.t. In addition, the standard k-ε model was adopted as the turbulence model. Under the above conditions, the bubble floating and deformation in the gravity field were simulated. The boundary information of the bubble was captured for the acoustic field calculation.

2.2 BEM for acoustic field

Sound is a mechanical wave existing in elastic medium. Acoustic field is the space where acoustic waves exist. Due to the perturbation of acoustic wave, parameters such as density and pressure of the medium change with time and space. The calculation of the acoustic field in this work is based on the following assumptions: 1) the medium is an ideal fluid without viscosity, 2) the medium is assumed to be homogeneous and stationary, 3) the process of the sound propagating is adiabatic, 4) the amplitude of acoustic wave is small.

Based on the above assumptions, according to the law of conservation of mass (continuity equation), the law of conservation of momentum (equation of motion) and the physical state of the medium (equation of matter), the corresponding linearized equations are obtained by omitting the higher order minima. So as to obtain the linear acoustic fluctuation equation in a homogeneous medium.

$$\nabla^2 p(r,t) - \frac{1}{c^2}\frac{\partial^2 p(r,t)}{\partial t^2} = 0 \tag{5}$$

in which $p(r,t)$ represents the pressure function, r is the distance of the wave propagation., c is the speed of sound.

Supposing there is a simple harmonic wave in the sound field, the sound pressure at any point can be expressed as

$$p = Pe^{i\omega t} \tag{6}$$

in which P is the amplitude of sound pressure at any point, i is an imaginary unit, and ω is the circular frequency, $\omega = 2\pi f$, f is the frequency of the wave.

Helmholtz equation can be obtained by bringing Eq. 6 into Eq. 5:

$$\nabla^2 p + k^2 p = 0 \tag{7}$$

in which k represents the wave number, $k = \omega/c$.

The calculation of the acoustic field is to solve Eq. 7 according to different boundary conditions. The acoustic boundary conditions are generally divided into the following three types: velocity boundary condition (Neumann boundary condition), acoustic pressure boundary condition (Dirichlet boundary condition) and impedance boundary condition (Robin boundary condition). The boundary condition of the bubble is the pressure and velocity are continuous on the bubble surface, Neumann and Dirichlet boundary conditions are both used in the following simulation. It needs to be noted that the velocity and pressure obtained from flow field calculations cannot be directly used as boundary conditions, which require Fourier transform to be coupled into acoustic calculations. Since the radius of the bubble is small relative to the wavelength of the plane wave, the computational situation can be simplified by using the Born approximation [30].

The BEM is based on the integral theorem to transform the differential equation in the solution domain into an integral equation on the boundary. Then the boundary is divided into finite size boundary elements, finally transformed into the algebraic equation to solve. The Helmholtz equation is discretized by Gaussian integration. The types of calculations include internal and external problems. Solving the radiated and scattered sound fields of the bubble belongs to the external problem. The general expression of the boundary integral equation of the field point can be obtained by numerical derivation of Eq. 7 using Green's formula.

$$\int_v (\Psi\nabla^2 p - p\nabla^2\Psi)dv = \int_s \left(\Psi\frac{\partial p}{\partial n} - p\frac{\partial \Psi}{\partial n}\right)ds \tag{8}$$

in which v is the vibration velocity, s is the area of integration, n is the normal vector of the integration surface, ψ is the fundamental solution of the accompanying equation.

$$\Psi = A\frac{e^{-ikr}}{r} + B\frac{e^{ikr}}{r} \tag{9}$$

in which A and B are directional factors, r is the distance from the measuring point to the boundary.

Assuming that the fundamental solution and the sound pressure satisfy Eq. 8, the relationship between the sound pressure at the field point and the boundary information is obtained as follows

$$p(P) = \int_s \left(\Psi\frac{\partial p}{\partial n} - p\frac{\partial \Psi}{\partial n}\right)ds \tag{10}$$

Therefore, for the problem of acoustic radiation in the external field, the sound pressure at any field point in the domain can be solved by the sound pressure on the surface of the objects and the vibration velocity of surface particles. However, there is a problem that the solution of boundary integral equation (CBIE) is not unique at the characteristic frequency in the common BEM. The following is the expression of the CBIE for the acoustic scattering problem.

$$c(\boldsymbol{x})p(\boldsymbol{x}) = \int_\Gamma G(\boldsymbol{x},\boldsymbol{y})q(\boldsymbol{y})\mathrm{d}\Gamma(\boldsymbol{y}) - \int_\Gamma \frac{\partial G(\boldsymbol{x},\boldsymbol{y})}{\partial n(\boldsymbol{y})}p(\boldsymbol{y})\mathrm{d}\Gamma(\boldsymbol{y}) + p_{in}(\boldsymbol{x}), \boldsymbol{x} \in \Gamma \tag{11}$$

In which, $G(\boldsymbol{x}, \boldsymbol{y})$ represents the Green's function, $p(\boldsymbol{x})$ and $q(\boldsymbol{x})$ represent the sound pressure and sound flux at the point on the boundary respectively, $c(\boldsymbol{x})$ determined by the geometric features at

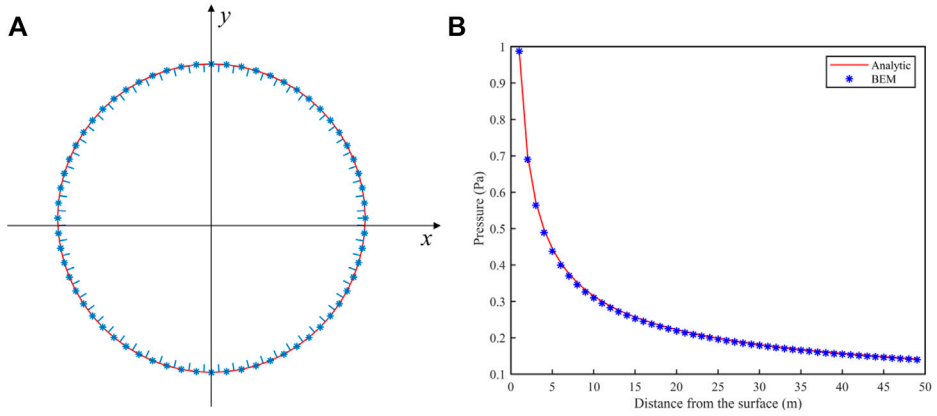

FIGURE 1
(A) Bubble boundary meshing. **(B)** Comparison between numerical and analytical solutions of acoustic radiation from an infinitely long rigid cylinder.

point $\boldsymbol{x}$, $p_{in}(\boldsymbol{x})$ is the incident sound pressure at point $\boldsymbol{x}$, Γ represents the integral region.

In this work, CHIEF method was used to configure some points (CHIEF points) outside the sound field area. The integral equation of CHIEF points can be combined with the boundary integral equation to form an overdetermined equation, thus solving the problem that the solution is not unique at the characteristic frequency.

In solving the coefficient matrix of boundary nodes, if the computational source point is close to or even coincides with the element node, the fundamental solution of Green's function has first-order singularity, which affects the calculation accuracy. For the singular integral problem, this paper used the method of coordinate transformation to introduce the Jacobi matrix to eliminate the singular integral.

3 Verification of acoustic BEM program and flow field simulation

Based on the assumptions of sound field calculation given in Chapter 2, the acoustic radiation of the bubble can be calculated by the analytical formula. Then the numerical solution calculated by BEM was compared with the analytical solution to verify the effectiveness of BEM. Subsequently, the accuracy of flow field calculation was verified through grid convergence analysis and literature comparison.

3.1 Acoustic radiation from an infinitely long rigid cylinder

The analytical formula for the acoustic radiation from an infinitely long cylindrical surface in *Fourier Acoustics* [31] is as follows

$$p(r,\phi) = i\rho_0 c u_0 \frac{H_0(kr)}{H_0'(ka)} \tag{12}$$

where H_0 is the Bessel function of the third kind, a is the radius of the cylinder, r is the distance between the measuring point and the cylindrical surface, ρ_0 is the medium density, u_0 is the vibration velocity of the cylindrical surface, ϕ is the angle in the three-dimensional space. When calculating, a = 1 m, ka = 1, u_0 = 1 m/s.

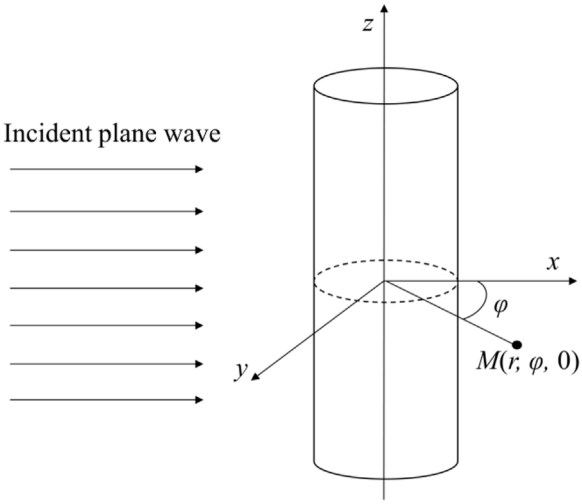

FIGURE 2
A scattering model of infinitely long rigid long cylinder.

Based on the BEM program, the circumferential boundary of the two-dimensional infinitely and long cylinder was discretized, and was divided into 64 linear elements, as shown in Figure 1A. Due to the symmetry of the cylinder, a Cartesian coordinate system was established with the center of the circle as the coordinate origin. Then, starting from the surface of the cylinder, a total of 40 monitoring points were evenly distributed along the positive direction of the x-axis with a spacing of 1 m. The decreasing trend of acoustic pressure along the positive direction of x-axis was analyzed.

Figure 1B shows the results of the analytical and numerical solutions of the sound pressure at the field points. At low frequency (ka = 1), the distribution of the sound pressure gradually decreases with the increase of the radiation distance. The sound pressure calculated by the two methods is basically the same, which proves that the analytical solution is in good agreement with the numerical

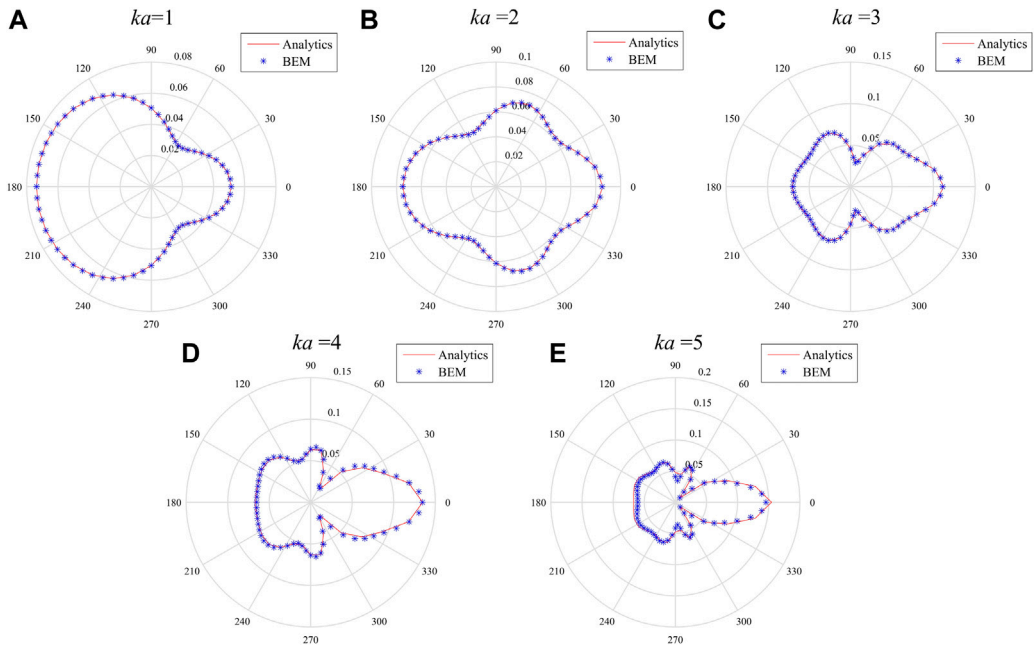

FIGURE 3
Far-field scattering comparison of theoretical and analytical solutions for infinitely long rigid cylinder with different *ka* values. **(A)** *ka* = 1. **(B)** *ka* = 2. **(C)** *ka* = 3. **(D)** *ka* = 4. **(E)** *ka* = 5.

solution. The BEM program used in this work is reliable and can be applied to the next part of the acoustic calculation of the bubble.

3.2 Acoustic scattering from an infinitely long rigid cylinder

Supposing there is a plane wave propagating along the *x*-axis, its sound pressure can be expressed as

$$p_i(x,t) = p_0 e^{j(\omega t - kx)} \tag{13}$$

in which p_0 is the amplitude of sound pressure, x is the distance between the field point and the cylindrical surface.

Based on the computational model in Figure 2, the analytical solution of the scattered sound pressure of the far field can be obtained from *The Fundamentals of Acoustics* [32].

$$p_s(r,\varphi,t) \approx p_0\sqrt{\frac{2a}{\pi}}\frac{e^{j(\omega t-kr)}}{\sqrt{r}}R(\varphi) \tag{14}$$

in which r is the monitoring distance, $R(\varphi)$ is represented as the acoustic directivity function.

$$R(\varphi) = \frac{1}{\sqrt{ka}}\sum_{n=0}^{\infty}\left[b_m e^{j\frac{2n+1}{4}\pi}\cos n\varphi\right] \tag{15}$$

$$b_m = -(-j)^n\varepsilon_n\left[\frac{\frac{dJ_m(\mu)}{d\mu}}{\frac{dH_m^{(2)}(\mu)}{d\mu}}\right]_{\mu=ka}\left(\varepsilon_n = \begin{cases}1, n=0\\ 2, n>0\end{cases}\right) \tag{16}$$

in which J is the Bessel function of the first kind, H is the Bessel function of the third kind, φ represents the angle between the monitoring point and the x-axis, ε_n is a parameter related to n. When calculating, a = 1 m, r = 100 m, p_0 = 1 Pa.

The analytical and BEM solutions of the far-field scattering sound pressure calculated at different *ka* values are given in Figure 3. The distribution of the scattered sound pressure has a clear relationship with *ka*, both for the theoretical solution and for the BEM. The calculation results of the two methods are in good agreement when *ka* is small. When *ka* increases, the finer grid needs to be used to reduce errors. The consistency of the BEM results with the theoretical solutions illustrates the effectiveness of the BEM program used in this work.

3.3 Acoustic scattering from an infinitely long elastic cylinder

The boundary condition of the bubble is different from the rigid cylinder. But the acoustic scattering of the bubble is similar to the scattering result of the infinitely long elastic cylinder [33]. Therefore, the analytical solution of the bubble can be calculated from the scattered sound pressure equation of the infinitely long elastic cylinder.

$$P_{sc}(r,\phi) = p_0\sum_{n=0}^{\infty}\varepsilon_n i^n A_n(x)H_n^{(2)}(kr)\cos n\phi \tag{17}$$

$$A_n(x) = A_n(x)^s = -\frac{J_n(x)}{H_n^{(2)}(x)} \tag{18}$$

in which, ε is a parameter that depends on n, ϕ is the angle between the measuring point and the x-axis, $A_n(x)$ is represented as the

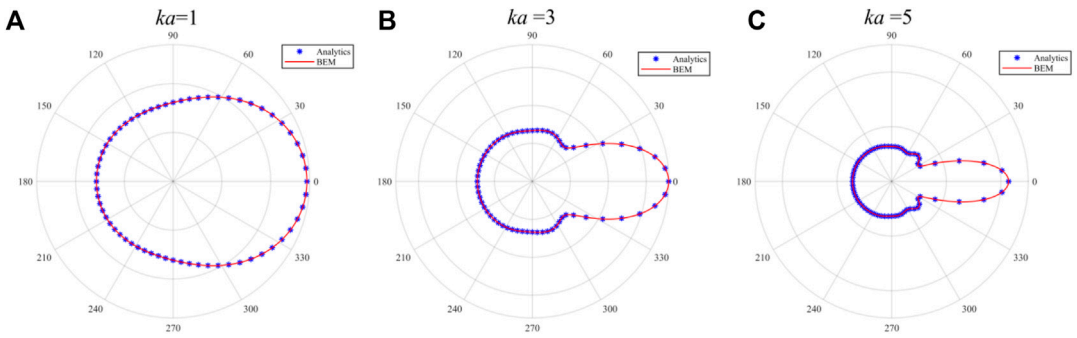

FIGURE 4
Comparison of the far-field scattering about theoretical and analytical solutions from infinitely long elastic cylinders with different *ka* values. **(A)** *ka* = 1. **(B)** *ka* = 3. **(C)** *ka* = 5.

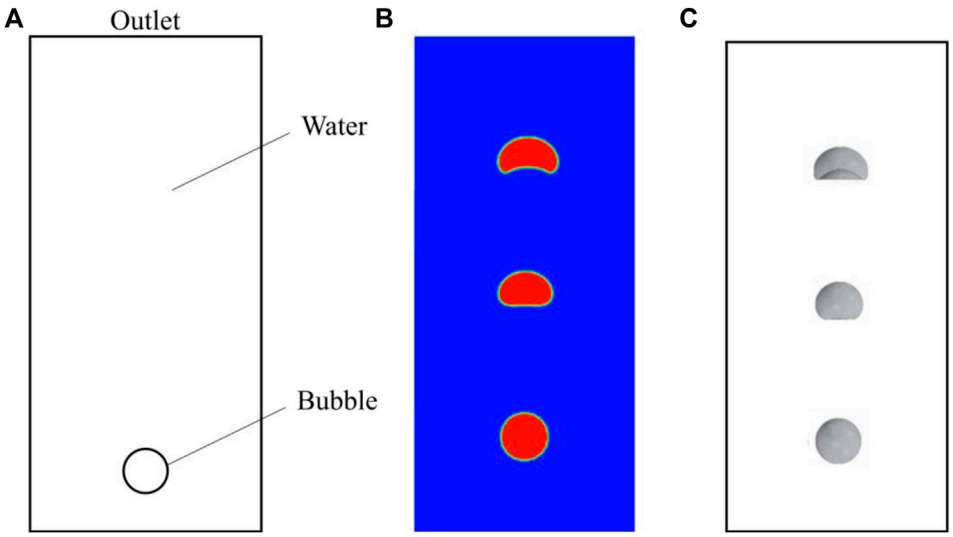

FIGURE 5
(A) Computation model of fluid field. **(B)** The variation of bubble shape with motion with a grid size of 0.5 mm. **(C)** The shape changes of the bubble with general cases in the literature.

acoustic directivity function. When calculating, a = 1 m, r = 100 m, p_0 = 1 Pa.

Figure 4 shows the calculation results of analytical solutions and BEM solutions with different *ka* values. Unlike the rigid cylinder, the energy of the scattered wave of the elastic cylinder is concentrated in the forward direction of the incident wave, which is independent of the increase of the equivalent frequency *ka*. With the increase of *ka* (Figures 4B, C), half of the scattered wave energy is concentrated in the positive direction of the incident wave, the other half is evenly distributed in other directions, and the side lobe energy is small. The directional characteristic of the sound pressure of the numerical solution and the theoretical solution at different *ka* is basically identical, which proves the correctness of the BEM program. On this basis, the acoustic scattering of bubbles under the incidence of plane wave can be discussed.

3.4 The motion of a bubble in water

In order to verify the correctness of the numerical model used for flow field calculation, it is necessary to conduct simulation of the floating process of a single bubble in a stationary viscous liquid. The geometry model is shown in Figure 5A.

In Figure 5A, a bubble with a radius of 10 mm is used for calculation, where the width of the calculation domain is 100 mm and the height is 200 mm. The left, right, and lower boundaries of the computational domain are both no-slip wall conditions, with the upper boundary being the pressure outlet and set to atmospheric pressure. Bubble moved upwards from rest under the action of gravity and buoyancy. Three grid systems of different sizes were used for calculation during the simulation process. The grids with lengths of 2, 1, and 0.5 mm were selected for convergence verification. Time steps were all taken as 0.001 s.

TABLE 1 Calculational parameters.

Parameter	Acoustic velocity	Liquid density	Bubble radius	Bubble velocity
	c/m·s^{-1}	ρ/kg·m^{-3}	a/m	v/m·s^{-1}
Value	1,500	1,000	0.01	0.1

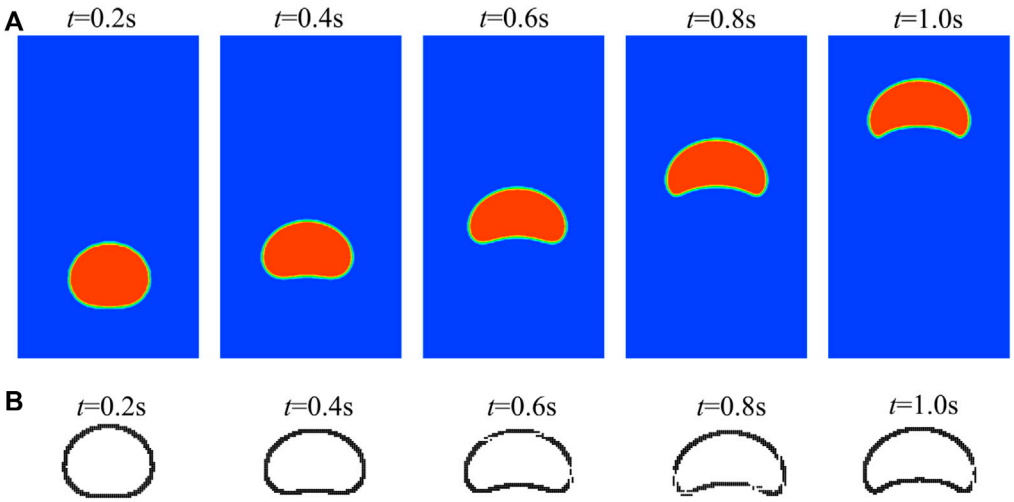

FIGURE 6
Comparison of the bubble boundary. **(A)** The contour of the bubble. **(B)** Capturing the bubble boundary.

Figure 5B shows the morphological change of the bubble during the motion with a grid size of 0.5 mm, which is basically consistent with the calculation results of Zhang and Li [34, 35] (Figure 5C). Through calculation, it was found that there was not much difference in bubble motion among the three grid sizes, and it can be considered that the calculation has reached a convergence state. For the sake of calculation accuracy and efficiency, the size of gird with 1 mm was selected for subsequent calculations.

4 Analysis of acoustic radiation from bubble

Underwater bubble can be seen as a typical monopole sound source, and the pressure pulsation from its own volume change is the main source of its noise generation.

4.1 The capture of bubble boundary

In the calculation of flow field, the movement of bubble within 1s was selected for analysis. The relevant computational parameters taken in the simulation in this section were shown in Table 1.

Figure 6 shows the shape changing of the bubble during the movement. The shape of the bubble after every 0.2 s was shown in Figure 6A. The bubble rising uniformly changes from a sphere to an ellipsoid firstly, then the bottom of bubble gradually depresses inward. With the increase of moving distance, the depression of bubble gradually deepens, and finally appears a cap shape and remains stable floating.

It can be found from Figure 6B that the boundary of the bubble is captured during the process of motion. The method of boundary capturing selected in this work is based on the air volume fraction. Firstly, deriving the data of all nodes from the fluid computing domain. According to Eq. 4 in Section 2, it can be known that $0 < C < 1$ represents the bubble boundary. Therefore, fluid particles within the range of $C < 0.5$ were selected through programming, and the bubble boundaries were ultimately captured.

4.2 Discussion of acoustic radiation

In the calculation of BEM with frequency, the calculation frequency and vibration frequency about bubble need to be considered. For a spherical bubble in water, the simplified expression for the resonant frequency can be obtained according to the literature [36].

$$f_b = \frac{3.25\sqrt{1 + 0.1h}}{a} \tag{19}$$

where h is the bubble depth and a is the bubble radius. According to the calculation, the resonant frequency of the bubble was about 300 Hz, so the calculated frequency was chosen as 300 Hz in this paper.

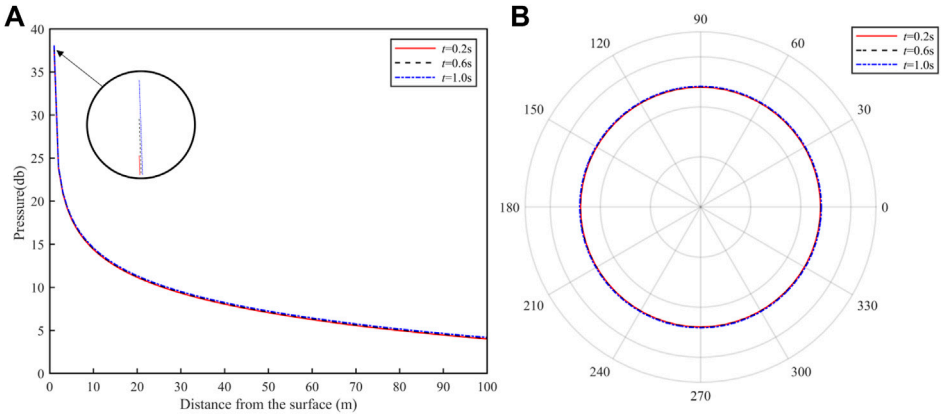

FIGURE 7
(A) Sound pressure of radiation with monitoring distance at different times. **(B)** The directivity of acoustic radiation.

Radiated sound pressure produced by the bubble in uniform linear motion was calculated. Figure 7A is the result of the acoustic radiation generated by the volume vibration caused by the deformation of the moving bubble at the time of 0.2, 0.6, and 1.0 s. The measurement range of the sound field is defined as within 1–100 m in the horizontal direction of the bubble. With the increase of the propagation distance of the sound wave, the pressure of the acoustic radiation decreases gradually. With the increase of movement time, the extreme value of the radiated sound field also increases slightly due to the deformation of the bubble. According to the comparison of bubble shapes at different time in Figure 7. Since the bubble size does not change significantly, the difference in the calculation is not significant.

Figure 7B depicts the acoustic directivity of the bubble at three moments. It can be clearly seen that the directivity of bubble acoustic radiation is uniform, and the sound pressure distribution in all directions is basically the same. The motion of the bubble has no obvious effect on the directivity of the acoustic radiation, but it slightly affects its amplitude. There are two reasons for this phenomenon. One is that the diameter of the bubble is too small, and the impact of deformation can be ignored. The other is that the distance of bubble movement is too short, which can be ignored relative to the length of the monitoring area.

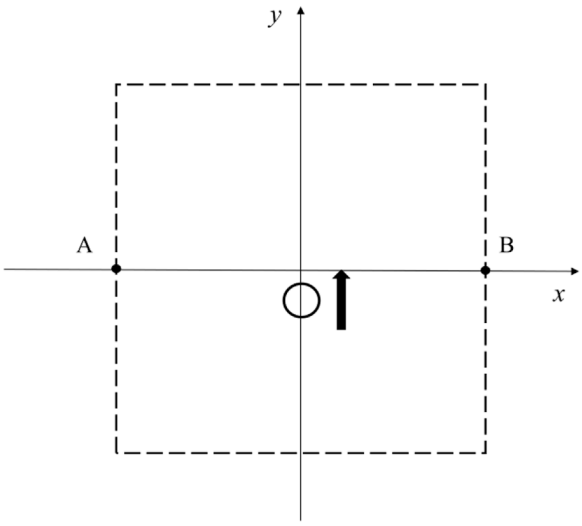

FIGURE 8
Location distribution of sampling points A, B and calculation domain.

5 Analysis of acoustic scattering from moving bubble

In the sound scattering of the bubble, the bubble can be regarded as a highly compressible elastic sphere. When a free wave encounters the elastic sphere on the propagation path, the sphere is going to have a scattering effect on the sound wave. It can also be considered that the bubble acts as a sound source under the excitation of the incident wave.

The parameters of bubble in the calculation process were the same as Table 1 in Chapter 4. The sound pressure amplitude of incident plane wave was 1 Pa. The calculation domain was taken as a circle with a radius of 100 m to calculate the acoustic scattering in the far field of the bubble.

5.1 A bubble moving in a straight line with uniform velocity

Considering an ideal condition, the bubbles were supposed to be undeformed, and moving uniformly upward at different speeds. The sampling points A and B, 100 m away from the center of the computational domain, were selected as shown in Figure 8. With coordinates of origin (0, 0), the bubble started to rise from (0, −10), and the coordinates of the sampling points were defined as A (−100, 0) and B (100, 0) respectively. The plane wave was assumed to propagate along the positive direction of the

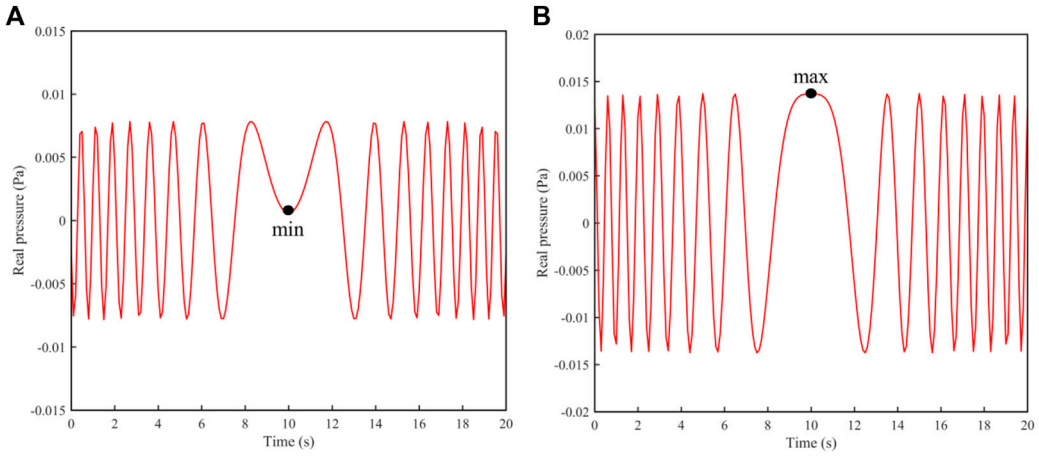

FIGURE 9
Variation of scattered sound pressure at **(A,B)** with time for *ka* = 1.

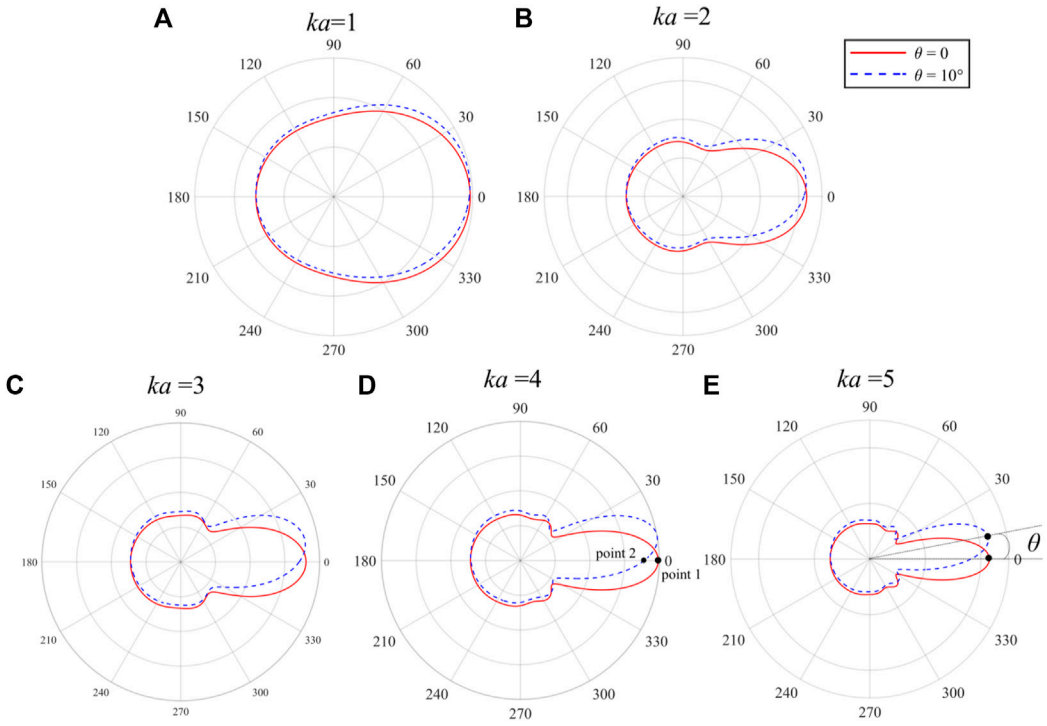

FIGURE 10
The change of the directivity of the acoustic scattering under different *ka*. **(A)** *ka* = 1. **(B)** *ka* = 2. **(C)** *ka* = 3. **(D)** *ka* = 4. **(E)** *ka* = 5.

x-axis. The sampling point A was defined as being on the back side of the wave propagation direction, and sampling point B was in the forward direction. The bubble has the radius of 1 cm and the velocity of 1 m/s. The amplitude of the sound pressure of the incident wave is 1 Pa.

Figure 9 shows the relationship between the scattered sound pressure and time at A and B from 0 to 20 s when *ka* = 1. The sound pressure at A and B both oscillates with time, and the amplitude of the sound pressure at point B is approximately twice that of point A. This phenomenon also indicates that due to the presence of the bubble, most of the energy of acoustic scattering is concentrated in the front of the sound propagation direction, so the sound pressure at point B is always greater than that at point A. When t = 10 s, the bubble is just at the center of A and B, both A and B have the extreme value of sound pressure. Figure 9A shows the minimum value about A, and Figure 9B shows the maximum value about B. This represents

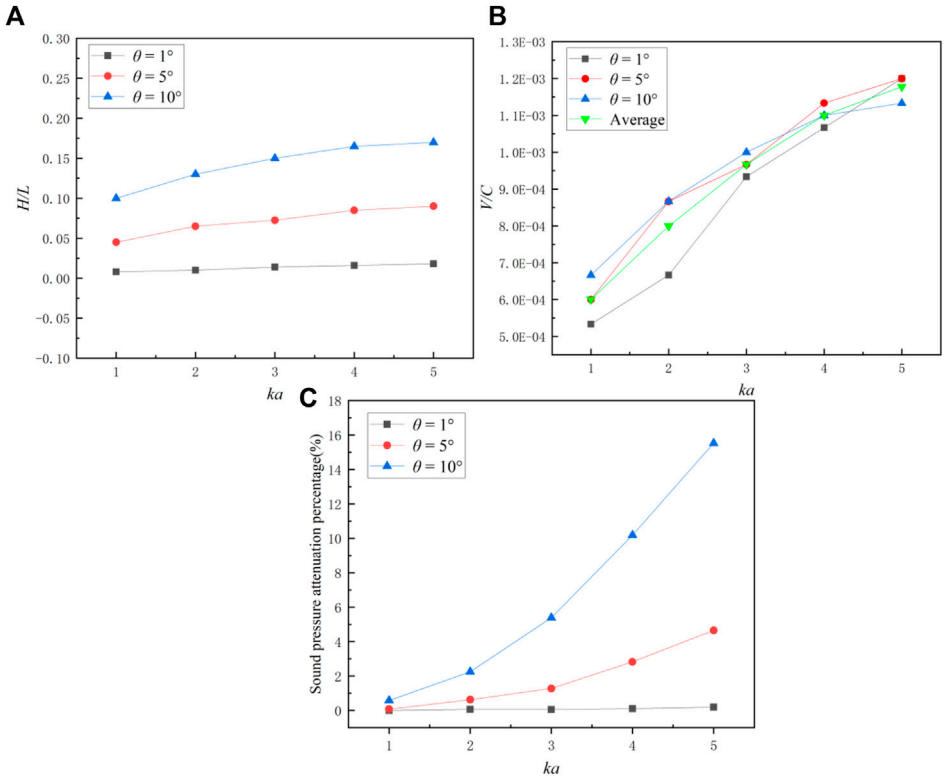

FIGURE 11
Changes of parameters of acoustic scattering when bubble moves at different *ka*. **(A)** Movement distance. **(B)** Movement speed. **(C)** Percentage of sound pressure attenuation.

that the forward sound pressure is at its maximum and the reverse sound pressure is at its minimum, reflecting the effect of the bubble on the scattered sound field.

At 100 m away from the bubble, the monitoring points were arranged every 5° and the acoustic directional diagram was drawn. With the motion of the bubble, the sound field changes, which can be demonstrated by the change in the acoustic directivity. This work defined the directional offset angle θ as shown in Figure 10E. θ represents the angle between the maximum sound pressure under two working conditions (the red solid line represents the distribution of acoustic filed at the initial moment of the bubble, and the blue dashed line represents the scattered sound field after a period of bubble movement).

It can be found that *ka* also has an effect on the distribution of the acoustic scattering in Chapter 3. Therefore, the comparison of $\theta = 10°$ under different *ka* was plotted in Figure 10. Figure 10 depicts the change in directionality offset caused by bubble motion, with the position of measurement points unchanged. The presence of the bubble has almost no obstruction effect on the sound wave, so that the energy of the acoustic scattering is mainly concentrated in the forward direction of the incident wave. When *ka* is small (Figure 10A), the directivity of the acoustic scattering in the far-field of the bubble is not very obvious, and no side lobes are produced. As *ka* increases, the distribution of sound pressure gradually has obvious directivity, the main lobe and a small part of the side lobes appear (Figures 10D, E).

According to the deviation of acoustic directivity, it is found that *ka* does not have much effect on the backward scattering. When *ka* increases, the shift of the main lobe becomes more obvious. That is, the larger the *ka* is, the more intense the disturbance of bubble motion on the acoustic field.

In order to further discuss the effect of bubble motion on sound field, the displacement and velocity of bubble motion required for $\theta = 1°, 5°, 10°$ at different *ka* were calculated. In Figure 11, H is the height of the bubble rising in the straight line, V is the speed of bubble motion, C is the speed of sound, and L is the radius of the monitoring domain, $C = 1{,}500$ m/s, $L = 100$ m.

Figure 11A depicts the effect of bubble moving displacement on sound scattering, representing the distance traveled by the bubble ($v = 1$ m/s) when the directionality offset angle $\theta = 1°, 5°, 10°$. Obviously, as the displacement of moving increases, the θ also increases. At the same θ, as the *ka* increases, the distance of bubble movement also needs to increase. When the offset angle $\theta = 1$, the motion distance of the bubble is 100 times radius of the bubble at least. This proves that the distance the bubble moves has some effect on the sound pressure of far-field, the farther the bubble moves, the more pronounced the change in directivity.

In this paper, the acoustic directivity changing velocity is defined as

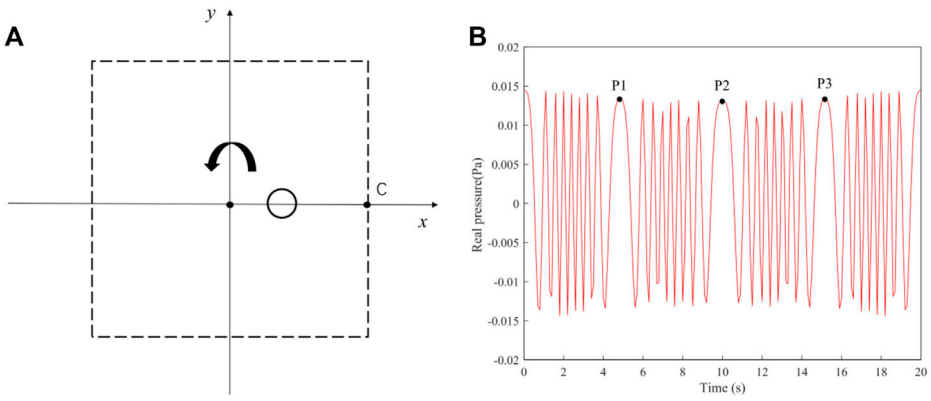

FIGURE 12
(A) The arrangement of measuring point. **(B)** The relationship between sound pressure and time at the point C.

$$w(i) = \frac{\theta(i)}{t(i)} \tag{20}$$

in which t is the time the bubble moves. w is used to evaluate the velocity of acoustic directionality shift, representing the angle that a bubble movement of 1 s can cause the point of maximum sound pressure to move, the unit is $^\circ\ s^{-1}$.

Figure 11B shows the bubble velocity v corresponding to $\theta = 1^\circ$, 5°, 10° when $w = 1^\circ{\cdot}s^{-1}$, representing the relationship between the offset velocity of acoustic directionality and the velocity of the bubble. As ka increases, the bubble velocity v also needs to increase when θ is fixed. When ka is small, the increase of v is proportional to θ. When ka is large, the speed corresponding to different offset angles θ has no obvious relationship. The average of the velocities at the three offset angles θ can be used to represent the velocity that a bubble needs to reach when $w = 1^\circ{\cdot}s^{-1}$. It can be seen that within the same movement time, the increase in bubble velocity does not cause a more significant shift in directionality.

Such as shown in Figure 10D, this work defined the percentage of sound pressure attenuation in the direction of 0° at a certain offset angle θ as

$$per = \frac{(p_1 - p_2)}{p_1} \times 100\% \tag{21}$$

where p_1 is the sound pressure at point 1 in Figure 10D and p_2 is the sound pressure at point 2.

Figure 11C discusses the percentage of sound pressure attenuation at different θ under different ka, representing the influence of bubble motion on the sound pressure in the positive x-axis direction. When $\theta = 1^\circ$, ka has no significant effect on the sound pressure in the direction of 0°. However, the influence of ka on attenuation of sound pressure increases when the θ increases. In addition, when ka is small, the offset angle of the acoustic directivity θ has little effect on the sound pressure attenuation. When ka is large, the increase of the θ will rapidly reduce the sound pressure value in the direction of 0°. This indicates that within a fixed monitoring domain, the upward movement of the bubble will reduce the sound pressure in the x-axis direction, and the farther the bubble moves, the more significant the decrease in the sound pressure.

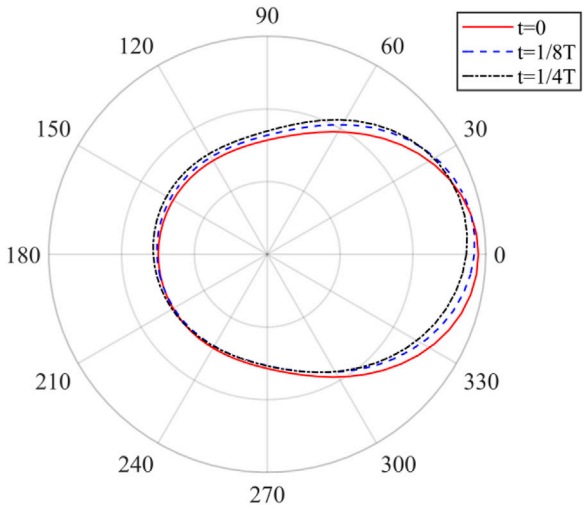

FIGURE 13
Variation of bubble acoustic directivity during uniform circular motion.

5.2 A bubble with uniform circular motion

Given a bubble motion period of 20 s, the uniform circular motion was carried out with a fixed circumferential radius of 10 m. During the motion, the measurement point C (100, 0) as shown in Figure 12A. The bubble moves in a uniform circular motion starting from (10,0). Figure 12B shows the change law of real sound pressure with time at the point C when the bubble moves for one cycle. It can be seen that the sound pressure is constantly oscillating during the bubble movement, and the influence of the circular movement on the extreme value of sound pressure is not obvious. Since the point C is always directly in front of the sound wave, that is, to the right of the bubble, its sound pressure depends on the distance between the bubble and point C. The scattered sound pressure increases when the bubble is close to point C, and decreases when it is far away from point C. This variation is not obvious, because the circular motion of

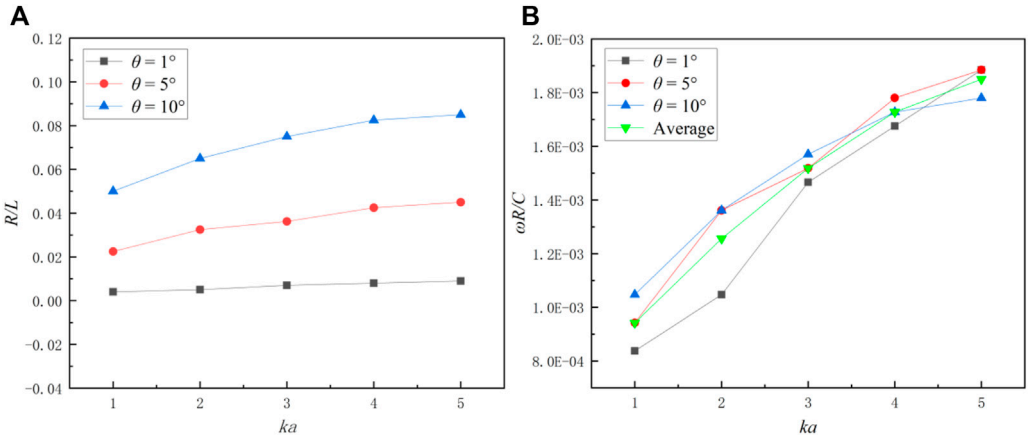

FIGURE 14
Relationship between the offset angle and circumferential radius **(A)** and angular velocity **(B)** during uniform circular motion at different *ka* values.

the bubble is relatively small relative to the far-field measurement point. When the bubble moves to the *x*-axis and *y*-axis, the sound pressure at point C reach to the maximum (P1, P2, P3).

Figure 13 shows the directivity diagram of the acoustic scattering at three selected moments in a period of bubble movement when $ka = 1$. During the uniform circular motion of the bubble, the sound energy is mainly concentrated in the forward direction of the incident wave. Since the direction of motion about the bubble is counterclockwise, the acoustic directivity shifts upward with the bubble motion, but the offset angle θ is small. At the same time, the forward sound pressure slightly decreases and the backward sound pressure slightly increases, which shows the effect of the circular motion of the bubble on the sound field distribution.

To further discuss the effect of bubble circular motion on the sound field, the circumferential radius and angular velocity for bubble motion at $\theta = 1^{\circ}, 5^{\circ}, 10^{\circ}$ at different *ka*were calculated. In Figure 14A, *R* is the radius of the bubble's circular motion, and *L* is the distance between the measuring point and the bubble. At the same θ, the *ka* value increases and the circumferential radius required for bubble motion increases. When *ka* is fixed, the bubble's circular motion radius increases proportionally with the increase of θ. This proves that the radius of circular motion of the bubble has a certain impact on far-field sound pressure, and the larger the radius of motion, the more significant the change in directionality.

Figure 14B shows the relationship between the offset velocity of the acoustic directivity ($w = 1^{\circ}\cdot s^{-1}$) and the angular velocity of the bubble (ω). When the *ka* value increases, the ω also increases. When *ka* is the same, the ω corresponding to different θ is not much different. Therefore, the average of the three angular velocities can be selected to represent the relationship between the *w* and the ω. It can be seen that within the same movement time, an increase in the velocity of the bubble's circular motion will not cause a significant change in directionality. However, as *ka* increases, the bubble requires a greater circumferential velocity to shift the directionality of the sound by the same angle.

5.3 Small deformation bubbles

In reality, the bubble does not always keep spherical when moving, but deforms due to the pressure. The shape change of bubbles can be observed in Chapter 4. Therefore, this section discussed the property of acoustic scattering about ellipsoidal bubbles. The ratio of long and short axes of bubbles is defined as $N = a/b$, *a* is the long axes and *b* is the short axes. When $N = 1$, it represents an ideal spherical bubble. Figure 15 is the scattering directivity diagram of ellipsoid bubble at different *N* when $ka = 1$.

Figure 15A shows that when the bubble volume keeps constant, as *N* increases, the long axis *a* of the bubble increases and the short axis *b* decreases, which indicates the shape of the bubble becomes more and more flat. During this change, the forward sound pressure increases and the backward sound pressure decreases. The energy of the acoustic scattering is also concentrated in the forward direction of the incident wave, and the amplitude of the sound pressure increases slightly. By comparing the calculated results in Figure 15A with the literature [37], it can be found that the scattered sound pressure of the bubble is close to the minimum value for $N = 2$. Figure 15B represents the bubble with a change in volume, its long axis *a* remains constant. As the short axis *b* decreases, the volume of the bubble decreases, the amplitude of scattered sound pressure decreases, and the directivity decreases This indicates that the decrease in bubble volume has a greater impact on sound radiation than the change in the long and short axes of the bubble on the scattered sound field. Comparing Figures 15A, B, it can be found that both the size and thickness of the bubble have an effect on the scattered sound field.

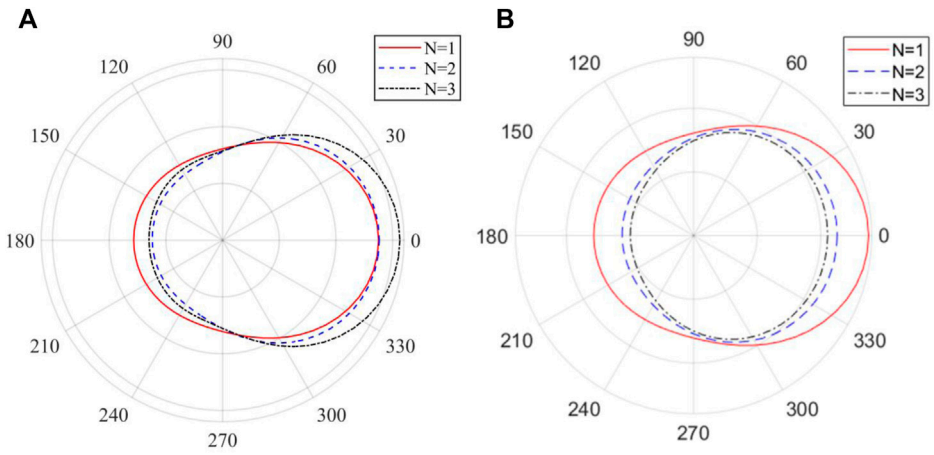

FIGURE 15
The relationship between the acoustic directivity of the ellipsoid bubble and the major and minor axes. **(A)** The bubble volume remains constant. **(B)** The long axis of the bubble remains constant.

6 Conclusion

Regarding the problem of the sound radiation and scattering of moving bubbles, this paper introduces a coupled CFD-BEM method to predict the acoustic radiation and scattering of bubbles under low motion velocity. Based on the motion boundary of bubbles obtained by CFD, the BEM program is used to solve the acoustic radiation and scattering of stationary spherical and ellipsoidal bubbles, uniform linear rising bubbles, and uniform circular motion bubbles respectively. The following conclusions are obtained.

(1) *ka* has an important influence on the acoustic scattering of the bubble. When the *ka* value is small, the directivity of the acoustic scattering is not obvious. With the increase of *ka* value, the main lobe and side lobe appears, and the energy of the acoustic scattering is gradually concentrated in the forward direction of the incident wave.
(2) For a bubble moving in a straight line, the distance of moving can deflect the far-field acoustic directivity (The far field distance is about 100 m). For a bubble with circular motion, the radius of motion (R) is positively proportional to the acoustic directivity changing velocity (w).
(3) For the ellipsoidal bubble, the flatter the bubble, the higher its forward scattering sound pressure. It is worth noting that the shape and volume changes of the bubble can both affect the distribution of scattered sound field.

Data availability statement

The original contributions presented in the study are included in the article, further inquiries can be directed to the corresponding author.

Author contributions

Y-FL writing (original draft), methodology, theoretical model analysis and data. Y-OZ and TZ: idea, conceptualization, writing and reviewing of the manuscript, structural scheme design, theoretical model analysis, supervision and funding. YQ: investigation, review of the manuscript. All authors contributed to the article and approved the submitted version.

Funding

This study is supported by the Innovative Research Foundation of Ship General Performance of China (No. 33122233) and the Open Fund of Science and Technology on Thermal Energy and Power Laboratory (No. TPL2021B03).

Conflict of interest

The authors declare that the research was conducted in the absence of any commercial or financial relationships that could be construed as a potential conflict of interest.

Publisher's note

References

1. Rayleigh L. On the pressure developed in a liquid during the collapse of a spherical Cavity. *Phil Mag J Sci* (1917) 200(34):504–7. doi:10.1080/14786440808635681

2. Plesset MS. The dynamics of cavitation bubbles. *J Appl Mech* (1949) 3(16):277–82. doi:10.1115/1.4009975

3. Neppiras EA. Acoustic cavitation. *Phys Rep* (1980) 61(3):159–251. doi:10.1016/0370-1573(80)90115-5

4. Sreedhar BK, Albert SK, Pandit AB. Cavitation damage: Theory and measurements–A review. *Wear* (2017) 372:177–96. doi:10.1016/j.wear.2016.12.009

5. Wang SP, Zhang AM, Liu YL. Bubble dynamics and its applications. *J Hydrodynamics* (2018) 30(6):975–91. doi:10.1007/s42241-018-0141-3

6. Zhang AM, Li SM, Cui P. A unified theory for bubble dynamics. *Phys Fluid* (2023) 35:03323. doi:10.1063/5.0145415

7. Minnaert M. On musical air-bubbles and the sounds of running water. *Phil Mag J Sci* (1933) 16(104):235–48. doi:10.1080/14786443309462277

8. Zhang AM, Ming FR, Liu YL. Review on the researches on underwater explosion related to load characteristics, ship damage and protection. *Chin J Ship Res* (2023) 2023: 1–16. doi:10.19693/j.issn.1673-3185.03273

9. Wang PP, Zhang AM, Peng YX. Numerical simulation of transient strongly-nonlinear fluid-structure interaction in near-field underwater explosion based on meshless method. *Chin J Theoret Appl Mech* (2022) 54(8):2194–209. doi:10.6052/0459-1879-22-271

10. Hu ZY, Cao ZE, Li S. Fluid-structure interaction between a high-pressure pulsating bubble and a floating structure. *Chin J Theoret Appl Mech* (2021) 53(4): 944–96. doi:10.6052/0459-1879-20-357

11. Twersky V. Rayleigh scattering. *Appl Opt* (1964) 3(10):1150–62. doi:10.1364/AO.3.001150

12. Kundu T, Bostrom A. Axisymmetric scattering of a plane longitudinal wave by a circular crack in a transversely isotropic solid. *J Appl Mech* (1991) 58(3):695–702. doi:10.1115/1.2897250

13. Chinnery PA, Humphrey VF, Beckett C. The schlieren image of two-dimensional ultrasonic fields and cavity resonances. *J Acoust Soc Am* (1997) 101(1):250–6. doi:10.1121/1.417976

14. Peregrine DH. The acoustic bubble. *J Fluid Mech* (1994) 272:407–8. doi:10.1017/S0022112094214519

15. Shi XG, Zhao GJ, Wu YY. CFD simulation of bubbles behavior in baffled bubbling fluidized bed. *Act Petrol Sin* (2020) 36(01):113–20. doi:10.3969/j.issn.1001-8719.2020.01.014

16. Gao H, Xu HT. Computing T matrix of sound scattering by object using the boundary integral equation method. *Act Acust* (2008) 33(5):396–401. doi:10.15949/j.cnki.0371-0025.2008.05.002

17. Waterman PC. New formulation of acoustic scattering. *J Acoust Soc Am* (1969) 45(6):1417–29. doi:10.1121/1.1911619

18. Marburg S, Nolte B. *Computational acoustics of noise propagation in fluids: Finite and boundary element methods*. Berlin: Springer (2008). p. 411—434.

19. Feuillade C. Acoustically coupled gas bubbles in fluids: Time-domain phenomena. *J Acoust Soc Am* (2001) 109(6):2606–15. doi:10.1121/1.1369102

20. Burgschweiger R, Schäfer I, Mohsen A. Results of an implementation of the dual surface method to treat the non-uniqueness in solving acoustic exterior problems using the boundary element method. *J Acoust Soc Am* (2013) 19(1):065060. doi:10.1121/1.4799569

21. Chen IL, Chen JT, Kuo SR. A new method for true and spurious eigensolutions of arbitrary cavities using the combined Helmholtz exterior integral equation formulation method. *J Acoust Soc Am* (2001) 109(3):982–98. doi:10.1121/1.1349187

22. Fan LX. *Research on calculation method of acoustic scattering characteristics of underwater moving sphere*. China: Huazhong Univ Sci Technol (2018). p. 06.

23. Liu J, Wang W, Chu N. Numerical simulations and experimental validation on passive acoustic emissions during bubble formation. *Appl Acoust* (2018) 130:34–42. doi:10.1016/j.apacoust.2017.09.005

24. Zhang Y, Dang S, Li W. Performance of the radial point interpolation method (RPIM) with implicit time integration scheme for transient wave propagation dynamics. *Comput Math Appl* (2022) 114:95–111. doi:10.1016/j.camwa.2022.03.031

25. Cong SH. *Study on bubble flow field and radiated sound characteristics*. China: Shandong Univ (2022). doi:10.27272/d.cnki.gshdu.2022.002821

26. Li Y, Liu C, Li W. Numerical investigation of the element-free Galerkin method (EFGM) with appropriate temporal discretization techniques for transient wave propagation problems. *Appl Math Comput* (2022) 442:127755. doi:10.1016/j.amc.2022.127755

27. Li W, Zhang Q, Gui Q. A coupled FE-Meshfree triangular element for acoustic radiation problems. *Int J Comput Methods* (2021) 18(03):2041002.

28. Hirt CW, Nichols BD. Volume of fluid (VOF) method for the dynamics of free boundaries. *J Comput Phys* (1981) 39(1):201–25. doi:10.1016/0021-9991(81)90145-5

29. Du H, Xiong AK, Zhang YO. Forward sound scattering from an underwater vortex. *J Acous* (2020) 45(01):55–61. doi:10.15949/j.cnki.0371-0025.2020.01.006

30. Liu WT, Gui Q, Jiang HY. Application of boundary element coupling radial basis point interpolation meshless method in acoustic scattering. *Ship Sci Technol* (2023) 45(2):02–7. doi:10.3404/j.issn.1672-7649.2023.02.026

31. Williams EG. *Fourier acoustics: Sound radiation and nearfield acoustical holography*. United States: Acad Press (2000). doi:10.1016/B978-0-12-753960-7.X5000-1

32. Du GH, Zhu Z, Gong XF. *Fundamentals of acoustics*. China: Nanjing Univ Press (2001).

33. Jamali J, Honarvar F, Naei MH. Acoustic wave scattering from infinite cylinders made from functionally graded materials. *J Acoust Soc Am* (2008) 123(5):3277. doi:10.1121/1.2933624

34. Zhang Y, Yang F. Numerical simulation of single bubble floating process. *Mod Manufacturing Technol Equip* (2016) 07:4–7. doi:10.16107/j.cnki.mmte.2016.0523

35. Li S, Zhang AM, Sun LQ. Dynamic behavior of rising bubble. *Acta Phys Sin* (2014) 63(18):291–303. doi:10.7498/aps.63.184701

36. Hua J. *Study on the dispersion characteristics of sound velocity in media containing bubbles*. China: Harbin Eng Univ (2018). p. 01.

37. Ma J, Wang HB. Acoustic scattering characteristics of rigid cylinder solved by boundary element method. *J Najing Univ* (2018) 54(05):875–86. doi:10.13232/j.cnki.jnju.2018.05.002

frontiers | Frontiers in Physics

TYPE Methods
PUBLISHED 02 June 2023
DOI 10.3389/fphy.2023.1170811

OPEN ACCESS

EDITED BY
Glauber T. Silva,
Federal University of Alagoas, Brazil

REVIEWED BY
Vladimir Rabinovich,
National Polytechnic Institute (IPN), Mexico
Bernhard Johan Hoenders,
University of Groningen, Netherlands

*CORRESPONDENCE
Wei Li,
hustliw@hust.edu.cn

RECEIVED 21 February 2023
ACCEPTED 17 May 2023
PUBLISHED 02 June 2023

CITATION
Yang Y, Gui Q, Zhang Y, Chai Y and Li W (2023), Acoustic scattering of a pair of rigid spheroids based on the *T*-matrix method.
Front. Phys. 11:1170811.
doi: 10.3389/fphy.2023.1170811

Acoustic scattering of a pair of rigid spheroids based on the *T*-matrix method

Yuzheng Yang[1], Qiang Gui[1], Yang Zhang[1], Yingbin Chai[2] and Wei Li[1,3,4]*

[1]School of Naval Architecture and Ocean Engineering, Huazhong University of Science and Technology, Wuhan, Hubei, China, [2]School of Naval Architecture, Ocean and Energy Power Engineering, Wuhan University of Technology, Wuhan, China, [3]Hubei Key Laboratory of Naval Architecture & Ocean Engineering Hydrodynamics (HUST), Wuhan, Hubei, China, [4]Collaborative Innovation Centre for Advanced Ship and Deep-Sea Exploration (CISSE), Shanghai, China

In this study, the *T*-matrix method combined with the addition theorems of spherical basis functions is applied to semi-analytically compute the underwater far-field acoustic scattering of a pair of rigid spheroids with arbitrary incident angles. The involvement of the addition theorems renders the multiple scattering fields of each spheroid to be translated into an identical origin. The accuracy and convergence property of the proposed method are verified and validated. The interference of specular reflection wave and Franz wave can be spotted from the oscillations of the form function. Furthermore, the propagation paths of specular reflection and Franz waves are quantitatively analyzed in the time domain with conclusions that the Franz waves reach the observation point subsequent to specular reflection waves and the time interval between these two wave series is equal to the time cost of the Franz waves traveling along the sphere surfaces. Finally, the effects of separation distances, aspect ratios (the ratio of the polar radius to equatorial radius), non-dimensional frequencies, and incidence angles of the plane wave on the far-field acoustic scattering of a pair of rigid spheroids are studied by the *T*-matrix method.

KEYWORDS

***T*-matrix method, addition theorems, a pair of rigid spheroids, acoustic scattering, far-field form function**

1 Introduction

The study of underwater target acoustic scattering gains attentions from researchers, and the relative research studies are widely applied in engineering practices such as underwater target detection, positioning, imaging, and underwater communication. The mechanism of multiple-target acoustic scattering is more complex than that of single-target scattering due to the existence of multiple scattering. In this study, a pair of rigid spheroids is chosen as the target to investigate the multiple acoustic scattering characteristics.

In the past decades, a series of numerical and analytical methods are proposed to solve the underwater acoustic scattering problem. Numerical methods such as the finite element method (FEM) and boundary element method (BEM) can solve acoustic scattering problems under complex conditions [1–3]. Recently, various extended methods, like the smooth finite element method and meshfree method [4–7], are proposed to solve the underwater acoustic scattering issues. However, the computational efficiency of those numerical methods decreases as the frequency increases because of the requirement of very dense meshes.

Compared to the numerical methods, the analytical method can provide precise solutions with a faster convergence speed. In addition, the physical understanding of the acoustic scattering wave can be explained by the analytical solutions. Rayleigh first derived the Bessel–Legendre series (mathematical) solution for the acoustic scattering of a sphere by the variable separation method. However, his works are only competent to cases with small non-dimensional frequencies *ka* [8]. Based on Rayleigh's work, various extended analytical methods, like the partial wave series (PWS) method and Sommerfeld–Watson transformation (SWT), are proposed to obtain the mathematical expressions of acoustic scattering of the single simple target (such as the sphere and circular cylinder) [9–11]. Záviška proposed the multipole method to solve the two-dimensional multiple scattering by a series of circular cylinders [12]. Eyges extended the multipole method to the multiple scattering of two spheres [13]. The key to the multipole method is the addition theorems of the spherical basis functions which transform the multiple scattering fields of different targets to a field with a uniform origin [14, 15]. Gabrielli derived the analytical solutions to the acoustic scattering problems of two spheres using the symmetry properties, which are widely used in quantum physics [15, 16]. However, there are some limitations to analytical methods in solving the acoustic scattering of non-spherical targets in the spherical coordinate system. Consequently, the semi-analytical method is applied to study the far-field acoustic scattering of a pair of rigid spheroids.

The *T*-matrix method, a typical semi-analytical method, is first proposed by Waterman for electromagnetic scattering problems [17] and later extended to the acoustic scattering field [18]. The *T*-matrix method is defined as the semi-analytical method derived from the Helmholtz integral equation and null-field theory, and the infinite matrix needs to be truncated. The crux of the *T*-matrix method is to expand all the field quantities by a set of orthogonal basis functions and solve the unknown expansion coefficients. In addition, the *T*-matrix method is suitable for the acoustic scattering problem with arbitrary incidence and scattering angles. Peterson derived the *T*-matrix expression for multi-target scattering based on the addition theorems of spherical basis functions and calculates the numerical result of a pair of identical spheres under the plane wave incidence [19]. Most of the published literature works focus on the acoustic scattering of a pair of spheres and spheroids with small aspect ratios (i.e., the ratio of the polar radius to equatorial radius is less than 2). However, it is important to study the acoustic scattering mechanism of a pair of rigid oblate spheroids and prolate spheroids, which are extensively used in hydrodynamics and underwater engineering.

In this work, the addition theorems are embedded in the *T*-matrix method to investigate the underwater far-field acoustic scattering characteristics of a pair of rigid spheroids with different aspect ratios ensonified by plane waves at different angles. The propagation paths of the returning backscattering waves from a pair of rigid spheres are analyzed by using the geometric and numerical method in the time domain. The structure of this work is as follows: In Section 2, acoustic scatterings of a single rigid spheroid are considered by the traditional *T*-matrix method; in addition, the addition theorems are embedded in the *T*-matrix method to investigate the scatterings of a pair of rigid spheroids. In Section 3, some numerical experiments are carried out to verify the accuracy and convergence of the *T*-matrix method for the acoustic scattering of a pair of rigid spheroids. Furthermore, the effects of the separation distance between spheroids, aspect ratios, non-dimensional frequencies, and incidence angles of the plane wave on the acoustic scattering of a pair of rigid spheroids are investigated, while conclusions are provided in Section 4.

2 *T*-matrix method

In this section, a rigid spheroid and a spheroid pair are considered. The acoustic scatterings of such models under plane wave incidence at an arbitrary angle are investigated using the *T*-matrix method.

2.1 For a rigid spheroid

As shown in Figure 1, a rigid rotation spheroid with the polar radius *b* (distance from the center point to the endpoint of the

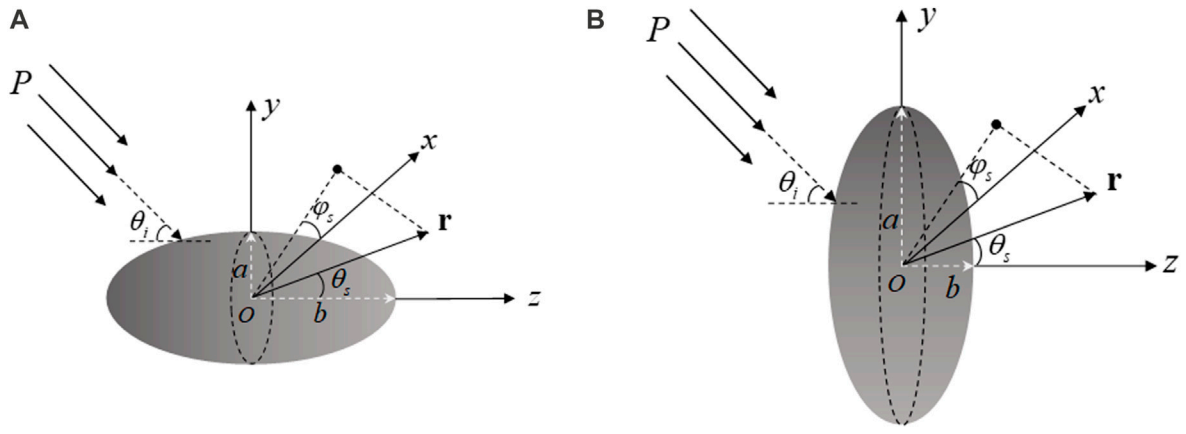

FIGURE 1
Geometry model for the acoustic scattering of a rigid **(A)** prolate and **(B)** oblate spheroid.

spheroid located in the rotation axis Oz) and equatorial radius a is positioned in an ideal fluid medium with density ρ and sound velocity c. The angle between the incident plane wave P and axis Oz is θ_i. The surface shape function $S(\theta)$ of the spheroid is only related to the polar angle θ, such that

$$S(\theta) = \left(\cos^2\theta/b^2 + \sin^2\theta/a^2\right)^{-1/2}. \tag{1}$$

The entire wave field can be constructed by the scalar velocity potential because the wave field exists only in the ideal fluid medium. For convenience, in what follows, the monochromatic time factor $\exp(-i\omega t)$ of all velocity potentials is omitted. The total wave field $\Phi(\mathbf{r})$ is the sum of the incident field $\Phi_i(\mathbf{r})$ and scattering field $\Phi_s(\mathbf{r})$:

$$\Phi(\mathbf{r}) = \Phi_i(\mathbf{r}) + \Phi_s(\mathbf{r}). \tag{2}$$

All of the aforementioned velocity potentials satisfy the Helmholtz equation:

$$\left(\nabla^2 + k^2\right)\begin{pmatrix}\Phi(\mathbf{r})\\ \Phi_i(\mathbf{r})\\ \Phi_s(\mathbf{r})\end{pmatrix} = 0, \tag{3}$$

where $k = \omega/c$ is the wave number. Waterman discussed the aforementioned three field functions in detail [18]. The outer surface S of the ellipsoid is smooth, so that the Poincare–Huygens principle and Gauss theorem can be applied. The Helmholtz integral representation equation can be expressed as

$$\begin{aligned}&\Phi_i(\mathbf{r}) + \int_S \left[\Phi_+ \mathbf{n}\cdot\nabla g(\mathbf{r},\mathbf{r}') - (\mathbf{n}\cdot\nabla_+\Phi) g(\mathbf{r},\mathbf{r}')\right] \mathrm{d}S\\ &= \begin{cases}\Phi(\mathbf{r}) & \mathbf{r}\ \text{outside}\ S\\ 0 & \mathbf{r}\ \text{inside}\ S,\end{cases}\end{aligned} \tag{4}$$

where Φ_+ is the velocity potential on the outer surface of the spheroid. $\mathbf{n}\cdot\nabla_+\Phi$ denotes the normal velocity on the outer surface of the spheroid. $g(\mathbf{r},\mathbf{r}')$ is the free-field Green's function, which can be expressed as

$$g(\mathbf{r},\mathbf{r}') = \exp\left(ik|\mathbf{r}-\mathbf{r}'|\right)/\left(k|\mathbf{r}-\mathbf{r}'|\right). \tag{5}$$

The crucial point is to expand the whole field quantities with a set of orthogonal basis functions and solve the corresponding unknown coefficients. The scalar spherical basis function is expressed as

$$\begin{aligned}\Phi_{nm\sigma}(\mathbf{r}) &= h_n^{(1)}(kr) Y_{nm\sigma}(\theta,\varphi)\\ &= h_n(kr)\xi'_{nm} P_n^m(\cos\theta)\begin{pmatrix}\cos(m\varphi), \sigma = e\\ \sin(m\varphi), \sigma = o\end{pmatrix},\end{aligned} \tag{6}$$

where $P_n^m(\cos\theta)$ is the associated Legendre function of order n and rank m. The azimuthal parity index σ is either even or odd. $h_n^{(1)}(kr)$ is a spherical Hankel function of the first kind. The normalization coefficients ξ'_{nm} can be expressed as

$$\xi'_{nm} = \left[\varepsilon_m(2n+1)(n-m)!\right]^{1/2} \times \left[4\pi(n+m)!\right]^{-1/2}, \tag{7}$$

with $\varepsilon_m = \begin{cases}1, m = 0\\ 2, m \neq 0\end{cases}$. The value range of the order index is $n = 0, 1, \cdots, \infty$, and the rank index m takes the integer values $m = 0, 1, \cdots, n$.

The incident and scattered field can be expanded into the form of the weighted sum of the scalar basis function with the expanded coefficients. The regular spherical basis function, denoted by $\mathrm{Re}\Phi_{nm\sigma}$, is obtained by substituting the first-kind spherical Bessel function $j_n(kr)$ for $h_n^{(1)}(kr)$ into Eq. 6. Therefore, the incident and scattered fields can be expanded as

$$\Phi_i(\mathbf{r}) = \sum_{nm\sigma} a_{nm\sigma}\mathrm{Re}\Phi_{nm\sigma}(\mathbf{r}), \tag{8}$$

$$\Phi_s(\mathbf{r}) = \sum_{nm\sigma} f_{nm\sigma}\Phi_{nm\sigma}(\mathbf{r}), \tag{9}$$

where $\sum_{nm\sigma} = \sum_{n=0}^{\infty}\sum_{m=0}^{n}\sum_{\sigma}$ is the triple summation symbol, $a_{nm\sigma}$ denotes the expanded coefficient of the incident field, and $f_{nm\sigma}$ denotes the unknown expanded coefficient of the scattering field. For a plane harmonic wave, the expanded coefficient is

$$a_{nm\sigma} = 4\pi\xi'_{nm} i^n P_n^m(\cos\theta_i)\begin{pmatrix}\cos(m\varphi_i), \sigma = e\\ \sin(m\varphi_i), \sigma = o\end{pmatrix}. \tag{10}$$

Furthermore, the free-field Green's function $g(\mathbf{r},\mathbf{r}')$ can be expanded using the spherical basis function as

$$g(\mathbf{r},\mathbf{r}') = \sum_{nm\sigma} ik\,\Phi_{nm\sigma}(r_>)\mathrm{Re}\Phi_{nm\sigma}(r_<), \tag{11}$$

where $r_> = \begin{cases}r, r > r'\\ r', r < r'\end{cases}$ and $r_< = \begin{cases}r, r < r'\\ r', r > r'\end{cases}$. r' is the modulus of the point $\mathbf{r}'$ on the surface S of the spheroid. r is the modulus of the field point $\mathbf{r}$. The expanded expression of the unknown surface field Φ_+ is

$$\Phi_+(\mathbf{r}') = \sum_{nm\sigma}\alpha_{nm\sigma}\mathrm{Re}\Phi_{nm\sigma}(\mathbf{r}'), \tag{12}$$

where $\alpha_{nm\sigma}$, which is omitted in the process of deriving the T-matrix, is the expanded coefficient of the unknown surface field.

For a rigid spheroid, the boundary of the spheroid at $\mathbf{r} = S(\theta)$ satisfies the Neumann boundary condition:

$$\mathbf{n}\cdot\nabla_+\Phi(\mathbf{r})\big|_{\mathbf{r}=S(\theta)} = 0. \tag{13}$$

Substituting Eqs 6–13 into Eq. 4 yields

$$i\sum_{n'm'\sigma'} Q_{nm\sigma,n'm'\sigma'}\alpha_{n'm'\sigma'} = -a_{nm\sigma}, \tag{14}$$

$$i\sum_{n'm'\sigma'} \mathrm{Re}Q_{nm\sigma,n'm'\sigma'}\alpha_{n'm'\sigma'} = f_{nm\sigma}, \tag{15}$$

where

$$Q_{nm\sigma,n'm'\sigma'} = k\int_S \mathrm{Re}\Phi_{n'm'\sigma'}(\mathbf{r}')\mathbf{n}\cdot\nabla\Phi_{nm\sigma}(\mathbf{r}')\mathrm{d}S. \tag{16}$$

The detailed expression of $Q_{nm\sigma,n'm'\sigma'}$ is obtained by substituting Eq. 6 into Eq. 16:

$$\begin{aligned}Q_{nm\sigma,n'm'\sigma'} = &\int_0^{\pi}\xi'_{n'm'} j_{n'}(kr) P_{n'}^{m'}(\cos\theta)\xi_{nm}\\ &\times\left[\frac{\partial h_n(kr)}{\partial r}P_n^m(\cos\theta) - \frac{r_\theta}{r^2}h_n(kr)\times\frac{\partial P_n^m(\cos\theta)}{\partial\theta}\right]\\ &\times r^2\sin\theta\mathrm{d}\theta\int_0^{2\pi}\begin{pmatrix}\cos m'\varphi\\ \sin m'\varphi\end{pmatrix}\begin{pmatrix}\cos m\varphi\\ \sin m\varphi\end{pmatrix}\mathrm{d}\varphi,\end{aligned} \tag{17}$$

where $r_\theta = \partial r(\theta)/\partial\theta$ and $r(\theta) = S(\theta)$. In the expression of the Q-matrix, the symmetry of the scatterer leads to certain elements in the Q-matrix becoming zero. In this study, the rotational symmetry

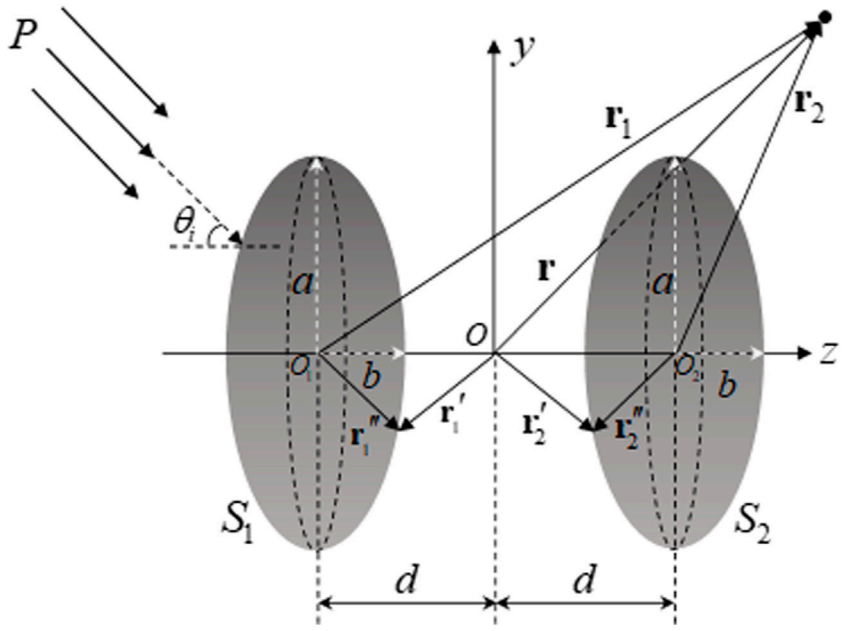

FIGURE 2
Geometry model for the acoustic scattering of a pair of rigid spheroids.

of the spheroid makes the Q-matrix block diagonal of the submatrices, and thus, the computation can be simplified.

From Eqs 14, 15, the relationship between scattering and incident expanded coefficients can be expressed as

$$f_{nm\sigma} = Ta_{nm\sigma}, \tag{18}$$

where the transition matrix T, showing the influence of the geometry of the spheroid, the incident angle, and the frequency of the plane wave [20, 21], is expressed as

$$T = -(\mathrm{Re}Q)Q^{-1}. \tag{19}$$

2.2 For a pair of rigid spheroids

In this part, the formula of the T-matrix method for a pair of rigid spheroids immersed in the idea fluid is derived. The geometry of the configuration to be considered is shown in Figure 2. The formula of the T-matrix method for a pair of rigid spheroids is derived exactly like Eq. 4:

$$\Phi_i(\mathbf{r}) + \int_{S_1+S_2} \left[\Phi_+ \mathbf{n}\cdot\nabla g(\mathbf{r},\mathbf{r}') - (\mathbf{n}\cdot\nabla_+\Phi) g(\mathbf{r},\mathbf{r}')\right] \mathrm{d}S = \begin{cases} \Phi(\mathbf{r}) & \mathbf{r}\ \text{outside}\ S_1\ \text{and}\ S_2 \\ 0 & \mathbf{r}\ \text{inside}\ S_1\ \text{or}\ S_2. \end{cases} \tag{20}$$

The incident field $\Phi_i(\mathbf{r})$ and the free-field Green's function $g(\mathbf{r},\mathbf{r}')$ need to be expanded at origins O_1 and O_2 to obtain the **Q**-matrix of each of the spheroids, which are analogous to Eq. 16. When the field point $\mathbf{r}$ is located inside S_1,

$$\mathbf{r} = \mathbf{r}_1 - \mathbf{d}, \mathbf{r}' = \mathbf{r}_1', \mathbf{r} - \mathbf{r}_1' = \mathbf{r}_1 - \mathbf{r}_1'', \mathbf{r} - \mathbf{r}_2' = \mathbf{r}_1 - \left(\mathbf{r}_2'' + 2\mathbf{d}\right), \tag{21}$$

where $\mathbf{d} = \overrightarrow{O_1O} = \overrightarrow{OO_2}$. According to Eq. 11, Green's functions $g(\mathbf{r},\mathbf{r}_1')$ and $g(\mathbf{r},\mathbf{r}_2')$ can be written as

$$g\left(\mathbf{r},\mathbf{r}_1'\right) = \sum_{nm\sigma} ik\,\Phi_{nm\sigma}\left(\mathbf{r}_1''\right)\mathrm{Re}\Phi_{nm\sigma}(\mathbf{r}_1), \tag{22}$$

$$g\left(\mathbf{r},\mathbf{r}_2'\right) = \sum_{nm\sigma} ik\,\Phi_{nm\sigma}\left(\mathbf{r}_2'' + 2\mathbf{d}\right)\mathrm{Re}\Phi_{nm\sigma}(\mathbf{r}_1). \tag{23}$$

From Eqs 8, 21, where $\mathbf{r} = \mathbf{r}_1 - \mathbf{d}$, the incident fields can be expressed as

$$\Phi_i(\mathbf{r}) = \sum_{nm\sigma} a_{nm\sigma}\mathrm{Re}\Phi_{nm\sigma}(\mathbf{r}_1 - \mathbf{d}). \tag{24}$$

The addition theorems of the spherical basis functions are used in Eqs 23, 24. The translation properties are as follows [22, 23]:

$$\begin{aligned} \mathrm{Re}\Phi_{nm\sigma}(\mathbf{r}+\mathbf{d}) &= \sum_{n'm'\sigma'} \hat{R}_{nm\sigma,n'm'\sigma'}(\mathbf{d})\mathrm{Re}\Phi_{n'm'\sigma'}(\mathbf{r}), \\ \Phi_{nm\sigma}(\mathbf{r}+\mathbf{d}) &= \begin{cases} \sum_{n'm'\sigma'} \hat{R}_{nm\sigma,n'm'\sigma'}(\mathbf{d})\Phi_{n'm'\sigma'}(\mathbf{r}), & |\mathbf{r}| > |\mathbf{d}|, \\ \sum_{n'm'\sigma'} R_{nm\sigma,n'm'\sigma'}(\mathbf{d})\mathrm{Re}\Phi_{n'm'\sigma'}(\mathbf{r}) & |\mathbf{r}| < |\mathbf{d}|, \end{cases} \end{aligned} \tag{25}$$

where the coordinates of the vector $\mathbf{d}$ in the spherical coordinate system are (d,η,ψ). $\hat{R}$ is the regular form of R by replacing the spherical Hankel function with spherical Bessel functions. The matrices $\hat{R}_{nm\sigma,n'm'\sigma'}(\mathbf{d})$ are given as

$$\begin{aligned} \hat{R}_{nm\sigma,n'm'\sigma'}(\mathbf{d}) &= \frac{(-1)^m}{2}[\varepsilon_m\cdot\varepsilon_{m'}]^{1/2}\Big[(-1)^{m'}C_{nm,n'm'}(d,\eta)\cos(m-m')\psi \\ &\quad + (-1)^{\sigma}C_{nm,-n'm'}(d,\eta)\cos(m+m')\psi\Big], \sigma=\sigma', \\ \hat{R}_{nm\sigma,n'm'\sigma'}(\mathbf{d}) &= \frac{(-1)^m}{2}[\varepsilon_m\cdot\varepsilon_{m'}]^{1/2}\Big[(-1)^{\sigma'+m'}C_{nm,n'm'}(d,\eta)\sin(m-m')\psi \\ &\quad + C_{nm,-n'm'}(d,\eta)\sin(m+m')\psi\Big], \sigma\neq\sigma', \end{aligned} \tag{26}$$

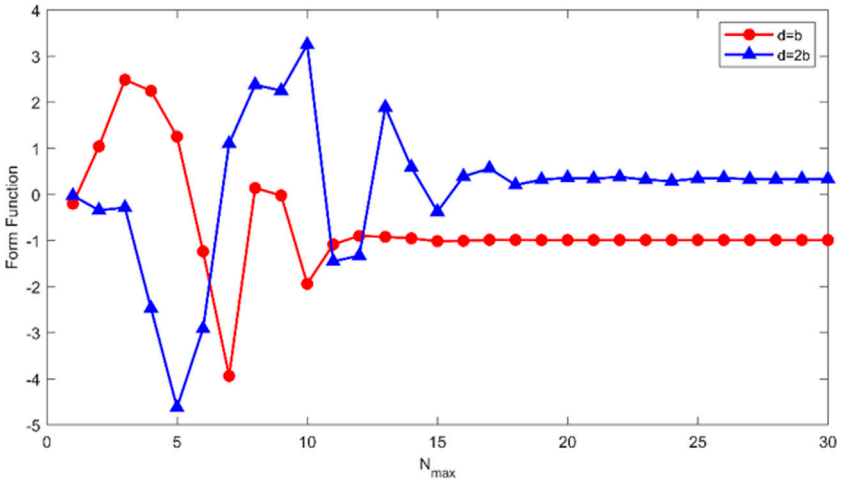

FIGURE 3
Convergence study of the *T*-matrix method for a pair of rigid spheres. The backscattering modulus $|f_{\infty}|$ of a pair of rigid spheres was calculated at end-on incidence (θ_i = 0°) with the dimensionless frequency kb = 5 versus N_{max} for a pair of rigid spheres with separation distances $2d = 2b$ and $4b$, respectively.

where

$$C_{nm,n'm'}(d,\eta) = \sum_{\lambda=|n-n'|}^{n+n'} (-1)^{m'+n+(n+n'+\lambda)/2}(2\lambda+1)\left[\frac{(2n+1)(2n'+1)[\lambda-(m-m')]!}{[\lambda+(m-m')]!}\right]^{1/2} \times \begin{pmatrix} n & n' & \lambda \\ 0 & 0 & 0 \end{pmatrix}\begin{pmatrix} n & n' & \lambda \\ m-m' & -(m-m') & \end{pmatrix} j_{\lambda}(kd)P_{\lambda}^{m-m'}(\cos\eta), \tag{27}$$

where $\begin{pmatrix} \cdots \\ \cdots \end{pmatrix}$ is the Wigner 3-*j* symbol [24]; its expression is given as follows:

$$\begin{pmatrix} j_1 & j_2 & j_3 \\ m_1 & m_2 & m_3 \end{pmatrix} = (-1)^{j_1-j_2-m_3}\delta_{-m_3,m_1+m_2}\left\{\frac{(j_1+j_2-j_3)!(j_2+j_3-j_1)!(j_1+j_3-j_2)!}{(j_1+j_2+j_3+1)!}\right. \times \left.\prod_{i=1,2,3}(j_i+m_i)!(j_i-m_i)!\right\}\sum_{\nu}[(-1)^{\nu}\nu!(j_1+j_2-j_3-\nu)! \times (j_2+m_2-\nu)!(j_3-j_1-m_2+\nu)!(j_3-j_2+m_1+\nu)! \times (j_1-m_1-\nu)!]^{-1}, \delta_{-m_3,m_1+m_2}=1, \delta_{-m_3,m_1+m_2}=0, -m_3 \neq m_1+m_2. \tag{28}$$

In this study, the expression of the matrices $\hat{R}_{nm\sigma,n'm'\sigma'}(\pm\mathbf{d})$ for the special case of the offset along the *z*-axis is

$$\hat{R}_{nm\sigma,n'm'\sigma'}(\pm\mathbf{d}) = \sum_{\lambda=|n-n'|}^{n+n'} (-1)^{m'+n+(n+n'+\lambda)/2}(2\lambda+1)[(2n+1)(2n'+1)]^{1/2} \times \begin{pmatrix} n & n' & \lambda \\ 0 & 0 & 0 \end{pmatrix}\begin{pmatrix} n & n' & \lambda \\ m-m' & 0 & \end{pmatrix}(\pm 1)^{\lambda} j_{\lambda}(kd) \times \delta_{\sigma\sigma'}\delta_{mm'}\begin{cases} 1, & m>0 \\ 1, & m=0, \sigma=e \\ 1, & m=0, \sigma=o. \end{cases} \tag{29}$$

Substituting Eqs 22–25 into the second formula of Eq. 20 yields

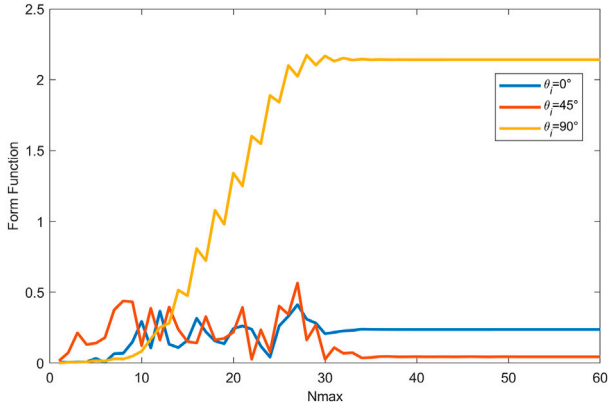

FIGURE 4
Convergence study of the *T*-matrix method for a pair of rigid spheroids with aspect ratio b/a = 4 for the separation distance $2d = 4r_0$. The backscattering modulus $|f_{\infty}|$ of a pair of rigid spheroids was calculated with the dimensionless frequency kb = 10 versus N_{max} under three incident cases (θ_i = 0°, 45°, and 90°).

$$0 = \sum_{nm\sigma}\sum_{n'm'\sigma'} a_{nm\sigma}\hat{R}_{nm\sigma,n'm'\sigma'}(-\mathbf{d})\mathrm{Re}\Phi_{n'm'\sigma'}(\mathbf{r}_1) + \sum_{nm\sigma} ik\int_{S_1}\mathrm{Re}\Phi_{nm\sigma}(\mathbf{r}_1)\left\{\Phi_+(\mathbf{r}_1'') \times \mathbf{n}\cdot\nabla\Phi_{nm\sigma}(\mathbf{r}_1'') - \left(\mathbf{n}\cdot\nabla_+\Phi(\mathbf{r}_1'')\right)\Phi_{nm\sigma}(\mathbf{r}_1'')\right\}\mathrm{d}S + \sum_{nm\sigma}\sum_{n'm'\sigma'} ik \times R_{nm\sigma,n'm'\sigma'}(2\mathbf{d})\int_{S_2}\mathrm{Re}\Phi_{nm\sigma}(\mathbf{r}_1)\left\{\Phi_+(\mathbf{r}_2'')\mathbf{n}\cdot\nabla\Phi_{n'm'\sigma'}(\mathbf{r}_2'') - \left(\mathbf{n}\cdot\nabla_+\Phi(\mathbf{r}_2'')\right)\mathrm{Re}\Phi_{n'm'\sigma}(\mathbf{r}_2'')\right\}\mathrm{d}S. \tag{30}$$

The expansion coefficients of the unknown surface fields of two spheroids are $\alpha^1_{nm\sigma}$ and $\alpha^2_{nm\sigma}$, respectively. The boundary of these two spheroids satisfies the Neumann boundary condition. In this way, Eq. 30 can be expressed as

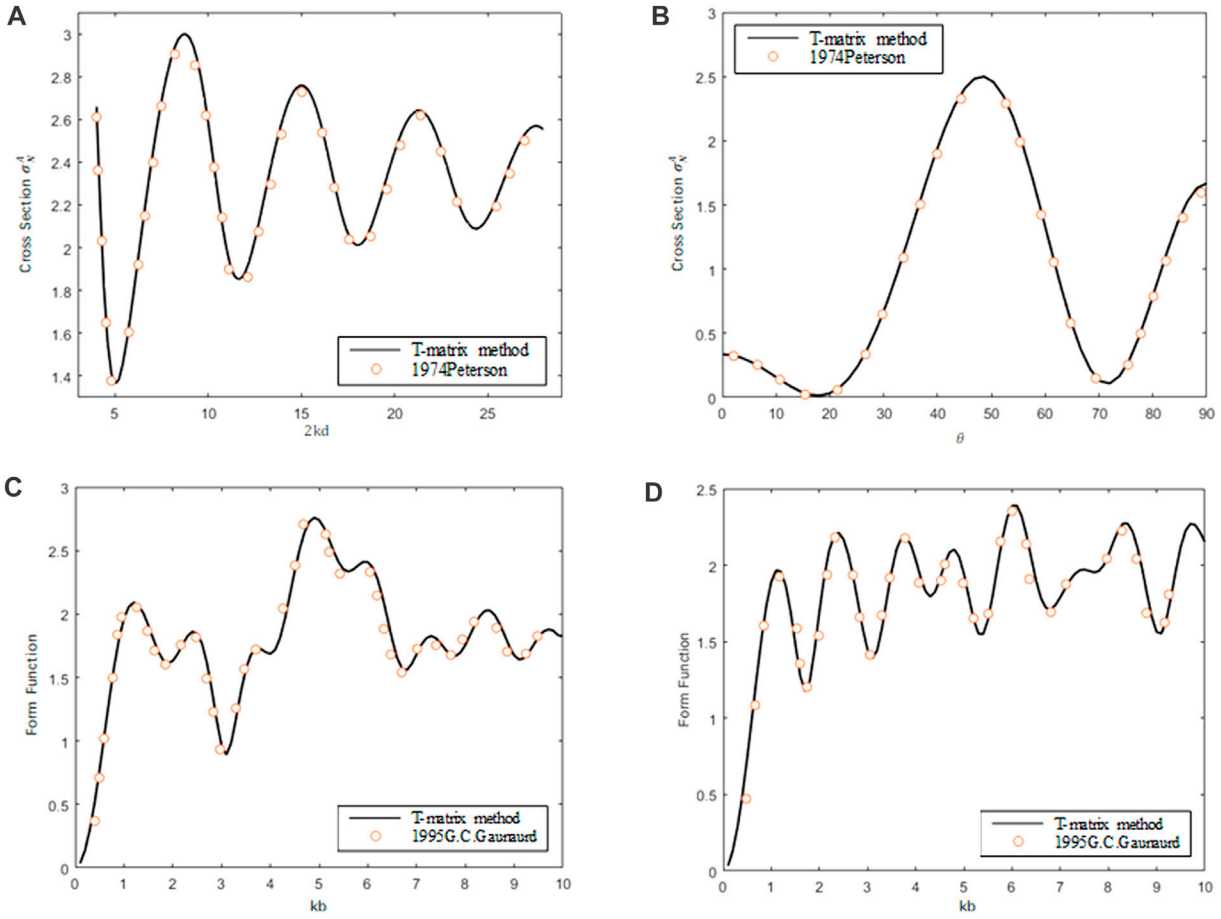

FIGURE 5
Accuracy study of the *T*-matrix method for a pair of rigid spheres. **(A)** Backscattering cross section of a pair of rigid spheres at broadside incidence (θ_i = 90°) for *kb* = 2 versus separation distance 2*kd*. **(B)** Backscattering cross section of a pair of rigid spheres for *kb* = 2 and 2*kd* = 4.5 versus the incidence angle θ_i. **(C)** Backscattering form function $|f_{\infty}|$ of a pair of rigid spheres at broadside incidence (θ_i = 90°) versus *kb* for the separation distance 2*d* = 2*b*. **(D)** Backscattering form function $|f_{\infty}|$ of a pair of rigid spheres at broadside incidence (θ_i = 90°) versus *kb* for the separation distance 2*d* = 2*b*.

$$0 = \sum_{n'm'\sigma'} a_{n'm'\sigma'} \hat{R}_{nm\sigma,n'm'\sigma'}(-\mathbf{d}) - i \sum_{n'm'\sigma'} Q^1_{nm\sigma,n'm'\sigma'} \alpha^1_{n'm'\sigma'} - i \sum_{n'm'\sigma'} \sum_{n''m''\sigma''} R_{nm\sigma,n'm'\sigma'}(2\mathbf{d}) \mathrm{Re} Q^2_{n'm'\sigma',n''m''\sigma''} \alpha^2_{n''m''\sigma''}, \tag{31}$$

where $Q^1_{nm\sigma,n'm'\sigma'}$ and $Q^2_{nm\sigma,n'm'\sigma'}$ are given by Eq. 17, with the integrals taken over S_1 and S_2. Expressing the aforementioned equation in terms of matrices and vectors yields

$$\hat{R}^t(-\mathbf{d})\mathbf{a} = i\mathbf{Q}^1\boldsymbol{\alpha}^1 + iR(2\mathbf{d})\mathrm{Re}\mathbf{Q}^2\boldsymbol{\alpha}^2, \tag{32}$$

where $\hat{R}^t(-\mathbf{d}) = \hat{R}(\mathbf{d})$ and the superscript "t" denotes the transposition of the matrix. In the same way, when the field point $\mathbf{r}$ is located inside S_2,

$$\hat{R}^t(\mathbf{d})\mathbf{a} = iR(-2\mathbf{d})\mathrm{Re}\mathbf{Q}^1\boldsymbol{\alpha}^1 + i\mathbf{Q}^2\boldsymbol{\alpha}^2. \tag{33}$$

Considering the field point $\mathbf{r}$ located outside the sphere S_O (the smallest external sphere containing both spheroids S_1 and S_2 with O as the center of the sphere), according to Eq. 11, the free-field Green's functions $g(\mathbf{r}, \mathbf{r}_1')$ and $g(\mathbf{r}, \mathbf{r}_2')$ can be written as

$$\begin{aligned} g(\mathbf{r}, \mathbf{r}_1') &= \sum_{nm\sigma} ik\,\Phi_{nm\sigma}(\mathbf{r})\mathrm{Re}\Phi_{nm\sigma}(\mathbf{r}_1') \\ &= \sum_{nm\sigma}\sum_{n'm'\sigma'} ik\Phi_{nm\sigma}(\mathbf{r})\hat{R}_{nm\sigma,n'm'\sigma'}(-\mathbf{d})\mathrm{Re}\Phi_{n'm'\sigma'}(\mathbf{r}_1''), \end{aligned} \tag{34}$$

$$\begin{aligned} g(\mathbf{r}, \mathbf{r}_2') &= \sum_{nm\sigma} ik\,\Phi_{nm\sigma}(\mathbf{r})\mathrm{Re}\Phi_{nm\sigma}(\mathbf{r}_2') \\ &= \sum_{nm\sigma}\sum_{n'm'\sigma'} ik\Phi_{nm\sigma}(\mathbf{r})\hat{R}_{nm\sigma,n'm'\sigma'}(\mathbf{d})\mathrm{Re}\Phi_{n'm'\sigma'}(\mathbf{r}_2''). \end{aligned} \tag{35}$$

Substituting Eqs 34, 35, 9 into the first formula of Eq. 20 yields

$$\mathbf{f} = -i\hat{R}(-\mathbf{d})\mathrm{Re}\mathbf{Q}^1\boldsymbol{\alpha}^1 - i\hat{R}(\mathbf{d})\mathrm{Re}\mathbf{Q}^2\boldsymbol{\alpha}^2. \tag{36}$$

From Eqs 32, 33, the surface field coefficients $\boldsymbol{\alpha}^1$ and $\boldsymbol{\alpha}^2$ can be solved into expressions in terms of the incident field coefficient $\mathbf{a}$. Afterward, the transition matrix $T(1,2)$ can be obtained by substituting the solved $\boldsymbol{\alpha}^1$ and $\boldsymbol{\alpha}^2$ into Eq. 36, such that

$$\begin{aligned} T(1,2) = \hat{R}(-\mathbf{d})\{&T(1)[I - R(2\mathbf{d})\mathrm{T}(2)R(-2\mathbf{d})\mathrm{T}(1)]^{-1} \\ &\times [I + R(2\mathbf{d})T(2)\hat{R}(-2\mathbf{d})]\}\hat{R}(\mathbf{d}) \\ &+ \hat{R}(\mathbf{d})\{T(2)[I - R(-2\mathbf{d})T(1)R(2\mathbf{d})T(2)]^{-1} \\ &\times [I + R(-2\mathbf{d})T(1)\hat{R}(2\mathbf{d})]\}\hat{R}(-\mathbf{d}), \end{aligned} \tag{37}$$

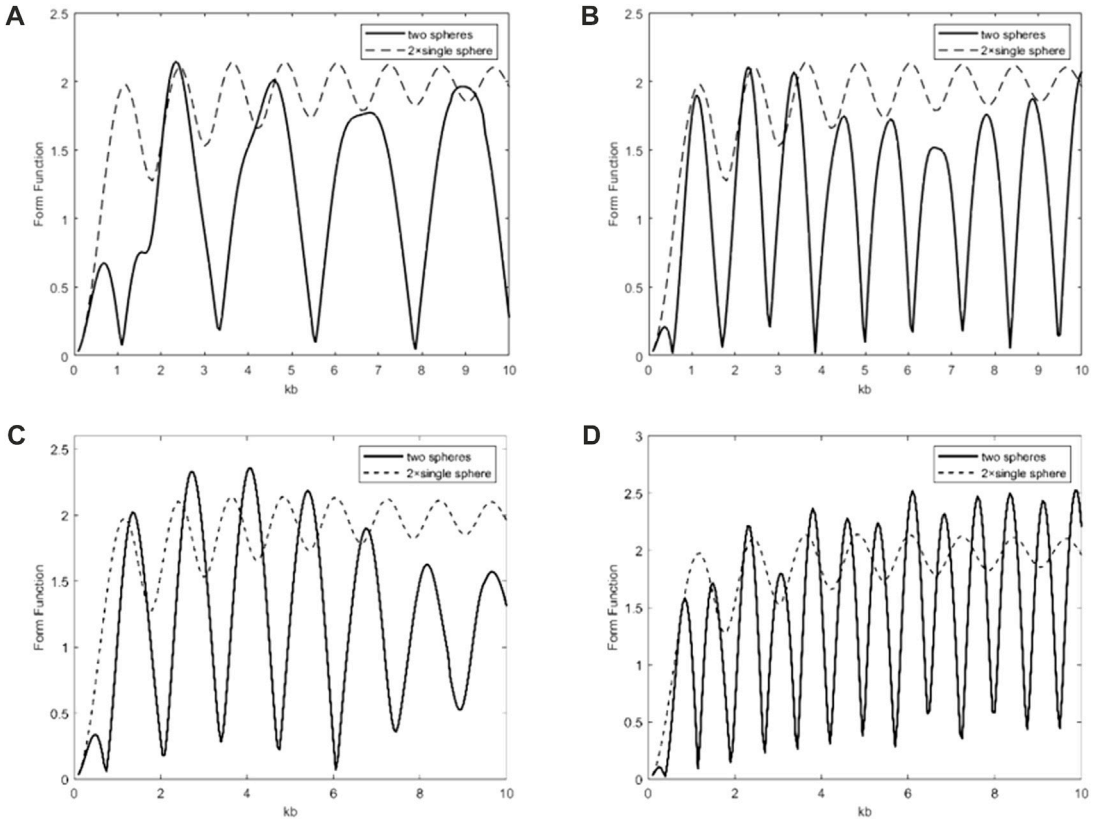

FIGURE 6
Backscattering form function $|f_{\infty}|$ (solid lines) of a pair of rigid spheres at oblique incidence ($\theta_i = 45°$) versus kb for the separation distances **(A)** $2d = 2b$ and **(B)** $2d = 4b$. The backscattering form function $|f_{\infty}|$ of a pair of rigid spheres at end-on incidence ($\theta_i = 0°$) versus kb for separation distances **(C)** $2d = 2b$ and **(D)** $2d = 4b$. The dashed lines represent twice the value of the backscattering form function $|f_{\infty}|$ of a single rigid sphere.

TABLE 1 Time intervals regarding the peak-to-peak intervals in Panel (a) of Figure 7.

Time interval	Predicted by the geometric model (ms)	Obtained from Figure 7 (ms)
t_2–t_1	3.41	3.29
t_3–t_1	5.30	5.37
t_4–t_3	3.41	3.30

TABLE 2 Time intervals regarding the peak-to-peak intervals in Panel (b) of Figure 7.

Time interval	Predicted by the geometric model (ms)	Obtained from Figure 7 (ms)
t_2–t_1	3.41	3.32
t_3–t_1	3.75	3.74
t_4–t_3	3.41	3.33

where I is the identity matrix and $T(1)$ $(T(2))$ is the T-matrix formulation of spheroids S_1 (S_2), which can be calculated using Eq. 19.

Since the far-field scattering characteristics are majorly considered in the current study, the form function f_{∞} can be defined by [25, 26]

$$f_{\infty}(kr_0, \theta, \varphi) = \lim_{r \longrightarrow \infty} \frac{2r}{r_0} \frac{\Phi_s}{\Phi_0} e^{-ikr}, \tag{38}$$

where $r_0 = \max(a, b)$. According to Eq. 38, the factors that affect the form function are the observation position of the scattering field, incident angle, and non-dimensional frequency.

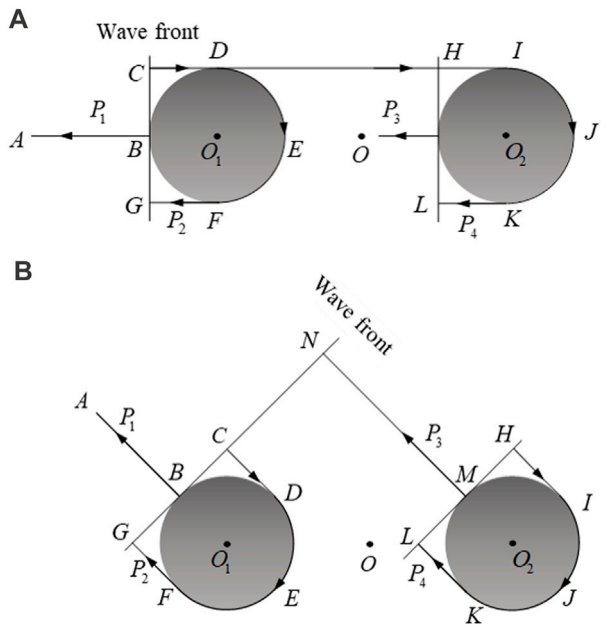

FIGURE 7
Propagation path of the backscattering waves by a pair of spheres at **(A)** end-on incidence and **(B)** oblique incidence.

3 Numerical examples and results

In this section, the convergence and accuracy of the T-matrix method for calculating the acoustic scattering of a pair of rigid spheres and spheroids are shown by several numerical experiments. Afterward, the monostatic and bistatic acoustic scattering form function modulus $|f_\infty|$ of a pair of rigid spheroids illuminated by the plane wave are calculated by the T-matrix method considering various models with a range of aspect ratios b/a, separation distances $2d$, non-dimensional frequencies kr_0 ($r_0 = \max(a, b)$), and incidence angles θ_i.

3.1 Numerical validation

The convergence of the T-matrix method for calculating the acoustic scattering of a pair of rigid spheres under the plane wave end-on incidence ($\theta_i = 0^\circ$) is verified. According to the aforementioned theoretical formulation, the infinite summation in the **Q**-matrix and **R**-matrix must be truncated at the appropriate limit $N_{\max}$. Figure 3 shows the results of $|f_\infty|$ versus $N_{\max}$ under the end-on incidence case with the non-dimensional frequency $kb = 5$ at separation distances $2d = 2b$ and $4b$. It can be seen from Figure 3 that the T-matrix method converges faster in calculating the acoustic scattering problem of a pair of spheres. The relative convergence error of $|f_\infty|$ can be given by [27]

$$\varepsilon(N_{\max}) = \left| \frac{f_\infty(N_{\max}) - f_\infty(N'_{\max})}{f_\infty(N'_{\max})} \right|. \tag{39}$$

The truncation factor $N'_{\max}$ in this study is expressed as $N'_{\max} = \mathrm{Int}(k \times (2d + r_0)) + 5$. When the dimensionless frequency $kb = 5$, the values of the truncation factor $N'_{\max}$ are taken as 20 and 30 for separation distances of $d = b$ and $2b$, respectively. As shown in Figure 3, the form function modulus begins to converge, where $N_{\max}$ is greater than 14 and 26, respectively, and the relative convergence error could reach $10^{-5} \sim 10^{-6}$. Therefore, the expression of the truncation factor $N_{\max}$ is verified to be correct and feasible. Furthermore, the convergence and accuracy of the T-matrix method for calculating the acoustic scattering of a pair of rigid spheroids are studied. Figure 4 shows the backscattering modulus $|f_\infty|$ of a pair of rigid spheroids with $b/a = 4$ for the separation distance $2d = 4r_0$ versus $N_{\max}$ with $kb = 10$ under three incident cases ($\theta_i = 0°$, 45°, and 90°). The results show that all the curves have good convergence and the solutions are stable and accurate. Similarly, the relative convergence error could reach $10^{-5} \sim 10^{-6}$.

In the following, some numerical experiment results of the acoustic scattering of a pair of rigid spheres calculated by the present method are compared with Peterson's works [19] and the analytical results. The comparison results are shown in Figure 5. The circles are values according to the data from Peterson's works, while the solid lines are calculated by the present method. Panel (a) of Figure 5 displays the backscattering cross section of a pair of rigid spheres at the broadside incidence case ($\theta_i = 90^\circ, \varphi_i = 0^\circ$) for $kb = 2$ versus the separation distance $2kd$. It can be seen from Panel (a) of the figure that the numerical results are in complete agreement with Peterson's solutions. The scattering cross section is defined by

$$\sigma_N(r, \theta_s, \varphi_s; \theta_i, \varphi_i) = 4\pi r^2 \frac{|\Phi_s|^2}{|\Phi_0|^2} \frac{1}{\pi b^2}. \tag{40}$$

Panel (b) of Figure 5 displays the far-field backscattering cross section σ_N versus the incidence angle θ_i of a pair of rigid spheroids for $kb = 2$ and $2kd = 4.5$. It is in complete agreement with the results in Figure 7 of Peterson's works. It can be assured that the T-matrix method is sufficiently accurate in calculating the acoustic scattering of a pair of rigid spheres at arbitrary angular incidence. As shown in panels (c) and (d), the results of the backscattering form function $|f_\infty|$ of a pair of rigid spheres at the broadside incidence case calculated by the present method are exactly the same as those calculated by the analytical method [28] for separation distances $2d = 2b$ and $4b$. It can be seen from the aforementioned comparison that the T-matrix method is effective in computing the acoustic scattering of a pair of rigid spheres and spheroids.

3.2 Far-field acoustic scattering properties of a pair of rigid spheres

In this part, the far-field scattering properties of a pair of rigid spheres under the plane wave at arbitrary incident angles are studied

TABLE 3 Time intervals regarding the peak-to-peak intervals in Panel (c) of Figure 7.

Time interval	Predicted by the geometric model (ms)	Obtained from Figure 7 (ms)
t_2–t_1 = t_4–t_3	3.41	3.54

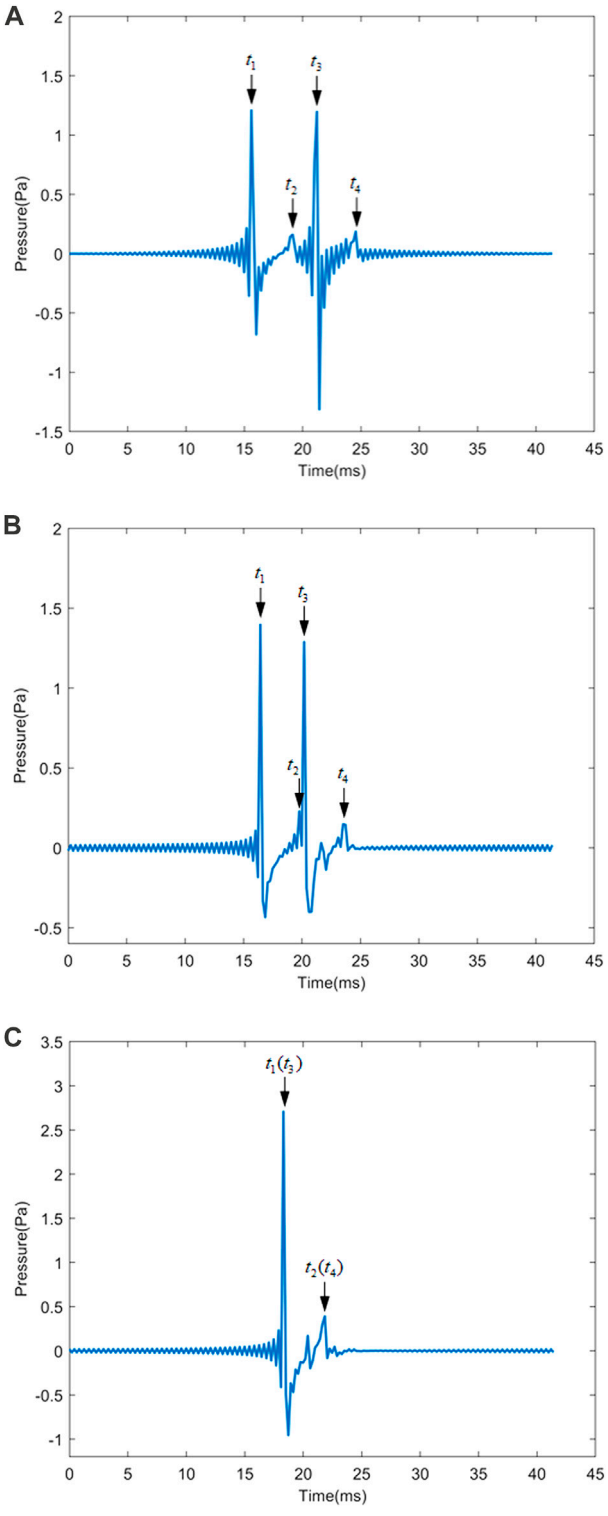

FIGURE 8
Backscattering response waves of a pair of rigid spheres in the time domain for the separation distance $2d = 4b = 4m$ under the pulse wave. **(A)** End-on incidence ($\theta_i = 0°$), **(B)** oblique incidence ($\theta_i = 45°$), and **(C)** broadside incidence ($\theta_i = 90°$).

by the *T*-matrix method. Figure 6 displays the backscattering form function $|f_\infty|$ versus the dimensionless frequency ka of a pair of rigid spheres with two values of the separation distance ($2d = 2b$ and $4b$) under oblique ($\theta_i = 45°$) incidence and end-on ($\theta_i = 0°$) incidence, respectively. As shown in Panels (a) and (b), it can be seen that the form function $|f_\infty|$ (solid line) of a pair of spheres is below the values (dashed line) of twice the form function modulus of a single rigid sphere under plane wave oblique incidence. Furthermore, the backscattering form function curves oscillate faster as the separation distance increases at the oblique incidence case. This phenomenon is similar to the end-on incidence case (see Panels (c) and (d) of Figure 6), but the number of peaks in the backscattering form function curves under the oblique incidence case at the same separation distance is less than the end-on incidence case. In the end-on incidence case, the amplitude of the backscattering form function $|f_\infty|$ tends to be stable as kb increases for the separation distance of $2d = 4b$ (see Panel (d) of Figure 6). The reason for these oscillations in the backscattering form function curves is due to the interference between the specular reflection wave components and Franz wave components in the backscattering response wave [29, 30]. It can be seen that the oscillation period in the backscattering form function curves (solid line) of a pair of rigid spheres is not a constant compared to that (dashed line) of the single rigid sphere [31, 32]. The propagation mechanisms of the specular reflection and Franz wave in the backscattering response wave by a pair of rigid spheres are discussed in the following paragraph.

The path of backscattering waves by a pair of rigid spheres ensonified by the pulse wave from end-on incidence and oblique incidence, respectively, is shown in Panels (a) and (b) of Figure 7. P_1 and P_3 represent specular reflection waves, which propagate backwards immediately when the incident wave reaches the front of the first sphere and the second sphere, respectively. P_2 and P_4 represent the backward Franz waves, which diffracted around the shadowed surface of the obstacle, from the first sphere and second sphere, respectively. We define the moments of the arrival of backscattering response wave components P_1, P_2, P_3, and P_4 at the observation point as t_1, t_2, t_3, and t_4, respectively. The time intervals under end-on incidence can be predicted by the following equations:

$$\begin{cases} t_2 - t_1 = \dfrac{(\overline{CD} + DEF + \overline{FG})}{c}, \\ t_3 - t_1 = 2 \times (\overline{CD} + \overline{DH})/c, \\ t_4 - t_3 = (\overline{HI} + IJK + \overline{KL})/c, \end{cases} \tag{41}$$

where c denotes the velocity of the specular reflection wave. Likewise, the time intervals under the oblique incidence can be predicted as

$$\begin{cases} t_2 - t_1 = (\overline{CD} + DEF + \overline{FG})/c, \\ t_3 - t_1 = 2 \times \overline{MN}/c, \\ t_4 - t_3 = \dfrac{(\overline{HI} + IJK + \overline{KL})}{c}. \end{cases} \tag{42}$$

The ideal fluid medium around the spheres is water. The velocity of the specular reflection wave is 1,510 m/s, and the scattering field point is located at (−30, 0). The time domain response results obtained by the inverse fast Fourier transform (IFFT) of the frequency domain response results [33] of a pair of rigid spheres at three incidence cases ($\theta_i = 0°, 45°$, and $90°$) of

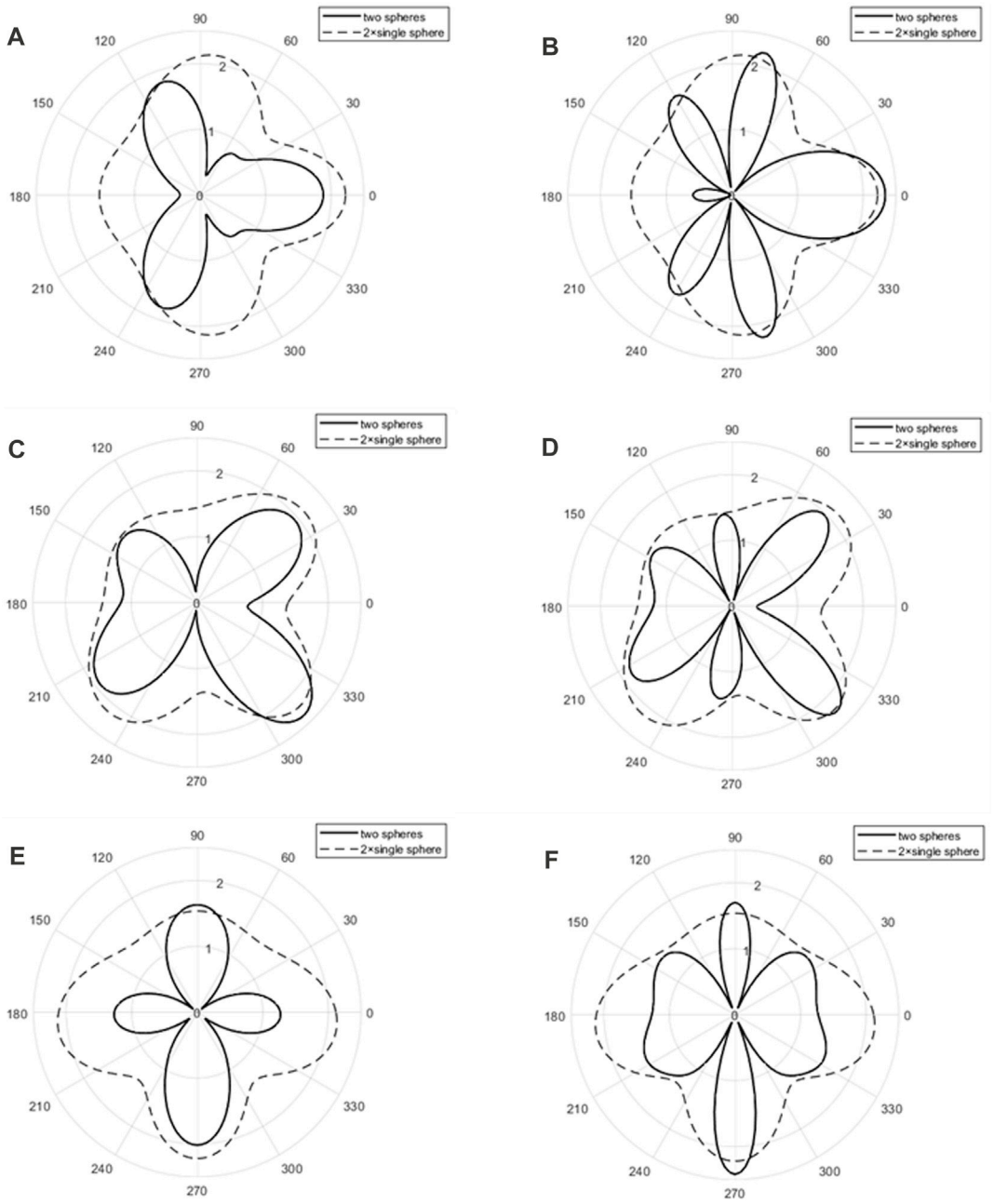

FIGURE 9
Bistatic 2D directivity pattern (solid line) of a pair of rigid spheres at end-on (θ_i = 0°) incidence with kb = 2 for separation distances **(A)** $2d = 2b$ and **(B)** $2d = 4b$. The bistatic 2D directivity pattern of a pair of rigid spheres at oblique (θ_i = 45°) incidence with kb = 2 for separation distances **(C)** $2d = 2b$ and **(D)** $2d = 4b$. The bistatic 2D directivity pattern of a pair of rigid spheres at broadside (θ_i = 90°) incidence with kb = 2 for separation distances **(E)** $2d = 2b$ and **(F)** $2d = 4b$. The dashed lines represent twice the value of the 2D directivity pattern of a single rigid sphere under three cases of incident angles (θ_i = 0°, 45°, and 90°) for kb = 2.

pulse waves for the separation distance $2d = 4b = 4m$ are shown in Figures 8A–C. Four obvious peaks can be obtained from Figures 8A, B. The specular reflection waves from the first sphere and second sphere lead to two peaks with the largest values. The two peaks with the smaller values are the Franz waves of the first sphere and second sphere, respectively. The values of Franz waves are smaller than those of specular reflection waves due to radiation damping when the Franz wave propagates in the shadowed area of the sphere. It can be seen that there are only two obvious peaks in Panel (c) of Figure 8 because the two spheres do not block each other in the direction of the pulse wave. In the case of broadside incidence (θ_i = 90°), the specular reflection waves of two spheres reach the observing point at the same time, and

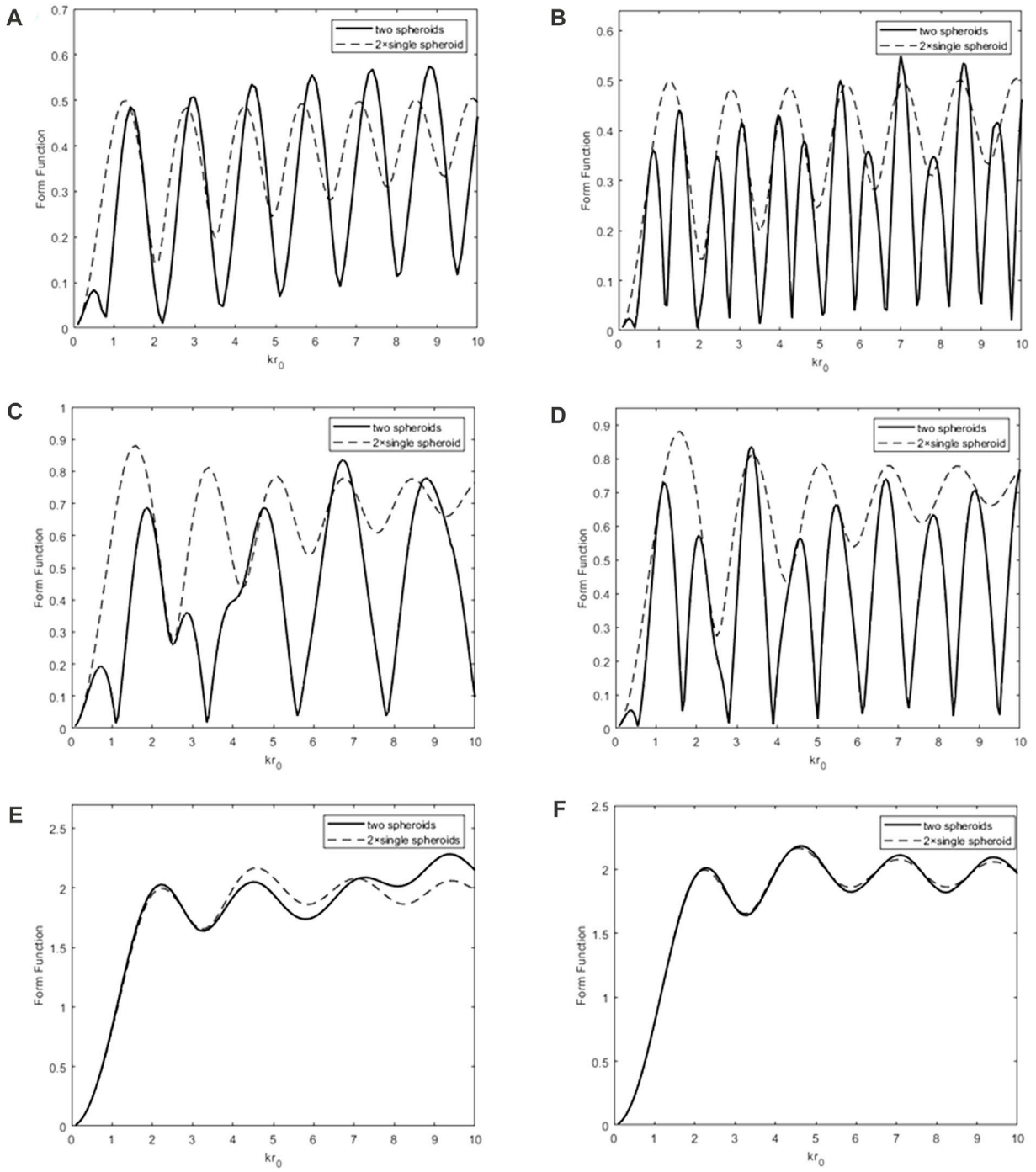

FIGURE 10
Backscattering form function $|f_{\infty}|$ (solid lines) of a pair of rigid prolate spheroids under end-on incidence ($\theta_i = 0°$) versus kr_0 ($r_0 = \max(a,b)$) for separation distances **(A)** $2d = 2r_0$ and **(B)** $2d = 4r_0$. The backscattering form function $|f_{\infty}|$ (solid lines) of a pair of rigid prolate spheroids under oblique incidence ($\theta_i = 45°$) versus kb for separation distances **(C)** $2d = 2r_0$ and **(D)** $2d = 4r_0$. The backscattering form function $|f_{\infty}|$ of a pair of rigid prolate spheroids under broadside incidence ($\theta_i = 90°$) versus kb for separation distances **(E)** $2d = 2b$ and **(F)** $2d = 4b$. The dashed lines represent twice the value of the backscattering form function $|f_{\infty}|$ of a single rigid prolate spheroid under three incident cases ($\theta_i = 0°$, 45°, and 90°).

subsequently, the Franz waves also reach the observing point at another identical time point. Furthermore, the time intervals corresponding to the peak-to-peak intervals for a pair of rigid spheres with three incidence cases ($\theta_i = 0°, 45°,$ and $90°$) of the pulse wave for the separation distance $2d = 4b = 4m$ in Figure 8 are listed in Tables 1, 2, 3. The predicted results based on the geometric model are calculated from Eqs 41, 42. As can be seen from Tables 1, 2, 3, the results calculated by the T-matrix method are consistent with the predicted results from the geometric model.

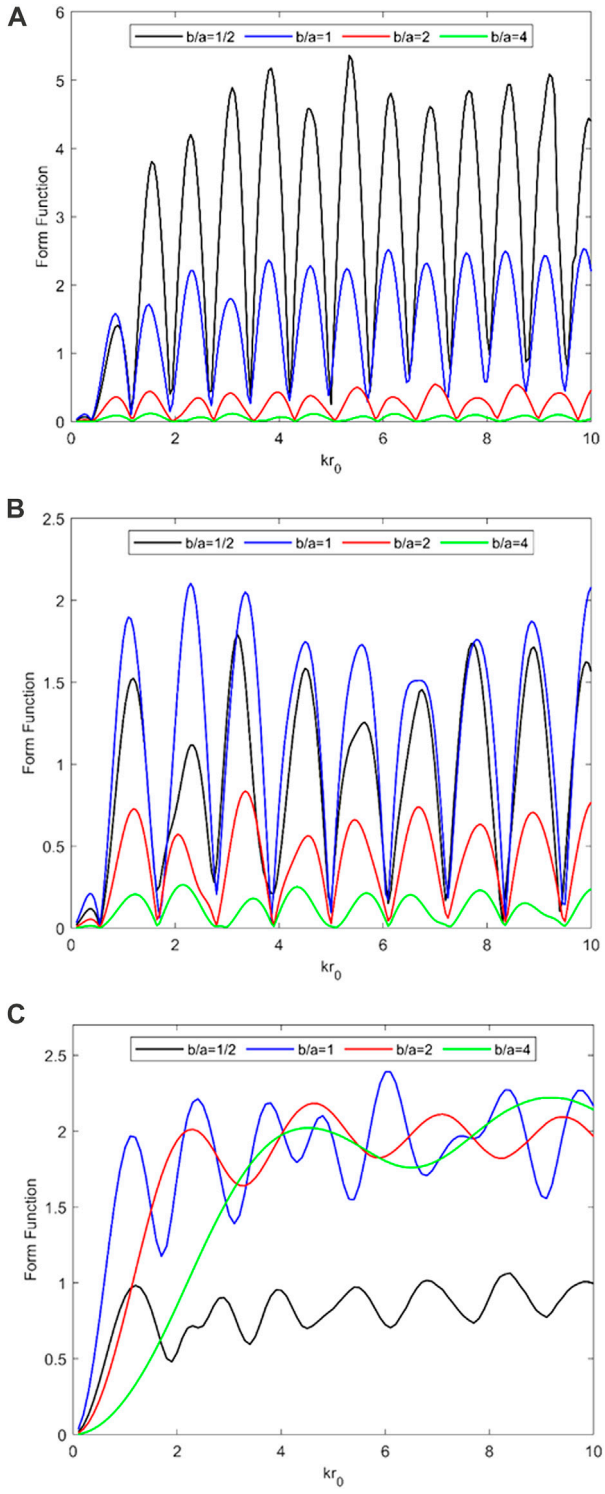

FIGURE 11
Backscattering form function $|f_\infty|$ of a pair of rigid spheroids with different aspect ratios (b/a = 1/2, 1, 2, and 4) versus kr_0 for the separation distance $2d = 4r_0$ under the plane wave. **(A)** End-on incidence ($\theta_i = 0°$), **(B)** oblique incidence ($\theta_i = 45°$), and **(C)** broadside incidence ($\theta_i = 90°$).

In order to quantitatively study the scattering of a pair of rigid spheres, the bistatic 2D directivity plots of a pair of rigid spheres under three cases ($\theta_i = 0°, 45°$, and $90°$) of the plane waves for the dimensionless frequency $kb = 2$ and separation distances $2d = 2b$ and $4b$, respectively, are shown in Figures 9A–F. It can be found that the scattering form function $|f_\infty|$ (solid line) of a pair of spheres is mostly below the dashed line, which is twice the value of the form function of the single sphere. The maximum values of the scattering form function $|f_\infty|$ in the 2D far-field directivity plots are in the forward scattering direction under three cases. The 2D far-field directivity plots under the oblique incidence are asymmetric in Figures 9C, D because the obstacles are asymmetric along the wave axis in the oblique incidence case. It is clearly shown that the number of petals increased as the separation distance increases at the same incident angles.

3.3 Far-field acoustic scattering properties of a pair of rigid spheroids

In this section, the far-field scattering properties of a pair of rigid spheroids under arbitrary incident angles of the plane wave are studied by the T-matrix method. The results of the backscattering form function $|f_\infty|$ (solid lines) of a pair of rigid prolate ($b/a = 2$) spheroids at three incidence cases ($\theta_i = 0°, 45°$ and $90°$) versus the non-dimensional frequency kr_0 ($r_0 = \max(a, b)$) for the separation distance $2d = 2r_0$ and $4r_0$, respectively, are shown in Figures 10A–F. The dashed lines represent twice the value of the backscattering form function $|f_\infty|$ of a single rigid sphere at broadside incidence. As shown in Figures 10A–D, the backscattering form function curves oscillate faster as the separation distance increases in the end-on incidence and oblique incidence cases. This phenomenon is consistent with the results of a pair of rigid sphere scattering in Section 3.2. Those oscillations in backscattering form function curves are caused by the interference between the specular reflection wave components and Franz wave components in the backscattering response wave. The peaks in the backscattering form function curves occur when the wave path difference Δs between the Franz wave and specular reflection wave, which is related to the separation distance $2d$, is an integral multiple of the wavelength λ. The peak-to-peak interval $\Delta(kr_0)$ in the backscattering form function curves can be expressed as $\Delta(kr_0) = \frac{2\pi a}{\Delta s}$. Obviously, $\Delta(kr_0)$ decreases as the separation distance increases, making the backscattering form function curves oscillate faster. In the broadside incidence case, the solid line and dashed line overlap at low frequencies in Panel (e) of Figure 10, implying that there is no interaction between these two spheroids in this frequency band. As the separation distance grows, the solid line and dashed line still overlap at higher frequencies in Panel (f) of Figure 10. This is because the two spheroids do not block each other in the direction of the incident wave, and the interactions between these two spheroids decrease as the separation distance grows.

Figure 11 displays the backscattering form function $|f_\infty|$ of a pair of rigid spheroids with different aspect ratios (b/a = 1/2, 1, 2, and 4) versus kr_0 ($r_0 = \max(a, b)$) for the separation distance $2d = 4r_0$ at three incidence cases ($\theta_i = 0°, 45°$, and $90°$). As shown in Figure 11A, the values of the backscattering form function $|f_\infty|$ of a pair of rigid spheroids in the end-on incidence case decrease as the aspect ratios grow. This is because the backscattering response wave of a pair of rigid spheroids under plane wave end-on incidence is mainly composed of the specular reflection wave at the front point of

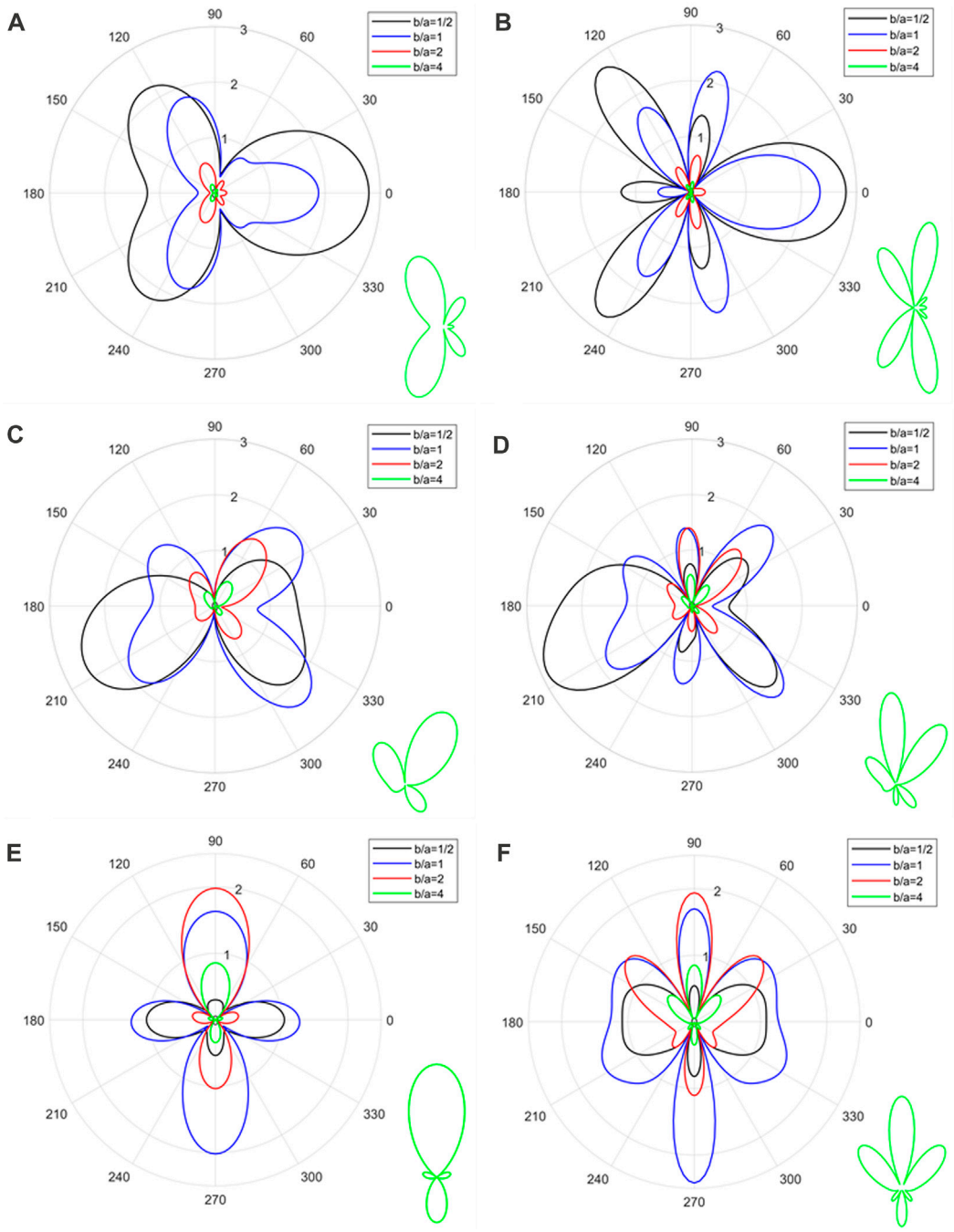

FIGURE 12
Bistatic 2D directivity pattern of a pair of rigid spheroids with different aspect ratios (b/a = 1/2, 1, 2, and 4) at end-on incidence (θ_i = 0°) with kr_0 = 2 for separation distances. **(A)** $2d = 2r_0$ and **(B)** $2d = 4r_0$. The bistatic 2D directivity pattern of a pair of rigid spheroids with different aspect ratios (b/a = 1/2, 1, 2, and 4) at oblique incidence (θ_i = 45°) with kr_0 = 2 for separation distances **(C)** $2d = 2r_0$ and **(D)** $2d = 4r_0$. The bistatic 2D directivity pattern of a pair of rigid spheroids with different aspect ratios (b/a = 1/2, 1, 2, and 4) at broadside incidence (θ_i = 90°) with kr_0 = 2 for separation distances **(E)** $2d = 2r_0$ and **(F)** $2d = 4r_0$.

the spheroids, and the intensity of the specular reflection wave increases as the radius of curvature at the front point of the spheroids increases [34]. It can be seen from Figure 11 that the number of peaks in the backscattering form function curves for a pair of rigid prolate ($b > a$) spheroids decreases with the increase in the incidence angle. In order to quantitatively study the scattering of a pair of rigid spheroids under the plane wave, the bistatic 2D directivity plots for a pair of rigid spheroids with different aspect ratios (b/a = 1/2, 1, 2, and 4) at three incidence cases (θ_i = 0°, 45°, and 90°) of the plane waves for the non-dimensional frequency $kb = 2$ and separation distances $2d = 2r_0$ and $4r_0$, respectively, are shown in Figures 12A–F. The zoomed-in plots

regarding the results of the 2D directivity diagrams of a pair of rigid prolate spheroids ($b/a = 4$) are also given in these panels. It is clearly seen that the number of petals in the 2D directivity plots is mainly influenced by the separation distance, and the number of petals increased as the separation distance increased. The 2D directivity plots are asymmetric in Figures 12C, D because the scatterers are asymmetric along the wave axis in the oblique incidence case, which is different from the end-on incidence and broadside incidence case. In the end-on incidence case (see Figures 12A, B), the 2D directivity plots of a pair of rigid spheroids change from the forward scattering dominant to the sideward scattering dominant, with the increase in the aspect ratio. The maximum values in the 2D far-field directivity plots of a pair of rigid spheroids decrease as the aspect ratio increases in the end-on incidence and oblique incidence cases. In the broadside incidence case (Figures 12E, F), the 2D directivity plots of a pair of oblate spheroids and prolate spheroids are sideward scattering dominant and backward scattering dominant, respectively. It can be found that the 2D far-field directivity plots of a pair of rigid prolate spheroids with different aspect ratios at the same incident angle and separation distance are very similar, and the values of the scattering form function $|f_\infty|$ decreases as the aspect ratio increases.

4 Conclusion

In this work, the *T*-matrix method combined with the addition theorems of spherical basis functions is applied to semi-analytically compute the far-field acoustic scattering of a pair of rigid spheroids under the plane wave at an arbitrary incidence angle. It is verified that the *T*-matrix method can accurately solve the far-field acoustic scattering problem of a pair of rigid spheres with different separation distances under the plane wave of any angle. In addition, some numerical experiments on a pair of rigid (oblate or prolate) spheroids are carried out by the *T*-matrix method with the following conclusions:

1) The acoustic scattering by a pair of rigid spheroids is more complicated than that of a single rigid spheroid, and the values of the scattering form function of a pair of rigid spheroids are not equal to twice the far-field scattering form function modulus of a single rigid spheroid.
2) The peak-to-peak interval of the backscattering response curve obtained by the IFFT in the time domain is consistent with the geometric prediction results, which makes it possible to estimate the geometrical dimension and separation distance of multiple scatterers from the scattering response wave.
3) The parameters affecting the far-field scattering form function modulus of a pair of rigid spheroids are aspect ratio b/a, separation distance $2d$, dimensionless frequency kr_0 ($r_0 = \max(a, b)$), and incident angle θ_i.

Data availability statement

The original contributions presented in the study are included in the article/Supplementary Material; further inquiries can be directed to the corresponding author.

Author contributions

WL conceptualized this investigation. YY performed the formal analysis and validation. YY performed the data analysis with advice from QG, YZ, YC, and WL. YY wrote the manuscript. All authors contributed to the article and approved the submitted version.

Conflict of interest

The authors declare that the research was conducted in the absence of any commercial or financial relationships that could be construed as a potential conflict of interest.

Publisher's note

References

1. Seybert AF, Rengarajan TK. The use of CHIEF to obtain unique solutions for acoustic radiation using boundary integral equations. *The J Acoust Soc America* (1987) 81(5):1299–306. doi:10.1121/1.2024508

2. Hunt JT, Knittel MR, Barach D. Finite element approach to acoustic radiation from elastic structures. *The J Acoust Soc America* (1974) 55(2):269–80. doi:10.1121/1.1914498

3. Seybert AF, Soenarko B, Rizzo FJ, Shippy DJ. An advanced computational method for radiation and scattering of acoustic waves in three dimensions. *J Acoust Soc America* (1985) 77(2):362–8. doi:10.1121/1.391908

4. Chai YB, Li W, Gong ZX, Li TY. Hybrid smoothed finite element method for two-dimensional underwater acoustic scattering problems. *Ocean Eng* (2016) 116:129–41. doi:10.1016/j.oceaneng.2016.02.034

5. Li W, Chai YB, Lei M, Li TY. Numerical investigation of the edge-based gradient smoothing technique for exterior Helmholtz equation in two dimensions. *Comput Structures* (2017) 182:149–64. doi:10.1016/j.compstruc.2016.12.004

6. You X, Gui Q, Zhang Q, Chai Y, Li W. Meshfree simulations of acoustic problems by a radial point interpolation method. *Ocean Eng* (2020) 218:108202. doi:10.1016/j.oceaneng.2020.108202

7. Gui Q, Zhang G, Chai Y, Li W. A finite element method with cover functions for underwater acoustic propagation problems. *Ocean Eng* (2022) 243:110174. doi:10.1016/j.oceaneng.2021.110174

8. Rayleigh JWSB. *The theory of sound*. London: Macmillan &Company (1896).

9. Faran JJ, Jr. Sound scattering by solid cylinders and spheres. *The J Acoust Soc America* (1951) 23(4):405–18. doi:10.1121/1.1906780

10. Morse PMC, Ingard KU. *Theoretical acoustics*. New Jersey: Princeton university press (1986).

11. Záviška F. Über die Beugung elektromagnetischer Wellen an parallelen, unendlich langen Kreiszylindern. *Annalen der physik* (1913) 4(40):1023–56. doi:10.1002/andp.19133450511

12. Williams KL, Marston PL. Backscattering from an elastic sphere: Sommerfeld–Watson transformation and experimental confirmation. *J Acoust Soc America* (1985) 78(3):1093–102. doi:10.1121/1.393028

13. Eyges L. Some nonseparable boundary value problems and the many-body problem. *Ann Phys* (1957) 2(2):101–28. doi:10.1016/0003-4916(57)90037-4

14. Sack RA. Three-dimensional addition theorem for arbitrary functions involving expansions in spherical harmonics. *J Math Phys* (1964) 5:252–9. doi:10.1063/1.1704115

15. Gabrielli P, Mercier-Finidori M. Acoustic scattering by two spheres: Multiple scattering and symmetry considerations. *J Sound Vibration* (2001) 241(3):423–39. doi:10.1006/jsvi.2000.3309

16. Gaspard P, Rice SA. Exact quantization of the scattering from a classically chaotic repellor. *J Chem Phys* (1989) 90(4):2255–62. doi:10.1063/1.456019

17. Waterman PC. Matrix formulation of electromagnetic scattering. *Proceeding of the IEEE* (1965) 53(8):805–12. doi:10.1109/PROC.1965.4058

18. Waterman PC. New formulation of acoustic scattering. *J Acoust Soc America* (1969) 45(6):1417–29. doi:10.1121/1.1911619

19. Peterson B, Ström S. Matrix formulation of acoustic scattering from an arbitrary number of scatterers. *J Acoust Soc America* (1975) 56:771–80. doi:10.1121/1.1903325

20. Mishchenko MI. *Electromagnetic scattering by particles and particle groups: An introduction*. New York: Cambridge University press (2014).

21. Mishchenko MI, Hovenier JW, Tracis LD. *Light scattering by nonspherical particles: Theory, measurements, and applications*. Academic Press (1986).

22. Danos M, Maximon LC. Multipole matrix elements of the translation operator. *J Math Phys* (1965) 6(5):766–78. doi:10.1063/1.1704333

23. Gonis A, Butler WH. *Multiple scattering in solids*. New York: Springer (2000).

24. Edmonds AR. *Angular momentum in quantum mechanics*. Princeton, NJ: Princeton University Press (1974).

25. Neubauer WG, Vogt RH, Dragonette LR. Acoustic reflection from elastic spheres. I. Steady-state signals. *J Acoust Soc America* (1974) 55:1123–9. doi:10.1121/1.1914676

26. Dragonette LR, Vogt RH, Flax L, Neubauer WG. Acoustic reflection from elastic spheres and rigid spheres and spheroids. II. Transient analysis. *J Acoust Soc America* (1974) 55:1130–7. doi:10.1121/1.1914677

27. Li W, Chai YB, Gong ZX, Marston PL. Analysis of forward scattering of an acoustical zeroth-order Bessel beam from rigid complicated (aspherical) structures. *J Quantitative Spectrosc Radiative Transfer* (2017) 200:146–62. doi:10.1016/j.jqsrt.2017.06.002

28. Gaunaurd GC, Huang H, Strifors HC. Acoustic scattering by a pair of spheres. *J Acoust Soc America* (1995) 98:495–507. doi:10.1121/1.414447

29. Pillai TAK, Varadan VV, Varadan VK. Sound scattering by rigid and elastic infinite elliptical cylinders in water. *J Acoust Soc America* (1982) 72:1032–7. doi:10.1121/1.388234

30. Eastland GC, Marston PL. Enhanced backscattering in water by partially exposed cylinders at free surfaces associated with an acoustic Franz wave. *J Acoust Soc America* (2014) 135:2489–92. doi:10.1121/1.4870240

31. Gong ZX, Li W, Mitri FG, Chai YB, Zhao Y. Arbitrary scattering of an acoustical Bessel beam by a rigid spheroid with large aspect-ratio. *J Sound Vibration* (2016) 383:233–47. doi:10.1016/j.jsv.2016.08.003

32. Gong ZX, Li W, Chai YB, Zhao Y, Mitri FG. T-matrix method for acoustical Bessel beam scattering from a rigid finite cylinder with spheroidal endcaps. *Ocean Eng* (2017) 129:507–19. doi:10.1016/j.oceaneng.2016.10.043

33. Li W, Liu GR. Estimation of radius and thickness of a thin spherical shell in water using the midfrequency enhancement of a short tone burst response. *J Acoust Soc America* (2005) 118:2147–53. doi:10.1121/1.2040027

34. Tang WL. Highlight model of echoes from sonar targets. *Chin J Acoust* (1994) 13:131–40. doi:10.15949/j.cnki.0217-9776.1994.02.004

Frontiers in Physics

Investigates complex questions in physics to understand the nature of the physical world

Addresses the biggest questions in physics, from macro to micro, and from theoretical to experimental and applied physics.

Discover the latest Research Topics

See more →

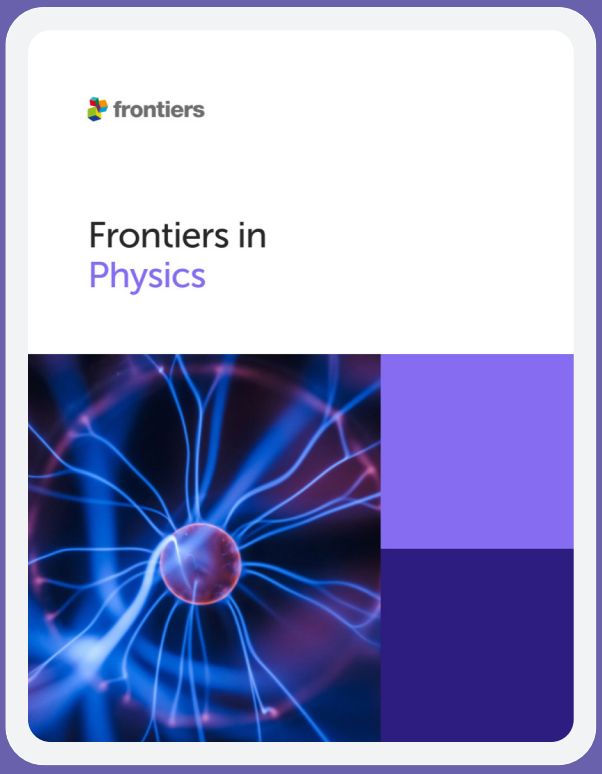

Frontiers

Avenue du Tribunal-Fédéral 34
1005 Lausanne, Switzerland
frontiersin.org

Contact us

+41 (0)21 510 17 00
frontiersin.org/about/contact